MULTIPLE THREE-PHASE INDUCTION GENERATORS FOR WIND ENERGY CONVERSION SYSTEMS

IVAN ZORIĆ

A thesis submitted in partial fulfilment of the requirements of Liverpool John Moores University for the degree of Doctor of Philosophy

January 2018

ABSTRACT

During the past decade, there has been a considerable increase in the number of published works on multiphase machines and drives. This increased interest has been largely driven by a need for the so-called green energy, i.e. energy generated from renewable sources such as wind, and also an increased emphasis on greener means for transportation. Some of the advantages multiphase machines offer over three-phase counterparts are better fault tolerance, smaller current and power per phase, and higher frequency torque ripple.

This thesis examines use of a multiphase induction generator in wind energy conversion systems (WECS). In particular, multiphase generators that comprise multiple 3-phase winding sets, where each winding set is supplied using an independent 3-phase voltage source inverter (VSI), are studied. It is claimed that these topologies offer advantages in cases where a WECS is connected to a multitude of independent ac or dc microgrids, systems where a single high-voltage dc link is needed or where a simple fault tolerance is achieved when a complete winding set is switched off. All of these examples require an arbitrary power or current sharing between winding sets.

In order to achieve arbitrary current and power sharing, the control can be implemented using multi stator (MS) variables, so that the flux and torque producing currents of each winding set can be arbitrarily set. As an alternative, this thesis uses vector space decomposition (VSD) to implement the control, while individual winding set flux/torque producing currents are governed by finding the relationships between MS and VSD variables. This approach has all the advantages of both MS and VSD, i.e. access to individual winding set variables of MS and the ability to implement control in the multiple decoupled two dimensional subspaces of VSD, while heavy cross coupling between winding set variables, a weakness of MS, is avoided.

Since the goal of the thesis is to present use of multiphase machines in WECS, modelling and simulation of a simple multiphase WECS in back-to-back configuration has been performed at first. All systems relevant to machine control where considered, such as grid and machine side VSIs, grid filter, indirect rotor field oriented control, current control in both flux/torque producing and non-producing subspaces, low order harmonic elimination, maximum power point tracking control, and voltage oriented control of the grid side VSI. Moreover, various WECS supply topologies were considered where developed current and power sharing would be a necessary requirement.

Development of the proposed current sharing control commences with an analysis of multiple 3-phase machine modelling in terms of both MS and VSD variables. Since the actual control is implemented using decoupled VSD variables, VSD modelling has been studied in detail, resulting in an algorithm for creation of the VSD matrix applicable to any symmetrical or asymmetrical multiphase machine with single or multiple neutral points. Developed algorithm always decouples the machine into orthogonal two-dimensional subspaces and zero sequence components while making sure that all odd-order harmonics are uniquely mapped. Harmonic mapping analysis is offered as well. Next, relationship between MS and VSD variables has been developed by mapping MS variables into VSD subspaces. Since VSD matrix creation algorithm is valid for any multiphase machine, relationship between MS and VSD variables is applicable to any multiple 3-phase machine regardless of the configuration (symmetrical/asymmetrical), number of neutral points or machine type (synchronous or induction).

Established relationship between MS and VSD has been used to implement current sharing control in decoupled VSD subspaces of the machine. It is shown that in order to achieve arbitrary current sharing it is only necessary to impose currents in flux/torque non-producing subspaces. Hence, total machine's flux and torque are not affected at all. Besides verification by Matlab simulations, two topologies are experimentally investigated, a parallel machine side converter configuration and the case when a single high voltage dc link is created by cascading dc-links of the machine side VSIs. In the first case the ability of arbitrary current sharing between winding sets is validated, while the second tested topology demonstrates use of the developed control for the purpose of voltage balancing of the cascaded dc links.

ACKNOWLEDGMENT

I would like to express my sincere gratitude to several people who have helped me to develop as a researcher, become a better person as well as complete this thesis in the best possible way.

Firstly, my deepest gratitude goes to my supervisors, Dr Martin Jones and Prof Emil Levi, for their exceptional mentoring and wholehearted support during the course of my PhD studies. Without their immense patience and vast knowledge, completion of this thesis would not be possible. It was a privilege to study under your supervision.

Next, I would like to express my sincere appreciation to my friend Dr Milan Darijevic, without whom my PhD studies would not have commenced. Due to his unique ability to persuade people to look beyond their comfort zone, colloquially referred to as “Milan-isation”, I was offered this life changing opportunity. His friendship, ability to challenge everything and everybody as well as endless discussions have jump-started my career as a researcher.

My huge gratitude goes to Prof Predrag Pejovic and Prof Lazar Saranovac for believing in me and supporting my application for PhD studies. Furthermore, I owe a great deal of gratitude to Prof Pejovic and Prof Slobodan Vukosavic for introducing me to the fields of Power Electronics and Electric Machines and Drives. Their teachings have defined my career path, for which I am grateful.

During the course of my PhD studies, one of the most influential persons was Dr Obrad Dordevic. His help in development of my academic career was immense, as well as his friendship which made my stay in Liverpool a very enjoyable experience. All the discussions we had in the office and laboratory have vastly influenced my course of research and often made me know that I know nothing.

There are a few more people I would like to credit for being a true friends and exceptional colleagues during my stay in Liverpool. These are Dr Ivan Subotic, Dr Nandor Bodo, Dr Engku Ahmed Rafiqi, Mr Ahmad Abduallah, and Mr Marko Slunjski. Sharing an office with them was a pleasure and I could only feel honoured to call them friends. Further, I would like to acknowledge Mr Steven Gotts for his help and skills in assembling multiple experimental setups in our laboratory. Moreover, he was a true friend and his positive attitude towards everything I will never forget.

During my stay in Liverpool, I was lucky enough to meet Mr Sandro Rubino, Dr Ignacio Gonzalez-Prieto, Prof Mario Duran and Mr Aitor Tovar who have provided me with an opportunity to work outside my thesis topic, which broadened my views and understanding of electric machine drives. I am sure that during their stay I become wealthier for a few friends more, one of the priceless things in life!

Last but not least, I would like to thank my family for their endless love and understanding, which has always kept me inspired and has given me the strength to move forward. This includes my son Lazar, whose birth during the writing of this thesis has brought an unimaginable amount of joy to my family. Moreover, I would like to dedicate this thesis to my wife Vesna, who was always by my side and her love, patience and support have made this thesis her accomplishment as well as it is mine.

CONTENTS

LIST OF PRINCIPAL SYMBOLS

n	Number of phases of the machine/inverter
k	Number of phases in a single winding set of the machine
l	Number of winding sets
θ, α, φ	Angle in radians
ω	Angular speed in radians per second (if not stated otherwise)
v	Voltage in general (determined by index)
i	Current in general (determined by index)
ψ	Flux-linkage in general (determined by index)
V_{dc}	Dc-link voltage when constant, otherwise denoted as any other voltage, i.e. v_{dc}
P_m, P_t	Mechanical and wind turbine powers
P_g, Q_g	Active and reactive power transferred to the grid
$\underline{S}_i$, P_i, Q_i	Complex, active and reactive power of the i^{th} winding set of the machine
R	Resistance in general (determined by index)
L, M	Inductance in general (determined by index)
J	Inertia in general (determined by index)
T	Torque in general (determined by index)
P	Number of pole pairs
a, b, c, d, …	Machine/inverter phases/legs in general or in sub-script to denote principal symbol, e.g. v_a, i_a, θ_a – machine phase a voltage, current and angle
r	In sub-script denotes rotor variables
R, S, T	Grid phases in general or in sub-script to denote principal symbol, e.g. v_R phase R grid voltage
$[C_3(\alpha)]$	Clarke's transformation of the 3-phase winding set at the angular position α
$[T_{VSD}]$	Vector space decomposition transformation, e.g. $[T_{9a}]$ – transformation for asymmetrical 9-phase machine
α-β, x-y, z_+, z_-	Indices denoting values after vector space decomposition or Clarke's transformation in stationary reference frame
d-q	Indices denoting values in rotational reference frame
e_d, e_q	Indirect rotor field oriented control decoupling terms
$G(s)$	Transfer function in Laplace domain
S	Inverter leg gating signal (switching state)
$\underline{f}$	Line bellow the symbol denotes complex value
$\overline{f}$	Line above the symbol denotes complex conjugate value
F	Capital symbol denotes amplitude (if not stated otherwise)
$[F]$	Square brackets denote matrix or vector value
f^*	Asterisk in superscript denotes reference value

LIST OF USED ABBREVIATIONS

WECS	Wind energy conversion system
DSP	Digital signal processor
VSI	Voltage source inverter
CSI	Current source inverter
DFIG	Doubly fed induction generator
MS	Multi stator
VSD	Vector space decomposition
PWM	Pulse width modulation
CBPWM	Carrier based pulse width modulation
SVPWM	Space vector pulse width modulation
RFOC	Rotor field oriented control
DRFOC	Direct rotor field oriented control
IRFOC	Indirect rotor field oriented control
MMF	Magneto-motive force
EMF	Electro-motive force
NPC	Neutral point clamped
PI	Proportional-integral
PID	Proportional-integral-derivative
PIccd	Proportional-integral with cross-coupling decoupling
cvPI	Complex vector proportional-integral
PR	Proportional-resonant
VPI	Vector proportional integral
VOC	Voltage oriented control
PLL	Phase locked loop
MPPT	Maximum power point tracking
SRF	Synchronous reference frame
FEM	Finite element method

Chapter 1

INTRODUCTION

1.1 Preliminary Considerations

The search for alternative energy sources is of the utmost importance for the mankind, especially when most of the currently generated electrical energy comes from fossil fuels such as coal and oil. Fossil fuel reserves are limited and their usage pollutes the air, water and soil. Renewable energy sources can offer a solution to many of the problems associated with fossil fuels. The energy delivered to the Earth from the sun is manifested in different ways. Tidal, wind and light energy are the three renewable energy sources most frequently used. Wind energy has become one of the fastest growing renewable energy sources [Wu et al., 2011]. As a consequence, the demand for efficient and robust wind energy conversion systems (WECS) is growing.

Successful operation of a wind turbine depends on many factors such as the availability of the wind, mechanical construction of the turbine, ease of access and the electrical subsystem. Advancements in the mechanical subsystem are mainly related to the improvements of the gearbox design in order to increase its reliability. Further, it is possible to completely remove it by use of low speed high pole number synchronous machine. As far as the electrical subsystem is concerned, many improvements have been made over the years in terms of the efficiency and robustness of the electrical systems. Namely, in the last 20 years, there have been advancements in switching technology, digital control and electric generator design.

The early WECS comprised wind turbines with 3-phase induction machines used as a generator [Singh et al (2006)]. These were fixed speed WECS, consequently they were able to work in a narrow wind speed range and the generator itself was completely uncontrolled. A small amount of control was achieved by pitch and stall control of the wind turbine blades. The capability of these systems to extract the maximum possible power from the wind regardless of the wind conditions is very low. With the development of high power semiconductor switches and digital signal processors (DSPs), power electronics started to be used in WECS. They made it possible to use variable speed drives in WECS. This had a huge impact on the efficiency of the WECS. The operational wind speed range was significantly increased and WECS became more controllable to accommodate different operating conditions and strict grid codes.

Voltage source inverters (VSI) are usually used in variable speed drives due to their simple construction. If high performance operation is required, such as precision speed or position control, usage of a digital signal processor is usually mandatory. Variable speed operation of the electrical machines is not beneficial only for WECS. In almost any industrial application a lot of energy can be saved with variable speed drives. For example, a heating, ventilation and air conditioning (HVAC) system has huge improvement in efficiency if its compressor has variable speed. A lot of electrically driven machinery has peak efficiency at different speeds depending on its operating condition. On the other hand, in some applications variable speed is mandatory; but, before inverter control was developed variable speed drives were based on dc machines which were unreliable, mainly due to the commutator and carbon brushes.

Historically speaking, 3-phase machines were the first ac machines to be used in variable speed drives. Due to the 3-phase grid, 3-phase machines are the most researched ones and it was easy to implement variable speed operation once the high power switching technology and digital signal processors became available. One of the major issues with the 3-phase machines is that they are not inherently fault tolerant, meaning that when one of the phases fails usually the machine needs to be stopped. A special machine and/or inverter design would be needed to make a 3-phase machine fault tolerant. Furthermore, when a 3-phase machine is used in high power applications, due to the voltage and current limits a special winding construction is necessary. Furthermore, the limitations of semiconductor devices lead to a requirement for increasingly complex inverter structures.

Multiphase machines offer solutions to the aforementioned issues. Usually these machines have multiple 3-phase winding sets or a prime number of phases greater than 3. One of the obvious advantages is that power is shared between more phases, meaning that power per phase is smaller and there is no need to use special winding designs [Tessarolo (2010b)], i.e. an expensive Roebel bars technology. Moreover, simpler inverter structures with switches of a lower rating can be used, resulting in a cheaper system. Another huge advantage of the multiphase machines is fault tolerance. Machines with more than three phases can operate with reduced capacity if one or more phases are lost due to a fault. This is especially crucial for operation in critical applications such as more-electric aircraft.

Regardless of the number of phases, an inverter decouples the machine from the 3-phase grid. Hence, the machine phase number is a design parameter available to the engineer. Initially, researchers used 2-level voltage source inverters to supply the multiphase machine. Recently multilevel inverters have gained research interest [Dordevic 2013a] with the primary aim being to increase the power and quality of the output waveforms. Multiphase machines are particularly well suited to applications requiring high power, high performance variable speed drives, such as traction, ship propulsion, WECS, more electric aircraft and other high power industrial applications [Levi et al (2007), Levi (2008)].

With requirement of variable speed operation and multi-megawatt power ratings, WECS are an ideal candidate for multiphase machines. More than three phases will lead to less power per phase and inverter switches of the lower rating resulting in cheaper and easy for maintenance inverter design.

Fault-tolerance capability of the multiphase machines is ideal for offshore wind farms where maintenance is not easily available and every stop in operation is costly. Furthermore, mechanical gearbox which is commonly a part of the WECS, benefits greatly from the lower torque ripple of the multiphase machine.

Regarding the machine type, the most frequently used machines in WECS are induction, synchronous with wound rotor and permanent magnet machines. Asynchronous machines with the slip rings are predominantly used as a doubly-fed generator where the rotor winding is supplied from a smaller capacity converter. In this case, the controllability of the machine during the grid fault can be challenging when compared to a fully controllable drive with a converter that is rated to handle the full power of the drive. This is the most frequent machine type used in WECS [Wu et al (2011)]. A drawback of this system is an expensive rotor and slip rings maintenance issues. On the other hand, both permanent magnet and cage induction machines benefit from the brushless operation. Both types require a full capacity converter, but in return their fault ride-through performance is superior when compared to DFIG. When compared with a permanent magnet machine, larger rotor losses of the induction machine are usually insignificant when the robustness and low cost construction of the induction machine rotor is taken into consideration.

The connection to the main grid in the large offshore wind farms is sometimes made via a high voltage dc link. When a multiphase machine with multiple 3-phase winding sets is used as a generator, more than one 3-phase converter is used to supply the machine and a higher dc-link voltage can be achieved without step-up dc-dc converter. For example, in a 6-phase machine two 3-phase VSIs can be used with dc links connected in series [Che et al (2012b)]. As a result, the total dc voltage will be twice the value of the individual inverters dc-link voltages. There is always a trade-off and in this configuration the fault tolerance of the machine is compromised.

1.2 An Overview of Multiphase Machines in WECS

Due to the unavailability of the high power switches, firstly developed WECS had used constant speed induction motor as a generator and their speed was governed by the grid frequency [Blaabjerg and Chen (2006)]. This configuration has the advantage of robust and simple construction, but the lack of control has a consequence of very narrow operational speed range and high mechanical stress.

With the advancement in switching devices technology and development of energy efficient inverters, industry has moved to the variable speed WECS. The doubly-fed induction generator (DFIG) offers an alternative solution to WECS requiring full capacity converters. In this configuration the stator windings are directly connected to the grid, while a reduced capacity converter is used to supply the rotor windings. The smaller converter also brings disadvantages such as: wound rotor, slip rings and smaller wind speed range. On the other hand, induction generator with the squirrel cage rotor needs full capacity converter, but in return provides superior fault ride-through performance, robust construction and almost maintenance-free operation. Currently, the mostly utilized variable speed WECS are doubly-

fed or full capacity with induction or synchronous generator [Anaya-Lara et al (2009), Liserre et al (2011)].

The aim of this research is to explore the use of multiphase induction machines with full capacity converter in WECS. With its simple construction, induction machine is the machine of choice due to the robustness and low production and maintenance costs. When compared to the 3-phase counterparts, a multiphase machine has many benefits, such as lower power/current per phase and fault-tolerant operation [Levi et al (2008)]. In addition, machines with multiple 3-phase winding sets have an advantage of using widely available and well-understood 3-phase inverters. Furthermore, series or parallel connection of these inverters enables use of different topologies; hence various application specific requests can be accommodated. Other advantages of multiphase machines over the 3-phase counterparts have been reported in [Tessarolo (2010a)], where it is shown that production cost and complexity of the high power multiphase machines are less when compared to the 3-phase ones. This is mainly due the fact that multiphase machines have less current per phase and do not need special winding construction. On the other hand, a 3-phase machine is a very well-known and an off-the-shelf solution with a vast knowledge base on design and actual production process is available. Furthermore, adoption rate of multiphase machines in wind energy is very low and each application would represent a reach into unknown where design and production might be costly and challenging. Therefore, all these circumstances need to be taken into consideration when developing a real-world multiphase WECS.

When modelling of multiphase machines is concerned, three modelling approaches are usually used: phase domain modelling, vector space decomposition and the multi stator (MS) modelling approach. Modelling in phase variables is the simplest and most straightforward way. Namely, *n*-phase machine is modelled in its natural *n*-dimensional space [Dordevic et al (2010)]. A disadvantage of this modelling approach is its complexity and very difficult implementation of any high performance control, i.e. vector control. Contrary to the modelling in phase variables, when transformation to arbitrary reference frame is applied machine equation are simplified. Vector space decomposition (VSD) can be applied to decouple machine equations into flux/torque producing and non-producing subspaces [Zhao and Lipo (1995)]. As a result, flux/torque producing subspace will be used for high performance vector control, while non-producing subspaces may be used for some specific purposes, like fault tolerance [Che et al (2014b)]. Of course, depending on the number of phases and whether the machine has one or multiple isolated neutral points, a different transformation matrix will be used [Levi et al (2007)]. The third modelling approach is only applicable to multiphase machines with multiple winding sets and it is based on applying decoupling transformation to each of the winding sets [Nelson (1974)]. As a result, each winding set can be independently controlled, but the disadvantage is that it is hard to explain stator current harmonic content since this approach does not consider flux/torque non-producing components. The use of this approach has also been reported for the 9-phase case in [Jung et al (2009)] where a 9-phase machine is used in an ultra-high speed elevator. Comparison of the MS and VSD modelling

approaches for the 6-phase case has been presented in [Che et al (2014a)], where the currents in flux/torque non-producing subspaces are presented as circulating currents between winding sets.

Due to its simplicity, the most researched inverter type is 2-level voltage source inverter. Realisation of modulation strategies for VSI supplied multiphase drives varies. Firstly, developed modulation strategies were based on 180 degrees conduction mode, but development of high speed high power switches has enabled pulse width modulation (PWM) strategies to be implemented, specifically, carrier based PWM (CBPWM) and space vector PWM (SVPWM). Since CBPWM is based only on comparing the references with a carrier, it is easy to implement regardless of the number of phases. On the other hand, SVPWM requires a complex dwell time calculation algorithm even for the 3-phase drives. When extended to multiphase systems, complexity of SVPWM implementation gets more pronounced because the number of possible switching vectors is increased and the dwell time calculations become increasingly demanding.

A detailed analysis of 3-phase PWM strategies is given in [Holmes and Lipo (2003)]. For the case of a 6-phase induction machine with two isolated neutral points, comparison of the CBPWM with different SVPWM strategies has been presented in [Bojoi et al (2002)]. When the multiphase machines with nine and fifteen phases are concerned, work on CBPWM has been reported in [Dong et al (2008)] and [Benatmane and McCoy (1998)]. On the other hand, SVPWM is widely implemented in both 6-phase [Dujic et al (2007a), Zhao and Lipo (1995), Prieto et al (2010)] and 9-phase [Dujic et al (2007b), Grandi et al (2007a), Kelly et al (2003)] cases. Another important parameter to consider is the dc-link voltage utilization. It is well known that SVPWM has 15.4% better dc-link voltage utilisation than pure sinusoidal CBPWM for 3-phase systems. When extended to multiphase systems, dc-link voltage utilisation is highly dependent on the number of phases, whether the machine is symmetrical or asymmetrical, and the number of neutral points [Dujic et al (2010), Levi et al (2008)].

To be able to fully utilise available wind power, it is mandatory that the used machine has high performance speed or torque control. In almost all cases of variable speed WECS where induction machine with cage rotor is used, control of choice is the indirect rotor field oriented control (IRFOC) [Wu et al (2011)]. In the case of the multiphase machines, IRFOC is implemented by obtaining the flux/torque producing *d-q* components by means of the VSD or MS modelling approaches. For the 6-phase machine IRFOC implementation has been reported in [Singh et al (2005a)], while in the case of a 9-phase machine the same has been done in [Hu and Yung (2011)].

In any high performance control strategy, it is of the utmost importance to have high speed current controllers when compared to the mechanical time constants of the system. The current control algorithms used for multiphase machines vary. It is necessary to control currents in all subspaces. Due to the very low impedance in the flux/torque non-producing subspaces huge currents can be present due to the asymmetry of the machine phases [Jones et al (2009)]. One of the possible solutions is to have two PI regulators in *d-q* reference frame and resonant regulators in *x-y* planes tuned at specific harmonics [Che et al (2014c), Yepes et al (2013)]. Another solution to current control is proposed in

[Bojoi et al (2003b), Hua et al (2006)], where machines with multiple winding sets were modelled using the MS modelling approach and current control has been done in each of the *d-q* subspaces. Alternatively, current control of the subspaces can be achieved by the multiple resonant controllers [Yepes (2011)]. It was concluded in [Holmes et al (2012)] that all the investigated current regulator types will produce similar results when properly tuned.

One of the benefits of the multiphase machines when used in off-shore WECS is their fault tolerance, meaning that they can continue to operate with reduced capacity even if one or more phases is under fault. This is of great importance when the WECS are located in areas where easy access for maintenance purposes is not possible. The detection of the faults in multiphase machines by the means of analysing flux/torque non-producing subspaces has been proposed in [Zarri et al (2011)]. A number of different solutions for operation under fault conditions have been proposed. The simplest one is to switch off the entire winding set containing the faulted phase in the machines with multiple neutral points [Alberti and Bianchi (2012)]. Other solutions propose changes in the control so the MMF is kept at rated value [Fu and Lipo (1994)], minimisation of the losses in the remaining phases [Apsley (2010)] and minimum torque oscillations [Tani et al (2012)]. Another, very popular method is to change the transformation matrix to accommodate lost phases [Deilmani et al (2011)]. Alternatively, the same decoupling matrix can be used, but references to the current controllers in *x-y* plane should be changed according to the present fault [Che et al (2014a)].

The converter topologies used in WECS vary depending on the configuration of the WECS itself. If the WECS is connected to the local dc link of a wind farm or the high voltage cable than only machine-side inverters are used. On the other hand, if WECS is connected directly to the grid then use of the grid-side inverter is mandatory. Nevertheless, when a multiphase generator is used, there are many possible inverter configurations to accommodate specific needs. Namely, if the machine has composite number of phases multiple inverters can be used on the machine side. If dc links of the inverter are connected in parallel better fault tolerance and modularity is achieved [Sun et al (2015), Andersen and Birk (2007), Brisset et al (2008)]. On the other hand, if the dc links of the inverters are connected in series, high voltage level can be achieved which is highly desirable for offshore wind farms regardless of the actual connection to the mainland, i.e. HVDC or AC connection [Blaabjerg et al (2006)]. It should be pointed out that despite all of the advantages of HVDC, in reality there is only a handful of wind farms that use this technology. Series connection of the inverters has been proposed in [Duran et al (2011), Che et al (2012b), Che et al (2014b)]. Solutions for the grid-side inverters vary, but usually it is required to use multilevel inverters to accommodate strict grid codes. Due to its simple construction and easy control, one of the widely used multilevel inverters is of the neutral point clamped (NPC) type [Nabae et al (1982)].

Control of the grid-side inverter is usually done using the well-known voltage oriented control (VOC), where two PI current regulators in synchronous reference frame are used, plus one PI voltage regulator for dc-link voltage control [Blaabjerg et al (2006)]. Grid connected inverters require a grid

synchronisation which is usually achieved using a phase locked loop (PLL). PLL grid synchronisation techniques with regard to the grid voltage and phase unbalances are proposed in [Chung (2000a), Chung (2000b), Arruda et al (2001)].

In every WECS the outer control loop is the maximum power point tracking (MPPT) and it is related to the characteristics of the wind turbine. Depending on the wind speed and turbine profile, MPPT will provide a torque or speed reference so that the optimal tip speed of the turbine blades is achieved [Wu et al (2011)]. This results in the maximum power being extracted from the available wind.

1.3 Research Objectives and Novelty

The aim of this research is to explore the application of multiphase induction machines to wind energy conversion systems with the intent to develop current and power sharing between winding sets of multiple 3-phase machines that can accommodate rather different supply topologies and power needs. The aforementioned will be achieved by completing the following objectives:

1) To develop machine model using various modelling approaches: phase variables, multi stator (MS) and VSD. All models should be developed for a general *n*-phase case, with exception of the MS which is developed only for multiple 3-phase machines. Furthermore, used VSD matrix should be generalised so that it can be applied to both symmetrical and asymmetrical configurations. Analysis of harmonic mapping and comparison of modelling approaches should be carried out as well.
2) To develop a model of the complete WECS, including MPPT control, IRFOC, VOC, both grid-side current control and synchronisation and machine-side current control including current control of fundamental frequency components in α-β and x-y subspaces and resonant current control for low order harmonics elimination. Furthermore, models of machine-side 2-level VSI and grid-side 3-level NPC VSI should be implemented together with appropriate modulation techniques.
3) To understand the relationship between VSD and MS modelling approaches, so that the benefits of both can be utilised. This will enable access to both MS variables, which hold information on currents in individual winding sets, and decoupled VSD variables, which easies control implementation.
4) Use the relationship between MS and VSD modelling approaches to develop arbitrary current and power sharing between winding sets of multiple 3-phase winding machines so that it can be used in a general case.
5) One of the possible uses of developed power sharing between winding sets is to balance voltages of the cascaded dc links supplying the multiphase machine with isolated neutral points. This application will be explored and a dc-link voltage-balancing controller developed.
6) Develop an experimental prototype to verify proposed theoretical concepts and the developed control algorithms. Compare the results with the numerical simulations and analyse the performance.

The novelty of the conducted work comes from the completion of the objectives mentioned above. Starting with the modelling of the multiphase machines, an algorithm for the creation of VSD matrix for any multiphase machine has been proposed resulting in [Zoric et al (2017b)]. In addition, unbalance in the zero-sequence harmonics of the phase voltages in the case of asymmetrical multiphase machine with single neutral point is reported in [Zoric et al (2016)]. Analytical expression for unbalance in phase voltages that exists even if the leg voltages are balanced is found. When it comes to the current and power sharing technique, a review of power sharing techniques between winding sets of a multiple 3-phase machine is presented in [Zoric et al (2017)]. The current and power sharing has been developed for any multiple 3-phase machine in [Zoric et al (2018a)]. Here, a relation between MS and VSD variables is found so that benefits of both modelling approaches can be utilised to the full extent, i.e. decoupled control of VSD and information on individual winding set variables of MS modelling. Developed current sharing has been extended so that both *d*- and *q*-axis winding set currents of any multiple 3-phase machine can be arbitrarily set. This allows independent control of flux/torque contribution of each winding set to the total flux and torque of the machine. Results are reported in [Zoric et al (2018b)]. The developed power sharing technique is used to balance dc-link voltages of cascaded VSIs supplying a symmetrical 9-phase machine resulting in [Zoric et al 2017a].

1.4 Organisation of the Thesis

This thesis is divided into 8 chapters as follows:

Chapter 1 provides an introduction to the wind energy conversion systems and multiphase machines in general. A brief discussion of the advantages multiphase machines possess over 3-phase ones, with regard to application in WECS, is offered. This chapter is completed with list of research objectives and discussion of novelty and organisation of the thesis.

Chapter 2 provides a literature survey of current state-of-the-art in multiphase machine drives and their application in WECS. The literature covered deals with multiphase machines in general, modelling, modulation techniques, current control, current and power sharing between winding sets, fault tolerance, converter topologies and finally the control systems required for operation of a single WECS.

Chapter 3 introduces WECS and sets the context of the thesis by providing the possible applications of the developed control strategies. All necessary subsystems, relevant to the multiphase machine operation in WECS, are covered, such as: wind turbine blades, pitch control, gearbox, 2-level machine-side VSI, 3-level grid-side NPC VSI, IRFOC, VOC, PLL for grid synchronisation, MPPT control and various current control schemes. Different WECS topologies where a multiphase machine is used as a generator are covered showing applications where use of a 3-phase machine would not suffice.

Chapter 4 deals with the modelling of the multiphase machines in phase variables, by multi stator modelling approach and by the use of VSD. In order to develop VSD modelling in a general case, creation of VSD matrix has been dealt with in this chapter as well. Most importantly, this chapter

provides analytical relationship between MS and VSD variables, which sets the basis for current and power sharing developed in the following chapters. Furthermore, it is shown here that there is an imbalance in zero-sequence phase voltages and currents of an asymmetrical machine with single neutral point even in the case of balanced leg voltages.

Chapter 5 develops current and power sharing techniques between winding sets of a multiphase machine. The relationship between MS and VSD variables detailed in chapter 4 of the thesis is used as a starting point. Arbitrary current sharing is developed in both stationary (α-β) and synchronously rotation (d-q) coordinates. Further on in the chapter, current/power sharing in rotational coordinates has been verified on the example of asymmetrical 9-phase induction machine by simulation and experiment. Two different current sharing modes were developed and tested. The first one equally varies both d- and q-axis currents of each winding sets, while in the second case d- and q-axis current are independently changed.

Chapter 6 explores one possible use of developed power sharing technique. A 9-phase machine with three isolated neutral points is supplied by triple 3-phase VSI with cascaded dc links. This topology provides benefits of having a single high voltage dc link which easies step-up conversion, usually mandatory in high power WECS. The developed power sharing technique is employed here to balance individual dc-link voltages. Operation of symmetrical configuration is checked by numerical simulation, while asymmetrical one is verified by the experiment.

Chapter 7 summarises the work done in the thesis and provides conclusions. In addition, possibilities for future work are discussed in this chapter as well.

Chapter 8 provides list of references used in the thesis.

The last part of the thesis consists of appendices, where some important derivation and implementation codes are presented first (Appendix A). A description of the experimental setup, including hardware and software, is detailed next (Appendix B). Lastly, publications resulting from the thesis are listed (Appendix C).

Chapter 2

LITERATURE SURVEY

2.1 Introduction

This literature survey is focused on the application and control of multiphase machines in wind energy conversion systems (WECS). The principal topics covered are modelling, modulation techniques, current control, current sharing between winding sets, fault-tolerant operation, and converter configuration possibilities. Even though this literature survey primarily deals with multiphase machines, it is necessary to include other aspects of WECS as well. Hence, maximum power point tracking (MPPT), wind turbine basic operation, voltage oriented control (VOC), rotor field oriented control and grid synchronisation are covered. Multiphase machines of particular interest in WECS are 6-, 9-, 12- and 15-phase induction machines in both symmetrical and asymmetrical configurations. The 6-phase machine is the most researched multiphase machine; hence, the majority of the literature discussed here considers this type of multiphase machine. To begin, it is convenient to provide a short review of multiphase machines and WECS in general before moving on to a more detailed examination of the specific topics mentioned earlier.

One of the reasons for considering wind energy applications lays in the fact that it is one of the fastest growing renewable energy sources. In 2015 the annual growth of newly installed wind power reached 63 GW [REN21 (2016)]. The size of wind turbines has also increased with machines up to 8 MW now being offered by major manufacturers [Siemens AG (2016), MHI Vestas (2014)]. Although in terms of installed capacity the majority of WECS use the 3-phase doubly fed induction generator [Ma et al (2015)], high power requirements and the ability to continue operating under fault conditions has set multiphase machines as a technologically viable solution, especially the multiple 3-phase ones [Vizireanu et al (2007)]. Alongside multiphase WECS, other novel solutions can be found in the literature. These include superconducting wind generators [Wang et al (2013), Wang et al (2014)], integrated ac/dc generation [Feifei et al (2012)], double 3-phase machines with dissimilar number of poles per winding set [Munoz and Lipo (2000)] and cascaded generator usage [Kato et al (2001)]. None of these systems has attracted much attention from the point of view of real-world WECS and so they will not be considered further.

The basic operating principles of WECS can be found in [Wu et al (2011)]. Both mechanical and electrical subsystems are considered including turbine characteristics, WECS classification, grid synchronisation, and machine control for different types of 3-phase generators. Some of the earliest applications of WECS were based on the self-excited 3-phase induction generator. Similarly, use of self-excited 6-phase induction generator in WECS is examined in [Singh et al (2006), Singh et al (2009), Nounou et al (2014)]. In these cases, considered WECS supplies isolated load, i.e. it is a stand-alone power system configuration.

A comprehensive survey of multiphase machines in general is available in [Levi et al (2007), Levi (2008)]. Some of the covered areas are: basic characteristics of multiphase machines, advantages over 3-phase ones, modelling, harmonic mapping, modulation techniques, current control, field-oriented control, voltage oriented control, direct torque control, fault-tolerant operation and multi-motor drives. Another survey paper [Parsa (2005)] considers the advantages of multiphase machines such as smaller per-phase current, lower torque pulsation and improved reliability. Benefits of multiphase machines regarding winding construction/manufacturing are investigated in [Tessarolo (2010b)]. In addition, more recent review papers discussing newly published research in multiphase machine drives have become available [Barrero and Duran (2016), Duran and Barrero (2016), Levi (2016)].

2.2 Modelling

Successful control of multiphase generators with multiple 3-phase windings naturally requires an appropriate mathematical model. The most obvious way of modelling would be to model the machine in phase domain [Dordevic et al (2010)]. In doing so, an *n*-phase induction machine is represented with phase variables and the resulting model consists of $2n + 1$ nonlinear differential equations with time varying coefficients. Clearly, the problem with this approach is the model complexity, which makes the design and implementation of high performance control algorithms very difficult.

To overcome the complexity, the modelling process usually employs transformations to simplify the equations [Nelson and Krause (1974)] and therefore the control algorithm. This kind of modelling is based on a method proposed in [Park (1929)] where a 3-phase synchronous machine is represented in a synchronous rotating reference frame *d-q-0*. In the case of multiphase machines with multiple 3-phase windings, the modelling is undertaken using multiple *d-q* transformations. For example, a 6-phase induction machine can be modelled using the so-called double *d-q* approach [Lipo (1980)]. This method considers 6-phase machine as two 3-phase machines. Two separate *d-q* transformations are applied to the double 3-phase windings equations, resulting in two separate flux/torque producing subspaces. An example of the double *d-q* modelling can also be found in [Singh et al (2005b)], where a 6-phase self-excited induction generator is modelled using this approach. Two pairs of torque/flux producing currents in the double *d-q* synchronous reference frame are obtained. By aligning the *d*-axis of obtained reference frame with the machine's rotor flux, independent flux/torque control is achieved. This

corresponds to the rotor flux oriented control (RFOC) for 3-phase machines, so the *d*-current components will control machine flux and *q*-current components will control machine torque in a decoupled manner. The added complexity is that, in the case of a 6-phase machine, two *d-q* current controller pairs are needed and there is a coupling between two sets of *d-q* equations; hence additional decoupling is required. The multiple *d-q* modelling approach has been also applied to machines with more than two 3-phase winding sets. In [Jung et al (2009)] an ultra-high speed elevator using a 9-phase machine is presented. Triple *d-q* transformation is used to model the machine; hence, three current controller pairs in the *d-q* reference frame are used. Another example can be found in [Rubino et al (2016)] where a 12-phase machine is modelled and controlled by application of a quadruple *d-q* transformation. An unfortunate consequence of modelling the machine using multiple flux/torque producing subspaces is the presence of heavy cross-coupling between subspace equations [De Camillis et al (2001)]. In addition, due to the non-ideal nature of the machine and converter, low-order harmonics can appear in each subspace and their elimination is not easy to achieve. A solution for this is to introduce an additional transformation to diagonalize the inductance matrix [Kallio et al (2013)]**.** Furthermore, when there are more than two 3-phase sets, *d-q* axes of each set are not decoupled due to the coupling of stator leakage flux [Tessarolo et al (2013a), Tessarolo et al (2013b)]. This will take effect if the current amplitudes in the 3-phase sets are different due to any imbalance between sets. Finally, apart from these issues, it is obvious that with multiple 3-phase *d-q* modelling approach, machines with number of phases different than multiple of three cannot be modelled.

Multiple *d-q* modelling approach represents application of 3-phase Park's transformations to a specific type of a multiphase machine (6, 9, 12, etc. phases), where Park's transformation is a 3-phase Clarke's decoupling transformation plus rotation to an arbitrary reference frame. However, Clarke's transformation is a special case of the symmetrical components theory originally developed in [Fortescue (1918)]. Fortescue's method can be applied to any *n*-phase machine as discussed in [White and Woodson (1959)]. This theory has been used to model a 6-phase induction machine in [Zhao and Lipo (1995)] leading to the so-called vector space decomposition (VSD) modelling approach. The VSD is based on transforming original *n*-dimensional space into new *n*/2 (*n*-even number) or (*n*-1)/2 (*n*-odd number) orthogonal subspaces. The machine equations are decoupled into a single flux/torque producing subspace, multiple flux/torque non-producing subspaces and zero-sequence components [Levi et al (2007)]. Electro-mechanical energy conversion takes place in the first α-β subspace, while components in other subspaces (*x-y*) and the zero sequences (*z*) only produce losses. This feature provides better insight into machine operation, removes the need for complicated decoupling systems and eases the design and implementation for the control algorithm. Obtaining a VSD transformation matrix for symmetrical machines is straightforward and is developed from symmetrical components theory [Levi et al (2007)]. However, finding an appropriate transformation matrix for asymmetrical machines is less straightforward and multiple solutions have been proposed in [Tessarolo (2009a), Tessarolo (2009b), Abbas et al (1984), Rockhill and Lipo (2009), Rockhill and Lipo (2015)]. All of

them produce the same or very similar transformation matrices and have in common that odd-order harmonics are uniquely mapped into the subspaces.

Comparison between the double *d-q* and VSD modelling approaches for asymmetrical 6-phase induction machines is presented in [Che et al (2014c)]. It is shown that the currents in the non-flux/torque producing subspace can be physically interpreted as circulating currents between the two 3-phase sets. Asymmetries between the 3-phase sets will be visible as fundamental frequency currents in the non-flux/torque producing subspace. These currents can have different sequences depending on the nature of the asymmetry. This work has been extended to any symmetrical multiphase machine in [Liu et al (2016)]. It is shown that a pair of current controllers in each subspace can mitigate the imbalance originally present in phase values.

Another, recently developed, approach to multiphase machine modelling has been reported in [Zabaleta et al (2016a), Zabaleta et al (2016b)]. The work is part of a parallel research stream to this thesis and is a PhD research project exploring multiphase PMSGs for WECS. A transformation similar to VSD has been obtained by use of multiple Clarke's transformation. The flux/torque producing subspace is the same as in the case of VSD. However, the *x-y* subspaces contain information about the differences between flux/torque producing components in each winding set. This approach provides the benefits of VSD modelling, i.e. decoupled machine equations, but with the addition of having the ability to influence the contribution of each winding set to the total flux and torque production. However, unique harmonic mapping, available with VSD, is lost.

2.3 Modulation Techniques

In the early days of power electronics, due to the unavailability of fast switching high current devices, the first variable speed machines were supplied by inverters with 180 degrees conduction mode. One of the early examples of this supply technique applied to multiphase machines can be found in [Nelson and Krause (1974)]. A 6-phase induction machine was considered in both symmetrical and asymmetrical winding configurations. It was found that a machine in symmetrical configuration behaves in the same manner as the 3-phase machine, while in the case of an asymmetrical machine lower torque and current ripple was observed when compared to a 3-phase counterpart. Similarly, 180 degrees conduction mode was explored for 6- and 9-phase induction machines in [Kats (1997)] and the results were compared with a sinusoidally excited 3-phase machine. A more detailed analysis is offered in [Klingshirn (1983a), Klingshirn (1983b)] where various configurations of multiphase machines were compared in terms of torque ripple production. The first paper deals with theoretical considerations, while the second provides experimental validation. In [Wei et al (2014)] effects of current harmonics on magneto-motive force and consequently on machine torque have been analysed. The theory was tested using finite element simulations. With the advent of high power high-speed switches, this type of modulation has become obsolete due to the high harmonic content of currents and torque. Nowadays, high power machines can be supplied using modulation techniques such as space vector pulse-width

modulation (SVPWM) and carrier-based pulse-width modulation (CBPWM), albeit at sub kHz switching frequencies.

The SVPWM technique has been widely researched for multiphase machines. In combination with VSD modelling it provides good insight into machine operation and converter control algorithm development. SVPWM offers near-sinusoidal output waveforms, low harmonic distortion and increased dc-link voltage utilisation. An abundance of papers has been published considering SVPWM for 6-phase machines. In [Zhao and Lipo (1995)] an asymmetrical induction machine with two isolated neutral points was used. By using VSD for modelling, an illustration of space vector projections in different subspaces has been shown. It is concluded that, by proper selection of space vectors, an improvement can be made over the simplest CBPWM with pure sinusoidal references and triangular carrier in terms of dc-link voltage utilisation. A potential advantage of the SVPWM is a possibility to reduce common-mode voltage in certain cases. A symmetrical 6-phase machine was investigated in [Correa et al (2003)] and it was shown that, by properly selecting the space vectors, the instantaneous common-mode voltage can be reduced, so bearing currents and therefore deterioration of bearings will be reduced. The SVPWM technique can produce phase voltages that are sinusoidal or near sinusoidal while the average common-mode voltage is kept at zero [Dujic et al (2007a)]. Further research for a symmetrical 6-phase machine has been conducted in [Kianinezhad et al (2005)]. It is concluded that the proposed multi-vector SVPWM technique using symmetrical switching sequences gives better performance than traditional SVPWM using asymmetrical switching sequences. Phase voltages are near sinusoidal and the harmonic content is lower.

SVPWM has been considered for the asymmetrical 6-phase machines as well [Hadiouche et al (2006)]. The performances of various SVPWM strategies have been studied by analysing maximum modulation indices and current harmonics. It is shown that performance is dependent on the ratio between leakage inductance in the *d-q* and *x-y* subspaces. Furthermore, a comparison has been made between continuous and discontinuous SVPWM and it is verified by simulation and by experiment that both techniques can produce near-sinusoidal output currents. When SVPWM is used for 6-phase machines, subspaces are usually divided into 12 sectors and the dwell times are calculated accordingly. In [Marouani et al (2008)] subspaces are divided into 24 sectors, which yields reduced stator current harmonics when compared to the 12-sector SVPWM technique. Another SVPWM technique for an asymmetrical 6-phase machine is proposed in [Prieto et al (2010)]. By changing the distribution of zero space vectors, additional reduction in current and torque harmonics is achieved.

Inverters with higher phase number (i.e. 9) offer many more possibilities for space vector selection and proper application of SVPWM requires careful selection to ensure that the average voltage value in all non-producing flux/torque subspaces will be equal to zero. In [Dujic et al (2007b)] application of the VSD results in four orthogonal subspaces for a symmetrical 9-phase induction machine with one neutral point. Eight phase voltage active space vectors are used per switching period. Low-order harmonic components are successfully eliminated and sinusoidal output is achieved. Another

implementation of the SVPWM for a 9-phase machine based on 3-phase decomposition is proposed in [Grandi et al (2007b)]. The modulation is achieved by decomposing the 9-phase machine into three 3-phase machines (a triple *d-q* approach), and using three 3-phase SVPWM. If a machine has three isolated neutral points, three standard 3-phase SVPWM algorithms can be used. For the configuration with one neutral point, zero-sequence control for all three 3-phase SVPWM must be included. In [Grandi et al (2007a)] a multiple space vector approach is used to get four *d-q* subspaces. In order to get sinusoidal phase voltage output, average voltage vectors in non-producing flux/torque subspaces are set to zero.

An alternative to SVPWM is carrier-based pulse width modulation CBPWM. This technique offers simpler implementation than SVPWM. Modulation is achieved by a simple comparison between reference signals and a carrier. A zero-sequence injection technique can be used to achieve the same dc-link voltage utilisation as SVPWM. Comparison of different SVPWM strategies and CBPWM including zero-sequence injection has been presented in [Bojoi et al (2002)] for an asymmetrical 6-phase induction machine. It is shown that both modulation techniques achieve the same results regarding the torque/current harmonics and dc-link voltage utilisation, with the CBPWM method having the advantage of simpler implementation. The higher dc-link voltage utilisation of SVPWM reduces as number of phases is increased. An example has been reported for a symmetrical 9-phase induction machine [Kelly et al (2003)], where both modulation techniques were used and compared. Application of CBPWM technique for a 9-phase induction machine is examined in [Dong et al (2008)]. It is concluded that the CBPWM technique is superior to SVPWM for high phase numbers due to its simplicity and flexibility. While an improvement of 15.5% in dc-link voltage utilisation is possible for 3-phase VSI, this reduces to 1.54% for 9-phase or 0.55% for 15-phase cases. It should be noted that dc-link voltage utilisation for machines with a composite number of phases depends on the configuration (symmetrical or asymmetrical) and the number of neutral points [Dujic et al (2010)]. It is concluded that in the case of multiple neutral point configuration, maximum modulation index depends solely on number of phases in each winding set. On the other hand, when machine is with single neutral point, maximum modulation index is the same in both symmetrical and asymmetrical configurations if the number of phases is an odd number. However, if the number of phases is an even number and the machine is with single neutral point, better dc bus voltage utilisation is achieved in asymmetrical configuration (in the symmetrical case maximum modulation index is equal to 1). For the machines with a prime number of phases dc-link voltage utilisation has been analytically determined in [Levi et al (2008)]. It is shown that multi-frequency output voltage generation increases maximum dc voltage utilisation.

Control of the machines with high phase number (twelve or more), due to the aforementioned research, is usually done using CBPWM. An example is given in [Benatmane and McCoy (1998)], where a 19MW 15-phase induction machine, used for the ship propulsion, is supplied using CBPWM and scalar control. A more sophisticated approach is reported in [Sun et al (2015)], where a 20MW

asymmetrical 15-phase (triple 5-phase) induction machine is supplied via a 3-level neutral point clamped (NPC) inverter in open-end configuration. CBPWM is used as modulation technique and advanced vector control is implemented for speed regulation.

2.4 Current Control

Implementation of high performance control such as IRFOC requires proper current control. When a standard 3-phase machine is used, one pair of current controllers is enough for independent flux/torque control. Whereas, in the case of multiphase machines more than one current controller pair is usually required. Besides the flux/torque producing subspace, multiphase machines have one or more flux/torque non-producing subspaces. Consequently, the multiphase drive requires current control in every subspace, either to minimise the losses or to implement some advanced multiphase-specific control strategy. Current measuring in multiphase machines requires multiple current sensors that will increase the cost of the system. It is shown in [Bojoi et al (2006b)] that for a 6-phase machine a reduction of the number of current sensors to only two is possible with proper sensor placement.

Currently, the most common current control technique is based on proportional-integral (PI) regulators. It is capable of tracking a slowly varying or constant reference. In normal steady-state operation, the machine currents are near sinusoidal. Therefore, straightforward implementation of PI in stationary reference frame is not adequate since large error in current will be present during operation at high modulation index. In [Vukosavic et al (2005)], FOC for symmetrical 6-phase induction machines is presented. The VSD approach is used for modelling and current control has been implemented in the stationary reference frame. Since currents in the stationary reference frame are sinusoidal quantities, standard PI regulators require high bandwidth. Alternatively, PI regulators can be used in the synchronous reference frame (SRF) with frequency tuned at fundamental frequency. As a result, current references will be constant, thus the PI regulators can successfully achieve zero-error tracking in steady-state operation.

Asymmetry in machine windings will produce currents in non-flux/torque producing subspaces. A solution is proposed in [Jones et al (2009)], using an additional pair of PI regulators in SRF to control currents in *x-y* subspace. [Che et al (2012a)] shows that different types of windings imbalance will require different rotational transformations in order to successfully eliminate currents in the *x-y* subspace. These are synchronous and anti-synchronous reference frame transformations. This means that two PI regulators per current component, one in synchronous and another in anti-synchronous reference frame, will be needed to mitigate effect of asymmetries in machine phases [Che et al (2014c)]. Furthermore, in the aforementioned paper a proportional-resonant (PR) regulator in SRF is also proposed as a solution to remove current harmonics produced by the inverter dead time. Tuning PR regulator at six times fundamental frequency and placing it in an anti-synchronous reference frame is shown to successfully remove current components at $+5\omega_s$ and $-7\omega_s$. Similar results were reported in

[Hu et al (2014)] where a dual 3-phase permanent magnet machine is considered. A more detailed analysis of the application of the resonant regulators in symmetrical multiphase machines is available in [Yepes et al (2013)]. It has been shown that, by using multiple PR regulators in SRF, odd current harmonics can be effectively removed in symmetrical multiphase machines. A more generalised approach on asymmetry removal by use of additional current controllers in *x-y* subspaces is offered in [Liu et al (2016)]. It covers general case for the multiphase machines with symmetrical winding distribution.

Current control of the machines with number of phases equal to a multiple of three can be implemented as in a 3-phase machine. Namely, multiple 3-phase current controllers can be used. Such an approach has been reported in [Hua et al (2006)] where four pairs of PI regulators in SRF were used for current control of a 12-phase machine. Another example of current regulation in SRF has been reported in [Bojoi et al (2003b)], where different solutions are proposed depending on the modelling approach (VSD or double *d-q*). FOC with two pairs of PI regulators in SRF has also been reported in [Singh et al (2005b)].

A weakness of the classical PI regulator in SRF is that it needs decoupling between current components [Briz et al (2000)], otherwise a loss of performance can occur. One way of decoupling is based on moving the pole of the load to coincide with the zero of the regulator. Another way is to implement a so-called vector PI regulator. In doing so, the regulator zero is moved to match the pole of the load. The performances of both solutions are the same. However, more than one vector PI regulator can be implemented in parallel to control multiple sequences or harmonics simultaneously [Yepes (2011)].

Current control by means of PR regulators has been proposed in [Yepes (2011)]. Used regulators are in stationary reference frame but their resonant frequency is tuned at frequency of interest (fundamental or harmonic). Besides, PR regulators can be represented as a sum of two PI regulators in synchronous and anti-synchronous reference frames. In this case, they will effectively control both synchronous and anti-synchronous sequences. Furthermore, it is possible to use more than one PR regulator in parallel, so that multiple harmonics can be controlled. An example of use of resonant current control has been presented in [Bojoi et al (2006a)]. A PR regulator has been used for controlling currents in flux/torque non-producing subspace. 6-phase machine is used, but with additional pairs of PR regulators. The same approach can be extended to machines with more than two 3-phase windings. Tuning of resonant controllers is presented in [Rodriguez et al (2012)]. Good performance is verified for second-order generalised integrator resonant controller. Additionally, the resonant frequency must be precisely set. For fixed fundamental frequency operation (grid-side converters) use of resonant regulators is reported in [Zmood et al (2001), Guillaud et al (2007)]. On the other hand, operation of PR regulators under variable fundamental frequency (machine-side converters) has not been studied to a great extent [Yepes et al (2012)].

Another type of resonant regulators can be obtained as a sum of two vector PI regulators, one in the synchronous and another in the anti-synchronous reference frame. In the stationary reference frame, these so-called VPI regulators, tuned at the desired frequency, will act like a resonant regulator simultaneously controlling both synchronous and anti-synchronous sequences. VPI regulators are proposed and analysed in [Lascu et al (2007), Lascu et al (2009)] as current regulators for higher harmonics elimination in active power filter application (APF). Since the model of controlled system in APF has the similar form as the model of an induction machine, these regulators can be used for current control for both fundamental and harmonic components [Yepes (2011)].

Current control is essential for any field oriented machine control. When properly tuned, all mentioned current regulators will achieve similar performances [Holmes et al (2012)]. The selection of a specific controller will be governed by practical issues, such as complexity of implementation and sensitivity to parameter variations.

2.5 Current and Power Sharing Between Winding Sets

The machines with multiple 3-phase winding sets (e.g. 6-, 9-, 12-, 15-phase) are used most frequently since 3-phase inverters are a mature technology and widely available. Moreover, multiple winding sets can be isolated, a feature successfully utilised in development of an on-board charger for EVs [Subotic et al (2016)] and realisation of high-voltage dc link by cascading individual inverters [Sulligoi et al (2011)]. One of the important properties of machines with multiple winding sets is that each winding set can be supplied by an individual inverter. This may be used to develop arbitrary current and power flow between winding sets, leading to arbitrary power flow between different sources.

Developing an algorithm for arbitrary current or power sharing between multiple 3-phase winding sets usually involves a requirement that total flux and torque of the machine stay the same or within the defined derated values. Consequently, a multiple *d-q* modelling approach [Jung et al (2009)], Nelson and Krause (1974), Lipo (1980)] is an obvious choice. By applying the generalised Clarke's transformation to each winding set, it is possible to control the flux and torque production on a per-winding set basis [Scarcella et al (2016)]. The considered machine has multiple 3-phase stator windings that are spatially in phase. This is not a multiphase machine in a true sense of the word, but three 3-phase machines sharing the same rotor. Nevertheless, the same technique can be applied to multiphase machines with spatial displacement between 3-phase windings, as shown in [Rubino et al (2016), Bojoi et al (2016)]. A shortcoming of this approach is the presence of heavy coupling between winding set equations, leading to a requirement for more complicated current control, especially when low order harmonic elimination is considered.

Alternatively, the machine can be modelled by use of VSD. This yields a decoupled machine model with a single flux/torque producing subspace and multiple non-flux/torque producing (*x-y*) ones. However, this modelling approach does not provide insight into individual winding set variables and current sharing between winding sets is not easily achievable. Nevertheless, it is shown in [Che et al

(2012b), Che et al (2012c), Che et al (2014b), Duran et al (2017)] that the *x-y* subspace of a 6-phase machine can be utilised to develop power balancing between winding sets. For this purpose, a 6-phase induction machine has been supplied by two 3-phase voltage source inverters (VSI) with dc links connected in series. By doing so, the total dc-link voltage is doubled. The developed power sharing technique has enabled balancing of individual dc-link voltages even in the presence of imbalance in machine parameters. When machines with more than six phases are modelled by use of VSD, relation between *x-y* currents and individual winding set currents is not so obvious. Nevertheless, a current sharing technique has been developed for an asymmetrical 12-phase machine [Tani et al (2013), Mengoni et al (2016)]. The machine has been modelled and controlled using VSD; however, by combining VSD and multiple *d-q* modelling approaches, relations between individual winding set currents and *x-y* currents have been found. It is shown that current amplitudes in each winding set can be arbitrarily controlled, while currents within each winding set are balanced. Applied current sharing does not have any influence on the total flux and torque production.

An alternative approach to arbitrary control of power flow between winding sets of a 6- and a 9-phase permanent magnet synchronous machine is described in [Zabaleta et al (2016a), Zabaleta et al (2016b)]. A transformation similar to VSD is obtained by applying multiple generalised Clarke's transformation on each winding set. The machine is decoupled into a single flux/torque producing subspace and multiple auxiliary subspaces that define relation between flux/torque producing currents of individual winding sets. However, in contrast to VSD modelling, odd-order harmonics are not uniquely mapped within the created subspaces. Nevertheless, proposed technique combines all the benefits of decoupled control, a feature of VSD, and ability to influence currents in individual winding sets. Moreover, the developed method can be easily extended to any machine with multiple 3-phase winding sets.

2.6 Fault Tolerance

Fault-tolerant operation is of paramount importance in any critical application where electric machines are used, e.g. more electric aircraft or ship propulsion and generation. Similarly, in wind energy conversion systems uninterrupted operation is imperative, especially in the remote offshore wind farms where service is not readily available, so that any interrupt in operation would represent a significant energy and money loss. Evidently, multiphase machines represent an obvious choice in these circumstances due to their ability of continual operation under faults. Machine drives can become faulty due to the inverter or machine failure. A short or open connection of one or more machine phases is considered a machine fault, while an inverter fault is a failure of one or more semiconductors of the inverter. Open-phase machine and inverter faults can usually be regarded as an open-phase fault.

For successful implementation of any fault-tolerant control algorithm, machine modelling and fault detection must be firstly considered. The stator winding of the machine can be represented as set of coils [Apsley and Williamson (2006)]. Each coil is modelled individually and considered as a

concentrated winding so its impact on MMF and its harmonic content can be calculated. This will allow easy modelling of any type of fault; although possible, it is complex and impractical for real-time control implementation. Another approach to modelling and detection of faults in machines with an odd number of phases is presented in [Zarri et al (2011)]. Imbalance in machine phases, which essentially can be considered as a type of fault, is manifested as fundamental currents in non-flux/torque producing subspaces. By determining the type of the imbalance, the faulty phase can be identified.

Machines with multiple 3-phase windings offer one of the easiest and most obvious ways of achieving fault-tolerant operation, due to the possibility of simple disconnection of the faulty 3-phase winding set. In the case of 6-phase machine, when one 3-phase winding set is disconnected, machine will continue to work as a 3-phase one. Depending on coil configuration different magneto-motive force (MMF) can be expected; hence, different performance under fault will be achieved [Alberti and Bianchi (2012)]. Here, an experimental verification has been conducted by suppling the machine in open loop configuration. Open-circuit fault has been emulated by opening one of the 3-phase winding sets, while the supply of the healthy winding set is unchanged. During the no-load test, phase current in the remaining winding set is found to be 1.8 times larger than the no-load current in healthy operation regardless of the coils configuration. However, when the same test is repeated while the machine is under 50% of the nominal load, phase current exceeds nominal 1.28 – 1.5 times depending on the coil configuration. Furthermore, a test where one of the winding sets is shorted while the other's supply is unchanged has been performed as well. Machine load has been reduced again to 50% of a nominal value. It is found that not all coil configurations offer a viable solution and that the phase currents in the remaining winding set are 1.75 – 2.5 larger than nominal. Another concept of fault-tolerant operation with multiple 3-phase machines is to supply each winding sets with two paralleled VSIs [Duran et al (2016b), Gonzalez-Prieto et al (2016)]. In the case of the VSI leg fault corresponding phase can be supplied with half of the rated current. Fault-tolerant operation under set condition has been achieved by offline calculation of appropriate current references for each phase. Suitable current references are calculated by use of optimisation software. It should be noted that in these examples, only electrical aspect of fault-tolerant control has been considered. When one or more phases of the machine are switched off, absence of flux production along the stator circumference due to the faulted phases may produce unwanted vibrations that will decrease bearing lifetime.

Machine control under fault can be adjusted to compensate for individual lost phases so that the machine MMF is kept at rated value. Naturally, currents in the remaining healthy phases will increase. Analysis has been performed for 3-, 5-, 6- and 7-phase machines with one open-phase fault [Fu and Lipo (1994)]. It is concluded that these machines can work with one phase opened (a 3-phase machine will require a neutral point connection) while the MMF is kept at rated value. Machines with higher phase number will need a smaller increase in healthy phase currents. Since currents in the remaining phases are increased, stator copper losses will be higher, so a technique for minimum stator losses has been proposed. In the case of the 6-phase machine, operation under fault has been analysed in [Apsley

(2010)] and two strategies were discussed: minimum stator losses and equalisation of currents in remaining healthy phases. In addition to the aforementioned strategies, keeping torque ripple at a minimum is essential for the mechanical subsystem (e.g. gearbox). A technique to keep torque ripple at the minimum possible value in 6-phase machine with up to three phases open is proposed in [Kianinezhad et al (2008)]. For machines with an odd number of phases fault-tolerant operation was explored in [Tani et al (2012)] where three different strategies for operation under open-phase fault have been presented: minimum stator losses, minimum current peak and minimum torque oscillation.

One of the ways to model and control a multiphase machine with an open-phase fault is to discard faulty phases and model the machine as one with a lower phase number. This can be achieved by using a different transformation matrix so controls in *d-q* reference frame will stay essentially the same. The aforementioned method is used for a 6-phase machine in [Deilamani et al (2011)] and for a 5-phase one in [Guzman et al (2012)]. A similar technique is used in the case of the 5-phase machine where different transformation matrices are used depending on whether the fault is present or not [Guzman et al (2014)]. In this case a model-based predictive current control is used.

An alternative way of dealing with open-phase faults is to consider that the fault will change machine currents, but not the construction. In this case, the same decoupling matrix can be used [Che et al (2014a)]. It is shown that depending on the machine construction (one or two neutral points) *x-y* or zero-sequence currents will not be decoupled when a fault is present. Moreover, new flux/torque producing α-β currents should be of a smaller value so that the phase currents in the faulted machine do not exceed rated. Effectively, this reduces the total available power. Ratio between post-fault and pre-fault flux/torque producing α-β currents is defined as derating factor. Current control uses PI regulators in a synchronous reference frame, while for the post-fault operation additional anti-synchronous regulators are added. Two strategies were used for post-fault operation: minimum stator losses and maximum torque. It is concluded that a machine with a single neutral point has better performance for both strategies, i.e. smaller derating is needed and consequently more power is available. Similarly, post-fault operation for the same machine type without changing the decoupling matrix has been proposed in [Miranda (2013)]. Namely, a faulty phase has been simulated in such a way that voltage imposed on the faulty phase is equal to back-EMF of that phase; consequently, the same decoupling matrix can be used. Since additional PI regulator in anti-synchronous reference frame was needed, a simplified one consisting of two PI regulators (one in synchronous and another in anti-synchronous reference frame) has been proposed. Furthermore, a modified resonant controller in stationary reference frame has been also presented as a viable solution for current control.

Fault tolerance by utilising hybrid converter configurations and multiphase machines has been investigated in [Ruba and Fodorean (2012), Gonzalez et al (2014)]. In the first paper, a 9-phase synchronous machine has been supplied using a 12-phase VSI in such a way that all three neutral points are connected to separate inverter legs. This solution offers fault-tolerant operation with up to 78% of

the machine faulted (7 phases under open-phase fault). The second paper proposes solution with a 6-phase induction generator with series-parallel VSIs. Namely, two VSIs per 3-phase stator winding are used and connected in parallel. Then these two pairs of VSIs are connected in series to form a medium voltage dc link. The fault is considered as an open connection of one of the legs of the VSIs. It is shown that imbalance in stator currents will produce different voltages on local dc links and if voltages are kept at the same level only 25% of power will be available. Proposed solution is based on lowering flux value depending on the machine torque. As a result, the available power is up to 50% of the nominal.

Concerning non-controlled permanent magnet brushless dc generators, a solution with a 12-phase generator and diode rectification is proposed in [Zhuoran et al (2010)]. One diode per phase is used and it is connected in series with phase winding, while all phase-diode combinations are connected in parallel to form a dc link. Various combinations of open-circuit faults are analysed by FEM analysis and on the experimental prototype. Similarly, in [Tessarolo (2010a)] diode rectification has been explored by using diode bridges and synchronous generator that can be reconfigured as 3-, 6-, 9- and 12-phase. 3-phase stator winding sets are connected in series to form a high voltage dc link. It is concluded that, when an open-phase fault is present, configurations with higher phase number will have smaller dc current drops.

2.7 Converter Topologies

Due to the presence of more than three phases, converters that supply multiphase machines can be configured in more than one way. Consequently, the system may have one or more desirable features such as better fault tolerance, higher output dc voltage and use of commercially available 3-phase VSIs. The configuration of the machine-side converters can vary depending on the machine type. On the other hand, grid-side converters are usually well-established 3-phase 2-level VSI or 3-level neutral point clamped (NPC) converters [Nabae et al (1981)] and so they will not be discussed further.

There are two basic categories of machine-side converters, namely uncontrolled and controlled. Uncontrolled converters are used in machines with excitation on the rotor, e.g. permanent magnet or synchronous machine. Numerous solutions have been proposed for dc voltage generation using uncontrolled diode bridge rectification. For example, a 6-phase synchronous generator is used for ship-based power generation in [Sulligoi et al (2010)]. Two sets of stator windings were connected to the diode bridges and then cascaded to form a medium voltage dc link. A continuation of work is presented in [Sulligoi et al (2011)], where an ultra-high speed (22000 rpm) 12-phase permanent magnet generator is used. Again, 3-phase diode bridges were used for rectification with difference that now four diode bridges were used to get four independent local dc links. Afterwards, these local dc links were connected to four cascaded dc-dc converters to form a single medium voltage dc link. Alternatively, for a grid-connected system, VSI was used on grid side and two 3-phase diode bridge rectifiers were employed with 6-phase axial-flux synchronous generator on the machine side [Di Gerlando et al (2012)]. In addition, both parallel and series connections of diode bridges were explored. Research involving

uncontrollable rectifiers was conducted for aircraft applications in [Jordan and Apsley (2011)]. On the one hand, advantages of diode bridge rectification are high robustness, efficiency and simple structure, but on the other hand the machine cannot be fully controlled and this will lead to non-optimal machine operation.

When controlled machine-side converters are considered, there are several available configurations: one multiphase converter, parallel connection of multiple VSIs to form one dc link, back-to-back design, series connection for high voltage dc link or hybrid approach when combination of series and parallel connections is used. Additionally, there are some application specific topologies of multiphase drives. For example, a single inverter is used to supply multiple multiphase machines connected in parallel [Jones et al (2009b)] or series [Duran et al (2005)]. By use of additional degrees of freedom available with multiphase machines independent flux and torque control over each machine is achieved. Another application specific example can be found in [Subotic et al (2016)], where a six phase machine drive doubles as propulsion and charger unit for electric vehicle.

A single multiphase converter is the most usual solution for systems where the number of phases is a prime number. When the machine has a composite number of phases, instead of one, multiple inverters connected in parallel with the dc link can be used. This approach was applied in [Sun et al (2015)] for a 15-phase machine where three 5-phase VSIs were connected in parallel. Doing so allows a modular design to be achieved and in the case of fault or service needs, one VSI can be disconnected while the others are still in operation. Another use of parallel VSIs can be found when the system is connected to the grid and multiple parallel back-to-back inverters are used [Andresen and Birk (2007)]. In this case, six 3-phase back-to-back VSIs where used to connect an 18-phase machine to the grid. This configuration permits independent VSIs to be switched off when the power level is below rated, giving rise to increased overall system efficiency. A similar solution has been presented in [Brisset et al (2008)], where a 9-phase axial-flux permanent magnet synchronous generator was connected to the grid using three 3-phase back-to-back converters.

Alternatively, VSI dc links can be connected in series to form one single high voltage dc link. This solution is of great interest in offshore wind farms where high dc voltage is usually used for energy transfer [Blaabjerg et al (2006)]. The main benefit is possibility to use low voltage generation in a high voltage dc system. This approach has been presented in [Duran et al (2011)] where a 6-phase permanent magnet synchronous generator is connected to the two 3-phase VSIs with dc links connected in series to form a high voltage dc output. The grid-side connection in presented solution has been achieved with 3-level NPC inverter. Similarly, in [Che et al (2012b), Che et al (2014b)] two 3-phase VSIs with series-connected dc links were used for an asymmetrical 6-phase induction generator. An innovative approach for controlling voltages in series connected dc links is presented. Namely, non-producing flux/torque subspace currents were used to balance the dc-links voltages. Another solution to creation of high voltage dc link is analysed in [Yuan et al (2012), Ng et al (2008)]. Each machine-winding coil is

supplied by a single full bridge inverter with inverter dc links connected in series. By doing so, a high voltage dc link is produced.

There are hybrid configurations that do not strictly fall into any of the aforementioned categories. An example of this type of topology can be found in [Xiang-Jun et al (2012)] where a 12-phase permanent magnet synchronous generator is connected to four 3-phase Vienna rectifiers. Two parallel-connected pairs of rectifiers are connected in series to form a high voltage dc link, while connection to the grid was achieved with two parallel-connected NPC converters. Another hybrid configuration is proposed in [Gonzalez et al (2014)] where four 3-phase VSIs are used to supply a 6-phase induction generator. To increase fault tolerance, a pair of parallel-connected VSIs is connected to each 3-phase stator set. Later on, the dc links of these pairs are connected in series to form a medium voltage dc link.

2.8 Control Systems of WECS

Wind energy control is a complex system with a number of control loops. In addition to the machine current control, in the back-to-back configuration there are three more major control subsystems: maximum power point tracking (MPPT), vector control for the machine-side converter and voltage-oriented control (VOC) for the grid-side converter [Liserre et al (2011)]. Furthermore, it is mandatory to implement a grid synchronisation system such as a phase locked loop (PLL).

When the wind is below the rated speed, the WECS needs to extract the maximum available power. This is done by the use of MPPT control that measures (directly or indirectly) wind speed and adjusts shaft rotation speed to obtain optimal tip speed ratio [Wu et al (2011)]. There are three different methods for implementation of MPPT: turbine power profile, optimal tip speed and optimal torque control. Input of the first and second MPPT methods is wind speed, while the output is the required power or speed. The optimal torque control is based on measuring the shaft rotational speed and calculating the optimal torque. All three methods provide optimal references (power, speed, and torque) required for maximum available energy extraction. The task of the machine-side converter is to set the machine operation to track the given references. This is usually achieved by implementing (RFOC). Moreover, additional control is required (speed regulator, power profile analyser) depending on the chosen MPPT control.

Two types of RFOC are used: direct RFOC (DRFOC) and indirect RFOC (IRFOC). The rotor field position can be obtained using flux sensors, or it can be estimated based on measurement of the rotor position, the stator voltages and currents. The RFOC for multiphase machines is the same as for the 3-phase case. Namely, VSD approach will result in only one flux/torque producing subspace and in the case of multiphase machines with multiple 3-phase windings, multiple 3-phase modelling can be applied. In both cases, the implementation is similar as for the standard 3-phase machine, the notable difference being the required transformation. An example of DRFOC applied to an asymmetrical 6-phase induction machine is presented in [Bojoi et al (2003a)]. The machine model is obtained by VSD, while carrier-based PWM with zero-sequence injection was used as a modulation strategy. It is shown that standard DRFOC control by use of single pair of PI regulators in rotational reference frame is not

sufficient to remove asymmetries between machine winding sets. Hence, the control strategy is modified so each winding set is controlled by single pair of PI regulators in rotational reference frame, called there a double synchronous frame current control. Applied rotational transformations are adapted to accommodate phase shift of the corresponding winding set, while standard 3-phase Clarke's transformations have been used to produce α-β currents as an input to the implemented rotational transformations.

When IRFOC is used, the rotor flux position is estimated by using the measured rotational speed or position of the shaft [Singh et al (2005a)]. In this paper, a 6-phase asymmetrical machine with arbitrary angle between stator winding sets is used. The machine model is obtained by using double *d-q* modelling approach, while current control is done with two pairs of PI regulators (one pair per 3-phase winding set). This current control approach can be extended to any number of 3-phase winding sets. Similarly, for the 9-phase case, IRFOC was applied in [Hu and Yang (2011)]. The machine was modelled using VSD so four subspaces were obtained. Two cases were explored: with and without current harmonics control. Hence, in the first case only currents in flux/torque producing subspace were controlled, while in the second case currents in all subspaces were considered. It is clearly seen in experimental results that current ripple is much smaller when currents in all subspaces are controlled.

Well-known VOC is used for the grid-side converter control in back-to-back configuration. This control is very simple and it is based on inner current control loop and voltage control [Blaabjerg et al (2006)]. The main task of VOC is to regulate the dc-link voltage by changing the current flow to the grid. Obviously, for the successful operation VOC needs to be synchronised with the grid. This is achieved by using one of the grid synchronisation techniques.

Grid synchronisation can be achieved using a zero-crossing detection method, filtering grid voltages, or by using phase locked loop (PLL). The first technique has the simplest implementation but poor performance when grid voltage variation is present. Filtering grid voltages gives better results, but the delay is present, which also leads to non-optimal operation. Current state-of-the-art synchronisation techniques are based on the 3-phase PLL [Blaabjerg et al (2006)]; this gives better performance than the first two techniques. This type of PLL consists of two main parts: phase detection device and the loop filter [Chung (2000a), Chung (2000b)]. Phase detection is achieved by using the *d-q* transformation and the loop filter is characterised with two parameters: damping factor and natural frequency. These parameters will define the dynamic characteristic of the system. It is shown that a trade-off between the filtering abilities and the speed must be made to accommodate voltage/frequency imbalances of the grid voltage. Furthermore, other types of PLLs have been analysed in [Arruda et al (2001)]. Besides 3-phase PLL structure, single-phase PLL and zero-crossing method were analysed. Another solution for 3-phase PLL based on the PID regulator is presented in [Martinez-G. et al (2013)]. This technique gives improved overshoot when cascaded lead compensators are used. Moreover, feed-forward can be implemented to improve PLL tracking performance [Liccardo et al (2011)].

2.9 Summary

A literature survey of the available research in areas relevant for this thesis has been presented in this chapter. Advantages of the multiphase machines over 3-phase ones are briefly explained. Furthermore, it is shown that these advantages can be beneficial in WECS. Different types of modelling approaches for multiphase machines have been reviewed, followed by the various modulation techniques including both CBPWM and SVPWM. Numerous current control techniques were surveyed and special attention has been devoted to resonant VPI current regulators. Next, section deals with the current and power sharing between winding sets. Since fault tolerance is one of the greatest advantages of the multiphase machine, many fault-tolerant operation strategies were considered. Depending on the type of the WECS one or more VSIs can be employed, so different VSI configurations have been reviewed. Since WECS requires some advanced control strategies, it is necessary to include a brief survey of MPPT and RFOC. Furthermore, grid-side converter topologies (2-level and 3-level) have been briefly surveyed followed by the grid synchronisation techniques, where a PLL is considered as current state-of-the-art.

Although adaption of multiphase machines in real world WECS is scarce, reviewed literature shows that abundance of research exists in the field of multiphase machines and that they offer multiple advantages over 3-phase ones for the WECS with fully rated converters. Further, it is shown that the most promising candidate for the use in WECS are multiple 3-phase machines. However, it was found that modelling and control of these machines is mainly done by use of either MS or VSD, governed by the requirements of the system at hand. Use of any modelling approach constrains design to benefit the advantages of the either a VSD (a decoupled machine model), or MS (an access to individual winding set variables) only, but not from both. Therefore, this thesis explores modelling and control of multiple 3-phase machine by considering both MS and VSD and bridging the gap between them, so that benefits of both can used. Thus, the machine can be modelled and controlled in decoupled subspaces of VSD, while access to individual winding set variables of MS is still possible. Subsequent chapters of this thesis will analyse the complete WECS with a multiphase machine. Different solutions will be considered for current control, fault tolerance, VSI configuration, grid-side VSI and grid synchronisation.

Chapter 3

WIND ENERGY CONVERSION SYSTEM

3.1 Introduction

The multiphase machine control methods developed in this thesis are targeted towards wind energy conversion systems (WECS). Throughout the thesis the developed control techniques are used in conjunction with well-known control techniques, usually applied in multiphase machine drives, such as carrier-based pulse width modulation, indirect rotor field oriented control and low order harmonic elimination by use of resonant controllers. Therefore, it is necessary to dedicate a single chapter of the thesis to explain all major control mechanisms used in WECS, so that the rest of the thesis can focus on work that is more novel. Furthermore, it is convenient to add a review of WECS topologies with multiphase machine used as a generator in the same chapter, with the aim of setting the context of the thesis and providing the reader with possible applications for the developed control techniques.

Here the basic WECS is considered to be the grid connected one with back-to-back inverter configuration; hence, all of its components relevant for the electrical domain will be considered. The complete systems will contain:

- Wind turbine model with gearbox and pitch control
- Maximum power point tracking (MPPT) control
- Multiphase machine model
- Indirect rotor field oriented control (IRFOC) for machine-side converter control
- 2-level and 3-level inverters in back-to-back configuration
- PLL for grid-side inverter synchronisation
- Voltage oriented control (VOC) for grid-side inverter control

A block diagram of the WECS with all aforementioned elements can be seen in Fig. 3.1. It should be noted that this is a simplified model with emphasis on converter control. Mechanical components are disregarded since they have little effect on the electrical subsystem. Since the generator is a multiphase machine, different control strategies can be utilised to minimise torque or current ripple; hence two-level inverter is used on the machine side. On the other hand, 3-phase grid provides very little possibilities to minimise current ripple since the switching frequency is usually very limited here

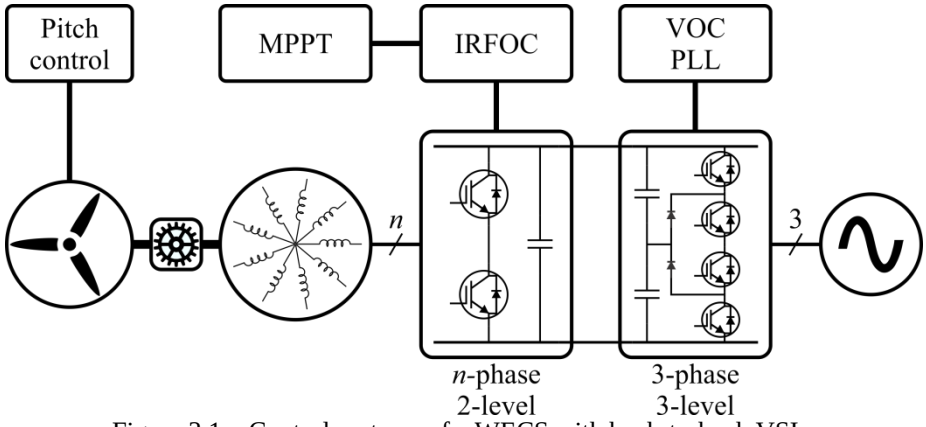

Figure 3.1 – Control systems of a WECS with back-to-back VSIs.

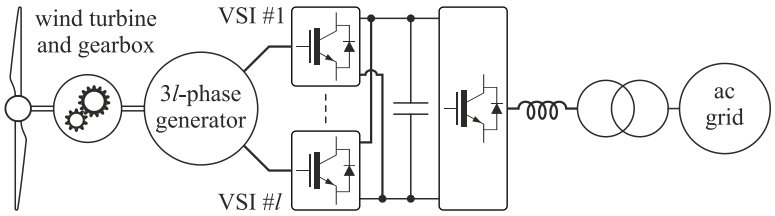

Figure 3.2 – WECS in back-to-back configuration.

due to the high switching losses in high power drives. Therefore, three-level, or any other multilevel, inverter is used on the grid side to abide to the strict grid code.

3.2 Topologies of WECS with Multiple Three-phase Machine as a Generator

In the back-to-back (B2B) configuration, shown in the Fig. 3.1, the use of a multiphase machine as a generator provides additional degrees of freedom so that different load requirements can be accommodated by having different converter configurations. It is safe to say that multiple 3-phase machines (i.e. 6-, 9-,… 12-phase) are by far the most used multiphase machine type. The reason is that they can be supplied using standard 3-phase VSIs, a case that is considered in this thesis. The simple back-to-back configuration, shown in Fig. 3.1 for a general case when a multiple 3-phase machine is used, is illustrated in Fig. 3.2.

The machine-side converter consists of multiple 3-phase VSIs with the dc links connected in parallel, forming a single dc link. The single dc link is connected to a 3-phase grid-side inverter. This configuration offers a fault-tolerant capability possible by use of a multiphase machine. If the multiphase machine has a single neutral point configuration, even better fault tolerance is possible, while the topology with multiple neutral points provides galvanic isolation between winding sets. Limitations of this topology are the voltage ratings of the inverters (i.e. power switches and capacitors) and insulation ratings of the machine. Namely, high-power transfer usually requires high voltage that is in this case limited by the dc-link voltage. Therefore, use of step-up transformer is necessary.

In order to partially mitigate this limitation, the configuration with multiple neutral points can utilise

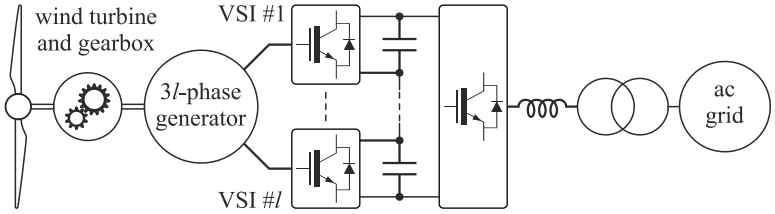

Figure 3.3 – WECS with cascaded machine-side VSIs.

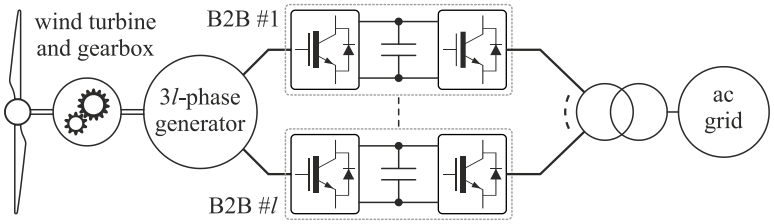

Figure 3.4 – WECS with modular back-to-back 3-phase VSIs.

the benefits of galvanic isolation of the machine-side VSIs. Dc links of the machine-side VSIs can be connected in series to form a single high-voltage dc link. By doing so, machine-side inverters can have *l* times smaller voltage rating, where *l* is the number of the winding sets. This configuration is shown in the Fig. 3.3. Having a larger dc link, step up conversion might not be needed or at least is made easier due to the smaller step-up ratio. It is noted that even though the machine-side inverter ratings are smaller, the machine's insulation still needs to withstand the total dc-link voltage, unless special SVPWM methods are used to restrict the application of zero vectors [Che et al (2014b)]. On the other hand, by far the largest drawback in this topology is the loss of fault-tolerant capability of the drive. If one of the inverters is lost due to the fault, the whole system needs to be shut down. In other words, this topology represents a trade-off between the higher dc-link voltage and fault-tolerant operation.

If high modularity is required, it is possible to build the power stage using isolated 3-phase back-to-back inverters, as shown in the Fig. 3.4. This configuration provides fault-tolerant operation with additional benefits of having the power stage composed of widely available 3-phase inverters in back-to-back configuration. Although a somewhat complicated step-up transformer needs to be designed in order to accommodate multiple inputs, having the galvanic isolation between B2B blocks can greatly improve fault tolerance and make maintenance easier since power stage building blocks are standard B2B 3-phase VSIs.

Until now, it was assumed that the system is supplying an ac grid. However, dc grids are also in use, especially in offshore wind farms where high voltage dc transmission can have benefit of smaller transmission losses. In this case, machine-side VSIs are the same as shown in Fig. 3.2 – 3.3, while the grid side is replaced with step up dc-dc converter. The system possesses the same features as in the case of the ac grid.

Another system where use of a multiple 3-phase machine may be advantageous is where the WECS supplies multiple ac or dc micro-grids [Duran et al (2017)], as illustrated in Fig. 3.5a – 3.5b. Each

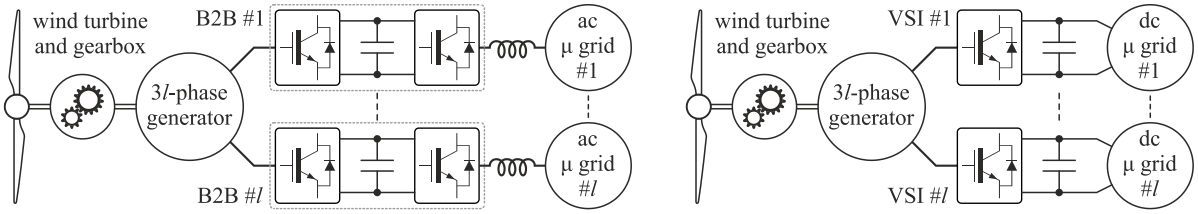

a) WECS supplying ac micro-grids. b) WECS supplying dc micro-grids.

Figure 3.5 – WECS supplying the isolated micro-grids.

winding set can supply an isolated ac micro-grid by the means of B2B inverter, or dc micro-grid, in which case there are only machine-side converters, and dc micro grids connect directly to the dc links. In both cases the machine-side control can be made such that it effectively satisfies potentially rather different power needs of the individual ac or dc micro-grids. Further, it is possible to use the machine as a means of transferring the energy between micro-grids, depending on whether the individual micro-grid acts as a load or as a source.

3.3 Wind Turbine with Gearbox and Pitch Control

Regardless of the load requirements and the topology of the WECS detailed in the previous section, majority of the wind turbines used today are horizontal-axis wind turbines; hence, they are considered in this chapter. Usually, modelling of the wind turbine is associated with the amount of wind energy generated by air mass of density ρ flowing at the speed v_w through an area A [Wu et al (2011)]. If C_p is wind turbine efficiency, equation for captured wind power by the turbine is:

$$P_t = \frac{1}{2}\rho A v_w^3 C_p \tag{3.1}$$

Turbine efficiency C_p is highly dependable on the approaching angle of the wind and blade pitch. Systems controlling these parameters are yaw and pitch control. Yaw mechanism directs the turbine blades to perpendicular position to the wind direction, while pitch limits captured wind power when wind speed is above nominal. Yaw control is omitted from the turbine model since it does not have any impact on the electrical subsystem, i.e. it is assumed that turbine blades are always perpendicular to the wind.

On the other hand, it is necessary to implement pitch control, so that a proper MPPT algorithm can be developed. Here the pitch mechanism is simplified and it keeps turbine efficiency at maximum while the captured power and consequently wind speed are below rated values. When the wind speed is above rated, captured power is limited to the nominal value by the pitch mechanism. This has been modelled by a simple limiter. Since the turbine torque value is necessary for the rest of the system, it is obtained by division of the turbine-produced power with the shaft speed. However, a problem with this approach is division by zero. To overcome this, turbine shaft speed has been limited to be larger than 10^{-6}, which has a negligible impact on system operation.

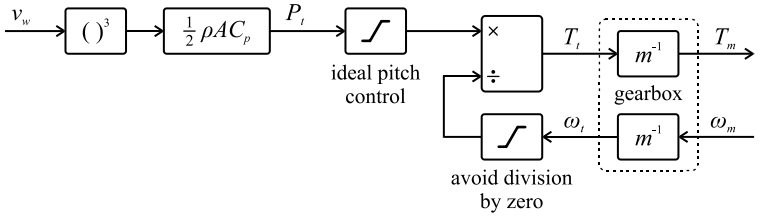

Figure 3.6 – Wind turbine model with gearbox and ideal pitch control.

Angular speed of large wind turbine shafts is usually very low. When generators do not have large pole number and their rated speed is high, a gearbox is used to connect wind turbine and generator shafts. In the developed model, the gearbox is considered ideal. Therefore, gearbox inertia and efficiency are disregarded and the only settable parameter is gearbox ratio.

Wind turbine inertia should be considered as well. Since there is a gearbox in the system it can be added to the model before or after the gearbox. In this case, the latter approach has been implemented, i.e. it has been added as an additional inertia of the generator. Hence, the value of the additional inertia is m^2 times smaller than the actual turbine inertia, where m is the gearbox transfer ratio. Complete wind turbine model is shown in the Fig. 3.6.

3.4 Maximum Power Point Tracking

The conversion efficiency of a horizontal axis wind turbine is dependent on two parameters, blade pitch angle and tip speed ratio [Wu et al (2011)].

The blade pitch angle is governed by a pitch mechanism. When the wind speed is below rated, the pitch mechanism should keep blade pitch at the optimal value so that maximum conversion efficiency can be achieved. On the other hand, when wind speed is above rated, blade pitch angle is decreased. Therefore, conversion efficiency is reduced and captured wind power is kept at the nominal value.

Tip speed ratio is defined as a ratio between blade tip speed and the speed of the wind. If ω_t is rotational speed of the turbine blades and r_t is turbine rotor radius, tip speed ratio is defined as follows:

$$\lambda = \frac{\omega_t \, r_t}{v_w} \tag{3.2}$$

Maximum turbine conversion efficiency will be achieved when both blade pitch angle and tip speed ratio are at their optimal values. If optimal tip speed ratio is λ_{opt} and blade pitch angle is kept at the optimal value, maximum conversion efficiency is achieved at the rotational speed:

$$\omega_t = \lambda_{opt} \frac{v_w}{r_t} \tag{3.3}$$

This means that, when the wind speed is variable and below rated, rotational speed of the wind turbine should be also variable so maximum power conversion efficiency can be achieved. A control mechanism that keeps WECS in maximum power conversion mode is the maximum power point tracking (MPPT) algorithm. There are many ways in which MPPT can be realised [Wu et al (2011)].

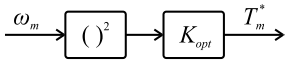

Figure 3.7 – Maximum power point tracking controller.

All of them use the turbine power characteristic given by the manufacturer and, depending on the wind speed, appropriate power, speed or torque is calculated. The MPPT method chosen here measures shaft speed and calculates optimal torque.

By analysing the turbine power characteristic, it can be noted that maximum power point dependence on shaft rotational speed is defined as follows:

$$P_t \sim \omega_t^3 \tag{3.4}$$

Considering the gearbox as ideal, the power available at the machine shaft P_m is equal to the captured power by the wind turbine P_t. Relationship between power and torque available on the machine shaft is given with:

$$P_m = T_m \omega_m \tag{3.5}$$

Considering the above, MPPT can be realised by keeping the machine's torque at the value proportional to the square of the shaft speed:

$$T_m \sim \omega_m^2 \tag{3.6}$$

Of course, the exact equation of an MPPT controller will be governed by the used wind turbine power characteristics and coefficient K_{opt} will be chosen accordingly. MPPT control block diagram is very simple and is illustrated in Fig. 3.7.

In this case, K_{opt} is chosen so that when the extracted power from the wind turbine is at nominal value, resulting torque reference sets the machine speed and power to their nominal values, respectively. One of the reasons for choosing this type of MPPT control is that it is very easy to regulate the machine torque when IRFOC is implemented, i.e. machine torque is proportional to the stator *q*-axis current. Therefore, there is no need to use any other controller, as would be the case when a MPPT controller provides the speed reference.

3.5 Indirect Rotor Field Oriented Control

Operation of WECS requires highly controllable speed or torque values of the generator. This requirement is achievable with high performance machine control. Since the machine used is an induction machine, rotor field oriented control (RFOC) will be used.

Successful implementation of RFOC requires that the machine is represented in a synchronously rotating reference frame, i.e. *d-q* variables [Singh et al (2005a)]. In chapter four, vector space decomposition (VSD) will be used to obtain a model in flux/torque producing α-β and non-producing *x-y-z* variables, where definition of all variables can be found as well. Since RFOC considers only the control of flux and torque, only equations in α-β subspaces are needed. Other machine subspaces are disregarded in this section. One of the advantages of the VSD modelling approach is that equations in

flux/torque producing subspace are always the same regardless of the phase number or whether the machine is symmetrical or asymmetrical. The number of neutral points is also irrelevant in establishing equations in the α-β subspace. In order to obtain equations in *d*-*q* variables, rotational transformation by arbitrary angle θ_a needs to be applied to the machine equations in stationary reference frame [Hu and Yang (2011)], as follows:

$$\begin{bmatrix} v_d \\ v_q \\ 0 \\ 0 \end{bmatrix} = \begin{bmatrix} [T_{\theta_a}] & [0] \\ [0] & [T_{\theta_a}] \end{bmatrix} \begin{bmatrix} R_s + L_s \frac{d}{dt} & 0 & L_m \frac{d}{dt} & 0 \\ 0 & R_s + L_s \frac{d}{dt} & 0 & L_m \frac{d}{dt} \\ L_m \frac{d}{dt} & \omega_e L_m & R_r + L_r \frac{d}{dt} & \omega_e L_r \\ -\omega_e L_m & L_m \frac{d}{dt} & -\omega_e L_r & R_r + L_r \frac{d}{dt} \end{bmatrix} \begin{bmatrix} [T_{\theta_a}]^{-1} & [0] \\ [0] & [T_{\theta_a}]^{-1} \end{bmatrix} \begin{bmatrix} i_d \\ i_q \\ i_{dr} \\ i_{qr} \end{bmatrix} \tag{3.7}$$

Matrix $[T_{\theta a}]$ is rotational transformation for arbitrary angle θ_a and is governed with:

$$[T_{\theta_a}] = \begin{bmatrix} \cos(\theta_a) & \sin(\theta_a) \\ -\sin(\theta_a) & \cos(\theta_a) \end{bmatrix} \tag{3.8}$$

Resulting equations in rotating *d*-*q* reference frame are divided in voltage and flux linkage equations for better interpretation and are as follows:

$$\begin{bmatrix} v_d \\ v_q \\ 0 \\ 0 \end{bmatrix} = \begin{bmatrix} R_s & -L_s\omega_a & 0 & -L_m\omega_a \\ L_s\omega_a & R_s & L_m\omega_a & 0 \\ 0 & -(\omega_a - \omega_e)L_m & R_r & -(\omega_a - \omega_e)L_r \\ (\omega_a - \omega_e)L_m & 0 & (\omega_a - \omega_e)L_r & R_r \end{bmatrix} \begin{bmatrix} i_d \\ i_q \\ i_{dr} \\ i_{qr} \end{bmatrix} + \frac{d}{dt} \begin{bmatrix} \psi_d \\ \psi_q \\ \psi_{dr} \\ \psi_{qr} \end{bmatrix} \tag{3.9a}$$

$$\begin{bmatrix} \psi_d \\ \psi_q \\ \psi_{dr} \\ \psi_{qr} \end{bmatrix} = \begin{bmatrix} L_s & 0 & L_m & 0 \\ 0 & L_s & 0 & L_m \\ L_m & 0 & L_r & 0 \\ 0 & L_m & 0 & L_r \end{bmatrix} \begin{bmatrix} i_d \\ i_q \\ i_{dr} \\ i_{qr} \end{bmatrix} \tag{3.9b}$$

Torque equation for the *n*-phase machine is as follows:

$$T_e = \frac{n}{2} P(\psi_d i_q - \psi_q i_d) \tag{3.10}$$

Angular speeds ω_a, ω_e and ω_{sl} are arbitrary reference frame rotational speed, rotor electrical rotational speed and rotor slip speed respectively. Together with rotor flux rotational speed ω_{el} and angle θ_{el} they are defined as follows:

$$\theta_a = \int \omega_a dt, \quad \theta_e = \int \omega_e dt, \quad \theta_{el} = \int \omega_{el} dt, \quad \theta_{sl} = \int \omega_{sl} dt, \quad \omega_{sl} = \omega_s - \omega_e \tag{3.11}$$

ω_s in equation (3.11) is the angular frequency of the stator variables.

To implement any high performance control it is necessary to have independent control over the machine's flux and torque, or in other words a control over the machine currents in the considered reference frame. In the case of an induction machine, independent control of flux and torque is achieved by aligning rotor flux vector with the *d*-axis of the arbitrary reference frame [Krishnan (2001)], i.e. $\theta_a = \theta_{el}$. Consequently, *q* component of the rotor flux vector ψ_{qr} is zero. Stator voltage, current and rotor flux space vectors together with stator, rotor and arbitrary reference frames are shown in Fig. 3.8.

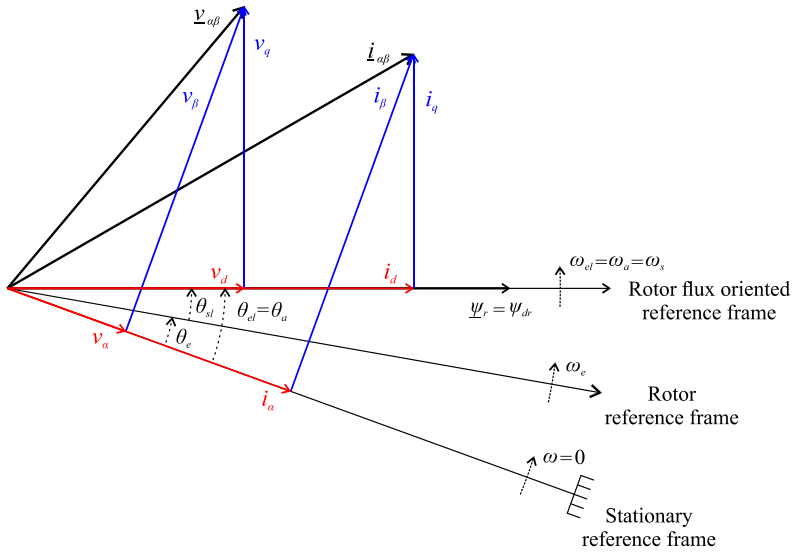

Figure 3.8 – Machine stator voltage, stator current and rotor flux space vectors.

From Fig 3.8 it can be seen that, when the arbitrary reference frame is aligned with rotor flux, ω_s is equal to the arbitrary reference frame rotational speed ω_a. In other words, ω_s and ω_a are equal to the rotor flux speed ω_{el}. Consequently, all stator variables will have dc values, allowing the use of standard PI controllers for current control.

Applying $\psi_{qr} = 0$ to the machine equations (3.9) - (3.10), the expressions for machine flux and torque become:

$$\psi_{dr} + \frac{L_r}{R_r}\frac{d\psi_{dr}}{dt} = L_m i_d \tag{3.12a}$$

$$T_e = \frac{n}{2} P \frac{L_m}{L_r} i_q \psi_{dr} \tag{3.12b}$$

Usually, in RFOC pre-fluxing is used, meaning that flux is kept constant during operation in the base speed region. Therefore, differential part in the (3.12a) can be omitted. To simplify the model further, it is assumed that the machine is not required to work in the field-weakening region. Hence, new rotor flux equation is now given with:

$$\psi_{dr} = L_m i_d \tag{3.13}$$

Equations (3.12b) and (3.13) show that the machine flux and torque control are decoupled when ψ_{dr} is considered constant. The torque is controlled by the *q* component of the stator current, while flux is controlled with the *d* component of the stator current. References for stator current are given with:

$$i_d^* = \frac{1}{L_m}\psi_{dr}^* \tag{3.14a}$$

$$i_q^* = \frac{2}{nP}\frac{L_r}{L_m}\frac{T_e^*}{\psi_{dr}^*} \tag{3.14b}$$

For successful implementation of RFOC it is necessary to know the instantaneous rotor field angle. If this angle is directly obtained, e.g. flux sensors and measured stator currents, then direct rotor field

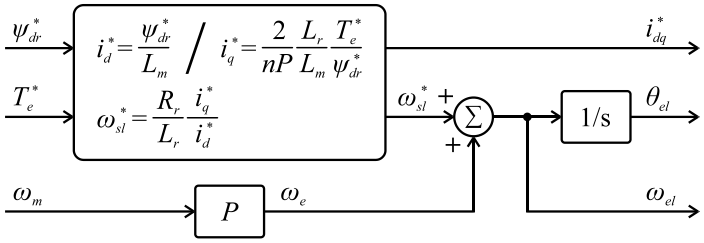

Figure 3.9 – Schematic of indirect rotor field oriented control.

oriented control (DRFOC) results. The problem with this solution is operation at zero speed. Another approach is indirect rotor field oriented control (IRFOC), where rotor mechanical position is measured with a resolver or optical encoder and slip is estimated. From Fig. 3.8 it can be seen that arbitrary reference frame angle needed for RFOC is a sum of rotor electrical angle θ_e and slip angle θ_{sl}. When stator variable angular frequency ω_s equals the arbitrary reference frame speed ω_a, slip angular frequency ω_{sl} can be estimated as:

$$\omega_{sl}^* = \frac{R_r}{L_r}\frac{i_q^*}{i_d^*} \tag{3.15}$$

Finally, angle of rotor flux oriented reference frame (rotor flux angle θ_{el}) can be calculated as follows:

$$\theta_a = \theta_{el} = \int\left(\frac{R_r}{L_r}\frac{i_q^*}{i_d^*} + \omega_e\right)dt \tag{3.16}$$

Schematic of an IRFOC is illustrated in the Fig. 3.9.

To complete the machine-side flux and torque control, it is necessary to implement current controllers as well. Since only flux and torque producing components will be considered, two current controllers are used, one for each of the *d*-*q* stator currents. Transformation from phase variables to *d*-*q* domain using VSD and rotational transformation will be explained in detail in the following chapter and will not be discussed further here.

The references produced by IRFOC control are current references. In this case, machine-side converter is voltage source inverter and it is necessary to provide appropriate voltage references. Therefore, machine stator equations (3.9a) – (3.9b) should be taken into account in designing current controllers. When IRFOC is applied, angle θ_{el} from (3.16) is used for transformation of the stator currents to rotor flux oriented reference frame. Now, rotor flux is aligned with *d*-axis and machine equations for stator currents can be rewritten in the following form:

$$v_d = R_s i_d + \left(L_s - \frac{L_m^2}{L_r}\right)\frac{d}{dt}i_d - \omega_{el}\left(L_s - \frac{L_m^2}{L_r}\right)i_q \tag{3.17a}$$

$$v_q = R_s i_q + \left(L_s - \frac{L_m^2}{L_r}\right)\frac{d}{dt}i_q + \omega_{el}L_s i_d \tag{3.17b}$$

From (3.17a) and (3.17b) it can be seen that *d*- and *q*-axis voltages are not decoupled, since there is a mutual dependency on currents in *d* and *q*-axis. Consequently, the current controller needs to be

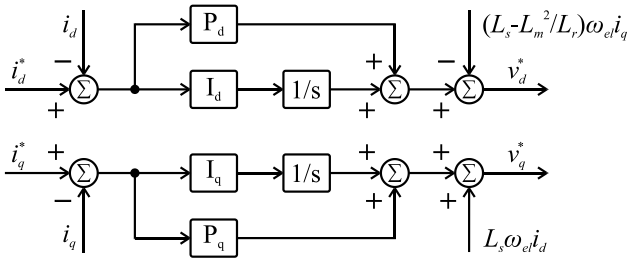

Figure 3.10 – Proportional-integral regulator with cross-coupling decoupling (PIccd).

complemented with the decoupling terms. Controlled variables and decoupling terms, which should be added to the current regulator outputs so that decoupled control can be achieved, are governed with:

$$v_d^{'} = R_s i_d + \left(L_s - \frac{L_m^2}{L_r} \right) \frac{d}{dt} i_d \tag{3.18a}$$

$$v_q^{'} = R_s i_q + \left(L_s - \frac{L_m^2}{L_r} \right) \frac{d}{dt} i_q \tag{3.18b}$$

$$e_d = -\omega_{el} \left(L_s - \frac{L_m^2}{L_r} \right) i_q \tag{3.19a}$$

$$e_q = \omega_{el} L_s i_d \tag{3.19b}$$

Finally, from (3.18a) and (3.18b) it can be seen that proper current control can be achieved with proportional-integral (PI) regulators. If *P* and *I* are proportional and integral constants, transfer function of the standard PI controller is as follows:

$$G_{PI}(s) = P + \frac{I}{s} \tag{3.20}$$

Integrator windup is one of the problems inherent to the integral control. When the output of regulator is saturated and there is still an error in the controlled variable, integrator will continue to sum up the error value. This will result in overshoot and oscillations of the controlled variable when the system returns from saturation. To avoid this, a simple anti-windup mechanism is implemented to stop integration once saturation occurs.

When decoupling parameters are taken into consideration, PI with cross-coupling decoupling (PIccd) regulator is created, illustrated in the Fig. 3.10. PIccd enables independent control over i_{dq} currents. Consequently, independent flux and torque control is achieved, which enables implementation of high performance speed or position control (so called servomechanism). In this case, implementation of servomechanism is not needed, since chosen MPPT regulator has torque reference as output variable.

3.6 *X-y* Current Control and Low Order Harmonic Elimination

Until now, only flux and torque control has been considered. Hence, it was only required to control flux/torque producing currents (α-β / *d*-*q*) and for that PIccd current controller has been used. However, as it will be shown later throughout the thesis, current control in *x*-*y* subspaces is necessary as well, either to produce imbalance between machine phases, or to eliminate low order harmonics induced by

non-ideal machine construction or inverter dead-time. A proper realisation of the control in both cases requires machine equations in *x-y* subspaces [Hu and Yang (2011)], which are for the convenience given here in complex domain in both stationary *x-y* and rotating *d-q*$_{x\text{-}y}$ reference frames as follows:

$$\underline{v}_{xy} = \left(R_s + L_{ls}s\right)\underline{i}_{xy} \tag{3.21a}$$

$$\underline{v}_{dqxy} = R_s \underline{i}_{dqxy} + sL_{ls}\underline{i}_{dqxy} + j\omega_{el}L_{ls}\underline{i}_{dqxy} \tag{3.21b}$$

Although the index *d-q*$_{x\text{-}y}$ used here is at the first glance very complicated, it is found to be convenient for distinguishing stationary VSD coordinates (α-β, *x-y*) and rotational ones (*d-q*). This nomenclature will be used throughout the thesis, while more details is available in chapter 4. Transformation to the rotational reference frame is done by simple Park transformation for the angle of rotor flux position θ_{el}. Since both (3.21a) and (3.21b) are of the same form as are the equations of an inductive filter, the chosen controller types are Complex Vector Proportional-Integral (cvPI) and its resonant variant, Vector Proportional Integral (VPI) [Lascu et al (2007), Lascu et al (2009), Yepes (2011)].

For the control of *x-y* currents of fundamental frequency cvPI controllers are chosen since they are internally decoupled and less sensitive to error in parameter estimation when compared to PI with cross-coupling decoupling (PIccd). Another advantage over PIccd is a possibility to use multiple cvPI controllers in parallel. Furthermore, when cvPI are properly tuned, there is no overshoot in current step response. If ω_1 is fundamental frequency, h is the controlled harmonic, k_{Ph} and k_{Ih} are regulator constants, the general form of the used cvPI controllers is as follows:

$$G_{cvPIh}(s) = \frac{sk_{Ph} + k_{Ih} + jh\omega_1 k_{Ph}}{s} \tag{3.22}$$

Since only components at the fundamental frequency are controlled, term $h\omega_1$ is equal to ω_{el} and controller constants become k_P and k_I. Furthermore, to compensate for the complex pole added by decoupling terms, cvPI regulator is tuned as follows:

$$\frac{k_I}{k_P} = \frac{R_s}{L_{ls}}, \quad k = \frac{k_p}{L_{ls}} \tag{3.23}$$

The constant k represents regulator bandwidth and it is the only parameter requiring tuning in order to get fast enough controller response, while at the same time avoiding influence of the switching noise on the controller performance. Schematic diagram of the tuned cvPI controller is given in the Fig. 3.11 and its transfer function is as follows:

$$G_{cvPI}(s) = k\frac{sL_{ls} + R_s + j\omega_{el}L_{ls}}{s} \tag{3.24}$$

Since the machine is inverter supplied, low order harmonics are induced by the inverter dead time [Yepes et al (2013)] and their elimination is a mandatory step when it comes to implementation of current control. Resonant controllers are chosen for this purpose, more specifically VPI type. The transfer function is as follows:

$$G_{VPIh}(s) = \frac{s^2 k_{Ph} + sk_{Ih}}{s^2 + h^2\omega_1^2} \tag{3.25}$$

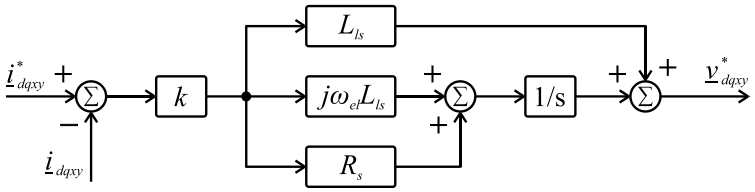

Figure 3.11 – Complex Vector Proportional-Integral controller.

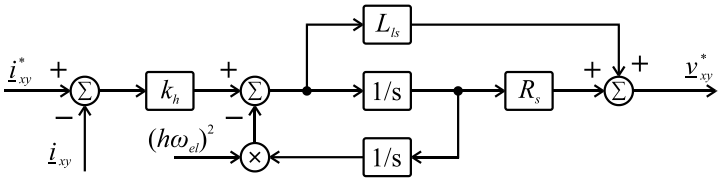

Figure 3.12 – Vector Proportional-Integral resonant controller.

VPI controllers are tuned according to the equations in the *x-y* subspace (3.21a) in the same manner as cvPI, i.e. as shown in (3.23). Transfer function of the tuned VPI is as follows:

$$G_{VPIh}(s) = k_h \frac{s(sL_{ls} + R_s)}{s^2 + h^2\omega_1^2} \tag{3.26}$$

Implementation of the VPI regulator is done by means of two integrators as shown in Fig. 3.12. Once again, it is only necessary to tune the controller bandwidth by setting the parameter k_h.

During the experimental validations, low order harmonic elimination was found to be necessary. Namely, the +5th and +7th harmonics are present due to the inverter dead time, while -29th and -31st harmonics are present due to the non-ideal machine construction. Harmonic elimination strategy by use of resonant controllers in synchronous reference frames, applicable to asymmetrical multiphase machines [Yepes et al (2016)], has been adopted here. In this particular case, not all low-order harmonics are present. Consequently, resonant controllers and synchronous reference frames are tuned to different harmonic orders than the optimal ones proposed in [Yepes et al (2016)]. Harmonic orders to which synchronous reference frames and VPIs are tuned are given in the Table 3.1. To further reduce harmonic content of phase currents, eight different harmonics are eliminated in total, as per Table 3.1.

Table 3.1 – Configuration of implemented resonant controllers.

Resonant Controller	Subspace	Rotation	Harmonic order	Controlled harmonics
VPI 1	x_1-y_1	-4	9	+5 / -13
VPI 2			27	+23 / -31
VPI 3	x_2-y_2	-2	9	+7 / -11
VPI 4			27	+25 / -29

In order to demonstrate the effectiveness of the VPI current controllers, experimental results are given in Fig. 3.13. Full description of the experimental setup, including both hardware and software, is available in the Appendix B of the thesis, while control implementation is detailed in the following chapters. The machine operates with IRFOC at 1000 rpm without harmonic elimination. One period of the phase current (i_{a1}) with the corresponding spectrum is shown in the two upper plots of the Fig. 3.13. It can be seen that, in addition to the fundamental frequency component, the 5th and the 29th harmonics are significant. The 7th, 11th, 23rd, 25th, and 31st harmonics are also present but to a lesser extent.

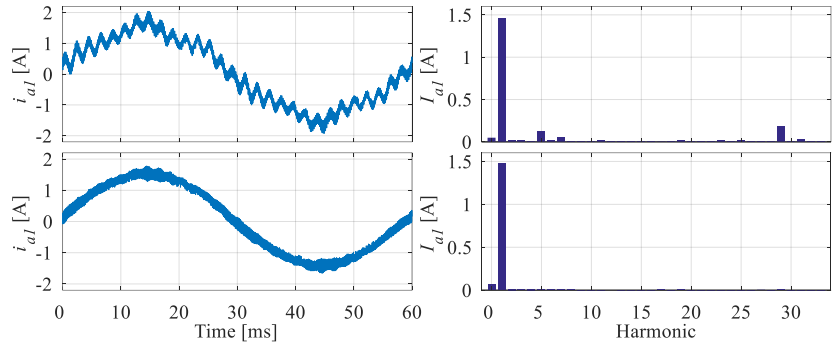

Figure 3.13 – Phase currents with the harmonic control switched off and on.

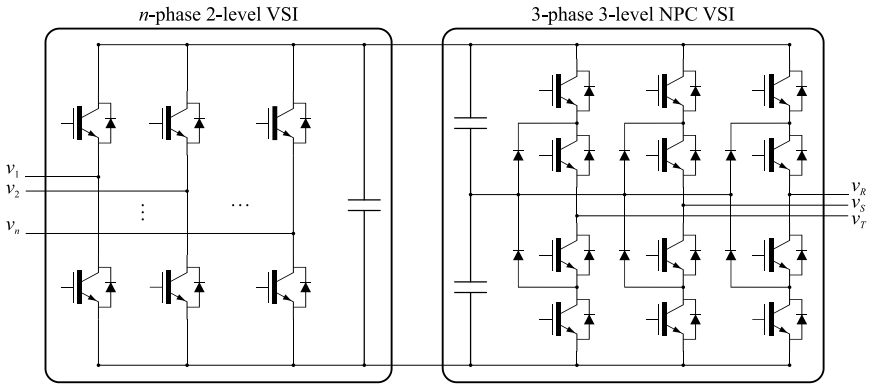

Figure 3.14 – Back-to-back inverter configuration.

The same experiment is repeated, but with activated VPI resonant controllers. The phase current and the spectrum are given in the lower plots of Fig. 3.13. The spectrum shows that the low-order harmonics are successfully eliminated.

3.7 Two-Level and Three-Level Voltage Source Inverters in Back-to-Back Configuration

To implement any control technique, it is mandatory to have a supply which is capable of providing variable frequency near-sinusoidal voltages. Two types of the supplies are typically used for driving the machines: voltage source inverters (VSI) and current source inverters (CSI). Since the majority of WECSs are connected to the grid, in addition to the requirement of full controllability and bidirectional power flow use of a back-to-back configuration is necessary. Keeping in mind that the goal of this chapter is modelling of the WECS in general, the simplest two-level VSI will be used on the machine side. However, it should be noted that in the high power applications, multilevel inverters are common due to the lower current ripple and smaller stress on the switches.

Due to the strict grid code, grid-side inverters usually have three or more levels to achieve lower current ripple with the smaller inductance values. Here a 3-level NPC inverter is used; block diagram of the inverter configuration is shown in Fig. 3.14.

Control of the machine-side inverter is done by pulse width modulation (PWM). As noted in chapter 2, two modulation strategies are predominantly used: space vector PWM (SVPWM) and carrier based

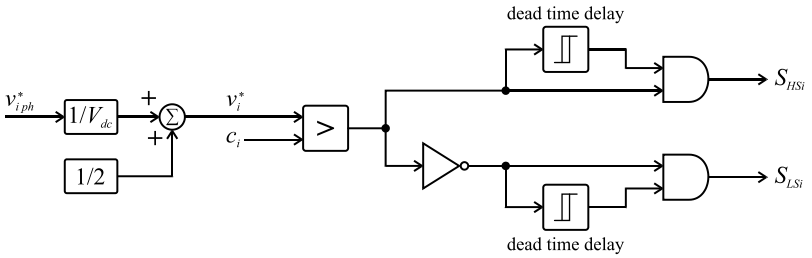

Figure 3.15 – CBPWM diagram for one of the phases.

PWM (CBPWM). SVPWM is based on selecting different voltage vectors and calculating appropriate application times in-order to produce desired waveforms. As the number of phases increases SVPWM becomes more complicated and requires more computational resources for implementation. On the other hand, CBPWM is simple and its complexity is not increased as the number of phase's increases. Since the controlled machine has nine phases, CBPWM is used.

CBPWM modulation strategy is based on comparing the reference signals with triangular carrier signal and switching the output voltage to zero or dc-link voltage value. Consequently, average value of the output voltage over one carrier period will be equal to the reference signal value. Diagram of CBPWM for one of the phases is illustrated in Fig. 3.15. Detailed analysis of CBPWM can be found in [Holmes and Lipo (2003)].

Signals v_i^* and c_i are references and the carrier respectively, where i represents phase number. References v_i^* are obtained by scaling phase voltage references $v^*_{i\,ph}$ by dc-link voltage value V_{dc}, as shown in the Fig. 3.15. Therefore, references v_i^* are in range [0, 1], the same as the carrier signal. Digital signals S_{HSi} and S_{HSi} are the high-side and low-side transistor gating signals. Due to the required semiconductor turn-off time, dead time is implemented so both switches in one inverter leg cannot be switched on at the same time. Otherwise, dc link will be shorted at each switching.

Carrier signal c_i is the same for all of the phases and it has triangular waveform ranging from 0 to 1. References v_i^* are governed by the current controllers. Depending on the machine configuration, whether it is symmetrical or asymmetrical or with one or three neutral points, different dc-bus voltage utilisation can be achieved by zero-sequence injection [Dujic et al (2010)]. It is concluded that the dc-bus voltage utilisation in the machines with multiple neutral points depends on the number of phases in the winding sets. On the other hand, multiphase machines with a single neutral point and odd number of phases have the same dc bus voltage utilisation for both symmetrical and asymmetrical configurations, while asymmetrical ones with even phase number have better dc bus voltage utilisation when compared to the symmetrical machines. Maximum dc bus voltage utilisation of the 9-phase machine depending on the configuration is given in the Table 3.2.

Table 3.2 – Maximum dc bus voltage utilisation of the 9-phase machine.

NP number	Symmetrical	Asymmetrical
1	$1.0154 \cdot V_{dc}$	$1.0154 \cdot V_{dc}$
3	$1.1547 \cdot V_{dc}$	$1.1547 \cdot V_{dc}$

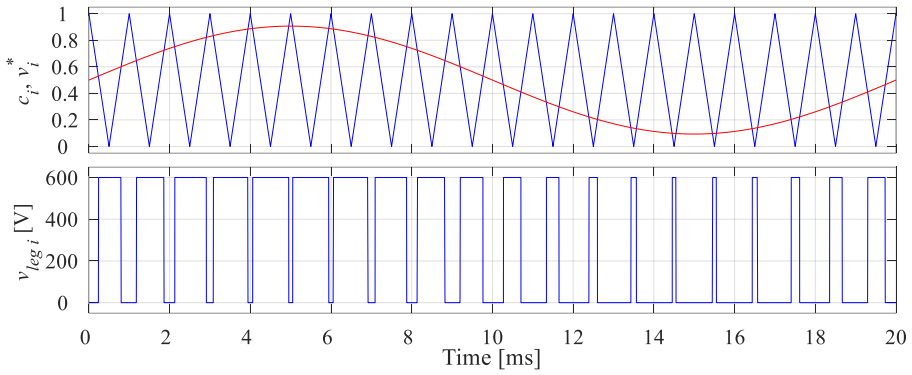

Figure 3.16 – Carrier, reference and leg voltage of one period of sinusoidal reference.

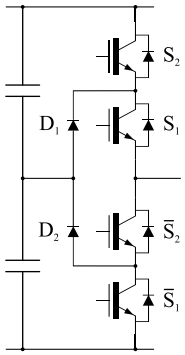

Figure 3.17 – One leg of a three-level NPC inverter.

In this thesis, only continuous PWM in the linear modulation region is considered. Discontinuous PWM schemes are out of the scope of this research. When the dc-link voltage is 600 V, one period of a sinusoidal reference and corresponding leg voltage are illustrated in Fig. 3.16.

Due to the strict grid code it is usually mandatory to use a multilevel voltage source inverter when connecting to the 3-phase grid. Among many possible types of these inverters, three structures are mostly used in medium voltage industrial drives [Rodriguez et al. (2007)]:

1. Neutral point clamped voltage source inverter
2. Flying capacitor voltage source inverter
3. Cascaded H-bridge voltage source inverter.

Three-level neutral point clamped (3L-NPC) will be used for the grid connection here due to simplicity. One leg of the 3L-NPC inverter is shown in Fig. 3.17.

Instead of one capacitor, as in the standard two level inverters, two capacitors in series are used here to split the dc link, so that one-half of the dc-link voltage can be obtained. Capacitor connecting point is called dc-link mid-point or neutral point. Diodes are used to clamp dc-link neutral point to the output voltage. Using the switches S_1, $\overline{S}_1$, S_2 and $\overline{S}_2$ four different values of the output voltage can be achieved: 0 V, $V_{dc}/2$, V_{dc} and high impedance. The truth table is given in Table 3.3.

The same as for the two-level inverter, 3L-NPC inverter switching can be governed by carrier based or space vector modulation. Due to the simplicity carrier based PWM has been chosen. In the case of 3L-NPC two carrier signals are needed for proper operation. If the reference signal is in the range [0, 1],

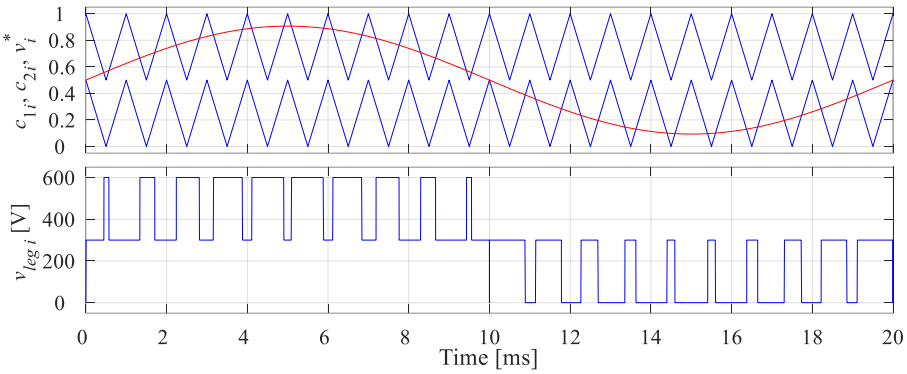

Figure 3.18 – Two carriers, reference, and leg voltage of one period of sinusoidal reference of 3L-CBPWM.

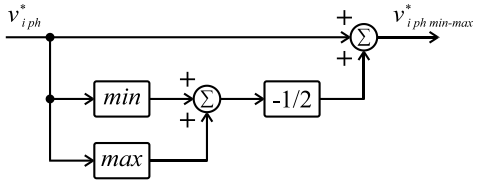

Figure 3.19 – Min-max injection.

Table 3.3 – Truth table of a three-level NPC inverter.

S_1	$\overline{S}_1$	S_2	$\overline{S}_2$	Leg voltage
0	1	0	1	0
0	1	1	0	High Z
1	0	0	1	$V_{dc}/2$
1	0	1	0	V_{dc}

to achieve linear operation, the first carrier is in range [0, 0.5] while the second carrier is in the range [0.5, 1]. Instead of one carrier, as shown for two-level operation in Fig 3.16, two are needed. Gating signals for the switches S_1 and $\overline{S}_1$ are obtained by comparing the reference with the first carrier spanning [0, 0.5], while comparison of the reference with the second carrier spanning [0.5, 1] produces gating signals for the switches S_2 and $\overline{S}_2$. When the dc-link voltage is 600 V, one period of a sinusoidal reference, both carriers, and leg voltage waveforms are shown in Fig. 3.18.

In a balanced 3-phase system the maximum dc-link voltage utilisation is achieved when peak value of the line voltage becomes equal to the dc-link voltage. If modulation index is defined as a ratio between phase voltage amplitude and half of the dc bus voltage, maximum modulation index in standard CBPWM is equal to 1. For SVPWM maximum modulation index is 1.15, while in the case of CBPWM the same maximum modulation index is achievable by applying the min-max injection. Complete equivalence between SVPWM and CBPWM for the 3-level case is achieved by use of double min-max injection. However, for the sake of simplicity the same min-max injection as for the 2-level case is adopted. This technique is based on positioning references in a way that their minimum and maximum values at each instant of time will be centred around mid-point. Effectively, this is done by applying

$$v^*_{i\,ph\,\min-\max} = v^*_{i\,ph} - \frac{\min\left(v^*_{i\,ph}\right) + \max\left(v^*_{i\,ph}\right)}{2} \tag{3.27}$$

to all phase voltage references. Implementation is shown in Fig. 3.19.

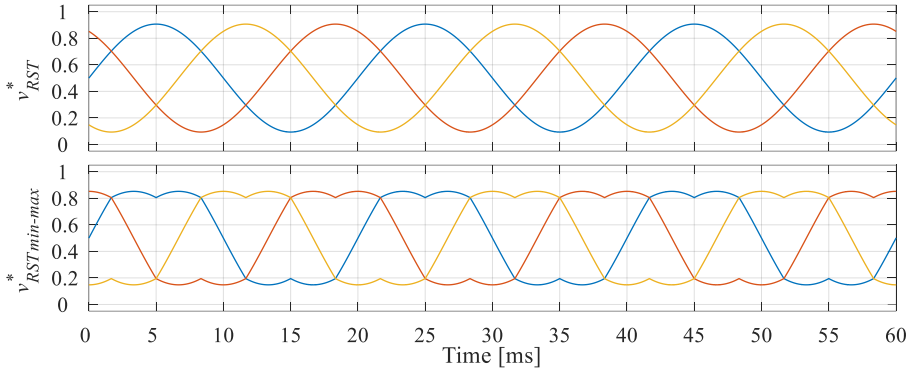

Figure 3.20 – 3-phase references before and after min-max injection.

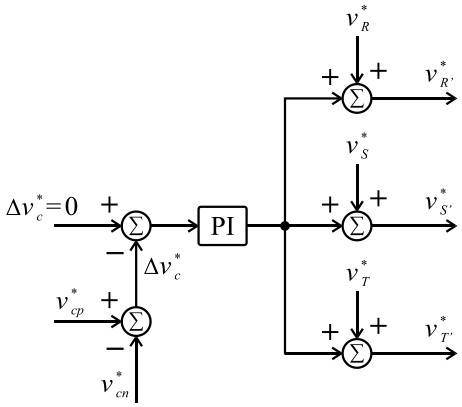

Figure 3.21 – NPC capacitor voltage balancing controller.

References used in the min-max injection are governed by the grid-side control and they will have sinusoidal waveforms if the grid voltages are balanced. Hence, sinusoidal 3-phase references, before and after min-max injection, are shown in Fig. 3.20. It can be seen that application of min-max injection has flattened the tops of the reference signal, thus allowing the fundamental to be increased by 15.5% without the references going outside of the carrier range [0, 1].

When a three-level NPC inverter is used, another issue to consider is the capacitor voltage balancing. Due to the non-ideal switches in the converter, voltage difference in the series capacitors may occur. Since CBPWM is used, simple capacitor balancing technique can be implemented by controlling the homopolar component added to all three references [Pereira and Martins (2009)]. Block diagram of the voltage balancing controller is shown on the Fig 3.21. v_{Cp} and v_{Cn} are voltages of the upper and lower capacitors, respectively.

3.8 Voltage Oriented Control of the Grid-Side Inverter

When a WECS is connected in the back-to-back configuration, the grid-side inverter needs to be independently controlled so the system can be interfaced with the grid. Usually there are two main tasks that grid-side inverter control needs to achieve:

1. Keep the dc-link voltage at the set level.
2. Deliver to the grid arbitrarily set reactive power.

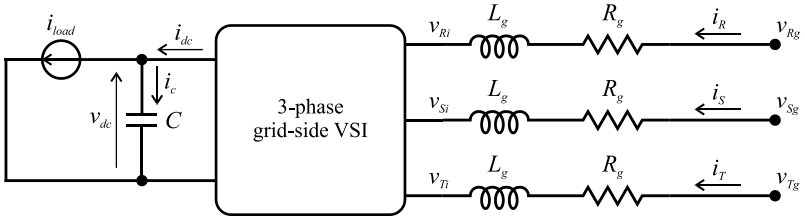

Figure 3.22 – Simplified schematic of the grid-side inverter.

Beside these two main tasks it is also required that the grid-side inverter complies with all grid codes regarding total harmonic distortion of the currents, ride-through-fault operation and sometimes change of the direction of power flow. These additional tasks are out of the scope of this research and they will not be considered further. One of the most popular ways of achieving the aforementioned main tasks is voltage oriented control (VOC). Grid voltage angle is detected and control is implemented in grid-synchronised rotating reference frame. Simplified schematic of the dc link, grid-side inverter and grid filter is shown in Fig. 3.22.

Dc side of the inverter consists of a dc-link capacitor and current source to emulate dc load. On the other side, connection of VSI to the grid requires grid filter. In this case simple inductive filter with inductance L_g and resistance R_g is chosen. Grid voltages have index *g*, while grid-side inverter voltages have index *i*. Equations of the grid currents are as follows:

$$\begin{bmatrix} v_{Ri} \\ v_{Si} \\ v_{Ti} \end{bmatrix} = \begin{bmatrix} v_{Rg} \\ v_{Sg} \\ v_{Tg} \end{bmatrix} - \begin{bmatrix} R_g + L_g \frac{d}{dt} & 0 & 0 \\ 0 & R_g + L_g \frac{d}{dt} & 0 \\ 0 & 0 & R_g + L_g \frac{d}{dt} \end{bmatrix} \begin{bmatrix} i_R \\ i_S \\ i_T \end{bmatrix} \tag{3.28}$$

Grid current control can be easily realised in the grid synchronous reference frame. Firstly, grid voltage angle needs to be detected. There are many ways of doing this, but the current state-of-the-art technology is the utilisation of a phase locked loop (PLL), which will be explained in the following section. After detection of the grid voltage angle, decoupling and rotational transformations are applied to the currents of (3.28). For the purpose of this chapter, the grid voltages are considered balanced, so zero sequence can be omitted. Grid voltage angle is θ_g. Decoupling and rotational transformations are given with:

$$\begin{bmatrix} f_\alpha \\ f_\beta \end{bmatrix} = \frac{2}{3} \begin{bmatrix} 1 & \cos\left(\frac{2\pi}{3}\right) & \cos\left(\frac{4\pi}{3}\right) \\ 0 & \sin\left(\frac{2\pi}{3}\right) & \sin\left(\frac{4\pi}{3}\right) \end{bmatrix} \begin{bmatrix} f_R \\ f_S \\ f_T \end{bmatrix} \tag{3.29}$$

$$\begin{bmatrix} f_d \\ f_q \end{bmatrix} = \frac{2}{3} \begin{bmatrix} \cos(\theta_g) & \sin(\theta_g) \\ -\sin(\theta_g) & \cos(\theta_g) \end{bmatrix} \begin{bmatrix} f_\alpha \\ f_\beta \end{bmatrix} \tag{3.30}$$

while the grid currents in synchronously rotating *d-q* reference frame are governed with:

$$\begin{bmatrix} v_{di} \\ v_{qi} \end{bmatrix} = \begin{bmatrix} v_{dg} \\ v_{qg} \end{bmatrix} - \begin{bmatrix} R_g + L_g \frac{d}{dt} & -\omega_g L_g \\ \omega_g L_g & R_g + L_g \frac{d}{dt} \end{bmatrix} \begin{bmatrix} i_{dg} \\ i_{qg} \end{bmatrix} \tag{3.31}$$

Equation (3.31) is of the same form as the equation for machine *x-y* currents in rotational reference

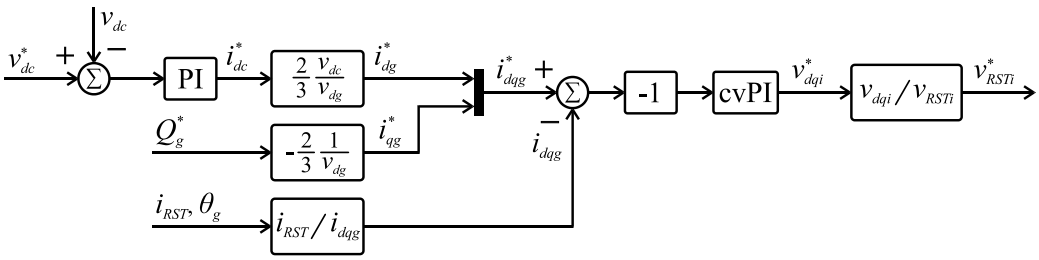

Figure 3.23 – Voltage oriented control of the grid-side inverter.

frame (3.21b). However, difference in sign due to the chosen grid currents orientation should be noted, so that it can be included in the regulator design. A cvPI regulator of the same form as the one used for the machine *x*-*y* current control can be utilised as a grid current controller as well. Furthermore, the same controller tuning as in (3.23) applies, so that the grid-side cvPI constants are as follows:

$$\frac{k_I}{k_P} = \frac{R_g}{L_g}, \quad k = \frac{k_p}{L_g} \tag{3.32}$$

In the applied synchronously rotating reference frame the grid voltage vector is aligned with the *d*-axis. Consequently, *q*-axis component is equal to zero. As a result, expressions for the active and reactive power are simplified and they are as follows:

$$P_g = \frac{3}{2} v_{dg} i_{dg} \tag{3.33a}$$

$$Q_g = -\frac{3}{2} v_{dg} i_{qg} \tag{3.33b}$$

When implementing grid-connected WECS it is usually required that reactive power can be arbitrarily set [Wu et al (2011)]. With VOC this is easily realised by controlling the *q*-axis current component of the grid-side inverter. From (3.33b), *q*-axis current reference is as follows:

$$i_{qg}^* = -\frac{2}{3}\frac{Q_g}{v_{dg}} \tag{3.34}$$

If the inverter and grid filter losses are neglected, active power on the grid side P_g is equal to the power delivered to the dc link P_{dc} and the following applies:

$$v_{dc} i_{dc} = \frac{3}{2} v_{dg} i_{dg} \quad \rightarrow \quad i_{dg}^* = \frac{2}{3}\frac{v_{dc}}{v_{dg}} i_{dc} \tag{3.35}$$

Since the grid voltage v_{dg} is considered constant, the component of the grid current along the *d*-axis controls active power and consequently dc-link power and current. Therefore, another PI regulator in the outer dc-link voltage control loop is used to provide reference for the *d*-axis current component i_{dg} [Wu et al (2011)]. Finally, the complete system with current controllers and the decoupling terms is shown in Fig. 3.23.

Variation of the dc-link current will result in change of the active power transferred to the grid. Since PI regulator will keep V_{dc} voltage at the set level, power transfer direction will depend solely on the direction of the i_{load} current. If i_{load} is positive, the system works in generating mode and power flow is

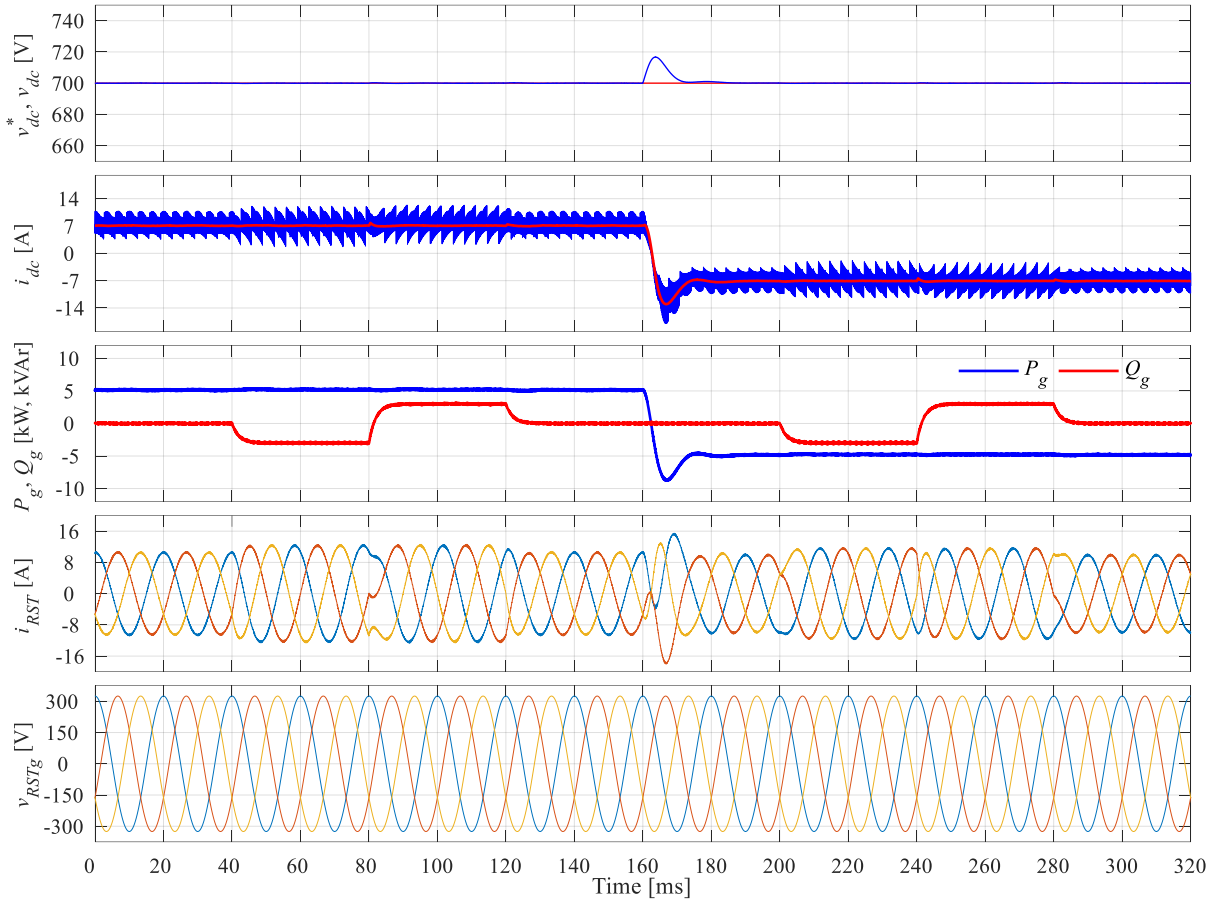

Figure 3.24 – Dc-link voltage and current, grid currents and active and reactive powers.

from the dc link to the grid. On the other hand, if i_{load} is negative, power flow is from the grid to the dc link and the inverter acts as a rectifier.

Operation of the VOC has been tested for different power transfer scenarios. In all cases VOC needs to keep the value of the dc-link voltage constant and provide set value of reactive power to the grid. To demonstrate both directions of power flow, i_{load} current has been changed from 7.14 A to -7.14 A resulting in +/-5 kW of active power at 700 V dc link. Consequently, the VSI is firstly working as an inverter and later on as a rectifier. Furthermore, during both modes of operation, the reference for the reactive power has been varied from positive to negative 3 kVAr. Results are shown in the Fig. 3.24. It can be seen that for the most part dc-link voltage is stable regardless of the power flow or the reactive power requirements. A small overshoot in the dc-link voltage is present due to the abrupt change in direction of power flow and the limited controller bandwidth. In normal operating condition, this abrupt change is not likely to happen, and this case thus represents the worst case scenario.

3.9 Grid Synchronisation and Phase Locked Loop

Since VOC and grid current controllers are implemented in the synchronous reference frame, it is necessary to detect grid phase angle. Therefore, grid synchronisation should be implemented. This is not a straightforward task and various methods have been developed over the years.

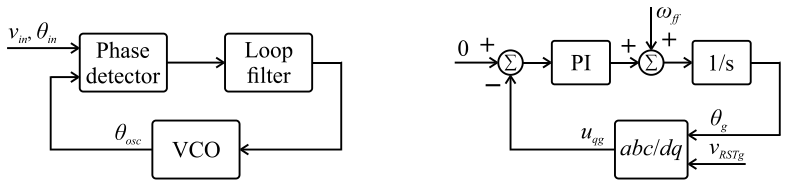

a) Standard PLL. b) 3-phase PLL.

Figure 3.25 – Standard (a) and modified (b) PLL structures.

One of the firstly developed methods is the zero crossing detection, where zero crossings of the grid voltages are detected and phase angles are calculated. Problem with this method is that it is sensitive to grid disturbances like phase unbalance and variation in frequency. Some improvement over zero crossing detection method can be achieved with filtering of the grid voltages, but extracting grid phase in unbalanced network remains difficult. Furthermore, filtering introduces the signal delay, which is unacceptable in this case.

A more sophisticated method of detecting the grid phase is by the use of a phase locked loop (PLL) [Blaabjerg et al (2006)]. It overcomes the problems that exist in the zero crossing detection and grid voltage filtering methods. A classic PLL is adapted to work with the 3-phase grid voltages [Chung (2000a), Chung (2000b)]. Namely, three main parts of the PLL, phase detection, voltage controlled oscillator, and loop filter are revised so it can be used in a 3-phase system. A standard PLL schematic is shown in Fig. 3.19a and a modified PLL structure is given in Fig. 3.19b.

Phase detection is achieved using standard Clarke and rotational transformations, while PI regulator acts as a loop filter. Voltage controlled oscillator is replaced by an integrator. Synchronisation to the grid is achieved when the grid voltage component on the *q*-axis is equal to zero. Therefore, PI controller keeps the *q*-axis component at the zero value by setting the phase angle of the rotational transformation. Since the grid frequency is known, it is common in 3-phase PLL to add a feed forward signal ω_{ff}, which is equal to the grid frequency in rad/s.

3.10 Simulation Results of the Complete WECS

To verify proper operation of the implemented WECS in the back-to-back configuration, simulations of the key system elements are carried out individually and later on the whole system has been simulated. Utilised motor model will be described in chapter 4. Some simulation specific analysis, such as controller limits, will be presented in this section. An asymmetrical 9-phase machine with 3 neutral points is used, and the parameters are given in table 3.3.

Table 3.3 – Machine parameters.

Phase number	9	Stator resistance [Ω]	5.3
Pole pair number	1	Rotor resistance [Ω]	2.0
Nominal speed [rpm]	2880	Stator leakage inductance [mH]	24
Nominal power [kW]	2.2	Rotor leakage inductance [mH]	11
Nominal voltage [V]	230	Magnetising inductance [mH]	520
Nominal current [A]	1.5	Rotor inertia [kg m^2]	0.043

The machine is rated at 5 kW and is for 3000 rpm synchronous speed, meaning that the rated torque is close to 16 Nm. Consequently, the selected turbine has the same rated power at the rated wind speed. Furthermore, used gearbox and MPPT controller are tuned so that at the rated wind speed turbine has optimal tip speed ratio and machine rotational speed is at the rated value. Accordingly, during steady state the machine torque is limited to the rated value. Since the flux is kept at the rated value by IRFOC at all times and the torque in steady state is equal or below rated value, the phase currents are equal or below rated value during the steady state. Furthermore, it should be taken into consideration that the machine is operating as a generator, and the torque reference should be negative at all times. Additionally, during the transient, machine torque may be larger than the rated during short periods of time. Therefore, torque limits are set to -24 Nm and 0 Nm, i.e. -150 % of the rated torque and zero.

Another limiting factor is the linear modulation limit that depends on the dc-link voltage value. Since zero-sequence injection is applied on the machine side, the amplitude of the phase voltages must be smaller than $v_{dc}/\sqrt{3}$. When the amplitude invariant transformation is applied and *x*-*y* currents are equal to zero, the following must be satisfied:

$$V_{phase} = |v_{dq}| = \sqrt{v_d^2 + v_q^2} \leq \frac{v_{dc}^*}{\sqrt{3}} \approx 404\,\text{V} \tag{3.36}$$

Equations (3.17a) and (3.17b) provide correlation between machine voltage and current in *d*-*q* subspace. Since it can be assumed that current controllers are fast enough, differential term may be omitted:

$$v_d \approx R_s i_d - \omega_s \left(L_s - \frac{L_m^2}{L_r} \right) i_q \tag{3.37a}$$

$$v_q \approx R_s i_q + \omega_s L_s i_d \tag{3.37b}$$

Nominal value of the i_d current is obtained from the (3.14a) by assuming nominal voltage, synchronous speed and no-load condition and is given as follows:

$$i_d^* = \left| \frac{230\sqrt{2}}{R_s + j2\pi 50(L_{ls} + L_m)} \right| \approx 1.9\,\text{A} \tag{3.38}$$

On the other hand, current limits along *q*-axis can be found by using torque limits and (3.14b). These values are -5.48 A and 0 A, respectively. Finally, by using obtained current values, nominal speed, and (3.37a) and (3.37b) maximum voltage values are: $v_{d,max}$ = 49.74 V, $v_{q,max}$ = 354.14 V and $|v_{dq}|$ = 357.61 V. Since the dc-link voltage is 700 V, condition (3.36) is satisfied and there is enough voltage reserve so the machine will stay in the linear modulation region even in the presence of harmonics and during the speed/load transients.

To test the machine-side control, the shaft is disconnected from the wind turbine and connected to a source of constant torque (16 Nm). Instead of using MPPT for generating torque reference, speed loop has been implemented by adding a simple PI regulator. Speed reference has been imposed so that the machine reversal test from positive to negative nominal speed is conducted. Torque limits are set to +/- 24 Nm. Machine speed and torque, i_{dq} currents and absolute value of IRFOC output voltage $|v_{dq}|$ are

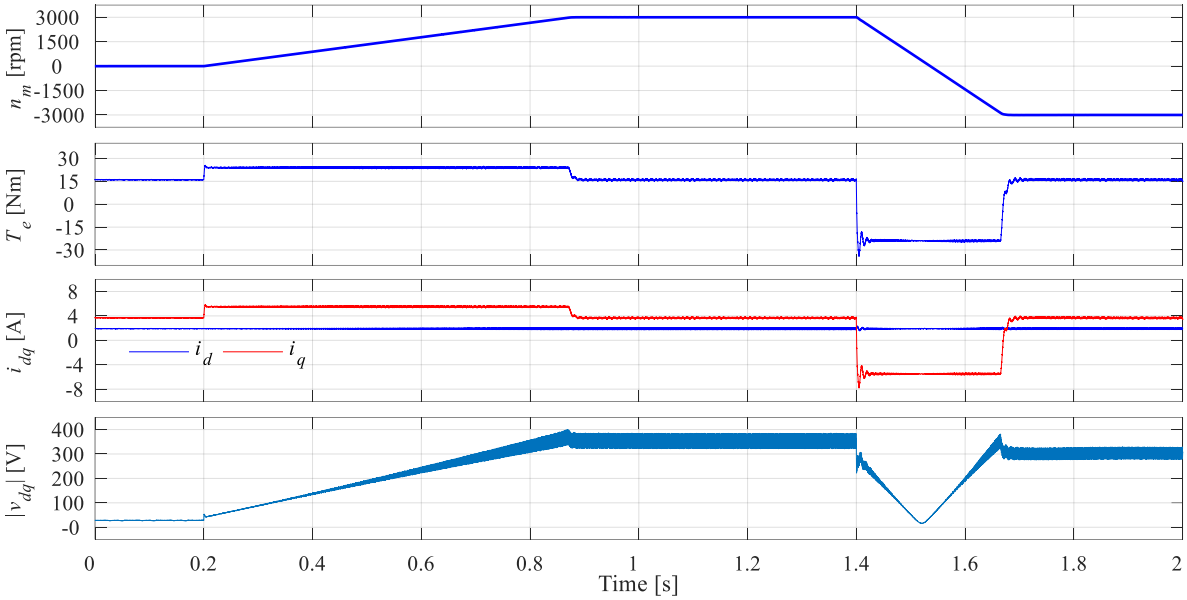

Figure 3.26 – Machine speed, torque, i_{dq} currents and absolute value of $|v_{dq}|$.

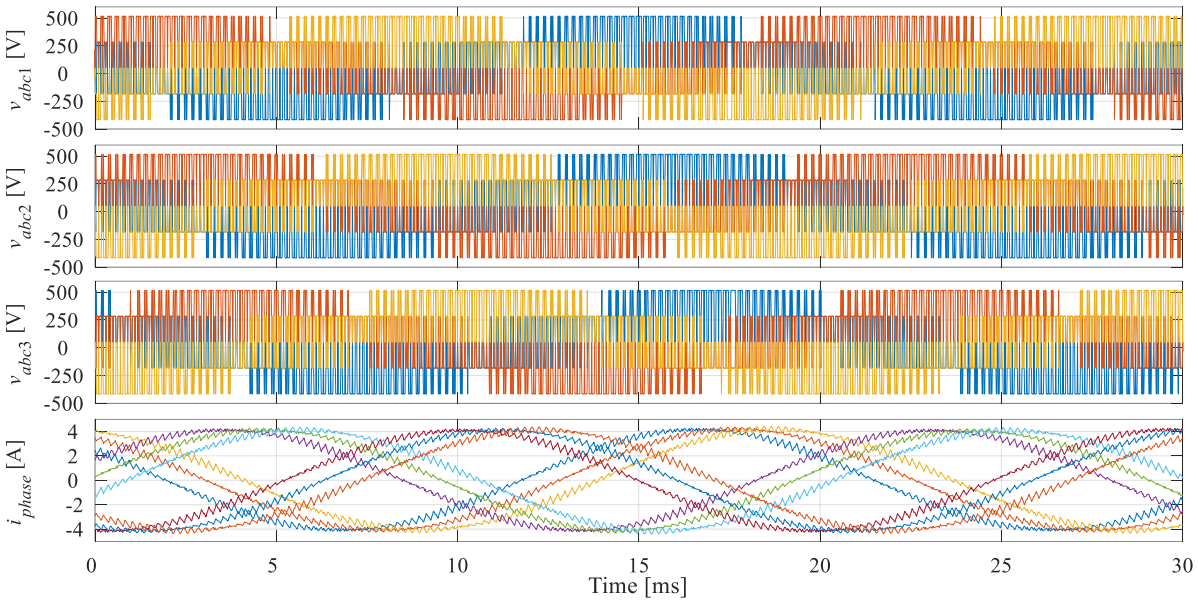

Figure 3.27 – Machine phase currents and voltages.

shown in Fig. 3.26. This test confirms the capability of the system to operate in full speed range with 150 % of the rated torque without saturating PWM modulator. Detailed view of the machine phase currents and voltages during nominal speed of 3000 rpm and torque equal to 16 Nm are shown in figure 3.27. Two-level operation can be seen in phase voltages, while both phase currents and voltages are balanced.

When the grid-side control is considered, there are also limits that must be respected so that the system stays in the linear modulation region. For example, inductance of the grid filter should be large enough to minimise the grid current ripple, but, at the same time, should not be too large so that the system stays in the linear modulation region for the given dc-link voltage. Furthermore, smaller grid

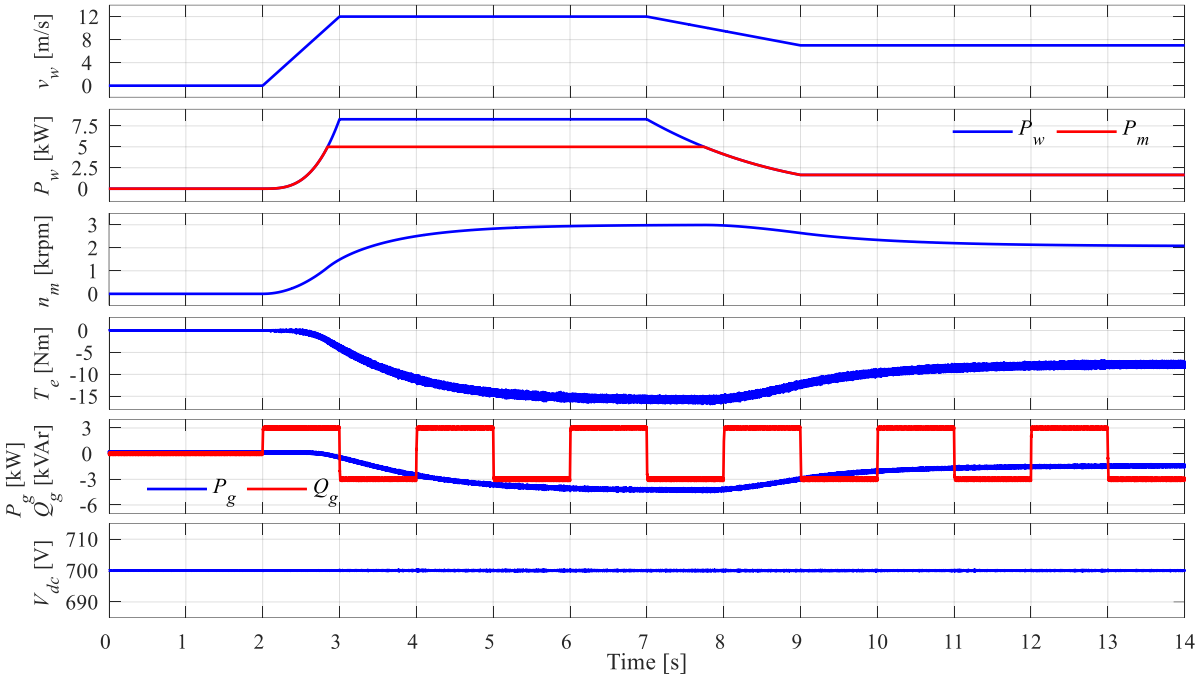

Figure 3.28 – Wind speed, actual and extracted wind power, machine speed and torque, active and reactive grid power and dc-link voltage.

filter value increases dynamic response of the system. Assuming an ideal grid filter, with resistance neglected, the maximum filter inductance is calculated according to the procedure given in [Malinowski (2001)]. When min-max injection is considered, maximum modulation index is 1.15 and expression for maximum value of the inductive grid filter is as follows:

$$L_{g\max} = \frac{\sqrt{\frac{V_{dc}^2}{3} - V_{g\max}^2}}{\omega_g I_{g\max}} \tag{3.39}$$

In the equation above V_{dc} is dc-link voltage, ω_g is grid frequency in rad/s and V_{gmax} and I_{gmax} are maximum values of the grid phase voltage and current. Since $\omega_g = 2\pi 50$ rad/s, $V_{dc} = 700$ V, $V_{gmax} = 325$ V and for the active power of 5 kW maximum grid phase current is $I_{gmax} = 10.5$ A, maximum grid filter inductance is $L_g = 73$ mH. This value is the absolute maximum value. However, maximum value of phase currents is increased during the transients or when the reactive power is supplied to the grid. Furthermore, smaller grid inductance increases dynamic response of the VOC, hence, smaller inductance of 10 mH is selected. Operation of the grid-side VOC has already been demonstrated in Fig. 3.24 where it can be seen that the dc-link voltage is kept stable for all combinations of active and reactive powers.

Simulation of the complete WECS has been carried out and the results are presented in the Fig. 3.28. Inputs to the system are wind speed and references for machine rotor flux, dc-link voltage and reactive power. System has been tested with varying wind speed and reactive power reference stepped from +3 kVAr to -3 kVAr and vice versa every 1 second. It can be seen that MPPT control provides torque reference so that varying wind speed and captured power can be properly followed by the machine speed, i.e. at nominal captured power of 5 kW machine speed is at expected value of 3000 rpm.

Arbitrary change of the reactive power is often required by the grid code. Hence, a step change of reactive power has been simulated and is shown as well. Captured wind power is limited by pitch control, so nominal power will be available even if the wind speed is above nominal value. It should be noted that the slow change of the machine speed is governed by the relatively large inertia of the wind turbine. The last plot shows dc-link voltage, which is kept constant at set value of 700 V by voltage oriented control at all operating conditions.

3.11 Summary

Complete model of a WECS in back-to-back configuration has been developed in this chapter. All major control structures are presented together with multiphase machine specific controls, i.e. *x-y* current control. Furthermore, WECS topologies where multiple 3-phase machine is used as a generator are shown as well. Control structures related to the machine-side control including MPPT control, IRFOC, flux/torque control by PIccd current controllers in synchronous reference frame, *x-y* current control by cvPI and resonant VPI regulators, and 9-phase two-level CBPWM are examined in the chapter. On the grid side, the control subsystem contains a PLL, VOC control realised with cvPI regulator for grid *d-q* current control and single PI regulator for dc-link voltage control and 3-phase three-level CBPWM. Min-max injection is implemented in both grid- and machine-side controllers. Wind turbine and gearbox form the mechanical subsystem. Since the focus of the research is on the multiphase machine, used wind turbine model is as simple as possible.

The presented control techniques are used throughout the thesis and it is therefore convenient to show them all in one place, so that they can be simply referred to later on. Moreover, the discussed control schemes do not constitute any new knowledge or contributions to the field and so placing them in a single chapter aids the narrative of the chapters to follow.

Chapter 4

MULTIPHASE INDUCTION MACHINE MODELLING

4.1 Introduction

The objective of this chapter is to develop generalised mathematical models of an *n*-phase induction machine and implement them in the Simulink environment. Three different modelling approaches will be considered: phase domain, vector space decomposition (VSD) and multi-stator (MS / multiple α-β / multiple *d*-*q*) modelling approaches. A comparison of the models will be carried out with the emphasis on their utilisation in machine control. Moreover, a simple to follow algorithm will be developed for a creation of VSD matrix applicable to any multiphase machine with sinusoidal winding distribution. The proposed algorithm will be used later on to find relation between MS and VSD variables for any multiple 3-phase machine. By doing so, the benefits of both VSD (decoupled control) and MS (information on individual winding set variables) modelling approaches will be used to their full extent. In addition to machine modelling, this chapter will cover harmonic mapping analysis as well. It will be shown that there is an imbalance present in zero-sequence phase voltage harmonics of any asymmetrical machine with single neutral point even in the case of balanced leg voltage harmonics. The work presented in this chapter has been published in [Zoric et al (2016)] and [Zoric et al (2017b)].

Even though the presented transformation (VSD) is applicable to any multiphase machine, only induction machines will be considered in this chapter. In a general case an *n*-phase machine has *l* winding sets and *k* phases per winding set. Number of winding sets *l* can be any integer larger or equal to 1, while *k* is the prime number larger or equal to 3. Consequently, the following expression must hold true:

$$n = kl,\ \ l \geq 1,\ \ k = 3,5,7,11,... \tag{4.1}$$

Depending on the phase propagation angle between winding sets, a machine can be symmetrical ($2\pi / n$) or asymmetrical (π / n). A special case are the machines with a single winding set (l = 1, i.e. 3-, 5-, 7-phase), which are always of a symmetrical configuration. Spatial angular position of the i^{th} phase in the j^{th} winding set for a symmetrical and asymmetrical configuration is as follows:

$$\theta_{j,i} = \begin{Bmatrix} \frac{2\pi}{n}\left(l(i-1)+j-1\right), & \text{symmetrical} \\ \frac{\pi}{n}\left(2l(i-1)+j-1\right), & \text{asymmetrical} \end{Bmatrix}, \begin{matrix} j = 1,2,...,l \\ i = 1,2,...,k \end{matrix} \tag{4.2}$$

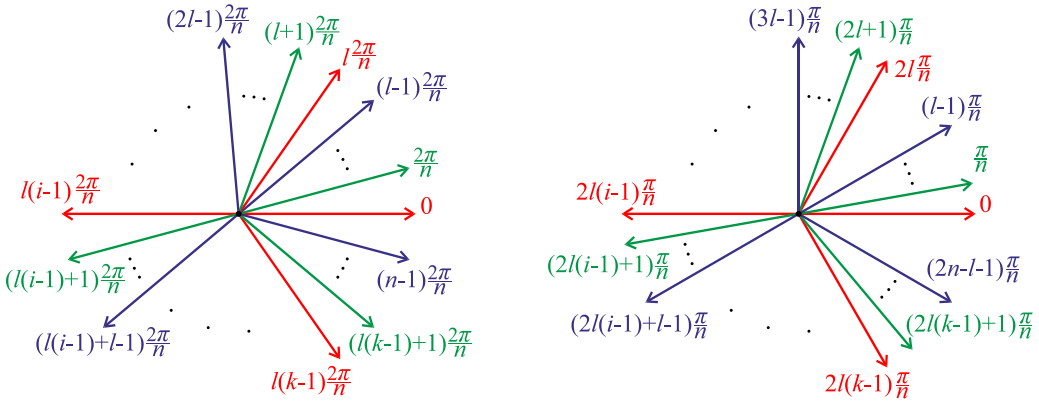

(a) (b)

Figure 4.1 – Phase propagation angles of symmetrical (a) and asymmetrical (b) multiphase machines.

A schematic of the machine phase angular positions is depicted in the Fig. 4.1a for a symmetrical case and in Fig. 1b for an asymmetrical machine configuration. Of course, the following standard assumptions in machine modelling are taken into account:

- The magneto-motive force is sinusoidally distributed along the air gap circumference.
- Magnetic core is linear and so the main flux saturation can be neglected.
- Magnetic core losses are neglected.
- Machine is balanced with uniform air gap.
- The resistances are constant.

4.2 Machine Model in Phase Variables

Considering all previously mentioned assumptions, with the addition that the squirrel cage rotor can be represented with the same configuration as stator but with shorted phase windings, electrical part of a *n*-phase machine can be modelled using 2*n* differential equations [Dordevic et al (2010)]. However, in this case, a simplification is introduced in order to reduce the number of equations resulting in faster simulations. Namely, instead of *n* equation for rotor, only two are going to be used, reducing the number of equations from 2*n* to *n* + 2. Therefore, machine stator is going to be modelled in its natural *n*-dimensional space, while rotor is going to be modelled in 2-dimensional space, i.e. rotor α-β variables. Of course, rotor parameters should be changed accordingly by multiplication with coefficient 2/*n*, so there is no change in behaviour of the machine. It should be noted that this change is justified, since in the squirrel cage rotor induction machines there are no means to measure rotor current. Hence, the form of the rotor model is unimportant as long as there is impact on the stator currents or torque production.

Machine equations are customarily divided into three matrix equations: voltage, flux linkage and torque equation. Voltage equation is given in a convenient matrix form as:

$$\begin{bmatrix} [v] \\ [v_r] \end{bmatrix} = [R] \begin{bmatrix} [i] \\ [i_r] \end{bmatrix} + \frac{d}{dt} \begin{bmatrix} [\psi] \\ [\psi_r] \end{bmatrix} \tag{4.3}$$

Variables [v], [v_r], [i], [i_r], [ψ], and [ψ_r] are vectors of machine stator and rotor voltages, currents and fluxes respectively. Symbols with the index r represent rotor values, while matrix [R] is a machine resistance matrix. These variables are defined as follows:

$$[v]=\begin{bmatrix} v_1 \\ v_2 \\ \vdots \\ v_n \end{bmatrix},\quad [v_r]=\begin{bmatrix} 0 \\ 0 \end{bmatrix},\quad [i]=\begin{bmatrix} i_1 \\ i_2 \\ \vdots \\ i_n \end{bmatrix},\quad [i_r]=\begin{bmatrix} i_{\alpha r} \\ i_{\beta r} \end{bmatrix},\quad [\psi]=\begin{bmatrix} \psi_1 \\ \psi_2 \\ \vdots \\ \psi_n \end{bmatrix},\quad [\psi_r]=\begin{bmatrix} \psi_{\alpha r} \\ \psi_{\beta r} \end{bmatrix}$$
$$[R]=\begin{bmatrix} R_s[I_n] & [0] \\ [0] & \frac{2}{n}R_r[I_2] \end{bmatrix} \tag{4.4}$$

Numbers (1 - n) represent stator phase numbers, while two rotor phases are denoted by αr and βr. R_s is the stator phase winding resistance and R_r is the rotor phase winding resistance. [I_n] is n x n unit matrix, while [I_2] is 2 x 2 unit matrix. Current-flux linkage equation is given as:

$$\begin{bmatrix} [\psi] \\ [\psi_r] \end{bmatrix}_{(n+2)\times 1} = [L]_{(n+2)\times(n+2)} \begin{bmatrix} [i] \\ [i_r] \end{bmatrix}_{(n+2)\times 1} \tag{4.5}$$

[L] is an inductance matrix, and it consists of stator [L_{ss}] and rotor [L_{rr}] self-inductance matrices, and stator-to-rotor [L_{sr}] and rotor-to-stator [L_{rs}] mutual inductance matrices:

$$[L]=\begin{bmatrix} [L_{ss}] & [L_{sr}] \\ [L_{rs}] & [L_{rr}] \end{bmatrix} \tag{4.6}$$

Since inductances [L_{ss}], [L_{rr}] are dependent on phase propagation angles and [L_{sr}], [L_{rs}] on rotor position as well, it is necessary to define these angles first. Considering the Fig. 4.1, phase propagation angles are denoted by numbers from 1 to n, where 1st phase is the one with propagation angle equal to 0, and positive direction is anti-clockwise. Phase propagation angles are:

$$[\theta]=[\theta_1 \quad \theta_2 \quad \dots \quad \theta_n] \tag{4.7}$$

If L_{ls}, L_{lr}, and M are stator/rotor leakage inductance and mutual inductance respectively, machine inductance matrices can be defined as follow:

$$\begin{aligned} [L_{ss}]_{n\times n} &= [L_{jk}] + L_{ls}[I_n],\ L_{jk} = M\cos(\theta_k - \theta_j),\ j,k \in [1,2,\dots n] \\ [L_{rr}]_{2\times 2} &= \begin{bmatrix} M+\frac{2}{n}L_{lr} & 0 \\ 0 & M+\frac{2}{n}L_{lr} \end{bmatrix} \\ [L_{sr}]_{n\times 2} &= [L_{jk}],\ L_{jk} = M\cos((\theta_k+\theta_e)-\theta_j),\ j \in [1,2,\dots n],\ \theta_k \in [0 \quad \tfrac{\pi}{2}] \\ [L_{rs}]_{2\times n} &= [L_{jk}],\ L_{jk} = M\cos(\theta_k-(\theta_j+\theta_e)),\ k \in [1,2,\dots n],\ \theta_j \in [0 \quad \tfrac{\pi}{2}] \end{aligned} \tag{4.8}$$

Angle θ_e represents rotor electrical angular position and it is equal to $P\theta_m$, where P and θ_m are number of pole pairs and rotor mechanical position. Finally, equation for electromechanical torque completes the model, and if expressed in phase variables, is as follows:

$$T_e = P[i]^T \frac{d}{d\theta}[L_{sr}][i_r] \tag{4.9}$$

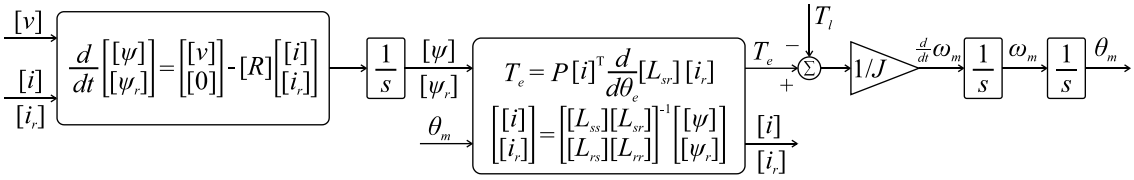

Figure 4.2 – Diagram of the machine model in phase variables.

Equations (4.2) – (4.9) define the machine model. However, equation for equilibrium of rotating masses is needed as well to incorporate the machine load and rotor moment of inertia. If T_l is the machine load torque and J rotor inertia, assuming motoring convention, equation for equilibrium of rotating masses is as follow:

$$\frac{d\omega_m}{dt} = \frac{1}{J}\left(T_e - T_l\right) \tag{4.10}$$

Machine model is now complete and it is applicable to any multiphase induction machine. The form of equations enables very easy implementation in Simulink environment by use of function blocks and integrators. Diagram of the implemented model in phase variables is given in the Fig. 4.2, while the code with more detailed description of the actual implementation can be found in the Appendix A of the thesis.

It should be pointed out that this machine model has already been used in section 3.10 and will be used in all simulations that follow, regardless of the machine configuration (symmetrical/asymmetrical with single or multiple neutral points) and number of phases.

4.3 Machine Model Using Multi-Stator Modelling Approach

When a multiphase machine has multiple winding sets, it is advantageous to have independent control over each individual winding set. For example, in generation systems this can be used to switch off any winding set in the case of fault. Another use would be to arbitrarily distribute power over each of the winding sets. With VSD modelling approach this is impossible to do directly because information on phase variables is lost. Therefore, stator winding sets are modelled independently [Nelson and Krause (1974)]. The most frequently used machines with multiple winding sets are the 6-, 9- and 12-phase machines, i.e. multiple 3-phase ones. A noticeable increase in research undertaken for this particular type of multiphase machine has been reported recently [Barrero and Duran (2016), Duran and Barrero (2016), Levi (2016)], hence they will be the only ones considered in this section.

Multiple 3-phase machines can be modelled by applying the well-known 3-phase Clarke's transformation to each 3-phase winding set [Nelson and Krause (1974), Singh et al (2005b)], followed by the standard 3-phase rotational transformation. By doing so, the machine is divided into multiple flux/torque producing subspaces and well-known control techniques developed for 3-phase machines can be implemented in each subspace [Jung et al (2009)]. The advantage of this modelling approach is the possibility for individual and independent control of all winding sets; hence, power/current sharing between winding sets is easily achieved. On the other hand, this multiple *d-q* modelling approach leads

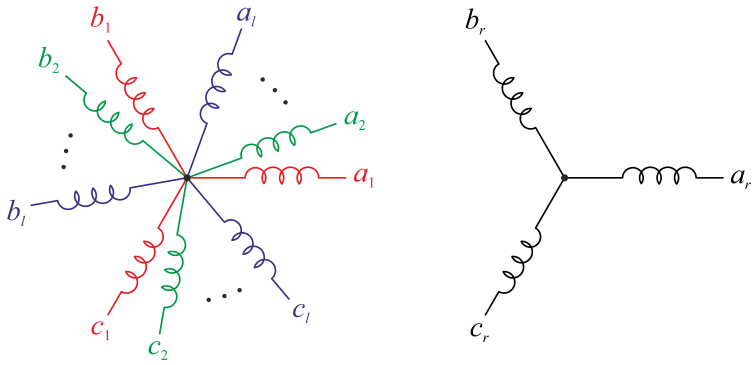

(a) (b)

Figure 4.3 – Schematic of stator (a) and rotor (b) of the multiple 3-phase machine when MS modelling approach is applied.

to heavy cross-coupling between equations of the different 3-phase winding sets [De Camillis et al (2001)]. Furthermore, it does not offer clear insight into machine operation and harmonic mapping. In addition, multiple pairs of PI controllers are required for simple flux/torque control.

In order to implement MS modelling it is firstly necessary to represent *n*-phase machine stator ($n = l \cdot k$, $k = 3$) with l 3-phase winding sets and rotor with a single 3-phase winding set, as shown for a 9-phase case in [Jung et al (2009)]. Application of standard 3-phase decoupling to each of the winding sets and rotational transformation to rotor should follow, resulting in machine model in stationary reference frame. For the sake of clarity, a schematic representation of a multiple 3-phase machine for a general case is shown in the Fig. 4.3.

Machine is now divided in l+1 3-phase winding sets, l stator and single rotor set. If winding set number is denoted by index j ($j = 1, 2 \ldots l$) and rotor by letter r, new machine equations can be written in form of voltage and flux linkage equations as follows:

$$\begin{aligned} [v_j] &= R_s [i_j] + \frac{d}{dt}[\psi_j], \quad j = 1,2,...l \\ [0] &= \tfrac{1}{l} R_r [i_r] + \frac{d}{dt}[\psi_r] \end{aligned} \tag{4.11}$$

$$\begin{aligned} [\psi_j] &= L_{ls}[i_j] + \sum_{k=1}^{l} [L_{jk}][i_k] + [L_{jr}][i_r], \quad j = 1,2,...l \\ [\psi_r] &= \tfrac{1}{l} L_{lr}[i_r] + \sum_{k=1}^{l} [L_{rk}][i_k] + [L_{rr}][i_r] \end{aligned} \tag{4.12}$$

Voltage, current and flux matrices are defined as follows:

$$[v_x] = \begin{bmatrix} v_{ax} \\ v_{bx} \\ v_{cx} \end{bmatrix}, \quad [i_x] = \begin{bmatrix} i_{ax} \\ i_{bx} \\ i_{cx} \end{bmatrix}, \quad [\psi_x] = \begin{bmatrix} \psi_{ax} \\ \psi_{bx} \\ \psi_{cx} \end{bmatrix}, \quad x \in [1,2,...,l,r] \tag{4.13}$$

R_s and R_r are stator and rotor phase resistances, while L_{ls} and L_{lr} represent stator and rotor leakage inductances. It should be noted that rotor variables are scaled by $1/l$ since rotor is represented with one 3-phase winding set instead of l, which is the case with stator. Rotor is squirrel cage type, hence rotor

voltages in eq. (4.11) – (4.13) are equal to zero. Inductances [L_{jk}], [L_{jr}], [L_{rk}], and [L_{rr}] are defined as follows:

$$[L_{jk}] = M\begin{bmatrix} \cos(\theta_{ak}-\theta_{aj}) & \cos(\theta_{bk}-\theta_{aj}) & \cos(\theta_{ck}-\theta_{aj}) \\ \cos(\theta_{ak}-\theta_{bj}) & \cos(\theta_{bk}-\theta_{bj}) & \cos(\theta_{ck}-\theta_{bj}) \\ \cos(\theta_{ak}-\theta_{cj}) & \cos(\theta_{bk}-\theta_{cj}) & \cos(\theta_{ck}-\theta_{cj}) \end{bmatrix} \tag{4.14}$$

$$[L_{jr}] = M\begin{bmatrix} \cos(\theta_{e}-\theta_{aj}) & \cos(\theta_{e}+\frac{2\pi}{3}-\theta_{aj}) & \cos(\theta_{e}+\frac{4\pi}{3}-\theta_{aj}) \\ \cos(\theta_{e}-\theta_{bj}) & \cos(\theta_{e}+\frac{2\pi}{3}-\theta_{bj}) & \cos(\theta_{e}+\frac{4\pi}{3}-\theta_{bj}) \\ \cos(\theta_{e}-\theta_{cj}) & \cos(\theta_{e}+\frac{2\pi}{3}-\theta_{cj}) & \cos(\theta_{e}+\frac{4\pi}{3}-\theta_{cj}) \end{bmatrix} \tag{4.15}$$

$$[L_{rk}] = M\begin{bmatrix} \cos(\theta_{ak}-\theta_{e}) & \cos(\theta_{bk}-\theta_{e}) & \cos(\theta_{ck}-\theta_{e}) \\ \cos(\theta_{ak}-(\theta_{e}+\frac{2\pi}{3})) & \cos(\theta_{bk}-(\theta_{e}+\frac{2\pi}{3})) & \cos(\theta_{ck}-(\theta_{e}+\frac{2\pi}{3})) \\ \cos(\theta_{ak}-(\theta_{e}+\frac{4\pi}{3})) & \cos(\theta_{bk}-(\theta_{e}+\frac{4\pi}{3})) & \cos(\theta_{ck}-(\theta_{e}+\frac{4\pi}{3})) \end{bmatrix} \tag{4.16}$$

$$[L_{rr}] = M\begin{bmatrix} \cos(0) & \cos(\frac{2\pi}{3}) & \cos(\frac{4\pi}{3}) \\ \cos(\frac{2\pi}{3}) & \cos(0) & \cos(\frac{2\pi}{3}) \\ \cos(\frac{4\pi}{3}) & \cos(\frac{2\pi}{3}) & \cos(0) \end{bmatrix} \tag{4.17}$$

Indices *j*, *k* and *abc* represent winding set and phase within that set, respectively, as per Fig. 4.3. Actual phase shift angle θ is defined by equation (4.2) depending on type of the machine (symmetrical or asymmetrical) and the number of phases. Rotor electrical position is denoted by θ_e.

Until now machine model was given in phase variables. However, it is written in a suitable form so multiple 3-phase Clarke's transformations can be easily applied. Clarke's transformation for 3-phase case is as follows:

$$[C_3(\alpha)] = \frac{2}{3}\begin{bmatrix} \cos(\alpha) & \cos\left(\alpha+\frac{2\pi}{3}\right) & \cos\left(\alpha+\frac{4\pi}{3}\right) \\ \sin(\alpha) & \sin\left(\alpha+\frac{2\pi}{3}\right) & \sin\left(\alpha+\frac{4\pi}{3}\right) \\ \frac{1}{2} & \frac{1}{2} & \frac{1}{2} \end{bmatrix} \tag{4.18}$$

Angle α in this equation represents spatial phase shift of the first phase in the winding set, e.g. for an asymmetrical 9-phase $\alpha \in [0, \pi/9, 2\pi/9]$. In the case of the rotor winding set α is set to θ_e, so rotor variables are transformed to stator reference frame. By doing so, rotational transformation has been implicitly applied to rotor variables resulting in the model in the stator reference frame. Transformations are applied to the equation (4.11) – (4.12) in the following manner:

$$\begin{aligned} [v_{\alpha\beta zj}] &= [C_3(\theta_{aj})]\left(R_s\,[C_3(\theta_{aj})]^{-1}[i_{\alpha\beta zj}] + \frac{d}{dt}\left([C_3(\theta_{aj})]^{-1}[\psi_{\alpha\beta zj}]\right)\right), \quad j = 1,2,\ldots l \\ [0] &= [C_3(\theta_e)]\left(\tfrac{1}{l}R_r\,[C_3(\theta_e)]^{-1}[i_{\alpha\beta zr}] + \frac{d}{dt}\left([C_3(\theta_e)]^{-1}[\psi_{\alpha\beta zr}]\right)\right) \end{aligned} \tag{4.19}$$

$$\begin{aligned}
[\psi_{\alpha\beta z j}] &= [C_3(\theta_{aj})]\left(L_{ls}[C_3(\theta_{aj})]^{-1}[i_{\alpha\beta z j}] + \sum_{k=1}^{l}[L_{jk}][C_3(\theta_{ak})]^{-1}[i_{\alpha\beta z k}] + [L_{jr}][C_3(\theta_e)]^{-1}[i_{\alpha\beta z r}] \right), \quad j = 1,2,\ldots l \\
[\psi_{\alpha\beta z r}] &= [C_3(\theta_e)]\left(\tfrac{1}{l} L_{lr}[C_3(\theta_e)]^{-1}[i_{\alpha\beta z r}] + \sum_{k=1}^{l}[L_{rk}][C_3(\theta_{ak})]^{-1}[i_{\alpha\beta z k}] + [L_{rr}][C_3(\theta_e)]^{-1}[i_{\alpha\beta z r}] \right)
\end{aligned} \tag{4.20}$$

Due to the change in rotor model and applied amplitude invariant transformations, new rotor parameters and mutual inductance are introduced:

$$R_r^{ms} = \tfrac{1}{l} R_r, \quad L_{lr}^{ms} = \tfrac{1}{l} L_{lr}, \quad M^{ms} = \tfrac{3}{2} M \tag{4.21}$$

Finally, there are l+1 sets of machine equations in stationary α-β-z variables, i.e. l for stator winding sets and single one for the rotor. Complete derivations are done in Wolfram Mathematica, a computer algebra system, while the code is available in the Appendix A of the thesis. Machine voltage equations and flux linkages in MS domain are as follows:

$$\begin{aligned}
[v_{\alpha\beta z j}] &= R_s[i_{\alpha\beta z j}] + \frac{d}{dt}[\psi_{\alpha\beta z j}], \quad j = 1,2,\ldots l \\
[0] &= R_r^{ms}[i_{\alpha\beta z r}] + \frac{d}{dt}[\psi_{\alpha\beta z r}] + \omega_e[I_{-1}][\psi_{\alpha\beta z r}]
\end{aligned} \tag{4.22}$$

$$\begin{aligned}
[\psi_{\alpha\beta z j}] &= L_{ls}[i_{\alpha\beta z j}] + M^{ms}[I_1]\left(\sum_{k=1}^{l}[i_{\alpha\beta z k}] + [i_{\alpha\beta z r}] \right), \quad j = 1,2,\ldots l \\
[\psi_{\alpha\beta z r}] &= L_{lr}^{ms}[i_{\alpha\beta z r}] + M^{ms}[I_1]\left(\sum_{k=1}^{l}[i_{\alpha\beta z k}] + [i_{\alpha\beta z r}] \right)
\end{aligned} \tag{4.23}$$

$$\begin{aligned}
[I_1] &= \begin{bmatrix} 1 & 0 & 0 \\ 0 & 1 & 0 \\ 0 & 0 & 0 \end{bmatrix}, \quad [I_{-1}] = \begin{bmatrix} 0 & 1 & 0 \\ -1 & 0 & 0 \\ 0 & 0 & 0 \end{bmatrix}, \quad [i_{\alpha\beta z r}] = \begin{bmatrix} i_{\alpha r} \\ i_{\beta r} \\ i_{z r} \end{bmatrix}, \quad [\psi_{\alpha\beta z r}] = \begin{bmatrix} \psi_{\alpha r} \\ \psi_{\beta r} \\ \psi_{z r} \end{bmatrix} \\
[v_{\alpha\beta z j}] &= \begin{bmatrix} v_{\alpha j} \\ v_{\beta j} \\ v_{z j} \end{bmatrix}, \quad [i_{\alpha\beta z j}] = \begin{bmatrix} i_{\alpha j} \\ i_{\beta j} \\ i_{z j} \end{bmatrix}, \quad [\psi_{\alpha\beta z j}] = \begin{bmatrix} \psi_{\alpha j} \\ \psi_{\beta j} \\ \psi_{z j} \end{bmatrix}, \quad j = 1,2,\ldots l
\end{aligned} \tag{4.24}$$

Since mutual inductance between stator and rotor M^{ms} in (4.23) only exists in α-β plane, as per matrices $[I_1]$ and $[I_{-1}]$ defined in (4.24), electromechanical energy conversion is happening only in the α-β plane. On the other hand, zero sequence equations contain resistances and leakage inductances only and do not contribute to the electromechanical energy conversion. Hence, flux/torque producing part of the machine equations (α-β) can be represented in complex form by means of space vectors, as follows:

$$\begin{aligned}
\underline{v}_{\alpha\beta j} &= R_s \underline{i}_{\alpha\beta j} + \frac{d}{dt}\underline{\psi}_{\alpha\beta j}, \quad j = 1,2,\ldots l \\
0 &= R_r^{ms} \underline{i}_{\alpha\beta r} + \frac{d}{dt}\underline{\psi}_{\alpha\beta r} - j\omega_e \underline{\psi}_{\alpha\beta r}
\end{aligned} \tag{4.25}$$

$$\begin{aligned}
\underline{\psi}_{\alpha\beta j} &= L_{ls}\underline{i}_{\alpha\beta j} + M^{ms}\left(\sum_{k=1}^{l}\underline{i}_{\alpha\beta k} + \underline{i}_{\alpha\beta r} \right), \quad j = 1,2,\ldots l \\
\underline{\psi}_{\alpha\beta r} &= L_{lr}^{ms}\underline{i}_{\alpha\beta r} + M^{ms}\left(\sum_{k=1}^{l}\underline{i}_{\alpha\beta k} + \underline{i}_{\alpha\beta r} \right)
\end{aligned} \tag{4.26}$$

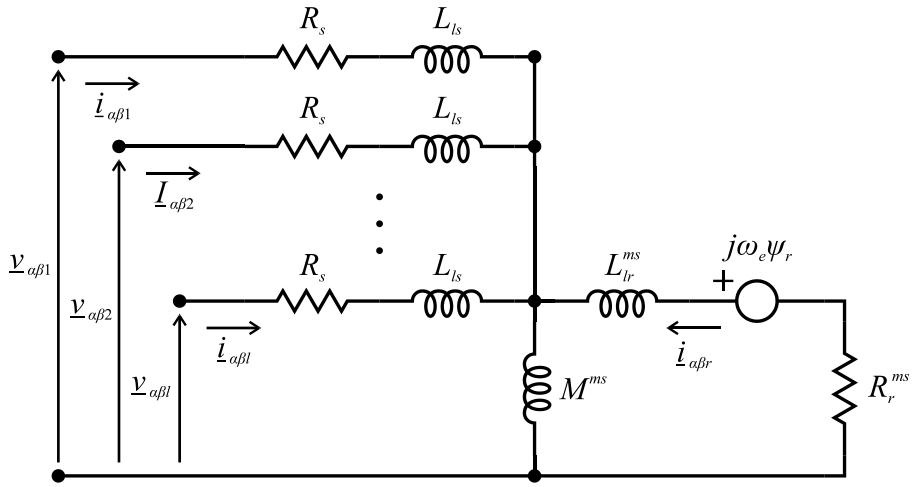

Figure 4.4 – Equivalent circuit of the *n*-phase machine modelled by MS modelling approach.

To complete the model, it is required to provide torque equation. It is the simple sum of contributions of each winding set, given as follows:

$$T_e = \frac{3}{2} P \sum_{k=1}^{l} \left(\psi_{\alpha j} i_{\beta j} - \psi_{\beta j} i_{\alpha j} \right) \tag{4.27}$$

It is now possible to create equivalent circuit for the α-β subspace, as shown in the Fig. 4.4. In accordance with the equations, flux/torque producing subspace has stator circuit with *l* terminals, i.e. each stator winding set is defined with its α-β current, while rotor is defined with single rotor α-β current. From the control point of view, it is now possible to control currents and thus the flux/torque production of each winding set. However, there is significant cross-coupling between winding sets complicating the control implementation.

4.4 Machine Model Using VSD Modelling Approach

Different to the modelling of a multiphase machine with multiple 3-phase winding sets by use of multiple 3-phase Clarke's transformation, VSD considers application of actual *n*-phase transformation, so all of the multiphase machine could be modelled and not only the multiple 3-phase ones. The VSD modelling approach is based on symmetrical components theory [Fortescue (1918)]. The machine phase variables are multiplied by VSD matrix resulting in multiple decoupled 2-dimensional subspaces and zero-sequence component(s) [Levi et al (2007)]. The first subspace is a flux/torque producing one, meaning that all electromechanical energy conversion is happening here, assuming the sinusoidal winding distribution. Having the decoupled machine, it is very convenient to implement any vector control strategy [Levi et al (2008)]. Moreover, other subspace variables can be used as additional degrees of freedom for some multiphase machine specific purpose, i.e. fault tolerance [Guzman et al (2012), Che et al (2014a)], dc-link voltage balancing [Che et al (2014b)] or harmonic elimination [Yepes et al (2013)].

The term Vector Space Decomposition was introduced in [Zhao and Lipo (1995)], where an asymmetrical 6-phase machine has been mapped into orthogonal subspaces by applying a real 6-phase

Clarke's transformation. It is shown that components at fundamental frequency and k^{th} order harmonics ($k = 12m\pm1$, $m = 1, 2, 3, \ldots$) map into the first subspace where electro-mechanical energy conversion takes place. Other odd-order harmonics map into the remaining two orthogonal subspaces. The resulting machine model has been used to develop a space vector pulse width modulation strategy. Since [Zhao and Lipo (1995)] introduces the concept of VSD by use of transformation matrix with real coefficients, i.e. multiphase Clarke's transformation, and actual transformation is a complex one, i.e. it creates multiple complex planes, in this thesis both representations are used, as deemed appropriate.

This section is divided into two subsections: the first one covers creation of actual VSD matrix and proposes unified algorithm applicable to any machine configuration, while the second subsection provides the model of an induction machine in VSD variables.

4.4.1 Generalised Algorithm for Creation of VSD Matrix

Creation of VSD transformation for any phase number for symmetrical winding configurations is well known and easily achievable by the use of symmetrical components theory or multiphase Clarke's transformation [Levi et al (2007)]. On the other hand, when machines with an asymmetrical winding configuration are concerned, there are various solutions dealing with creation of a proper decoupling transformation matrix [Abbas et al (1984), Tessarolo (2009a), Rockhill and Lipo (2015)].

To create a decoupling transformation of an asymmetrical n-phase machine, the decoupling transformation of a symmetrical $2n$-phase machine has been used in [Abbas et al (1984)] as the starting point. It is shown that an appropriate transformation matrix may be obtained by representing phases on the same magnetic axis of a symmetrical 12-phase machine with the equivalent pairs of phases of an asymmetrical 6-phase machine. As a result, half of the elements in the newly created matrix have zero value and can be omitted. What is left is a real decoupling transformation matrix of an asymmetrical 6-phase machine. Since the proposed technique is based on the actual machine construction, it can be applied to any asymmetrical n-phase machine, by using a $2n$-phase machine as the starting point.

Another method of producing a decoupling transformation matrix for an asymmetrical machine is presented in [Tessarolo (2009a)]. Here, a stator inductance matrix $[L_s]$ of an asymmetrical machine has been analysed and development of the VSD matrix is based on finding the solution, which will diagonalise the $[L_s]$ matrix. The obtained matrix is real and it can be considered as a multiphase Clarke's transformation, which is equivalent to the complex VSD transformation.

Work presented in [Rockhill and Lipo (2015)] introduces the concept of a fundamental winding configuration which represents the multiphase machine (or a network) based on a single-pole symmetry, rather than two-pole symmetry used in symmetrical components theory. The resulting fundamental vector diagram maps all the phases within the range 0 to π. This has enabled development of generalised n-phase symmetrical component and Clarke's transformations, which are valid for asymmetrical cases as well.

Most of these methods are developed either for symmetrical or asymmetrical configuration. Moreover, all of them yield the same or very similar VSD or Clarke's transformation matrix for a given machine type. Namely, produced matrix decouples the machine into multiple mutually orthogonal subspaces, with an additional feature that odd-order harmonics are mapped uniquely into specific subspaces. Therefore, the goal of this subsection is not to develop a novel way of deriving the VSD matrix, but to present an easy to follow algorithm, which summarises the aforementioned, is applicable to any multiphase machine (symmetrical or asymmetrical), and enables a rather simple creation of the required decoupling transformation matrix in real or complex form.

In order to develop a unified algorithm, the form of the VSD matrix needs to be defined first. Each row in the VSD matrix forms a single two-dimensional subspace and is created as a complex representation of vectors with amplitude equal to one and angle set by a multiple of phase propagation angle vector $[\theta]$, defined in (4.2), and the subspace constant C. For the sake of clarity, each complex row can be represented by two rows with real values as well. This leads to a generalised multiphase Clarke's transformation matrix. Each row of the VSD and generalised Clarke's transformation is defined as follows:

$$e^{jC[\theta]} = \begin{bmatrix} \mathrm{Re}\left(e^{jC[\theta]}\right) \\ \mathrm{Im}\left(e^{jC[\theta]}\right) \end{bmatrix} = \begin{bmatrix} \cos\left(C[\theta]\right) \\ \sin\left(C[\theta]\right) \end{bmatrix} \tag{4.28}$$

It should be noted that in the case of homopolar zero-sequence components, imaginary part is equal to zero, hence both VSD and generalised Clarke's transformation contain real values which are identical. Subspace harmonic mapping is determined by subspace constant C. If i is a positive integer (i = 1, 2, 3, …), C can be defined as follows:

1. $C \neq i \cdot k$ – non zero-sequence harmonics are mapped into these subspaces [T_{nZS}] (e.g. k = 3, C = 1, 2, 4, 5, …).
2. $C = i \cdot k$ – zero-sequence harmonics are mapped into these subspaces [T_{ZS}] (e.g. k = 3, C = 3, 6, 9, …).
3. $C = n/2$ or $C = n$ – a set of real values is produced, imaginary part is zero, so instead of a subspace, a homopolar zero-sequence component is obtained [ZS] (e.g. n = 9, C = 9).

Rows are arranged in such a way that the first subspaces are non zero-sequence subspaces, followed by zero-sequence subspaces and at the end zero-sequence homopolar components. For the single neutral point case VSD matrix is:

$$[T_{VSD}] = \sigma \begin{bmatrix} [T_{nZS}] \\ [T_{ZS}] \\ [ZS] \end{bmatrix} \tag{4.29}$$

With the VSD matrix rows arranged as in (4.29), definition of the subspace constants should follow. For the symmetrical case, the subspace constants are well known [Levi et al (2007)] and they take values

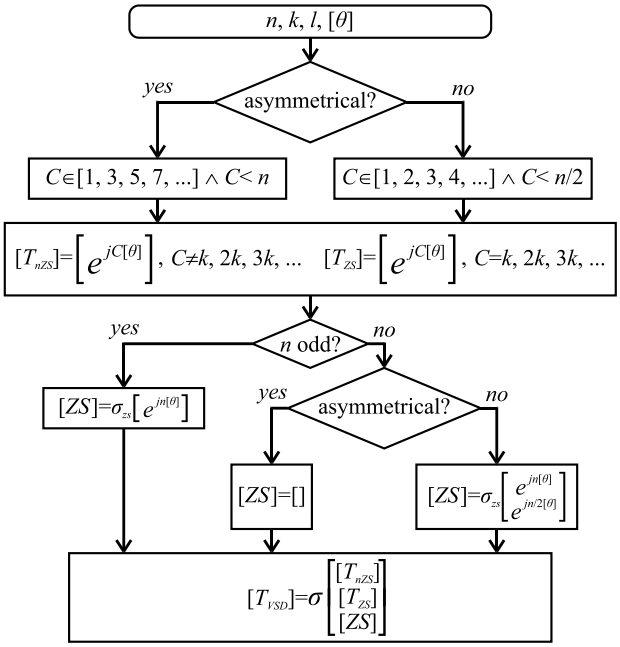

Figure 4.5 – VSD creation algorithm for multiphase machines with single neutral point.

from [1, 2, … (*n*-2)/2] when *n* is even, or in the case of odd *n*, [1, 2, …, (*n*-1)/2]. On the other hand, in the case of an asymmetrical machine, all subspace multiplication coefficients *C* are positive odd numbers smaller than *n* (i.e. $n = 9$, $k = 3$, $C \in [1, 3, 5, 7]$). This assures that all odd-order harmonics are uniquely mapped in *x-y* planes. Finally, the algorithm for obtaining VSD transformation for any multiphase machine with single neutral point is given in Fig. 4.5.

Constants σ and σ_{zs}, introduced in Fig. 4.5, define whether the produced VSD matrix is power or amplitude invariant. Their values are as follows:

$$\begin{aligned} &\text{amplitude inv. } \sigma = \frac{2}{n}, \sigma_{zs} = \frac{1}{2} \\ &\text{power inv. } \sigma = \sqrt{\frac{2}{n}}, \sigma_{zs} = \frac{1}{\sqrt{2}} \end{aligned} \tag{4.30}$$

It can be seen that in the case of an asymmetrical machine with even number of phases (i.e. 6, 10, 12, 14, …) there are no homopolar zero-sequence components. Instead, an additional zero-sequence subspace exists. This naming convention is different from many published works, where this last subspace ($C = n-k$) is considered as two zero-sequence components ($z+$, $z-$). The reason for treating it as an additional subspace lays in the fact that this last row is obtained as $[e^{j(n-k)[\theta]}]$, hence an additional subspace.

Until now, only machines with a single neutral point have been considered. However, if the machine is with multiple neutral points, thanks to the suitable arrangement of the matrix rows, an easy modification provides the appropriate VSD matrix. In this case, zero-sequence subspaces and homopolar components should be replaced by zero sequences of each winding set (z_1, z_2, …). Individual zero-sequence components are created as follows:

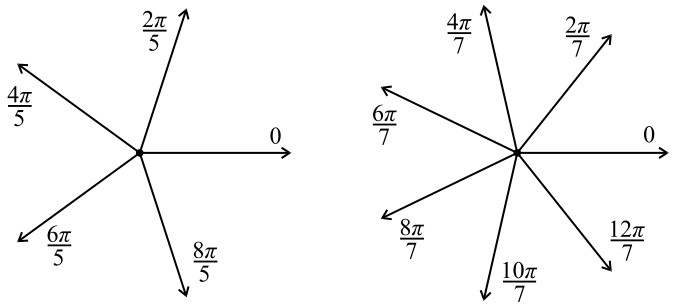

(a) 5-phase machine (b) 7-phase machine

Figure 4.6 – Phase propagation angles of the machines with 5 (a) and 7 (b) phases.

$$[ZS]=\begin{bmatrix} \sigma_{ws} & 0 & 0 & \cdots & 0 & \cdots & \sigma_{ws} & 0 & 0 & \cdots & 0 \\ 0 & \sigma_{ws} & 0 & \cdots & 0 & \cdots & 0 & \sigma_{ws} & 0 & \cdots & 0 \\ & & & & & \vdots & & & & & \\ 0 & 0 & 0 & \cdots & \sigma_{ws} & \cdots & 0 & 0 & 0 & \cdots & \sigma_{ws} \end{bmatrix} \tag{4.31}$$

Constant σ_{ws} takes value of $1/k$ if an amplitude invariant transformation is desired, and square root of $1/k$ in the case of the power invariant transformation. This modification completes the algorithm, so that it is applicable to any multiphase machine with standard windings configuration (winding set propagation angle equal to π/n or $2\pi/n$).

In order to verify the proposed algorithm, created VSD matrices are compared with ones available in the literature. Only configurations with a single neutral point are considered. The reason for this is the simplicity of zero sequences in multiple neutral point case, so additional discussion is not considered necessary. Depending on the machine configuration (symmetrical or asymmetrical), phase propagation angles $[\theta]$ take values as shown in (4.2). Furthermore, angles within the $[\theta]$ are arranged in increasing order. The first phase has propagation angle of 0° and the positive direction is counter-clockwise.

In the general case, the multiphase machine with the least number of phases is the 3-phase machine. The proposed algorithm is applicable in this case as well, resulting in standard 3-phase Clarke's transformation. When actual multiphase machines with single winding set are considered (l = 1), the frequently researched ones are (k = 5) 5- and (k = 7) 7-phase machines [Guzman et al (2012), Dordevic et al (2013b)], depicted in Fig. 4.6. In these cases, both are considered to be of a symmetrical configuration.

In the case of the 5-phase machine subspace constant is C ∈ [1, 2], whereas 7-phase case produces constant C ∈ [1, 2, 3]. If phase propagation angles are $[\theta_5]$ and $[\theta_7]$, proposed algorithm yields amplitude invariant VSD matrices as follows:

$$[T_5]=\frac{2}{5}\begin{bmatrix} e^{j[\theta_5]} \\ e^{j2[\theta_5]} \\ \frac{1}{2}e^{j5[\theta_5]} \end{bmatrix}\begin{matrix}\alpha,\beta \\ x_1,y_1, \\ z_+\end{matrix} \qquad [T_7]=\frac{2}{7}\begin{bmatrix} e^{j[\theta_7]} \\ e^{j2[\theta_7]} \\ e^{j3[\theta_7]} \\ \frac{1}{2}e^{j7[\theta_7]} \end{bmatrix}\begin{matrix}\alpha,\beta \\ x_1,y_1 \\ x_2,y_2 \\ z_+\end{matrix} \tag{4.32}$$

Presented matrices are amplitude invariant, whereas power invariant transformations are obtained by simple coefficient change (4.30). Nevertheless, VSD matrices in (4.32) are identical to the ones used

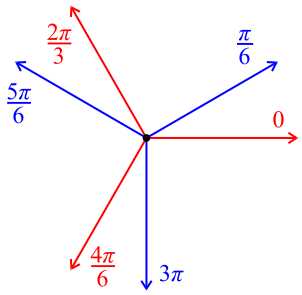

Figure 4.7 – Phase propagation angles of the asymmetrical 6-phase machine.

in [Guzman et al (2012), Dordevic et al (2013b)] with the only difference being amplitude invariance. Subspace and zero-sequence notations are on the right hand side of the corresponding matrix. Clearly, the same technique is easily applicable to any other multiphase machine with symmetrical winding configuration, with both single (5-, 7-, 11-phase, …) and multiple winding sets (symmetrical 6-, 9-, 10-, 12-phase, ...). The algorithm is in accordance to the well-known technique for symmetrical machines shown in [Levi et al (2007)].

When it comes to the machines with multiple winding sets, 6-phase ones are by far the most used and researched type. Asymmetrical 6-phase configuration is depicted in Fig. 4.7. In this case input parameters for the algorithm are $n = 6$, $l = 2$, and $k = 3$. Subspace constant takes a value from $C \in [1, 5, 3]$. Instead of two zero-sequence components, an additional zero-sequence subspace exists, defined by the coefficient $C = 3$. Phase propagation angles $[\theta_{6a}]$ are obtained by use of (4.2). Comparison of the resulting matrix with power invariant transformation presented in [Zhao and Lipo (1995)] shows full equivalence:

$$[T_{6a}] = \frac{2}{6}\begin{bmatrix} e^{j[\theta_{6a}]} \\ e^{j5[\theta_{6a}]} \\ e^{j3[\theta_{6a}]} \end{bmatrix} \begin{matrix} \alpha, \beta \\ x_1, y_1 \\ x_2, y_2 \end{matrix} \tag{4.33}$$

In addition to 6-phase machines, 9-phase and 12-phase machines are widely investigated as well [Rockhill and Lipo (2015), Tani et al (2013)]. Their asymmetrical configurations are shown in Fig. 4.8. When the developed algorithm is applied for the single neutral point case, obtained subspace coefficients are [1, 5, 7, 3] and [1, 5, 7, 11, 3, 9] for 9- and 12-phase topologies, respectively. It should be noted that coefficient $C = 9$ for the 9-phase machine creates homopolar zero-sequence component, while coefficients C = [3, 9] produce two zero-sequence subspaces in the case of the 12-phase machine. Produced VSD transformation matrices are equivalent to the ones available in [Rockhill and Lipo (2015), Tani et al (2013)] and are as follows:

$$[T_{9a}] = \frac{2}{9}\begin{bmatrix} e^{j[\theta_{9a}]} \\ e^{j5[\theta_{9a}]} \\ e^{j7[\theta_{9a}]} \\ e^{j3[\theta_{9a}]} \\ \frac{1}{2}e^{j9[\theta_{9a}]} \end{bmatrix} \begin{matrix} \alpha, \beta \\ x_1, y_1 \\ x_2, y_2, \\ x_3, y_3 \\ z_+ \end{matrix} \quad [T_{12a}] = \frac{2}{12}\begin{bmatrix} e^{j[\theta_{12a}]} \\ e^{j5[\theta_{12a}]} \\ e^{j7[\theta_{12a}]} \\ e^{j11[\theta_{12a}]} \\ e^{j3[\theta_{12a}]} \\ e^{j9[\theta_{12a}]} \end{bmatrix} \begin{matrix} \alpha, \beta \\ x_1, y_1 \\ x_2, y_2 \\ x_3, y_3 \\ x_4, y_4 \\ x_5, y_5 \end{matrix} \tag{4.34}$$

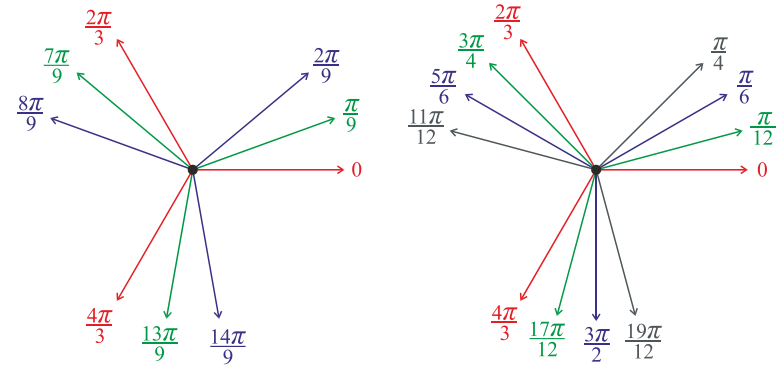

(a) 9-phase machine (b) 12-phase machine

Figure 4.8 – Phase propagation angles of the asymmetrical 9-phase (a) and 12-phase (b) machines.

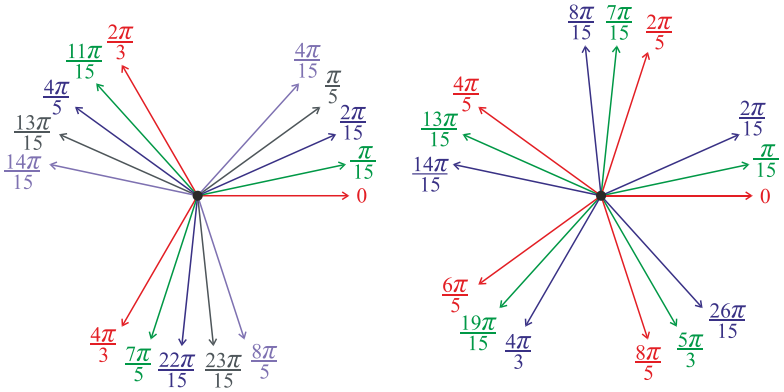

(a) (l = 5, k = 3) (b) (l = 5, k = 3)

Figure 4.9 – Phase propagation angles of an asymmetrical 15-phase machine: (a) (l = 5, k = 3), and (b) (l = 5, k = 3).

As far as machines with higher number of phases are concerned, a 15-phase machine has found its place predominantly in ship propulsion [Sun et al (2015), Moinoddin et al (2015), Liu et al (2013)]. It is interesting for analysis since it can be comprised of five 3-phase winding sets (5x3) or three 5-phase ones (3x5). In the first case l = 5 and k = 3, while in the second case l = 3 and k = 5. Both configurations with asymmetrical winding set distribution are shown in the Fig. 4.9. Phase propagation angles are $[\theta_{5x3a}]$ and $[\theta_{3x5a}]$, while amplitude invariant VSD matrices are as follows:

$$[T_{5\times 3a}]=\frac{2}{15}\begin{bmatrix} e^{j[\theta_{5\times 3a}]} \\ e^{j5[\theta_{5\times 3a}]} \\ e^{j7[\theta_{5\times 3a}]} \\ e^{j11[\theta_{5\times 3a}]} \\ e^{j13[\theta_{5\times 3a}]} \\ e^{j3[\theta_{5\times 3a}]} \\ e^{j9[\theta_{5\times 3a}]} \\ \frac{1}{2}e^{j15[\theta_{5\times 3a}]} \end{bmatrix} \begin{matrix} \alpha,\beta \\ x_1,y_1 \\ x_2,y_2 \\ x_3,y_3 \\ x_4,y_4 \\ x_5,y_5 \\ x_6,y_6 \\ z_+ \end{matrix}, \quad [T_{3\times 5a}]=\frac{2}{15}\begin{bmatrix} e^{j[\theta_{3\times 5a}]} \\ e^{j3[\theta_{3\times 5a}]} \\ e^{j7[\theta_{3\times 5a}]} \\ e^{j9[\theta_{3\times 5a}]} \\ e^{j11[\theta_{3\times 5a}]} \\ e^{j13[\theta_{3\times 5a}]} \\ e^{j5[\theta_{3\times 5a}]} \\ \frac{1}{2}e^{j15[\theta_{3\times 5a}]} \end{bmatrix} \begin{matrix} \alpha,\beta \\ x_1,y_1 \\ x_2,y_2 \\ x_3,y_3 \\ x_4,y_4 \\ x_5,y_5 \\ x_6,y_6 \\ z_+ \end{matrix} \tag{4.35}$$

Expressions (4.35) are in accordance with existing literature [Sun et al (2015), Moinoddin et al (2015), Liu et al (2013)] dealing with 15-phase machines. The only difference is in the row ordering, which only influences a subspace position within the matrix.

It should be noted that even though subspace coefficients are identical for both asymmetrical configurations (3x5 and 5x3), actual subspaces are at different positions within the matrix. The reason

for this is the different phase number of the winding sets (k). Namely, subspaces are arranged in such a way that zero-sequence subspaces are always positioned just above homopolar zero-sequence component, as explained in relation to (4.29). Consequently, when matrix needs to be changed to accommodate multiple neutral point case, it is only required to replace the last (l+1)/2 rows. It should be noted that simulation results verifying the algorithm are presented in section 4.4.3 where harmonic mapping is dealt with. Furthermore, Matlab and Mathematica codes for creation of VSD matrix by the proposed algorithm are available in the Appendix A of the thesis.

4.4.2 Machine Model in VSD Variables

In the previous subsection, an algorithm for producing VSD matrix for any multiphase machine type has been introduced. It enables development of the VSD transformation matrix in a systematic and simple manner regardless of the machine's winding configuration (symmetrical or asymmetrical, with a single or with multiple neutral points). The results obtained coincide with individual transformation matrices available in the literature. Both power and amplitude invariant transformations are considered. The resulting transformation matrix always decouples the machine in multiple 2-dimensional subspaces and homopolar zero-sequence components.

It is now appropriate to introduce an actual machine model by use of the VSD transformation. However, for the sake of simplicity, derivation is provided only for an asymmetrical 9-phase machine with single and multiple neutral points. Furthermore, this type of machine is used extensively throughout the thesis, including experiments, so it is convenient to deal with this particular case in more detail. Nevertheless, the outlined technique is easily extended to any machine type, with only difference being in the number of subspaces/zero sequences which are governed by the VSD transformation produced with the presented algorithm. Hence, there is no actual loss of generality.

It is firstly necessary to find the appropriate VSD transformation. For the 9-phase asymmetrical machine with single neutral point, VSD transformation is given in the first equation of (4.34), and in its full form, it is as follows:

$$[T_{9a1}]=\frac{2}{9}\begin{bmatrix}
1 & \cos\left(\frac{\pi}{9}\right) & \cos\left(\frac{2\pi}{9}\right) & \cos\left(\frac{6\pi}{9}\right) & \cos\left(\frac{7\pi}{9}\right) & \cos\left(\frac{8\pi}{9}\right) & \cos\left(\frac{12\pi}{9}\right) & \cos\left(\frac{13\pi}{9}\right) & \cos\left(\frac{14\pi}{9}\right) & \alpha \\
0 & \sin\left(\frac{\pi}{9}\right) & \sin\left(\frac{2\pi}{9}\right) & \sin\left(\frac{6\pi}{9}\right) & \sin\left(\frac{7\pi}{9}\right) & \sin\left(\frac{8\pi}{9}\right) & \sin\left(\frac{12\pi}{9}\right) & \sin\left(\frac{13\pi}{9}\right) & \sin\left(\frac{14\pi}{9}\right) & \beta \\
1 & \cos\left(5\frac{\pi}{9}\right) & \cos\left(5\frac{2\pi}{9}\right) & \cos\left(5\frac{6\pi}{9}\right) & \cos\left(5\frac{7\pi}{9}\right) & \cos\left(5\frac{8\pi}{9}\right) & \cos\left(5\frac{12\pi}{9}\right) & \cos\left(5\frac{13\pi}{9}\right) & \cos\left(5\frac{14\pi}{9}\right) & x_1 \\
0 & \sin\left(5\frac{\pi}{9}\right) & \sin\left(5\frac{2\pi}{9}\right) & \sin\left(5\frac{6\pi}{9}\right) & \sin\left(5\frac{7\pi}{9}\right) & \sin\left(5\frac{8\pi}{9}\right) & \sin\left(5\frac{12\pi}{9}\right) & \sin\left(5\frac{13\pi}{9}\right) & \sin\left(5\frac{14\pi}{9}\right) & y_1 \\
1 & \cos\left(7\frac{\pi}{9}\right) & \cos\left(7\frac{2\pi}{9}\right) & \cos\left(7\frac{6\pi}{9}\right) & \cos\left(7\frac{7\pi}{9}\right) & \cos\left(7\frac{8\pi}{9}\right) & \cos\left(7\frac{12\pi}{9}\right) & \cos\left(7\frac{13\pi}{9}\right) & \cos\left(7\frac{14\pi}{9}\right) & x_2 \\
0 & \sin\left(7\frac{\pi}{9}\right) & \sin\left(7\frac{2\pi}{9}\right) & \sin\left(7\frac{6\pi}{9}\right) & \sin\left(7\frac{7\pi}{9}\right) & \sin\left(7\frac{8\pi}{9}\right) & \sin\left(7\frac{12\pi}{9}\right) & \sin\left(7\frac{13\pi}{9}\right) & \sin\left(7\frac{14\pi}{9}\right) & y_2 \\
1 & \cos\left(3\frac{\pi}{9}\right) & \cos\left(3\frac{2\pi}{9}\right) & \cos\left(3\frac{6\pi}{9}\right) & \cos\left(3\frac{7\pi}{9}\right) & \cos\left(3\frac{8\pi}{9}\right) & \cos\left(3\frac{12\pi}{9}\right) & \cos\left(3\frac{13\pi}{9}\right) & \cos\left(3\frac{14\pi}{9}\right) & x_3 \\
0 & \sin\left(3\frac{\pi}{9}\right) & \sin\left(3\frac{2\pi}{9}\right) & \sin\left(3\frac{6\pi}{9}\right) & \sin\left(3\frac{7\pi}{9}\right) & \sin\left(3\frac{8\pi}{9}\right) & \sin\left(3\frac{12\pi}{9}\right) & \sin\left(3\frac{13\pi}{9}\right) & \sin\left(3\frac{14\pi}{9}\right) & y_3 \\
\frac{1}{2} & -\frac{1}{2} & \frac{1}{2} & \frac{1}{2} & -\frac{1}{2} & \frac{1}{2} & \frac{1}{2} & -\frac{1}{2} & \frac{1}{2} & z_+
\end{bmatrix} \quad (4.36)$$

Next, VSD transformation (4.36) should be applied to the machine equations in terms of phase variables. However, for the sake of simplicity, in contrast to the phase equation presented in section 4.2, equations used here model rotor in the same manner as the stator, with 9 equations, i.e. there are going to be 9 phase currents for both stator and rotor. Hence, both rotor and stator equations in phase variables

are of the same form and VSD transformation can be applied to both in the same way. Consequently, inductance matrix [*L*] is somewhat different than the one defined in (4.6) and (4.8), and it is now as follows:

$$
\begin{aligned}
&[L]=\begin{bmatrix}[L_{ss}] & [L_{sr}]\\ [L_{rs}] & [L_{rr}]\end{bmatrix}\\
&[L_{ss}]_{9\times 9}=[L_{jk}]+L_{ls}[I_n],\ L_{jk}=M\cos(\theta_k-\theta_j),\ j,k\in[1,2,\ldots 9]\\
&[L_{rr}]_{9\times 9}=[L_{jk}]+L_{lr}[I_n],\ L_{jk}=M\cos(\theta_k-\theta_j),\ j,k\in[1,2,\ldots 9]\\
&[L_{sr}]_{9\times 9}=[L_{jk}],\ L_{jk}=M\cos((\theta_k+\theta_e)-\theta_j),\ j,k\in[1,2,\ldots 9]\\
&[L_{rs}]_{9\times 9}=[L_{jk}],\ L_{jk}=M\cos(\theta_k-(\theta_j+\theta_e)),\ j,k\in[1,2,\ldots 9]
\end{aligned}
\tag{4.37}
$$

Parameters of the machine are denoted as follows: R_s/R_r – stator/rotor phase resistance, $L_{ls}/L_{lr}/L_m$ – stator/rotor leakage and mutual inductances. Mutual inductance L_m in decoupled model is related to the stator to rotor mutual inductance in phase domain M by coefficient 2/9, i.e. $M = 2/9\ L_m$. VSD transformation is applied to machine voltage and current equations as follows:

$$
\begin{aligned}
&\begin{bmatrix}[T_{9a1}] & 0\\ 0 & [T_{9a1}]\end{bmatrix}\left(\frac{d}{dt}\begin{bmatrix}[T_{9a1}]^{-1} & 0\\ 0 & [T_{9a1}]^{-1}\end{bmatrix}\begin{bmatrix}[\psi_{vsd}]\\ [\psi'_{vsdr}]\end{bmatrix}\right)=\begin{bmatrix}[T_{9a1}] & 0\\ 0 & [T_{9a1}]\end{bmatrix}\left(\begin{bmatrix}[T_{9a1}]^{-1} & 0\\ 0 & [T_{9a1}]^{-1}\end{bmatrix}\begin{bmatrix}[v_{vsd}]\\ [v'_{vsdr}]\end{bmatrix}-\begin{bmatrix}R_s[I_9] & 0\\ 0 & R_r[I_9]\end{bmatrix}\begin{bmatrix}[T_{9a1}]^{-1} & 0\\ 0 & [T_{9a1}]^{-1}\end{bmatrix}\begin{bmatrix}[i_{vsd}]\\ [i'_{vsdr}]\end{bmatrix}\right)\\
&\begin{bmatrix}[T_{9a1}] & 0\\ 0 & [T_{9a1}]\end{bmatrix}\left(\begin{bmatrix}[T_{9a1}]^{-1} & 0\\ 0 & [T_{9a1}]^{-1}\end{bmatrix}\begin{bmatrix}[\psi_{vsd}]\\ [\psi'_{vsdr}]\end{bmatrix}\right)=\begin{bmatrix}[T_{9a1}] & 0\\ 0 & [T_{9a1}]\end{bmatrix}\left([L]\begin{bmatrix}[T_{9a1}]^{-1} & 0\\ 0 & [T_{9a1}]^{-1}\end{bmatrix}\begin{bmatrix}[i_{vsd}]\\ [i'_{vsdr}]\end{bmatrix}\right)
\end{aligned}
\tag{4.38}
$$

resulting in the following equations:

$$
\begin{aligned}
&\frac{d}{dt}\begin{bmatrix}[\psi_{vsd}]\\ [\psi'_{vsdr}]\end{bmatrix}=\begin{bmatrix}[v_{vsd}]\\ [v'_{vsdr}]\end{bmatrix}-\begin{bmatrix}R_s[I_9] & 0\\ 0 & R_r[I_9]\end{bmatrix}\begin{bmatrix}[i_{vsd}]\\ [i'_{vsdr}]\end{bmatrix}\\
&\begin{bmatrix}[\psi_{vsd}]\\ [\psi'_{vsdr}]\end{bmatrix}=[L_{vsd}]\begin{bmatrix}[i_{vsd}]\\ [i'_{vsdr}]\end{bmatrix}
\end{aligned}
\tag{4.39}
$$

Index *vsd* denotes VSD variables, while prime (`) symbolise that variables are in the rotor reference frame. All other symbols are consistent with the ones defined in previous section of this chapter. Machine is now decoupled and machine variables in VSD subspaces are as follows:

$$
[f_{vsd}]=\begin{bmatrix}f_\alpha\\ f_\beta\\ f_{x1}\\ f_{y1}\\ f_{x2}\\ f_{y2}\\ f_{x3}\\ f_{y3}\\ f_{z+}\end{bmatrix},\ [f'_{vsdr}]=\begin{bmatrix}f'_{r\alpha}\\ f'_{r\beta}\\ f'_{rx1}\\ f'_{ry1}\\ f'_{x2}\\ f'_{y2}\\ f'_{x3}\\ f'_{y3}\\ f'_{rz+}\end{bmatrix},\ f=[v,i,\psi]
\tag{4.40}
$$

Since induction machine is with the squirrel cage, rotor voltages are equal to zero. If modelled machine is with three neutral points, expressions (4.40) will have three zero-sequence components (z_1, z_2, z_3) instead of the last subspace and the zero sequence (x_3-y_3, z+). Inductance matrix [L_{vsd}] is defined as follows:

$$\left[L_{vsd}\right]=\begin{bmatrix}\left[T_{9a1}\right] & 0\\ 0 & \left[T_{9a1}\right]\end{bmatrix}\left[L\right]\begin{bmatrix}\left[T_{9a1}\right]^{-1} & 0\\ 0 & \left[T_{9a1}\right]^{-1}\end{bmatrix}=\begin{bmatrix}L_{ssvsd} & L_{srvsd}\\ L_{rsvsd} & L_{rrvsd}\end{bmatrix} \tag{4.41}$$

Stator and rotor self-inductances and rotor-to-stator and stator-to-rotor inductances are governed with:

$$\begin{aligned}\left[L_{ssvsd}\right]&=\begin{bmatrix}L_{ls}+L_m & 0 & 0 & \cdots & 0\\ 0 & L_{ls}+L_m & 0 & \cdots & 0\\ 0 & 0 & L_{ls} & \cdots & 0\\ \vdots & \vdots & \vdots & \ddots & 0\\ 0 & 0 & 0 & 0 & L_{ls}\end{bmatrix},\ \left[L_{srvsd}\right]=\begin{bmatrix}L_m\cos(\theta_e) & -L_m\sin(\theta_e) & 0 & \cdots & 0\\ L_m\sin(\theta_e) & L_m\cos(\theta_e) & 0 & \cdots & 0\\ 0 & 0 & 0 & \cdots & 0\\ \vdots & \vdots & \vdots & \ddots & 0\\ 0 & 0 & 0 & 0 & 0\end{bmatrix}\\ \left[L_{rsvsd}\right]&=\begin{bmatrix}L_m\cos(\theta_e) & L_m\sin(\theta_e) & 0 & \cdots & 0\\ -L_m\sin(\theta_e) & L_m\cos(\theta_e) & 0 & \cdots & 0\\ 0 & 0 & 0 & \cdots & 0\\ \vdots & \vdots & \vdots & \ddots & 0\\ 0 & 0 & 0 & 0 & 0\end{bmatrix},\ \left[L_{rrvsd}\right]=\begin{bmatrix}L_{lr}+L_m & 0 & 0 & \cdots & 0\\ 0 & L_{lr}+L_m & 0 & \cdots & 0\\ 0 & 0 & L_{lr} & \cdots & 0\\ \vdots & \vdots & \vdots & \ddots & 0\\ 0 & 0 & 0 & 0 & L_{lr}\end{bmatrix}\end{aligned} \tag{4.42}$$

The obtained model decouples machine into multiple subspaces. However, stator and rotor variables are associated with two different reference frames. Therefore, rotational transformation must be applied to rotor variables in α-β subspace, to represent both stator and rotor in the same stationary reference frame, as follows:

$$\left[f_{\alpha\beta r}\right]=\left[T_{rot}(\theta_e)\right]\left[f'_{r\alpha\beta}\right],\ \left[T_{\theta_e}\right]=\begin{bmatrix}\cos(\theta_e) & \sin(\theta_e)\\ -\sin(\theta_e) & \cos(\theta_e)\end{bmatrix},\ f=[v,i,\psi] \tag{4.43}$$

If stator and rotor inductances are defined as $L_s = L_{ls} + L_m$ and $L_r = L_{lr} + L_m$ respectively, inductance matrix is governed with:

$$\begin{aligned}\left[L_{ssvsd}\right]&=\begin{bmatrix}L_s & 0 & 0 & \cdots & 0\\ 0 & L_s & 0 & \cdots & 0\\ 0 & 0 & L_{ls} & \cdots & 0\\ \vdots & \vdots & \vdots & \ddots & 0\\ 0 & 0 & 0 & 0 & L_{ls}\end{bmatrix},\ \left[L_{srvsd}\right]=\begin{bmatrix}L_m & 0 & 0 & \cdots & 0\\ 0 & L_m & 0 & \cdots & 0\\ 0 & 0 & 0 & \cdots & 0\\ \vdots & \vdots & \vdots & \ddots & 0\\ 0 & 0 & 0 & 0 & 0\end{bmatrix}\\ \left[L_{rsvsd}\right]&=\begin{bmatrix}L_m & 0 & 0 & \cdots & 0\\ 0 & L_m & 0 & \cdots & 0\\ 0 & 0 & 0 & \cdots & 0\\ \vdots & \vdots & \vdots & \ddots & 0\\ 0 & 0 & 0 & 0 & 0\end{bmatrix},\ \left[L_{rrvsd}\right]=\begin{bmatrix}L_r & 0 & 0 & \cdots & 0\\ 0 & L_r & 0 & \cdots & 0\\ 0 & 0 & L_{lr} & \cdots & 0\\ \vdots & \vdots & \vdots & \ddots & 0\\ 0 & 0 & 0 & 0 & L_{lr}\end{bmatrix}\end{aligned} \tag{4.44}$$

With the terms of the inductance matrix simplified as shown in (4.44), final equations in VSD subspaces are relatively simple and they are as follows:

$$\begin{bmatrix}v_\alpha\\ v_\beta\\ 0\\ 0\end{bmatrix}=\begin{bmatrix}R_s+L_s\frac{d}{dt} & 0 & L_m\frac{d}{dt} & 0\\ 0 & R_s+L_s\frac{d}{dt} & 0 & L_m\frac{d}{dt}\\ L_m\frac{d}{dt} & \omega_e L_m & R_r+L_r\frac{d}{dt} & \omega_e L_r\\ -\omega_e L_m & L_m\frac{d}{dt} & -\omega_e L_r & R_r+L_r\frac{d}{dt}\end{bmatrix}\begin{bmatrix}i_\alpha\\ i_\beta\\ i_{\alpha r}\\ i_{\beta r}\end{bmatrix} \tag{4.45a}$$

$$\begin{bmatrix} v_{xj} \\ v_{yj} \\ 0 \\ 0 \end{bmatrix} = \begin{bmatrix} R_s + L_{ls}\frac{d}{dt} & 0 & 0 & 0 \\ 0 & R_s + L_{ls}\frac{d}{dt} & 0 & 0 \\ 0 & 0 & R_r + L_{lr}\frac{d}{dt} & 0 \\ 0 & 0 & 0 & R_r + L_{lr}\frac{d}{dt} \end{bmatrix} \begin{bmatrix} i_{xj} \\ i_{yj} \\ i_{xjr} \\ i_{yjr} \end{bmatrix}, \quad j = 1,2,3$$
$$\begin{bmatrix} v_{z+} \\ 0 \end{bmatrix} = \begin{bmatrix} R_s + L_{ls}\frac{d}{dt} & 0 \\ 0 & R_r + L_{lr}\frac{d}{dt} \end{bmatrix} \begin{bmatrix} i_{z+} \\ i_{zr+} \end{bmatrix} \tag{4.45b}$$

It can be seen that mutual inductance between stator and rotor exists only in the α-β subspace (4.45a) and the rotor *x*-*y* subspaces cannot be excited. Consequently, torque is only produced in the α-β subspace and rotor *x*-*y* subspaces can be omitted from the equations. Machine torque is defined as:

$$T_e = \frac{9}{2} P\left(\psi_\alpha i_\beta - \psi_\beta i_\alpha\right) \tag{4.46}$$

The 9-phase machine is fully described by equations (4.45) – (4.46). Furthermore, when VSD algorithm developed in the previous section of this chapter is applied to any other multiphase induction machine, resulting equations will be of the same form. All equations for α-β, *x*-*y* subspaces and homopolar zero-sequence components will be completely identical. The only difference is in the number of subspaces and zero sequences, which is governed by the VSD creation algorithm. Hence, equations (4.45) – (4.46), together with the given algorithm, are valid for any other multiphase induction machine type. In other words, the algorithm will produce VSD matrix which will diagonalise terms [L_{ss}], [L_{sr}], [L_{rs}], [L_{rr}] of the inductance matrix [L].

Since VSD transformation produces multiple complex planes, instead of representation by real values, it is possible to express model in complex form as follows:

$$\begin{aligned} \underline{v}_{\alpha\beta} &= \left(R_s + L_s\frac{d}{dt}\right)\underline{i}_{\alpha b} + L_m\frac{d}{dt}\underline{i}_{\alpha\beta r} \\ 0 &= \left(R_r + L_r\frac{d}{dt}\right)\underline{i}_{\alpha\beta r} + L_m\frac{d}{dt}\underline{i}_{\alpha\beta} - j\omega_e\left(L_m\underline{i}_{\alpha\beta} + L_r\underline{i}_{\alpha\beta r}\right) \\ \underline{v}_{xyj} &= \left(R_s + L_{ls}\frac{d}{dt}\right)\underline{i}_{xyj}, \quad j = 1,2,3 \end{aligned} \tag{4.47}$$

Equivalent circuits for α-β and *x*-*y* subspaces can be now created as shown in Fig. 4.10. Equivalent circuit for the α-β subspace is shown in Fig. 4.10a, while the equivalent circuit for the *x*-*y* subspaces is shown in Fig. 4.10b. It should be noted that these equivalent circuits are valid for any multiphase induction machine, and the one of Fig. 4.10b has already been used to formulate (3.21a).

By analysing the final equations and produced equivalent circuit, it is easily noticeable that electromechanical energy conversion is taking place only in the α-β subspace, so machine can be controlled in the same well-known way as the 3-phase machine. Additional controllers in *x*-*y* subspaces may be needed to utilise additional degrees of freedom for multiphase machine specific applications, such as fault tolerance, multi-motor drives, power sharing or low order harmonic elimination. It is easily

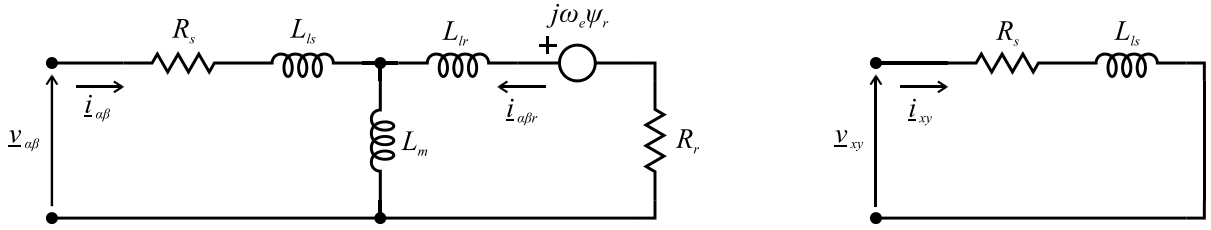

(a) α-β subspace (b) x-y subspaces

Figure 4.10 – Equivalent circuit of the α-β (a) and x-y (b) subspaces.

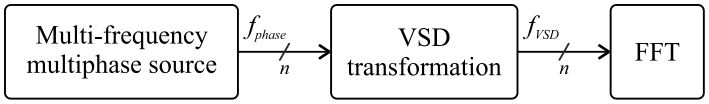

Figure 4.11 – Simulation diagram for harmonic mapping analysis.

seen that due to the orthogonality of the subspaces each one can be independently controlled without disturbing the other subspaces. When compared to the MS modelling approach, absence of cross-coupling is by far the largest advantage of controlling the machine in terms of VSD variables.

4.4.3 Harmonic Mapping

Low impedance of x-y subspaces can result in large inverter induced low-order harmonics in phase currents. Since x-y current components do not contribute to the total flux/torque production, they should be eliminated. Use of the proper VSD transformation will not only decouple the machine into flux/torque producing and non-producing components, but will also uniquely map odd-order harmonics in the x-y subspaces as well. This means that each odd-order harmonic is mapped only into a single subspace or zero sequence. Consequently, their elimination is made relatively easy by the use of resonant controllers [Yepes et al (2013)]. When harmonic mapping in VSD variables is compared to the ones obtained by MS approach, there is significant advantage of the VSD modelling approach. In the case of the MS modelling all non zero-sequence harmonics are mapped in the α-β subspaces, hence their elimination is relatively complicated since they exist in α-β currents of all winding sets.

In order to demonstrate harmonic mapping produced by the presented VSD algorithm, a multi-frequency multiphase signal generator has been created to produce phase variables containing component at the fundamental frequency and the odd-order harmonics up to the phase number n. Amplitudes of all the harmonic components are equal to one. VSD transformation created by the proposed algorithm has been applied to phase values resulting in VSD variables (α-β, x-y, z), as shown in the Fig. 4.11. Amplitude invariant transformation has been used in this case, so after applying FFT, all values are equal to one enabling easier insight into harmonic mapping. It should be noted that even-order harmonics can be present as well, e.g. sideband harmonics of switching frequency [Jones et al (2011)]. They are usually at much higher frequencies where impedance is high when compared to the VSI induced odd-order dead-time harmonics. Hence, they are not discussed any further.

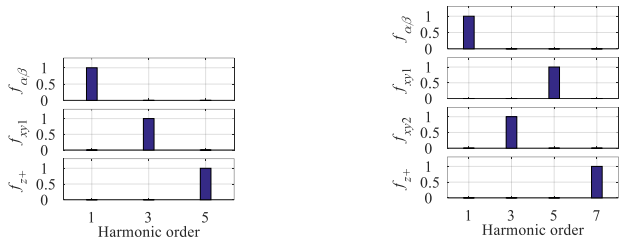

(a) 5-phase (b) 7-phase

Figure 4.12 – Harmonic mapping for 5-phase (a) and 7-phase (b) machine.

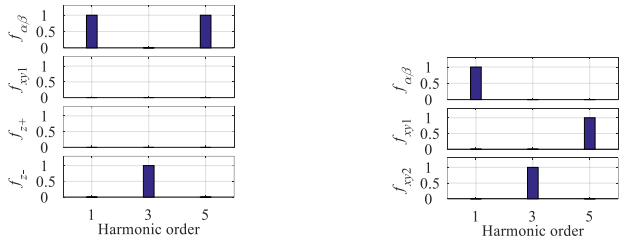

(a) symmetrical (b) asymmetrical

Figure 4.13 – Harmonic mapping for a symmetrical (a) and asymmetrical (b) 6-phase machine with single neutral point.

Harmonic mapping for 5- and 7-phase machines is shown in the Fig. 4.12. It can be seen that the component at fundamental frequency is mapped in the α-β subspace, while subsequent odd-order harmonics are uniquely mapped in *x*-*y* subspaces and positive zero sequence. Furthermore, any other multiphase machine with single winding set (i.e. 11, 13) has similar harmonic mapping, hence no further analysis is offered.

When a 6-phase machine with single neutral point is considered, simulation results are shown in the Fig. 4.13. Fundamental is mapped in the first subspace for both symmetrical and asymmetrical configurations. However, symmetrical 6-phase machine has identical odd-order harmonic mapping as the standard 3-phase one, i.e. the 5th harmonic is mapped in the α-β subspace and that is the first odd-order harmonic that can produce torque pulsation. On the other hand, in the case of the asymmetrical 6-phase machine, the 5th harmonic is mapped in the first *x*-*y* plane (x_1-y_1), hence it cannot produce torque pulsation. Triplen harmonics are the zero-sequence ones and they are mapped either in the last subspace (x_2-y_2) of the asymmetrical 6-phase machine or in the homopolar zero-sequence component (z_-) of the symmetrical 6-phase machine. If a 6-phase machine is with 2 neutral points, zero-sequence harmonics will be mapped in individual zero sequences (z_1, z_2).

Due to the proper selection of subspace constants, odd-order harmonic mapping is identical for any other multiple 3-phase machine: fundamental and non-triplen harmonics are mapped in the first *l* subspaces, while triplen ones exist in the rest of the subspaces/zero sequences. Examples are given for 9- and 12-phase machines with a single neutral point. Simulation results are shown in the Fig. 4.14, where it can be easily seen that odd-order harmonics are mapped in the same manner as for the 6-phase case, the only difference being in the number of subspaces.

The 15-phase machine is considered in all 4 possible configurations with a single neutral point,

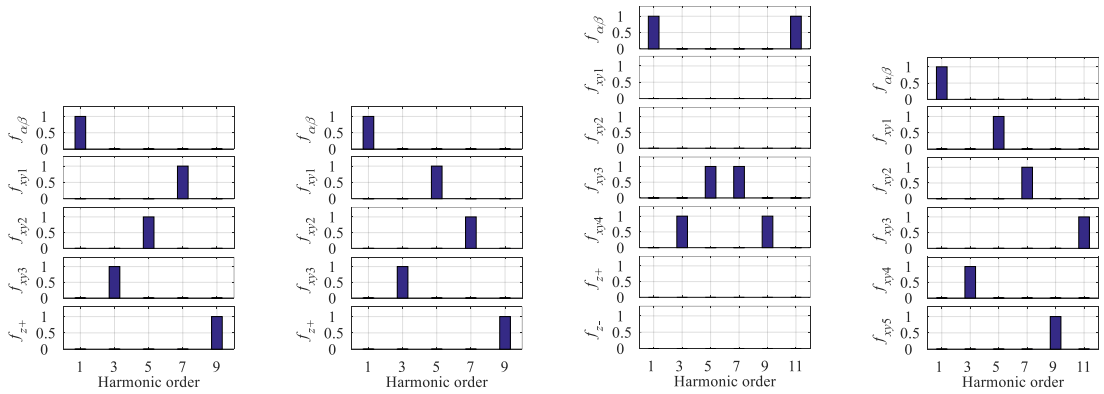

(a) (b) (c) (b)

Figure 4.14 – Harmonic mapping for a symmetrical (a) and asymmetrical (b) 9-phase machine and a symmetrical (c) and asymmetrical (d) 12-phase machine with single neutral point.

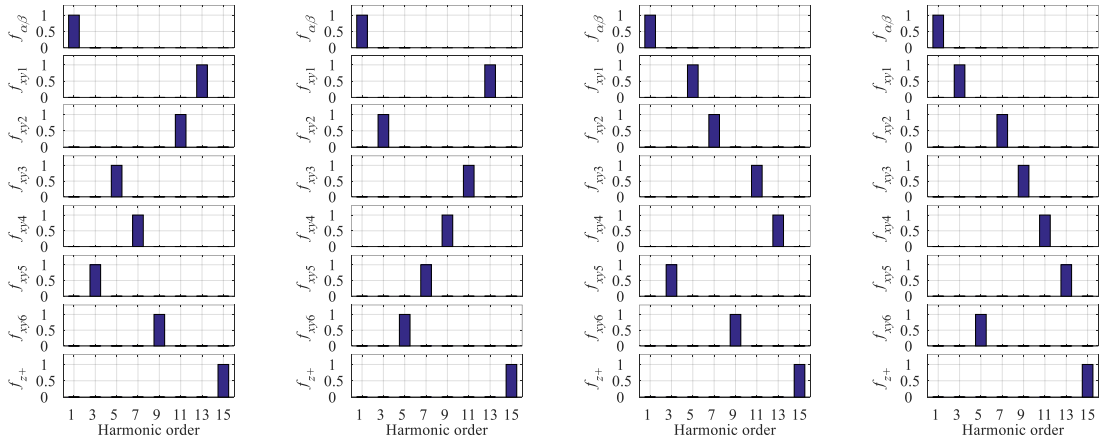

(a) Symmetrical (5×3) (b) Symmetrical (5×3) (c) Asymmetrical (5×3) (d) Asymmetrical (3×5)

Figure 4.15 – Harmonic mapping for a symmetrical and asymmetrical 15-phase machine in both 5×3 and 3×5 configurations.

symmetrical and asymmetrical case with five 3-phase winding sets or three 5-phase ones. Harmonic mapping for symmetrical cases is shown in the Fig. 4.15 (a) and (b), while asymmetrical cases can be seen in the same figure, plots (c) and (d). Unique harmonic mapping is easily seen. In this case there are 7 subspaces and a single positive zero sequence, as shown in the Fig. 4.15. However, depending on the construction of the machine (5x3-phase or 3x5-phase), there is a different number of non zero-sequence subspaces. This holds true even in the symmetrical case, where both machine configurations are identical in terms of phase propagation angles. The only difference is in which harmonics are considered to be zero-sequence ones, or, if VSD matrices are observed, some of the rows are swapped. On the other hand, in asymmetrical case, machines are different. Nonetheless harmonic mapping is similar once again. The 3rd, 9th, and 15th harmonics are zero-sequence ones in 5x3-phase configuration, while in the case of 3x5-phase machine the 5th and 15th are considered to be zero-sequence harmonics.

If a 15-phase machine is reconfigured to be with multiple neutral points, zero-sequence harmonics map into winding set's individual zero sequences. In the 5x3-phase case, the last two subspaces and positive zero sequence are replaced with individual zero sequences, while in the 3x5-phase case, a single subspace and positive zero-sequence component are replaced.

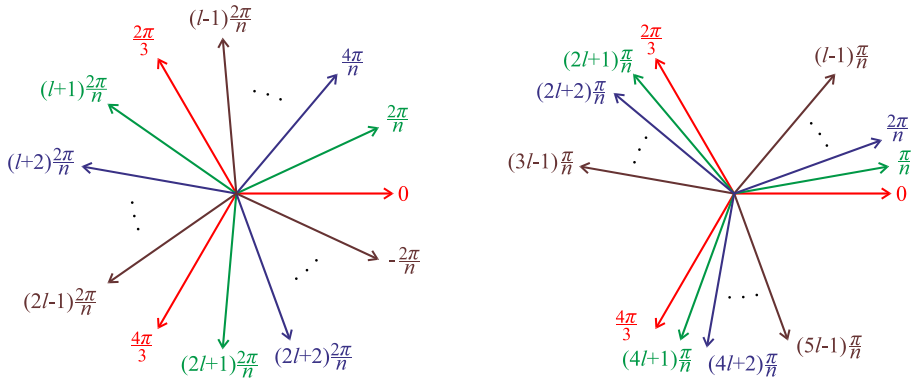

Figure 4.16 – Phase propagation angles of symmetrical (a) and asymmetrical (b) multiple 3-phase machines.

4.5 Relationship Between VSD and Multi-Stator Modelling Approaches

Until now, in order to simplify the machine, it was modelled either by MS modelling approach or by use of VSD transformation. Both approaches have their benefits and drawbacks. Hence, the goal of this section is to combine both VSD and multiple *d-q* modelling approaches in order to preserve the benefits of VSD (decoupled machine model leading to relatively easy control) while still being able to ascertain information about flux and torque producing components (i.e. α-β currents) in individual winding sets, a feature of MS modelling. It is shown that imbalance in individual winding set currents is manifested through *x-y* currents at fundamental frequency. Hence, additional current control in *x-y* planes can enable arbitrary power/current sharing between winding sets, a desirable feature in a multiphase generator. Moreover, if only currents in the *x-y* planes are changed to impose or remove an imbalance between winding sets or phases, there is no actual change in total flux and torque since they are produced only in the α-β subspace. The work reported in [Tani et al (2013), Mengoni (2016)] for an asymmetrical 12-phase machine is taken here further by considering a general case of a multiphase machine with multiple 3-phase windings in both symmetrical and asymmetrical configurations, with both single and multiple neutral points. It should be pointed out that this section deals with the relationship between variables in MS and VSD domains, and actual current/power sharing development and implementation is explained further on in the thesis.

The relationship between MS and VSD variables is firstly developed for most commonly used multiphase machines, i.e. 6- and 9-phase, and for somewhat not so common 12-, 15-, and 18-phase. All winding set configurations are considered. Next, set of equations valid for any multiple 3-phase machine is presented and verified by Matlab simulation. It is shown that use of an appropriate VSD matrix, presented in a previous section of this chapter, provides the set of equations that are valid for all machine topologies (symmetrical/asymmetrical with single/multiple neutral points). Since the equations are obtained by only combining transformation matrices, results are independent of the machine type (i.e. induction or synchronous).

Even though a machine diagram for the general case has been given in the Fig. 4.1, for convenience, another one showing only multiple 3-phase machine is presented in the Fig. 4.16. Since multiple 3-

phase machines are considered, number of phases within the winding set is equal to 3 and phase propagation angles are given in (4.2) when $k = 3$.

Firstly, phase variables are expressed by use of MS transformation, i.e. multiple inverse Clarke's transformations are applied to the α-β-z variables of each winding set as follows:

$$\begin{bmatrix} f_{1,1} \\ f_{1,2} \\ f_{1,3} \end{bmatrix} = [C(\theta_1)]^{-1} \begin{bmatrix} f_{\alpha 1} \\ f_{\beta 1} \\ f_{z1} \end{bmatrix}$$

$$\begin{bmatrix} f_{2,1} \\ f_{2,2} \\ f_{2,3} \end{bmatrix} = [C(\theta_2)]^{-1} \begin{bmatrix} f_{\alpha 1} \\ f_{\beta 1} \\ f_{z1} \end{bmatrix} \qquad [C(\theta)] = \frac{2}{3} \begin{bmatrix} \cos(\theta) & \cos\left(\theta + \frac{2\pi}{3}\right) & \cos\left(\theta + \frac{4\pi}{3}\right) \\ \sin(\theta) & \sin\left(\theta + \frac{2\pi}{3}\right) & \sin\left(\theta + \frac{4\pi}{3}\right) \\ \frac{1}{2} & \frac{1}{2} & \frac{1}{2} \end{bmatrix} \tag{4.48}$$

$$\vdots$$

$$\begin{bmatrix} f_{l,1} \\ f_{l,2} \\ f_{l,3} \end{bmatrix} = [C(\theta_l)]^{-1} \begin{bmatrix} f_{\alpha l} \\ f_{\beta l} \\ f_{zl} \end{bmatrix}$$

Produced expressions for phase variables are arranged in proper order and VSD transformation is applied as follows:

$$\begin{matrix} flux/torque\ subspace \\ non\ zero-seq.\ subspaces \\ zero-seq.\ components \end{matrix} \begin{bmatrix} [f_{\alpha\beta}]_{2\times 1} \\ [f_{xy}]_{2(l-1)\times 1} \\ [f_{xy}]_{l\times 1} / [f_{xyz}]_{l\times 1} / [f_z]_{l\times 1} \end{bmatrix} = [T_{VSD}]_{n\times n} [f_{phase}]_{n\times 1} \tag{4.49}$$

$$[f_{phase}] = [f_{1,1} \quad f_{2,1} \quad \cdots \quad f_{l,1} \quad f_{1,2} \quad f_{2,2} \quad \cdots \quad f_{l,2} \quad f_{1,3} \quad f_{2,3} \quad \cdots \quad f_{l,3}]^T_{1\times n}$$

VSD variables are divided as per VSD matrix creation algorithm presented in subsection 4.4.1 of this chapter. Hence, there is a single flux/torque producing subspace and multiple non zero-sequence subspaces, followed by zero-sequence subspaces and/or homopolar zero-sequence components. Number of subspaces and zero sequences is governed by the machine configuration (symmetrical/ asymmetrical with single/multiple neutral points). For the sake of clarity, values in (4.48) are all real, and VSD transformation used [T_{VSD}] is in real form as well.

All variables are denoted by *f*, so that they might be voltage, current or flux linkage, while indices define domain they are belonging to, i.e. phase, VSD or MS. In the case of the phase variables, the first index represents winding set number (1 – *l*) and the second index signifies phase within the winding set (1 to 3). Variables in MS domain are denoted by indices α-β-z followed by the number of the winding set they are belonging to. VSD subspaces are identified by letters $\alpha\beta$, *xy*, and *z*, defining flux/torque producing, non-producing subspaces and zero sequences respectively. Numbers next to the *xy* indices show the subspace number.

In order to obtain relationship between MS and VSD variables, it is only necessary to combine (4.48) and (4.49), i.e. to replace phase variables in (4.49) with expression for phase variables from (4.48) as follows:

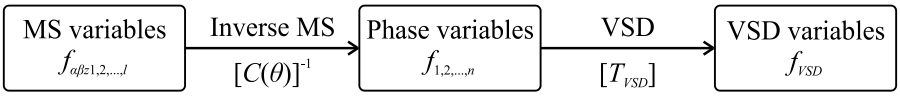

Figure 4.17 – Relationship between VSD and MS modelling approaches.

$$\left[f_{VSD}(\alpha\beta z)\right]_{n\times 1} = \left[T_{VSD}\right]_{n\times n}\left[f_{phase}(\alpha\beta z)\right]_{n\times 1} \tag{4.50}$$

For the sake of clarity, besides explanation in (4.50), creation of the relationship between VSD and MS variables is depicted in Fig. 4.17 as well. Firstly, inverse MS transformation has been applied to the MS variables in order to produce phase variables. Then, VSD transformation has been applied on such obtained expression for phase variables resulting in relationship between VSD and MS variables.

It should be emphasised here that it is necessary to use the proposed algorithm for creation of the VSD matrix. It will be shown later that by doing so a unified expression for relationship between modelling approaches is obtained. MS equations are the same regardless of the number of neutral points, and VSD transformation is identical for all non zero-sequence subspaces for a given machine type. It follows that the relationship between VSD and MS variables is going to be the same for all non zero-sequence subspaces for a given machine type. Furthermore, in the case of the multiple neutral points zero-sequence subspaces are replaced by individual neutral points and the relationship is a trivial one (e.g. $f_{z1} = f_{z1}$, $f_{z2} = f_{z2}$, …). Therefore, only the cases with a single neutral point are dealt with. In the following equations both real and complex forms are used. It is assumed that all α and x components are aligned along the real axis of the respective subspace, while β and y are represented by imaginary value for all subspaces as follows:

$$\underline{f}_{\alpha\beta} = f_\alpha + jf_\beta, \qquad \underline{f}_{xy} = f_x + jf_y \tag{4.51}$$

When (4.50) is applied to a symmetrical and asymmetrical 6-phase case with a single neutral point, the following sets of equations are obtained:

$$\begin{bmatrix} f_\alpha \\ f_\beta \\ f_{x1} \\ f_{y1} \\ f_{z+} \\ f_{z-} \end{bmatrix} = \frac{1}{2}\begin{bmatrix} f_{\alpha1} + f_{\alpha2} \\ f_{\beta1} + f_{\beta2} \\ f_{\alpha1} - f_{\alpha2} \\ -f_{\beta1} + f_{\beta2} \\ (f_{z1} + f_{z2}) \\ (f_{z1} - f_{z2}) \end{bmatrix} \Rightarrow \begin{aligned} \underline{f}_{\alpha\beta} &= \frac{1}{2}\left(\underline{f}_{\alpha\beta1} + \underline{f}_{\alpha\beta2}\right) \\ \underline{f}_{xy1} &= \frac{1}{2}\left(\overline{\underline{f}}_{\alpha\beta1} - \overline{\underline{f}}_{\alpha\beta2}\right) \\ f_{z+} &= \frac{1}{2}(f_{z1} + f_{z2}) \\ f_{z-} &= \frac{1}{2}(f_{z1} - f_{z2}) \end{aligned} \tag{4.52}$$

$$\begin{bmatrix} f_\alpha \\ f_\beta \\ f_{x1} \\ f_{y1} \\ f_{x2} \\ f_{y2} \end{bmatrix} = \frac{1}{2}\begin{bmatrix} f_{\alpha1} + f_{\alpha2} \\ f_{\beta1} + f_{\beta2} \\ f_{\alpha1} - f_{\alpha2} \\ -f_{\beta1} + f_{\beta2} \\ 2f_{z1} \\ 2f_{z2} \end{bmatrix} \Rightarrow \begin{aligned} \underline{f}_{\alpha\beta} &= \frac{1}{2}\left(\underline{f}_{\alpha\beta1} + \underline{f}_{\alpha\beta2}\right) \\ \underline{f}_{xy1} &= \frac{1}{2}\left(\overline{\underline{f}}_{\alpha\beta1} - \overline{\underline{f}}_{\alpha\beta2}\right) \\ \underline{f}_{xy2} &= f_{z1} + f_{z2}e^{j\frac{\pi}{2}} \end{aligned} \tag{4.53}$$

Line above symbol designates complex conjugate. It can be seen that the relationship between MS variables and the non zero-sequence subspaces of the VSD (α-β and x_1-y_1) is identical for both symmetrical and asymmetrical configurations. Hence, the same set of equations is valid for all 6-phase

cases. Furthermore, all flux/torque producing components are mapped in these subspaces and if power sharing is desired, only these subspaces need to be used.

To continue the analysis, (4.50) is applied to a 9-phase case for symmetrical and asymmetrical configurations with a single neutral point. The obtained equations are as follows:

$$\begin{bmatrix} f_{\alpha} \\ f_{\beta} \\ f_{x1} \\ f_{y1} \\ f_{x2} \\ f_{y2} \\ f_{x3} \\ f_{y3} \\ f_{z+} \end{bmatrix} = \frac{1}{3} \begin{bmatrix} f_{\alpha 1} + f_{\alpha 2} + f_{\alpha 3} \\ f_{\beta 1} + f_{\beta 2} + f_{\beta 3} \\ f_{\alpha 1} - \frac{1}{2}\left(f_{\alpha 2} + f_{\alpha 3}\right) + \frac{\sqrt{3}}{2}\left(f_{\beta 2} - f_{\beta 3}\right) \\ \frac{\sqrt{3}}{2}\left(f_{\alpha 2} - f_{\alpha 3}\right) - f_{\beta 1} + \frac{1}{2}\left(f_{\beta 2} + f_{\beta 3}\right) \\ f_{\alpha 1} - \frac{1}{2}\left(f_{\alpha 2} + f_{\alpha 3}\right) + \frac{\sqrt{3}}{2}\left(-f_{\beta 2} + f_{\beta 3}\right) \\ \frac{\sqrt{3}}{2}\left(f_{\alpha 2} - f_{\alpha 3}\right) + f_{\beta 1} - \frac{1}{2}\left(f_{\beta 2} + f_{\beta 3}\right) \\ 2f_{z1} - f_{z2} - f_{z3} \\ \sqrt{3}\left(f_{z2} - f_{z3}\right) \\ f_{z1} + f_{z2} + f_{z3} \end{bmatrix} \Rightarrow \begin{bmatrix} \underline{f}_{\alpha\beta} = \frac{1}{3}\left(\underline{f}_{\alpha\beta 1} + \underline{f}_{\alpha\beta 2} + \underline{f}_{\alpha\beta 3}\right) \\ \underline{f}_{xy1} = \frac{1}{3}\left(\overline{\underline{f}}_{\alpha\beta 1} + \overline{\underline{f}}_{\alpha\beta 2} e^{j\frac{2\pi}{3}} + \overline{\underline{f}}_{\alpha\beta 3} e^{j\frac{4\pi}{3}}\right) \\ \underline{f}_{xy2} = \frac{1}{3}\left(\underline{f}_{\alpha\beta 1} + \underline{f}_{\alpha\beta 2} e^{j\frac{2\pi}{3}} + \underline{f}_{\alpha\beta 3} e^{j\frac{4\pi}{3}}\right) \\ \underline{f}_{xy3} = \frac{2}{3}\left(f_{z1} + f_{z2} e^{j\frac{2\pi}{3}} + f_{z3} e^{j\frac{4\pi}{3}}\right) \\ f_{z+} = \frac{1}{3}\left(f_{z1} + f_{z2} + f_{z3}\right) \end{bmatrix} \quad (4.54)$$

$$\begin{bmatrix} f_{\alpha} \\ f_{\beta} \\ f_{x1} \\ f_{y1} \\ f_{x2} \\ f_{y2} \\ f_{x3} \\ f_{y3} \\ f_{z+} \end{bmatrix} = \frac{1}{3} \begin{bmatrix} f_{\alpha 1} + f_{\alpha 2} + f_{\alpha 3} \\ f_{\beta 1} + f_{\beta 2} + f_{\beta 3} \\ f_{\alpha 1} - \frac{1}{2}\left(f_{\alpha 2} + f_{\alpha 3}\right) + \frac{\sqrt{3}}{2}\left(f_{\beta 2} - f_{\beta 3}\right) \\ \frac{\sqrt{3}}{2}\left(f_{\alpha 2} - f_{\alpha 3}\right) - f_{\beta 1} + \frac{1}{2}\left(f_{\beta 2} + f_{\beta 3}\right) \\ f_{\alpha 1} - \frac{1}{2}\left(f_{\alpha 2} + f_{\alpha 3}\right) + \frac{\sqrt{3}}{2}\left(-f_{\beta 2} + f_{\beta 3}\right) \\ \frac{\sqrt{3}}{2}\left(f_{\alpha 2} - f_{\alpha 3}\right) + f_{\beta 1} - \frac{1}{2}\left(f_{\beta 2} + f_{\beta 3}\right) \\ 2f_{z1} + f_{z2} - f_{z3} \\ \sqrt{3}\left(f_{z2} + f_{z3}\right) \\ f_{z1} - f_{z2} + f_{z3} \end{bmatrix} \Rightarrow \begin{bmatrix} \underline{f}_{\alpha\beta} = \frac{1}{3}\left(\underline{f}_{\alpha\beta 1} + \underline{f}_{\alpha\beta 2} + \underline{f}_{\alpha\beta 3}\right) \\ \underline{f}_{xy1} = \frac{1}{3}\left(\overline{\underline{f}}_{\alpha\beta 1} + \overline{\underline{f}}_{\alpha\beta 2} e^{j\frac{2\pi}{3}} + \overline{\underline{f}}_{\alpha\beta 3} e^{j\frac{4\pi}{3}}\right) \\ \underline{f}_{xy2} = \frac{1}{3}\left(\underline{f}_{\alpha\beta 1} + \underline{f}_{\alpha\beta 2} e^{j\frac{2\pi}{3}} + \underline{f}_{\alpha\beta 3} e^{j\frac{4\pi}{3}}\right) \\ \underline{f}_{xy3} = \frac{2}{3}\left(f_{z1} + f_{z2} e^{j\frac{\pi}{3}} + f_{z3} e^{j\frac{2\pi}{3}}\right) \\ f_{z+} = \frac{1}{3}\left(f_{z1} + f_{z2} e^{j\pi} + f_{z3}\right) \end{bmatrix} \quad (4.55)$$

Equations (4.54) and (4.55) are for the symmetrical and asymmetrical case, respectively. Again, they are of the same form, as in the 6-phase case. MS flux and torque producing variables (α-β) are mapped in the VSD non zero-sequence subspaces, while individual winding set zero sequences are mapped in VSD zero-sequence subspaces and homopolar zero-sequence component.

Analysis is continued by applying (4.50) to the 12-phase and 15-phase case. In the case of the symmetrical and asymmetrical 12-phase machine with single neutral point, equations are, respectively, as follows:

$$\begin{bmatrix} f_{\alpha} \\ f_{\beta} \\ f_{x1} \\ f_{y1} \\ f_{x2} \\ f_{y2} \\ f_{x3} \\ f_{y3} \\ f_{x4} \\ f_{y4} \\ f_{z+} \\ f_{z-} \end{bmatrix} = \frac{1}{4} \begin{bmatrix} f_{\alpha 1} + f_{\alpha 2} + f_{\alpha 3} + f_{\alpha 4} \\ f_{\beta 1} + f_{\beta 2} + f_{\beta 3} + f_{\beta 4} \\ f_{\alpha 1} - f_{\alpha 3} + f_{\beta 2} - f_{\beta 4} \\ f_{\alpha 2} - f_{\alpha 4} - f_{\beta 1} + f_{\beta 3} \\ f_{\alpha 1} - f_{\alpha 3} - f_{\beta 2} + f_{\beta 4} \\ f_{\alpha 2} - f_{\alpha 4} + f_{\beta 1} - f_{\beta 3} \\ f_{\alpha 1} - f_{\alpha 2} + f_{\alpha 3} - f_{\alpha 4} \\ -f_{\beta 1} + f_{\beta 2} - f_{\beta 3} + f_{\beta 4} \\ 2\left(f_{z1} - f_{z3}\right) \\ 2\left(f_{z2} - f_{z4}\right) \\ f_{z1} + f_{z2} + f_{z3} + f_{z4} \\ f_{z1} - f_{z2} + f_{z3} - f_{z4} \end{bmatrix} \Rightarrow \begin{bmatrix} \underline{f}_{\alpha\beta} = \frac{1}{4}\left(\underline{f}_{\alpha\beta 1} + \underline{f}_{\alpha\beta 2} + \underline{f}_{\alpha\beta 3} + \underline{f}_{\alpha\beta 4}\right) \\ \underline{f}_{xy1} = \frac{1}{4}\left(\overline{\underline{f}}_{\alpha\beta 1} + \overline{\underline{f}}_{\alpha\beta 2} e^{j\frac{\pi}{2}} + \overline{\underline{f}}_{\alpha\beta 3} e^{j\pi} + \overline{\underline{f}}_{\alpha\beta 4} e^{j\frac{3\pi}{2}}\right) \\ \underline{f}_{xy2} = \frac{1}{4}\left(\underline{f}_{\alpha\beta 1} + \underline{f}_{\alpha\beta 2} e^{j\frac{\pi}{2}} + \underline{f}_{\alpha\beta 3} e^{j\pi} + \underline{f}_{\alpha\beta 4} e^{j\frac{3\pi}{2}}\right) \\ \underline{f}_{xy3} = \frac{1}{4}\left(\overline{\underline{f}}_{\alpha\beta 1} + \overline{\underline{f}}_{\alpha\beta 2} e^{j\pi} + \overline{\underline{f}}_{\alpha\beta 3} + \overline{\underline{f}}_{\alpha\beta 4} e^{j\pi}\right) \\ \underline{f}_{xy4} = \frac{1}{2}\left(f_{z1} + f_{z2} e^{j\frac{\pi}{2}} + f_{z3} e^{j\pi} + f_{z4} e^{j\frac{3\pi}{2}}\right) \\ f_{z+} = \frac{1}{4}\left(f_{z1} + f_{z2} + f_{z3} + f_{z4}\right) \\ f_{z-} = \frac{1}{4}\left(f_{z1} + f_{z2} e^{j\pi} + f_{z3} + f_{z4} e^{j\pi}\right) \end{bmatrix} \tag{4.56}$$

$$\begin{bmatrix} f_{\alpha} \\ f_{\beta} \\ f_{x1} \\ f_{y1} \\ f_{x2} \\ f_{y2} \\ f_{x3} \\ f_{y3} \\ f_{x4} \\ f_{y4} \\ f_{x5} \\ f_{y5} \end{bmatrix} = \frac{1}{4} \begin{bmatrix} f_{\alpha 1} + f_{\alpha 2} + f_{\alpha 3} + f_{\alpha 4} \\ f_{\beta 1} + f_{\beta 2} + f_{\beta 3} + f_{\beta 4} \\ f_{\alpha 1} - f_{\alpha 3} + f_{\beta 2} - f_{\beta 4} \\ f_{\alpha 2} - f_{\alpha 4} - f_{\beta 1} + f_{\beta 3} \\ f_{\alpha 1} - f_{\alpha 3} - f_{\beta 2} + f_{\beta 4} \\ f_{\alpha 2} - f_{\alpha 4} + f_{\beta 1} - f_{\beta 3} \\ f_{\alpha 1} - f_{\alpha 2} + f_{\alpha 3} - f_{\alpha 4} \\ -f_{\beta 1} + f_{\beta 2} - f_{\beta 3} + f_{\beta 4} \\ 2f_{z1} + \sqrt{2} f_{z2} - \sqrt{2} f_{z4} \\ \sqrt{2} f_{z2} + 2f_{z3} + \sqrt{2} f_{z4} \\ 2f_{z1} - \sqrt{2} f_{z2} + \sqrt{2} f_{z4} \\ \sqrt{2} f_{z2} - 2f_{z3} + \sqrt{2} f_{z4} \end{bmatrix} \Rightarrow \begin{bmatrix} \underline{f}_{\alpha\beta} = \frac{1}{4}\left(\underline{f}_{\alpha\beta 1} + \underline{f}_{\alpha\beta 2} + \underline{f}_{\alpha\beta 3} + \underline{f}_{\alpha\beta 4}\right) \\ \underline{f}_{xy1} = \frac{1}{4}\left(\overline{\underline{f}}_{\alpha\beta 1} + \overline{\underline{f}}_{\alpha\beta 2} e^{j\frac{\pi}{2}} + \overline{\underline{f}}_{\alpha\beta 3} e^{j\pi} + \overline{\underline{f}}_{\alpha\beta 4} e^{j\frac{3\pi}{2}}\right) \\ \underline{f}_{xy2} = \frac{1}{4}\left(\underline{f}_{\alpha\beta 1} + \underline{f}_{\alpha\beta 2} e^{j\frac{\pi}{2}} + \underline{f}_{\alpha\beta 3} e^{j\pi} + \underline{f}_{\alpha\beta 4} e^{j\frac{3\pi}{2}}\right) \\ \underline{f}_{xy3} = \frac{1}{4}\left(\overline{\underline{f}}_{\alpha\beta 1} + \overline{\underline{f}}_{\alpha\beta 2} e^{j\pi} + \overline{\underline{f}}_{\alpha\beta 3} + \overline{\underline{f}}_{\alpha\beta 4} e^{j\pi}\right) \\ \underline{f}_{xy4} = \frac{1}{2}\left(f_{z1} + f_{z2} e^{j\frac{\pi}{4}} + f_{z3} e^{j\frac{\pi}{2}} + f_{z4} e^{j\frac{3\pi}{4}}\right) \\ \underline{f}_{xy4} = \frac{1}{2}\left(f_{z1} + f_{z2} e^{j\frac{3\pi}{4}} + f_{z3} e^{j\frac{3\pi}{2}} + f_{z4} e^{j\frac{\pi}{4}}\right) \end{bmatrix} \tag{4.57}$$

Due to the size of the equations, correlation between VSD and MS variables for the 15-phase case is given only in complex form. In the case of symmetrical and asymmetrical configurations, relationships are as follows:

$$\begin{bmatrix} \underline{f}_{\alpha\beta} = \frac{1}{5}\left(\underline{f}_{\alpha\beta 1} + \underline{f}_{\alpha\beta 2} + \underline{f}_{\alpha\beta 3} + \underline{f}_{\alpha\beta 4} + \underline{f}_{\alpha\beta 5}\right) \\ \underline{f}_{xy1} = \frac{1}{5}\left(\overline{\underline{f}}_{\alpha\beta 1} + \overline{\underline{f}}_{\alpha\beta 2} e^{j\frac{2\pi}{5}} + \overline{\underline{f}}_{\alpha\beta 3} e^{j\frac{4\pi}{5}} + \overline{\underline{f}}_{\alpha\beta 4} e^{j\frac{6\pi}{5}} + \overline{\underline{f}}_{\alpha\beta 5} e^{j\frac{8\pi}{5}}\right) \\ \underline{f}_{xy2} = \frac{1}{5}\left(\underline{f}_{\alpha\beta 1} + \underline{f}_{\alpha\beta 2} e^{j\frac{2\pi}{5}} + \underline{f}_{\alpha\beta 3} e^{j\frac{4\pi}{5}} + \underline{f}_{\alpha\beta 4} e^{j\frac{6\pi}{5}} + \underline{f}_{\alpha\beta 5} e^{j\frac{8\pi}{5}}\right) \\ \underline{f}_{xy3} = \frac{1}{5}\left(\overline{\underline{f}}_{\alpha\beta 1} + \overline{\underline{f}}_{\alpha\beta 2} e^{j\frac{4\pi}{5}} + \overline{\underline{f}}_{\alpha\beta 3} e^{j\frac{8\pi}{5}} + \overline{\underline{f}}_{\alpha\beta 4} e^{j\frac{2\pi}{5}} + \overline{\underline{f}}_{\alpha\beta 5} e^{j\frac{6\pi}{5}}\right) \\ \underline{f}_{xy4} = \frac{1}{5}\left(\underline{f}_{\alpha\beta 1} + \underline{f}_{\alpha\beta 2} e^{j\frac{4\pi}{5}} + \underline{f}_{\alpha\beta 3} e^{j\frac{8\pi}{5}} + \underline{f}_{\alpha\beta 4} e^{j\frac{2\pi}{5}} + \underline{f}_{\alpha\beta 5} e^{j\frac{6\pi}{5}}\right) \\ \underline{f}_{xy5} = \frac{2}{5}\left(f_{z1} + f_{z2} e^{j\frac{2\pi}{5}} + f_{z3} e^{j\frac{4\pi}{5}} + f_{z4} e^{j\frac{6\pi}{5}} + f_{z5} e^{j\frac{8\pi}{5}}\right) \\ \underline{f}_{xy6} = \frac{2}{5}\left(f_{z1} + f_{z2} e^{j\frac{4\pi}{5}} + f_{z3} e^{j\frac{8\pi}{5}} + f_{z4} e^{j\frac{2\pi}{5}} + f_{z5} e^{j\frac{6\pi}{5}}\right) \\ f_{z+} = \frac{1}{5}\left(f_{z1} + f_{z2} + f_{z3} + f_{z4} + f_{z5}\right) \end{bmatrix} \tag{4.58}$$

$$\begin{bmatrix}
\underline{f}_{\alpha\beta} = \frac{1}{5}\left(\underline{f}_{\alpha\beta1} + \underline{f}_{\alpha\beta2} + \underline{f}_{\alpha\beta3} + \underline{f}_{\alpha\beta4} + \underline{f}_{\alpha\beta5}\right) \\
\underline{f}_{xy1} = \frac{1}{5}\left(\overline{\underline{f}}_{\alpha\beta1} + \overline{\underline{f}}_{\alpha\beta2}e^{j\frac{2\pi}{5}} + \overline{\underline{f}}_{\alpha\beta3}e^{j\frac{4\pi}{5}} + \overline{\underline{f}}_{\alpha\beta4}e^{j\frac{6\pi}{5}} + \overline{\underline{f}}_{\alpha\beta5}e^{j\frac{8\pi}{5}}\right) \\
\underline{f}_{xy2} = \frac{1}{5}\left(\underline{f}_{\alpha\beta1} + \underline{f}_{\alpha\beta2}e^{j\frac{2\pi}{5}} + \underline{f}_{\alpha\beta3}e^{j\frac{4\pi}{5}} + \underline{f}_{\alpha\beta4}e^{j\frac{6\pi}{5}} + \underline{f}_{\alpha\beta5}e^{j\frac{8\pi}{5}}\right) \\
\underline{f}_{xy3} = \frac{1}{5}\left(\overline{\underline{f}}_{\alpha\beta1} + \overline{\underline{f}}_{\alpha\beta2}e^{j\frac{4\pi}{5}} + \overline{\underline{f}}_{\alpha\beta3}e^{j\frac{8\pi}{5}} + \overline{\underline{f}}_{\alpha\beta4}e^{j\frac{2\pi}{5}} + \overline{\underline{f}}_{\alpha\beta5}e^{j\frac{6\pi}{5}}\right) \\
\underline{f}_{xy4} = \frac{1}{5}\left(\underline{f}_{\alpha\beta1} + \underline{f}_{\alpha\beta2}e^{j\frac{4\pi}{5}} + \underline{f}_{\alpha\beta3}e^{j\frac{8\pi}{5}} + \underline{f}_{\alpha\beta4}e^{j\frac{2\pi}{5}} + \underline{f}_{\alpha\beta5}e^{j\frac{6\pi}{5}}\right) \\
\underline{f}_{xy5} = \frac{2}{5}\left(f_{z1} + f_{z2}e^{j\frac{\pi}{5}} + f_{z3}e^{j\frac{2\pi}{5}} + f_{z4}e^{j\frac{3\pi}{5}} + f_{z5}e^{j\frac{4\pi}{5}}\right) \\
\underline{f}_{xy6} = \frac{2}{5}\left(f_{z1} + f_{z2}e^{j\frac{3\pi}{5}} + f_{z3}e^{j\frac{6\pi}{5}} + f_{z4}e^{j\frac{9\pi}{5}} + f_{z5}e^{j\frac{2\pi}{5}}\right) \\
f_{z+} = \frac{1}{5}\left(f_{z1} + f_{z2}e^{j\pi} + f_{z3} + f_{z4}e^{j\pi} + f_{z5}\right)
\end{bmatrix} \tag{4.59}$$

Even though 18-phase machines are seldomly used and literature on the subject is scarce [Andresen and Birk (2007)], for the sake of completeness, relationship between MS and VSD variables is given as well and is as follows:

$$\begin{bmatrix}
\underline{f}_{\alpha\beta} = \frac{1}{6}\left(\underline{f}_{\alpha\beta1} + \underline{f}_{\alpha\beta2} + \underline{f}_{\alpha\beta3} + \underline{f}_{\alpha\beta4} + \underline{f}_{\alpha\beta5} + \underline{f}_{\alpha\beta6}\right) \\
\underline{f}_{xy1} = \frac{1}{6}\left(\overline{\underline{f}}_{\alpha\beta1} + \overline{\underline{f}}_{\alpha\beta2}e^{j\frac{\pi}{3}} + \overline{\underline{f}}_{\alpha\beta3}e^{j\frac{2\pi}{3}} + \overline{\underline{f}}_{\alpha\beta4}e^{j\pi} + \overline{\underline{f}}_{\alpha\beta5}e^{j\frac{4\pi}{3}} + \overline{\underline{f}}_{\alpha\beta6}e^{j\frac{5\pi}{3}}\right) \\
\underline{f}_{xy2} = \frac{1}{6}\left(\underline{f}_{\alpha\beta1} + \underline{f}_{\alpha\beta2}e^{j\frac{\pi}{3}} + \underline{f}_{\alpha\beta3}e^{j\frac{2\pi}{3}} + \underline{f}_{\alpha\beta4}e^{j\pi} + \underline{f}_{\alpha\beta5}e^{j\frac{4\pi}{3}} + \underline{f}_{\alpha\beta5}e^{j\frac{5\pi}{3}}\right) \\
\underline{f}_{xy3} = \frac{1}{6}\left(\overline{\underline{f}}_{\alpha\beta1} + \overline{\underline{f}}_{\alpha\beta2}e^{j\frac{2\pi}{3}} + \overline{\underline{f}}_{\alpha\beta3}e^{j\frac{4\pi}{3}} + \overline{\underline{f}}_{\alpha\beta4} + \overline{\underline{f}}_{\alpha\beta5}e^{j\frac{2\pi}{3}} + \overline{\underline{f}}_{\alpha\beta6}e^{j\frac{4\pi}{3}}\right) \\
\underline{f}_{xy4} = \frac{1}{6}\left(\underline{f}_{\alpha\beta1} + \underline{f}_{\alpha\beta2}e^{j\frac{2\pi}{3}} + \underline{f}_{\alpha\beta3}e^{j\frac{4\pi}{3}} + \underline{f}_{\alpha\beta4} + \underline{f}_{\alpha\beta5}e^{j\frac{2\pi}{3}} + \underline{f}_{\alpha\beta5}e^{j\frac{4\pi}{3}}\right) \\
\underline{f}_{xy5} = \frac{1}{6}\left(\overline{\underline{f}}_{\alpha\beta1} + \overline{\underline{f}}_{\alpha\beta2}e^{j\pi} + \overline{\underline{f}}_{\alpha\beta3} + \overline{\underline{f}}_{\alpha\beta4}e^{j\pi} + \overline{\underline{f}}_{\alpha\beta5} + \overline{\underline{f}}_{\alpha\beta6}e^{j\pi}\right) \\
\underline{f}_{xy6} = \frac{1}{3}\left(f_{z1} + f_{z2}e^{j\frac{\pi}{3}} + f_{z3}e^{j\frac{2\pi}{3}} + f_{z4}e^{j\pi} + f_{z5}e^{j\frac{4\pi}{3}} + f_{z6}e^{j\frac{5\pi}{3}}\right) \\
\underline{f}_{xy7} = \frac{1}{3}\left(f_{z1} + f_{z2}e^{j\frac{2\pi}{3}} + f_{z3}e^{j\frac{4\pi}{3}} + f_{z4} + f_{z5}e^{j\frac{2\pi}{3}} + f_{z6}e^{j\frac{4\pi}{3}}\right) \\
\underline{f}_{z+} = \frac{1}{3}\left(f_{z1} + f_{z2} + f_{z3} + f_{z4} + f_{z5} + f_{z6}\right) \\
\underline{f}_{z-} = \frac{1}{3}\left(f_{z1} + f_{z2}e^{j\pi} + f_{z3} + f_{z4}e^{j\pi} + f_{z5} + f_{z6}e^{j\pi}\right)
\end{bmatrix} \tag{4.60}$$

$$\begin{bmatrix}
\underline{f}_{\alpha\beta} = \frac{1}{6}\left(\underline{f}_{\alpha\beta1} + \underline{f}_{\alpha\beta2} + \underline{f}_{\alpha\beta3} + \underline{f}_{\alpha\beta4} + \underline{f}_{\alpha\beta5} + \underline{f}_{\alpha\beta6}\right) \\
\underline{f}_{xy1} = \frac{1}{6}\left(\overline{\underline{f}}_{\alpha\beta1} + \overline{\underline{f}}_{\alpha\beta2}e^{j\frac{\pi}{3}} + \overline{\underline{f}}_{\alpha\beta3}e^{j\frac{2\pi}{3}} + \overline{\underline{f}}_{\alpha\beta4}e^{j\pi} + \overline{\underline{f}}_{\alpha\beta5}e^{j\frac{4\pi}{3}} + \overline{\underline{f}}_{\alpha\beta6}e^{j\frac{5\pi}{3}}\right) \\
\underline{f}_{xy2} = \frac{1}{6}\left(\underline{f}_{\alpha\beta1} + \underline{f}_{\alpha\beta2}e^{j\frac{\pi}{3}} + \underline{f}_{\alpha\beta3}e^{j\frac{2\pi}{3}} + \underline{f}_{\alpha\beta4}e^{j\pi} + \underline{f}_{\alpha\beta5}e^{j\frac{4\pi}{3}} + \underline{f}_{\alpha\beta5}e^{j\frac{5\pi}{3}}\right) \\
\underline{f}_{xy3} = \frac{1}{6}\left(\overline{\underline{f}}_{\alpha\beta1} + \overline{\underline{f}}_{\alpha\beta2}e^{j\frac{2\pi}{3}} + \overline{\underline{f}}_{\alpha\beta3}e^{j\frac{4\pi}{3}} + \overline{\underline{f}}_{\alpha\beta4} + \overline{\underline{f}}_{\alpha\beta5}e^{j\frac{2\pi}{3}} + \overline{\underline{f}}_{\alpha\beta6}e^{j\frac{4\pi}{3}}\right) \\
\underline{f}_{xy4} = \frac{1}{6}\left(\underline{f}_{\alpha\beta1} + \underline{f}_{\alpha\beta2}e^{j\frac{2\pi}{3}} + \underline{f}_{\alpha\beta3}e^{j\frac{4\pi}{3}} + \underline{f}_{\alpha\beta4} + \underline{f}_{\alpha\beta5}e^{j\frac{2\pi}{3}} + \underline{f}_{\alpha\beta5}e^{j\frac{4\pi}{3}}\right) \\
\underline{f}_{xy5} = \frac{1}{6}\left(\overline{\underline{f}}_{\alpha\beta1} + \overline{\underline{f}}_{\alpha\beta2}e^{j\pi} + \overline{\underline{f}}_{\alpha\beta3} + \overline{\underline{f}}_{\alpha\beta4}e^{j\pi} + \overline{\underline{f}}_{\alpha\beta5} + \overline{\underline{f}}_{\alpha\beta6}e^{j\pi}\right) \\
\underline{f}_{xy6} = \frac{1}{3}\left(f_{z1} + f_{z2}e^{j\frac{\pi}{6}} + f_{z3}e^{j\frac{\pi}{3}} + f_{z4}e^{j\frac{\pi}{2}} + f_{z5}e^{j\frac{2\pi}{3}} + f_{z6}e^{j\frac{5\pi}{6}}\right) \\
\underline{f}_{xy7} = \frac{1}{3}\left(f_{z1} + f_{z2}e^{j\frac{\pi}{2}} + f_{z3}e^{j\pi} + f_{z4}e^{j\frac{3\pi}{2}} + f_{z5} + f_{z6}e^{j\frac{\pi}{2}}\right) \\
\underline{f}_{xy8} = \frac{1}{3}\left(f_{z1} + f_{z2}e^{j\frac{5\pi}{6}} + f_{z3}e^{j\frac{5\pi}{3}} + f_{z4}e^{j\frac{\pi}{2}} + f_{z5}e^{j\frac{4\pi}{3}} + f_{z6}e^{j\frac{\pi}{6}}\right)
\end{bmatrix} \tag{4.61}$$

By analysing all of the discussed cases, it is quite obvious that correlation between MS and VSD variables in the first l subspaces is identical in each particular case and valid for all possible topologies (symmetrical/asymmetrical with single/multiple neutral points). Furthermore, flux/torque producing currents are mapped here, hence power transfer can be produced by only considering these subspaces. In a general case, relationship between MS and VSD variables for the first l subspaces (flux/torque producing ones) is as follows:

$$\begin{aligned}
\underline{f}_{\alpha\beta} &= \frac{1}{l}\sum_{i=1}^{l} \underline{f}_{\alpha\beta i} \\
\underline{f}_{xy_{ss}} &= \begin{cases} \dfrac{1}{l}\displaystyle\sum_{i=1}^{l} \overline{\underline{f}}_{\alpha\beta i}\, e^{j(ss+1)(i-1)\frac{\pi}{l}}, & ss = 1,3,5,\ldots \\ \dfrac{1}{l}\displaystyle\sum_{i=1}^{l} \underline{f}_{\alpha\beta i}\, e^{jss(i-1)\frac{\pi}{l}}, & ss = 2,4,6,\ldots \end{cases}
\end{aligned} \tag{4.62}$$

If a machine is with multiple neutral points, zero-sequence currents cannot flow and (4.62) completely defines the relationship between MS and VSD variables. On the other hand, if a machine is with single neutral point, then the zero-sequence subspaces and homopolar components must be considered as well. Even though there is no power transfer in these subspaces, they should be included in analysis since they can be utilised to implement a fault-tolerant operation. By examining (4.52) – (4.61), relationship between MS zero-sequence variables (f_{z1}, f_{z2}, …) and VSD zero-sequence subspaces and/or homopolar components (f_{xy}, f_{z+}, f_{z-}) is as follow:

$$\begin{aligned}
&\left\{ \begin{aligned} \underline{f}_{xy_{ss}} &= \frac{2}{l}\sum_{i=1}^{l} f_{zi}\, e^{j2(ss-l+1)(i-1)\frac{\pi}{l}} \\ f_{z+} &= \frac{1}{l}\sum_{i=1}^{l} f_{zi}\cos\left((i-1)2\pi\right) \\ f_{z-} &= \frac{1}{l}\sum_{i=1}^{l} f_{zi}\cos\left((i-1)\pi\right) \end{aligned} \right\} \quad \textit{symmetrical} \\
&\left\{ \begin{aligned} \underline{f}_{xy_{ss}} &= \frac{2}{l}\sum_{i=1}^{l} f_{zi}\, e^{j(2(ss-l)+1)(i-1)\frac{\pi}{l}} \\ f_{z+} &= \frac{1}{l}\sum_{i=1}^{l} f_{zi}\cos\left((i-1)\pi\right) \end{aligned} \right\} \quad \textit{asymmetrical}
\end{aligned} \tag{4.63}$$

Equations (4.62) and (4.63) provide the relationship between VSD and MS variables for multiple 3-phase machines in general case. They are applicable to any machine configuration, i.e. symmetrical or asymmetrical with single or multiple neutral points. Equation (4.63) can be omitted in the case of multiple neutral points. Moreover, the discussion presented in this section is based only on transformation matrices, hence it is irrelevant whether the machine is induction or of a synchronous type – the presented equations are still valid. Of course, in order for equations to be valid, VSD matrix needs to be created as explained in section 4.4.1 of this chapter. Validity of the developed equations is verified by the Wolfram Mathematica software, where the code is available in Appendix A of the thesis.

The presented relationships are used later on in the thesis to implement control of induction 9-phase machine by use of VSD variables, while still being able to control flux and torque production in each winding set, a feature usually available only when a machine is controlled in MS variables.

4.6 Phase Voltage Harmonic Imbalance in Asymmetrical Multiphase Machines with Single Neutral Point

Until now, this chapter has exclusively dealt with different modelling approaches of multiphase induction machines and relationship between them. However, it is noticed that when asymmetrical configurations with single neutral points are used there is an imbalance in certain phase voltage harmonics, a phenomenon which has not been explored in the past. Therefore, this section deals with harmonic imbalance in the phase voltages that appear in almost all asymmetrical machines with single neutral point. Yet, imbalance in the phase voltage harmonics does not appear in asymmetrical 6-phase machines, which have been by far the most frequent subject of study in the multiphase drive area. Indeed, such an imbalance does not take place as long as the complete winding consists of only two sub-windings.

It is shown that balanced low-order leg voltage harmonics, usually present in high power multiphase drives with low PWM switching frequency, can produce unbalanced phase voltage harmonics in the case of the asymmetrical machines with a single neutral point. Unequal phase voltage harmonics may lead to unequal thermal losses among phases and uneven stress on the switching devices, which should be taken into consideration during the drive design stage. Starting from the analysis of the neutral point voltage harmonics, analytical expressions for phase voltage harmonics are provided and verified by simulations and experiments. The developed theory is general and it covers all cases of the asymmetrical machines with a single neutral point. The appearance of phase voltage harmonic imbalance requires existence of at least three sub-windings in the stator winding, as it will be shown in the following considerations.

Asymmetrical machine phase propagation angles and order of phases are the same as defined in equations (4.1) – (4.2) and Fig. 4.1b. It is assumed that when the machine is inverter supplied, leg voltages may contain harmonics. All leg voltage harmonics of the given harmonic order are considered balanced, i.e. they have the same amplitude in each leg. Moreover, all harmonics of the leg 1 are taken as being in phase, with maximum value at time instant zero. Hence, by using (4.2), leg voltages for the harmonic order h have amplitude A_h and are defined as:

$$v_{j,i,h}^{\text{leg}}(t) = A_h \cos\left(h\left(\omega t + \frac{\pi}{n}\left(2l(i-1)+j-1\right)\right)\right),\ j=1,2,...,l,\ i=1,2,...,k \tag{4.64}$$

The fundamental is of course the first harmonic. Without loss of generality, harmonic order h is a positive integer. Firstly, the neutral point voltage is analysed, and afterwards the expression for phase voltages is developed. In what follows it is assumed that the machine phases are balanced, so the impedance of every phase is the same.

The single neutral point voltage is found by firstly establishing the neutral point voltage of each sub-winding. From (4.64), the neutral point voltage for the harmonic order h of the winding set j can be found as a sum of all leg voltages of that sub-winding, divided with the number of phases in the sub-winding:

$$v_{j,h}^{\mathrm{NP}}(t)=\frac{1}{k}\sum_{i=1}^{k}\left\{A_h\cos\left(h\left(\omega t+\frac{\pi}{n}\left(2l(i-1)+j-1\right)\right)\right)\right\} \tag{4.65}$$

After expanding (4.65) and applying trigonometric identities, a simplified expression is obtained:

$$v_{j,h}^{\mathrm{NP}}(t)=\frac{A_h}{k}\cos\left(h\left(\omega t+\frac{\pi}{n}(j-1)\right)\right)\sum_{i=1}^{k}\cos\left((i-1)\frac{h}{k}2\pi\right) \tag{4.66}$$

The summands in summation of (4.66) yield zero when the harmonic order is not an integer multiple of the number of phases in the sub-winding, k. Otherwise the summation is equal to k. Therefore, neutral point voltage for the harmonic order h of the sub-winding j is defined as:

$$v_{j,h}^{\mathrm{NP}}(t)=\left\{\begin{matrix}A_h\cos\left(h\left(\omega t+\frac{\pi}{n}(j-1)\right)\right), & h=h_n k\\ 0, & h\neq h_n k\end{matrix}\right\},\ h_n=1,2,\ldots \tag{4.67}$$

Here the newly introduced variable $h_n = h/k$ represents the normalised harmonic order. This is introduced to simplify the equations that follow and provide a tool for derivation of the phase voltage harmonics in the general case.

Finding the value of the single neutral point voltage for the harmonic order h is achieved by summing the values of individual neutral point voltages of each sub-winding (4.67) and dividing the result with the number of sub-windings l. Since harmonics of the order $h \neq h_{nk}$ cannot exist in any neutral point voltage of the sub-windings, they also do not exist in the single neutral point voltage. Keeping in mind that in this analysis the phase voltage is defined as a difference between leg and single neutral point voltage, it follows that leg and phase voltage harmonics are identical for the cases where $h \neq h_{nk}$. Consequently, there is no unbalance and these cases are omitted from further analysis.

Hence the single neutral point voltage harmonics are given with:

$$v_h^{\mathrm{NP}}(t)=\frac{1}{l}\sum_{j=1}^{l}A_h\cos\left(kh_n\left(\omega t+\frac{\pi}{n}(j-1)\right)\right) \tag{4.68}$$

When the sum of cosine functions in (4.68) is calculated the neutral point voltage for the harmonic order h is defined as follows:

$$v_h^{\mathrm{NP}}(t)=\frac{A_h}{l}\frac{\sin\left(h_n\frac{\pi}{2}\right)}{\sin\left(h_n\frac{\pi}{2l}\right)}\cos\left(kh_n\left(\omega t+(l-1)\frac{\pi}{2n}\right)\right) \tag{4.69}$$

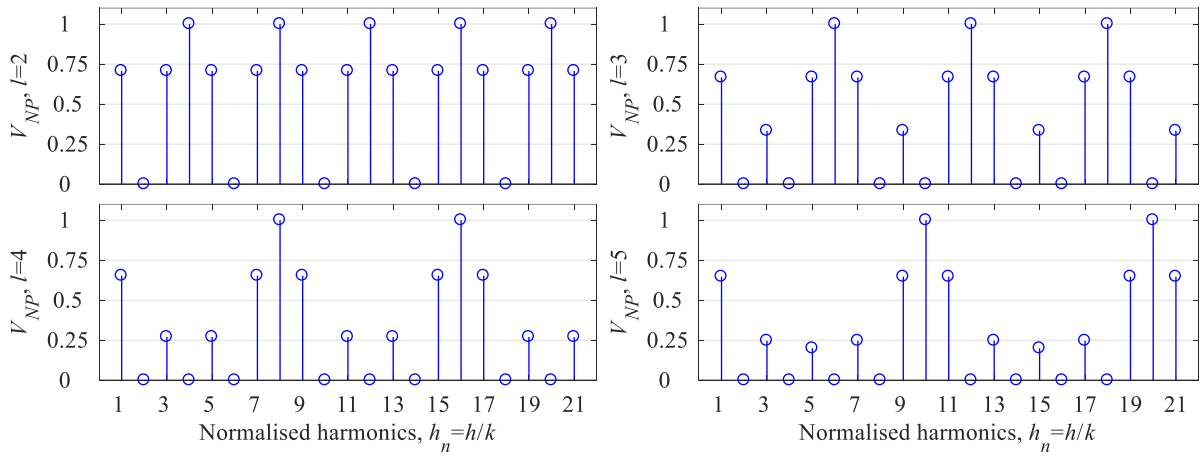

Figure 4.18 – Amplitudes of the neutral point voltage normalised harmonics for the machines with 2, 3, 4, and 5 winding sets.

When the phase angle in the expression (4.69) is divided by the harmonic order ($h = kh_n$) and compared with phase disposition angles, given in Fig. 4.1b, it can be seen that it is always equal to the half of the phase disposition angle of the first phase in the last sub-winding $(l\text{-}1)\pi/n$. This fact will be used later to show the source and nature of the unbalance in the phase voltage harmonics.

Expression (4.69) also shows that the amplitudes of the neutral point voltage normalised harmonics are not dependant on the number of phases in the sub-winding. This means that every normalised neutral point voltage harmonic $h_n = h/k$ has the same amplitude for any asymmetrical machine with a single neutral point that has the same number of sub-windings (l). Visualisation of the neutral point voltage normalised harmonic (h_n) amplitudes in the case of the machines with 2, 3, 4, and 5 sub-windings is shown in Fig. 4.18 (all values are per-unit).

For the sake of clarity, an example can be made by comparing the 9-phase ($k = 3$, $l = 3$) and the 15-phase ($k = 5$, $l = 3$) machines, plots on the right hand side in Fig. 4.18. For example, cases of the 1st and the 3rd normalised harmonics ($h_n = h/k$) are the 3rd and the 9th harmonics of the 9-phase machine, while in the 15-phase case they are the 5th and the 15th harmonics. Since both machines have the same number of sub-windings, their normalised harmonics are the same. Therefore, the 3rd harmonic of the 9-phase machine has the same amplitude as the 5th harmonic of the 15-phase machine. The same applies for the 9th and the 15th harmonics of the 9-phase and 15-phase machines, respectively.

Even-order normalised harmonics of the neutral point voltage are always zero, so there is no imbalance in phase voltage even-order harmonics whatsoever. Therefore, they are not considered any further. It should be pointed out that (4.69) will become limit equation when h_n becomes integer multiple of 2l. One way of solving this is to use L'Hôpital's rule, so instead of $\sin(\pm\pi)$, $\cos(\pm\pi)$ is obtained.

Now, the phase voltage can be calculated as a difference between leg voltage (4.64) and neutral point voltage (4.69) as follows:

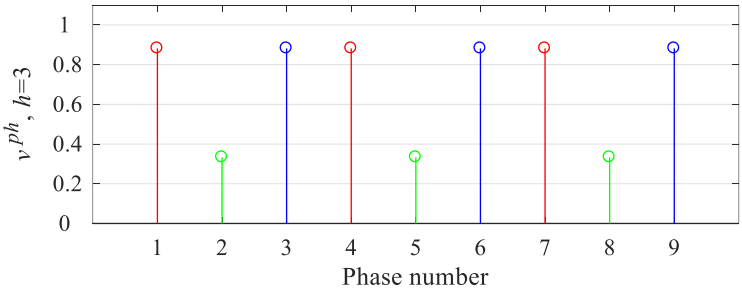

Figure 4.19 – The 3rd harmonic phase voltage amplitudes of the asymmetrical 9-phase machine with a single neutral point.

$$v_{j,i,h}^{\text{phase}}(t) = A_h \cos\left(kh_n\left(\omega t + \frac{\pi}{n}\left(2l(i-1) + j - 1\right)\right)\right) - \frac{A_h}{l}\frac{\sin\left(h_n\frac{\pi}{2}\right)}{\sin\left(h_n\frac{\pi}{2l}\right)}\cos\left(kh_n\left(\omega t + (l-1)\frac{\pi}{2n}\right)\right) \tag{4.70}$$

When (4.70) is simplified and h_n is replaced by h/k, the expressions for amplitude and phase of the phase voltage harmonics become as follows:

$$A_{j,i,h}^{\text{phase}} = A_h\sqrt{1 + \left(\frac{1}{l}\frac{\sin\left(h\frac{\pi}{2k}\right)}{\sin\left(h\frac{\pi}{2n}\right)}\right)^2 - \frac{2}{l}\frac{\sin\left(h\frac{\pi}{2k}\right)}{\sin\left(h\frac{\pi}{2n}\right)}\cos\left(\frac{h}{n}j\pi + \frac{h}{k}i\,2\pi - \frac{h(5l+1)}{2n}\pi\right)} \tag{4.71}$$

$$\theta_{j,i,h}^{\text{phase}} = \text{atan2}\left\{\frac{\frac{\sin\left(h\frac{\pi}{2k}\right)}{\sin\left(h\frac{\pi}{2n}\right)}\sin\left(h\frac{\pi}{2n}(l-1)\right) - l\sin\left(h\frac{\pi}{n}(2l(i-1)+j-1)\right)}{\frac{\sin\left(h\frac{\pi}{2k}\right)}{\sin\left(h\frac{\pi}{2n}\right)}\cos\left(h\frac{\pi}{2n}(l-1)\right) - l\cos\left(h\frac{\pi}{n}(2l(i-1)+j-1)\right)}\right\} + \pi \tag{4.72}$$

where, again, j and i designate the sub-winding and the phase within that sub-winding, respectively. When the expression for phase voltage amplitude (4.71) is analysed, it can be seen that all phases within one sub-winding have the same amplitude of the given voltage harmonic (because i is multiplied by 2π, which is the period of the cosine function). On the other hand, voltage harmonic amplitudes of the phases in different sub-windings are different.

For the sake of clarity, this is demonstrated using the example of the 9-phase machine. Per-unit amplitudes of phase voltage 3rd harmonic, normalised with the amplitude of the leg voltage 3rd harmonic, are shown in Fig. 4.19. As expected, amplitudes of the 3rd harmonic of the phase voltages within each sub-winding are the same. On the other hand, there is a difference between phases of different sub-windings. Amplitudes of the 3rd harmonic of the phase voltages of the second sub-winding (2nd, 5th, and 8th phase) are different from the ones of the first sub-winding (1st, 4th, and 7th phase). As previously mentioned, this behaviour is easily explained when the phase angle of the neutral point voltage harmonics (4.69) is taken into consideration.

In the neutral point harmonic analysis, it has been shown that when the phase angle of the neutral point voltage is divided by the harmonic order, it is always equal to half of the phase shift angle of the

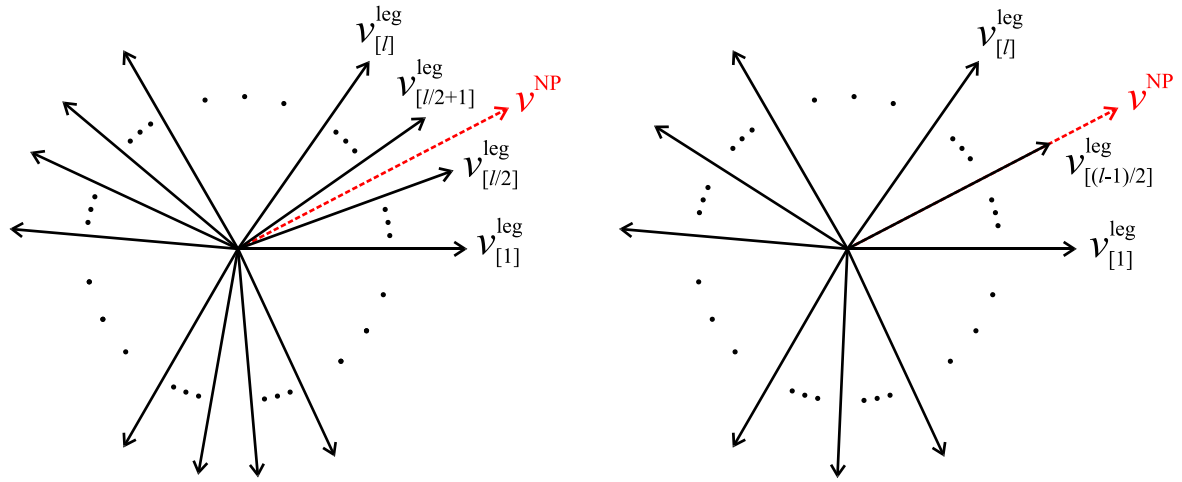

Figure 4.20 – Influence of the neutral point voltage on the phase voltages in the case of the even (a) and odd (b) number of winding sets.

first phase in the last sub-winding. Hence, the neutral point voltage is always positioned in the middle of the first group of the leg voltages, as shown schematically in Fig. 4.20. In this figure phase angles of the leg voltages are divided by the harmonic order; thus this analysis holds true for all harmonic orders.

The phase voltages are calculated as a difference between leg voltages and neutral point voltage. It can be seen that leg voltages are located at an equal angular distance from the neutral point voltage. Therefore, the corresponding phase voltages are equally influenced by the neutral point voltage and so have the same amplitude. In the case of the even number of sub-windings, Fig. 4.20a, each two pairs of the phase voltages have the same amplitude. On the other hand, in the case of the odd number of sub-windings, Fig. 4.20b, neutral point voltage coincides with one of the leg voltages, i.e. with (l-1)/2.

As stated before, phase voltage harmonics of the same order in one sub-winding have the same amplitude. Hence, the number of phases per sub-winding is irrelevant for the analysis. Consequently, only the first phases of all the sub-windings will be analysed, while the 2nd, 3rd, or any other phase in the sub-winding has the same amplitude of the considered phase voltage harmonic.

Amplitudes of the first five odd normalised phase voltage harmonics in the case of the machines with 2, 3, 4, and 5 sub-windings are given in Fig. 4.21. In the ideal case with a symmetrical supply, even harmonics do not exist. If even harmonics are present they are balanced and their amplitude is equal to zero or to the amplitude of the corresponding leg voltage harmonics. Hence, they are not of interest in the analysis and are omitted from Fig. 4.21.

Looking at Fig. 4.21, it can be seen that for the same number of sub-windings l, phase voltage harmonic unbalance is symmetrical around the imaginary line l/2 (dashed red line). If the line coincides with a phase number, l is odd and phase voltage harmonic amplitude of that phase has a unique value, while phase voltage harmonic amplitudes of the other phases are the same if they are at the same distance from l/2. Alternatively, if the line l/2 is between two phases, l is even and then phases equidistant from the line l/2 have the same value of the phase voltage harmonic amplitudes.

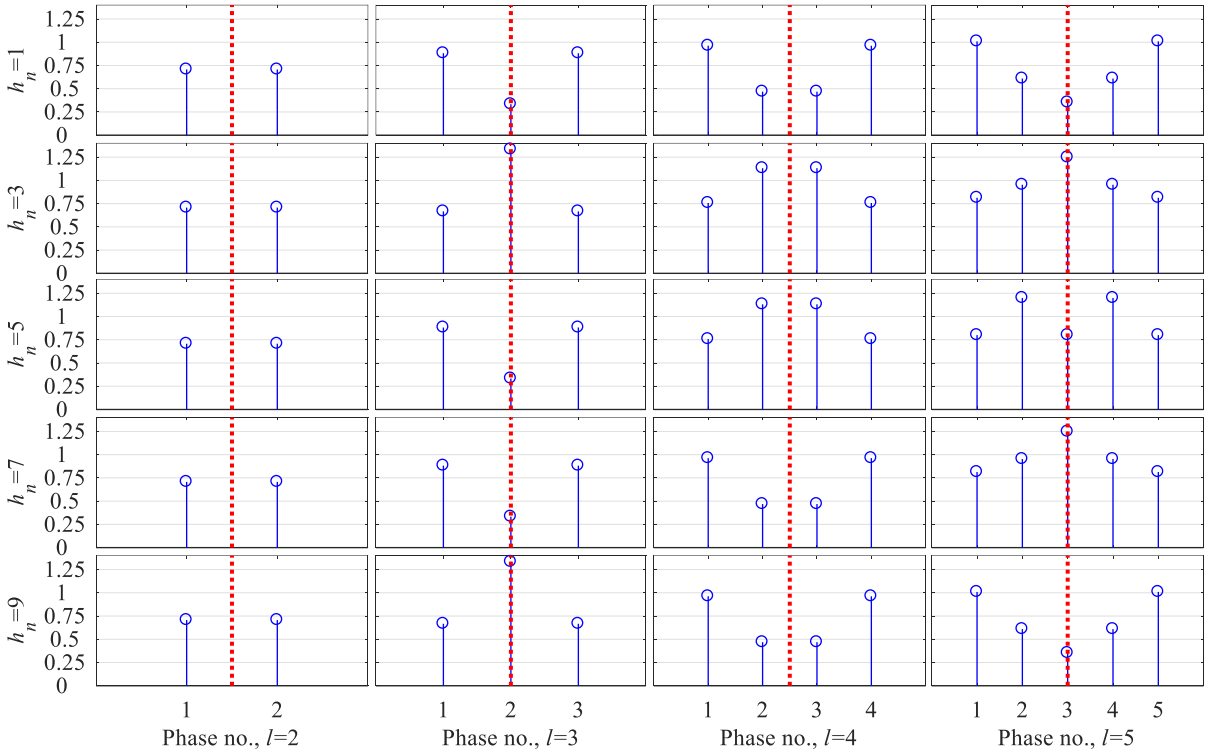

Figure 4.21 – Per-unit amplitudes of the 1st, 3rd, 5th, 7th and 9th phase voltage normalised harmonics. The 1st phases of all sub-windings, for the machines with 2, 3, 4, and 5 winding sets, are shown.

Examining the harmonic order in Fig. 4.21, it can be seen that pattern of unbalance in the phase voltage harmonics is repeated after each 2*l* normalised harmonics. For example, if the machine has three sub-windings, the 1st, 7th, 13th, … normalised harmonics of the phase voltages will have the same unbalance. If the given machine has three phases per sub-winding, for example a 9-phase machine, harmonics with the same unbalance pattern will be the 3rd, 21st, 39th, …, effectively, the 3rd, $(2n+3)^{th}$, $(4n+3)^{th}$ … harmonic. It should be noted that in the case when there are two sub-windings (6-, 10-, 14-phase machine), unbalance does not exist due to the fact that the phases of both sub-windings are affected in the same way by the neutral point voltage, as shown in Fig. 4.20a and first column of the Fig. 4.21. However, the amplitudes of the phase voltage harmonics are different from the corresponding amplitudes of the leg voltage harmonics.

To verify the analysis, simulations have been carried out for a 12-phase asymmetrical induction machine with a single isolated neutral point. The machine is considered ideal and balanced and is supplied by 12-phase two-level inverter in 180° conduction mode. As a consequence, the supply generates all odd-order harmonics. Dc-link voltage is set to 600V and the fundamental frequency is 50Hz. Leg, phase and neutral point voltages, with the corresponding spectra, are shown in Fig. 4.22. Only the first phase is shown in time domain (three plots on the left), but all phases are included in the FFT analysis (three plots on the right). The first 21 harmonics are illustrated.

Even harmonics are omitted from the plot, since they are equal to zero, along with the dc component. It can be seen that harmonics of the leg voltages are balanced, meaning that amplitudes of the leg

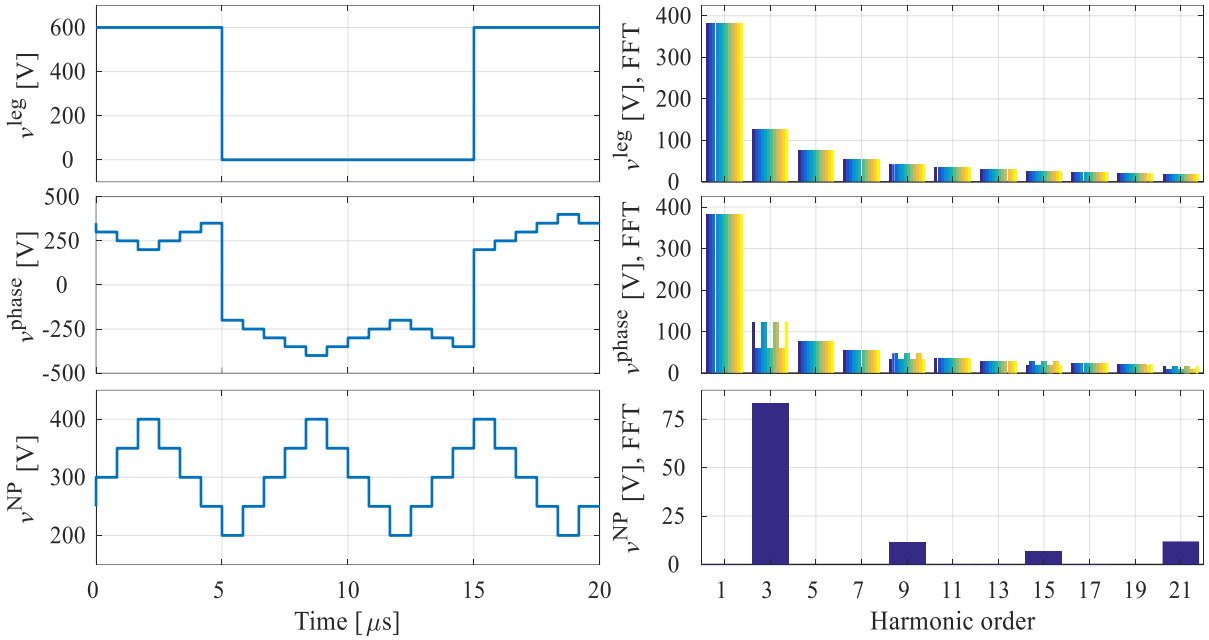

Figure 4.22 – Leg, phase and neutral point voltages with corresponding spectra for an asymmetrical 12-phase machine.

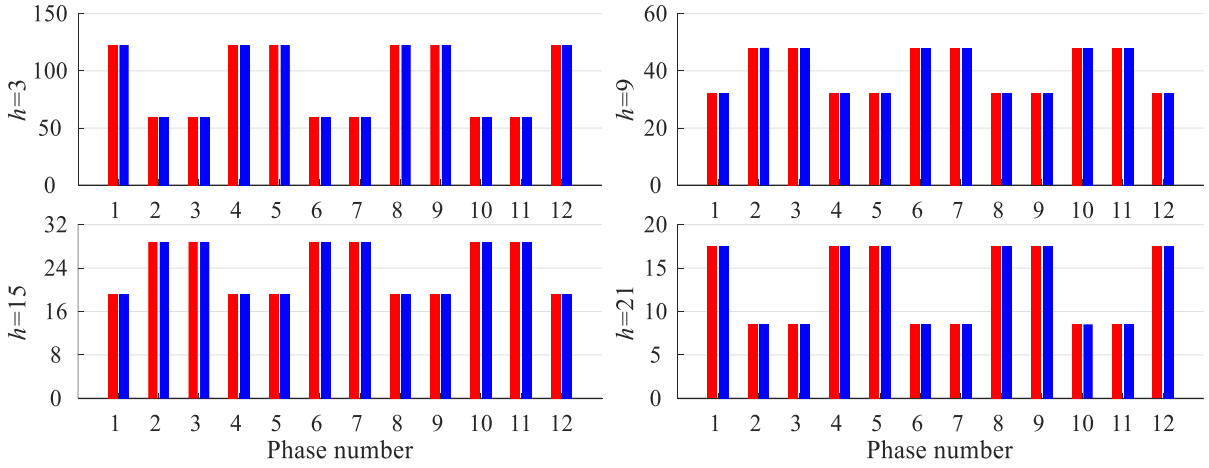

Figure 4.23 – Amplitudes of the 3rd, 9th, 15th, and 21st phase voltage harmonics (red – simulation, blue – calculation based on 4.71).

voltages for the considered harmonic order have the same value. On the other hand, the imbalance exists in the case of some harmonics, such as the 3rd, 9th, 15th, and 21st, or, in terms of the normalised harmonics $h_n = h/k$, 1st, 3rd, 5th, and 7th. Essentially, unbalance in the phase voltage harmonics is present for the harmonic orders that exist in the neutral point voltage.

The theory is verified by comparing the values of the phase voltage harmonics obtained by the simulation and equation (4.71). Leg voltage harmonic amplitudes obtained by FFT are used as input to the equation (4.71). The simulated and calculated amplitudes of phase voltage harmonics, for the harmonic orders where unbalance exists, are shown in Fig. 4.23. It can be seen that both simulation and calculation of the unbalanced phase voltage harmonics produce the same results, confirming the presented theory.

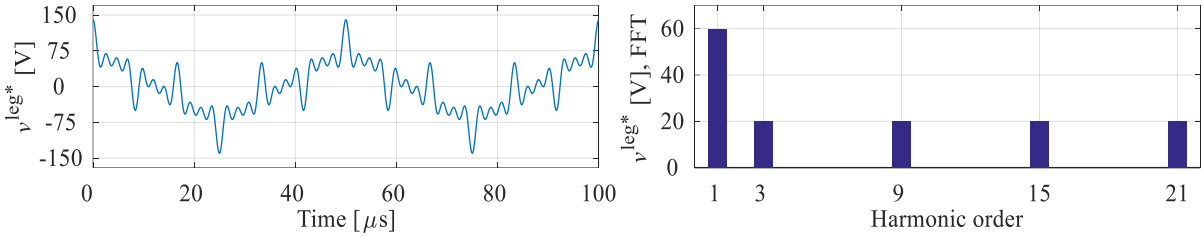

Figure 4.24 – Experimental results: Waveform and the spectrum of one of the references supplied to the inverter PWM unit.

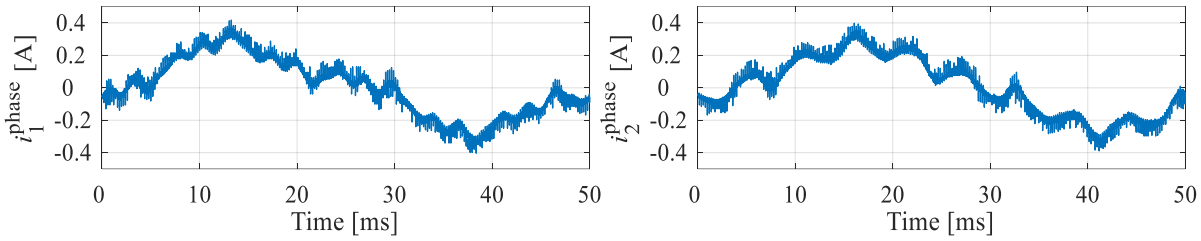

Figure 4.25 – Experimental results: Waveform of the first (a) and second (b) phase currents.

Experimental verification has been performed using a 9-phase *R-L* load supplied from a bespoke 9-phase two-level voltage source inverter. The dc supply for the inverter is provided by a Sorensen SGI 600/25 dc voltage source. The inverter has hardware implemented dead time of 6 μs. A simple carrier-based PWM is used as a modulation strategy. Inverter control is performed by dSPACE rapid prototyping platform. Measurements have been taken with Tektronix MSO2014 scope. Leg, phase and neutral point voltages are measured using a Tektronix P5205A active voltage differential probe, while phase currents have been measured using Tektronix TCP0030 active current probe. Resistance and inductance values of the used *R-L* load are 43 Ω and 250 mH, respectively. The load is connected to form a single neutral point. Dc-link voltage has been set to 300 V.

To verify the theory, references provided to the modulator consist of a component at fundamental frequency and the 3rd, 9th, 15th, and 21st harmonics. The amplitude of the fundamental is set to 60 V, while all harmonics have the same amplitude of 20 V. Fundamental frequency is 20 Hz; hence harmonics are at 60 Hz, 180 Hz, 300 Hz, and 420 Hz, respectively. Switching frequency is 5 kHz, which is in this case high enough so that the PWM switching process does not influence the harmonics of interest. Waveform and the spectrum of one of the references used to supply the *R-L* load are shown in Fig. 4.24. It should be noted that the reference settings are such as to ensure that the CBPWM stays in the linear modulation region.

Phase currents of the first and second phase are shown in Fig. 4.25. It can be appreciated that these two currents are different. Furthermore, in order to obtain more detailed insight into phase currents unbalance, spectra of all leg, phase, and neutral point voltages and phase currents for the 3rd, 9th, 15th, and 21st harmonics are shown in Fig. 4.26. Each vertical bar represents one phase. Dashed lines in the bottom left plot of Fig. 4.26 represent calculated harmonic amplitudes based on the measured amplitudes of the leg voltage harmonics as follows:

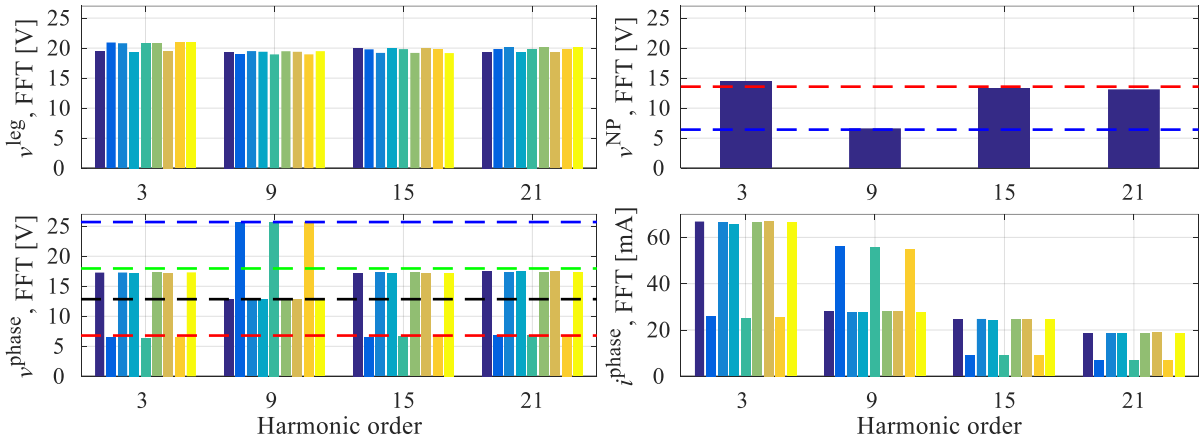

Figure 4.26 – Experimental results: Spectra of all leg, phase and neutral point voltages and phase currents for the selected harmonics in the case of the 9-phase *R-L* load.

- blue dashed line – 9th harmonic of the 2nd, 5th, and 8th phases.
- black dashed line – 9th harmonic of 1st, 3rd, 4th, 6th, 7th, and 9th phases.
- red dashed line – 3rd, 15th, and 21st harmonics of 2nd, 5th, and 8th phases.
- green dashed line – 3rd, 15th, and 21st harmonics of 1st, 3rd, 4th, 6th, 7th, and 9th phases.

Similarly, red and blue dashed lines in the top right plot of Fig. 4.26 represent calculated harmonic amplitudes of the neutral point voltage. Red line represents 3rd, 15th, and 21st harmonics, while blue line represents 9th harmonic amplitude. It can be seen that unbalance in the phase voltage harmonics exists and measured harmonic amplitudes are in a good agreement with the predicted values. Small differences between the predicted and the measured values are predominantly due to the tolerances of the *R-L* load values.

4.7 Summary

This chapter dealt with multiphase induction machine modelling in general and the relationship between modelling approaches and imbalance in phase voltage harmonics. Firstly, machine model has been presented in phase variables for a general case. It is shown that model in phase variables is not convenient for control purposes, so machine has been modelled by MS modelling approach. After a brief discussion regarding the limitations of MS modelling approach (i.e. heavy cross-coupling between equations), VSD modelling has been discussed. An easy to follow algorithm for producing VSD transformation in a general case has been developed, followed by the model of the 9-phase induction machine. It is shown that if the proposed algorithm for VSD matrix creation is used, VSD model of any multiphase induction machine is of the same form with only difference being in the number of subspaces and/or zero-sequence homopolar components. Benefits of the VSD modelling have been discussed along with harmonic mapping for the most commonly used multiphase machines (5-, 6-, 7-, 9-, 12-, and 15-phase). Next, relation between MS and VSD variables has been found for a general case and it was concluded that it can be used for any multiphase machine (i.e. induction or synchronous) since it is only based on transformation matrices and not the actual machine construction. Final section of the chapter

dealt with imbalance in the phase voltage harmonics of the asymmetrical multi-phase machines with single neutral point. Analytical expression for the phase voltage harmonics has been developed for a general case, while the validity of the solution is confirmed by simulation and experimental results.

The work presented in this chapter is utilised throughout the thesis and sets in place the mathematical foundations for the work presented in chapters 5 and 6. The validity of the mathematical modelling techniques is verified through simulation and/or experiment. The Matlab and Mathematica code confirming this chapter findings are available in the Appendix A of the thesis.

Chapter 5

CURRENT SHARING TECHNIQUE FOR MULTIPLE THREE-PHASE MACHINES

5.1 Introduction

Induction machine modelling using three modelling techniques, namely, phase variables, multi-stator (MS) and vector space decomposition (VSD), has been presented in chapter 4 of the thesis. The relationship between MS and VSD variables for any multiple 3-phase machine is also developed, so that the benefits of both modelling approaches can be utilised, i.e. decoupled machine equations of VSD and access to variables of individual winding sets of MS. The intention of this chapter is to take this work further and implement current and power sharing techniques between winding sets by using control in the decoupled VSD machine model.

The current sharing technique is solely based on 3-phase Clarke's and multiphase VSD transformation matrices, hence, it is applicable to any multiple 3-phase machine (induction or synchronous) in both symmetrical/asymmetrical configurations with single/multiple neutral points. Moreover, only *x-y* currents are used to impose imbalance in the machine fundamental currents, so that total flux and torque production are unaffected. Current sharing is realised in the stationary α-β and rotational *d-q* reference frames. In each case, independent control of currents on both axes of individual winding sets is realised (i.e. α-β or *d-q*). Later on, current sharing coefficients for two axes are equalised so that independent control of currents is lost. Potential applications of the devised current sharing depend on the actual WECS topology used and on whether the WECS supplies isolated loads or is connected to the grid, as discussed in the chapter 3 of the thesis.

The developed theory is confirmed by numerical simulations for 6-, 9-, 12-, and 15-phase cases, while experimental verification is provided for an asymmetrical 9-phase induction machine. It is shown that the developed power/current sharing technique does not have any negative effects on the total flux/torque control. The work presented in this chapter has been published in [Zoric et al (2018a)] and [Zoric et al (2018b)].

5.2 Current Sharing in Stationary Reference Frame

VSD modelling of the machine is preferable from the control point of view. It provides a decoupled machine model that makes implementation of the current control very easy. However, information of currents in individual winding sets is lost so they cannot be controlled just by applying the basic VSD transformation. For that purpose, MS modelling is needed. Equations providing relations between VSD and MS modelling are derived in the fourth chapter of the thesis ((4.62) and (4.63)), and are repeated here for convenience:

$$\begin{aligned}
&\underline{f}_{\alpha\beta} = \frac{1}{l}\sum_{i=1}^{l}\underline{f}_{\alpha\beta i} \\
&\underline{f}_{xyss} = \begin{cases} \frac{1}{l}\sum_{i=1}^{l}\overline{\underline{f}}_{\alpha\beta i}\, e^{j(ss+1)(i-1)\frac{\pi}{l}}, & ss = 1,3,5,\ldots \\ \frac{1}{l}\sum_{i=1}^{l}\underline{f}_{\alpha\beta i}\, e^{jss(i-1)\frac{\pi}{l}}, & ss = 2,4,6,\ldots \end{cases}
\end{aligned} \tag{5.1a}$$

$$\begin{cases} \underline{f}_{xyss} = \frac{2}{l}\sum_{i=1}^{l} f_{zi}\, e^{j2(ss-l+1)(i-1)\frac{\pi}{l}} \\ f_{z+} = \frac{1}{l}\sum_{i=1}^{l} f_{zi}\cos\left((i-1)2\pi\right) \\ f_{z-} = \frac{1}{l}\sum_{i=1}^{l} f_{zi}\cos\left((i-1)\pi\right) \end{cases} \quad \textit{symmetrical}$$

$$\begin{cases} \underline{f}_{xyss} = \frac{2}{l}\sum_{i=1}^{l} f_{zi}\, e^{j(2(ss-l)+1)(i-1)\frac{\pi}{l}} \\ f_{z+} = \frac{1}{l}\sum_{i=1}^{l} f_{zi}\cos\left((i-1)\pi\right) \end{cases} \quad \textit{asymmetrical} \tag{5.1b}$$

The relationships between flux/torque producing α-β currents of each winding set and first l subspaces of the VSD are governed with (5.1a). Equations in (5.1b) can be used to find the relationship between zero-sequence currents in the case of the machines with a single neutral point. However, zero-sequence currents only produce losses and, in the case when power transfer between winding sets is required, they should be kept at zero. Therefore, (5.1b) can be omitted from further discussion, while (5.1a) governs the relationship between VSD and MS currents:

$$\begin{aligned}
&\underline{i}_{\alpha\beta} = \frac{1}{l}\sum_{i=1}^{l}\underline{i}_{\alpha\beta i} \\
&\underline{i}_{xyss} = \begin{cases} \frac{1}{l}\sum_{i=1}^{l}\overline{\underline{i}}_{\alpha\beta i}\, e^{j(ss+1)(i-1)\frac{\pi}{l}}, & ss = 1,3,5,\ldots \\ \frac{1}{l}\sum_{i=1}^{l}\underline{i}_{\alpha\beta i}\, e^{jss(i-1)\frac{\pi}{l}}, & ss = 2,4,6,\ldots \end{cases}
\end{aligned} \tag{5.2}$$

Indices *ss* and *i* represent *x-y* subspace number and winding set number, respectively. Equations (5.2) are valid for all topologies of multiple 3-phase machines (symmetrical and asymmetrical with single and multiple neutral points). In order to control the flux and torque producing currents of each winding set ($\underline{i}_{\alpha\beta i}$, i = 1, 2, 3, …), it is convenient to define their value in relation to the total flux and torque requirements of the machine, expressed through $\underline{i}_{\alpha\beta}$ current, as follows:

$$\underline{i}_{\alpha\beta} = i_\alpha + ji_\beta$$
$$\left.\begin{aligned}\underline{i}_{\alpha\beta i} &= k_{\alpha i}i_\alpha + jk_{\beta i}i_\beta \\ \underline{i}_{\alpha\beta i} &= k_{\alpha i}i_\alpha - jk_{\beta i}i_\beta\end{aligned}\right\} \rightarrow \quad k_{\alpha i} = \frac{i_{\alpha i}}{i_\alpha},\ k_{\beta i} = \frac{i_{\beta i}}{i_\beta}, \quad i = 1,2,3,...,l \tag{5.3}$$

When (5.3) is applied to (5.2), correlation between flux/torque producing currents in VSD and MS domains is as follows:

$$i_\alpha + ji_\beta = \frac{1}{l}i_\alpha\sum_{i=1}^{l}k_{\alpha i} + \frac{1}{l}ji_\beta\sum_{i=1}^{l}k_{\beta i} \quad \rightarrow \quad \sum_{i=1}^{l}k_{\alpha i} = l,\ \sum_{i=1}^{l}k_{\beta i} = l$$
$$\underline{i}^*_{xyss} = \left\{\begin{aligned}&\frac{1}{l}\sum_{i=1}^{l}\left(k_{\alpha i}i_\alpha - jk_{\beta i}i_\beta\right)e^{j(ss+1)(i-1)\frac{\pi}{l}}, \quad ss = 1,3,5,... \\ &\frac{1}{l}\sum_{i=1}^{l}\left(k_{\alpha i}i_\alpha + jk_{\beta i}i_\beta\right)e^{j3ss(i-1)\frac{\pi}{l}}, \quad ss = 2,4,6,...\end{aligned}\right\} \tag{5.4}$$

The first expression in (5.4) sets the constraint that the sum of all current sharing coefficients along the same axis needs to be equal to the number of winding sets *l*. When this condition is met, it is possible to arbitrarily vary the currents in each winding set by use of the second expression in (5.4). It provides references for *x-y* currents governed by the flux and torque requirements of the machine and by the values of current sharing coefficients $k_{\alpha\beta i}$. Furthermore, since current sharing is achieved by imposing currents in flux/torque non-producing *x-y* subspaces, the total flux and torque of the machine will not be affected. The only limitation comes from the constraint imposed previously in (5.4), i.e. *l*-1 winding set currents can be arbitrarily controlled, while the currents in the last one are imposed by the total flux and torque requirements. It should be noted that, if all current sharing coefficients are equal to 1, *x-y* currents references are equal to zero and the machine is balanced.

In order to verify the derived equations, numerical simulations in Simulink have been performed. Amplitudes of the flux and torque producing VSD currents i_α and i_β are equal to one, while the frequency is 50 Hz, i.e. $\underline{i}_{\alpha\beta} = e^{j2\pi 50t}$. The current sharing coefficients are randomly varied in three time intervals as follows:

- 0.00 s – 0.05 s – all coefficients are equal to one (balanced operation)
- 0.05 s – 0.10 s – coefficients take the 1st random value
- 0.10 s – 0.15 s – coefficients take the 2nd random value
- 0.15 s – 0.20 s – coefficients take the 3rd random value
- 0.20 s – 0.25 s – all coefficients are equal to one (balanced operation).

A block diagram of the simulated system is shown in the Fig. 5.1. The current sharing block contains equations (5.4) while VSD and inverse VSD transformation are implemented as discussed in chapter 4 of the thesis. Multiple 3-phase winding machines up to 15 phases (6, 9, 12, and 15) have been simulated and the results are presented here. In the following simulation results, the first column shows VSD currents measured at the output (blue trace – i_α, i_x, red trace – i_β, i_y), the second column shows phase currents in each winding set, the third column shows α-β currents of each winding set (blue trace – i_x,

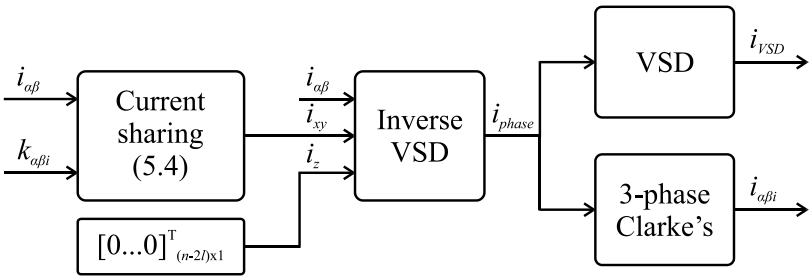

Figure 5.1 – Simulation block diagram of the current sharing in stationary reference frame.

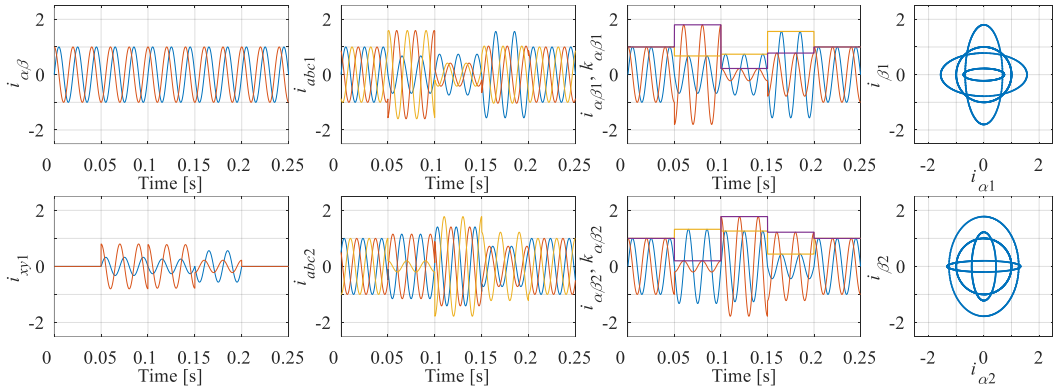

Figure 5.2 – Current sharing in stationary reference frame for a 6-phase machine.

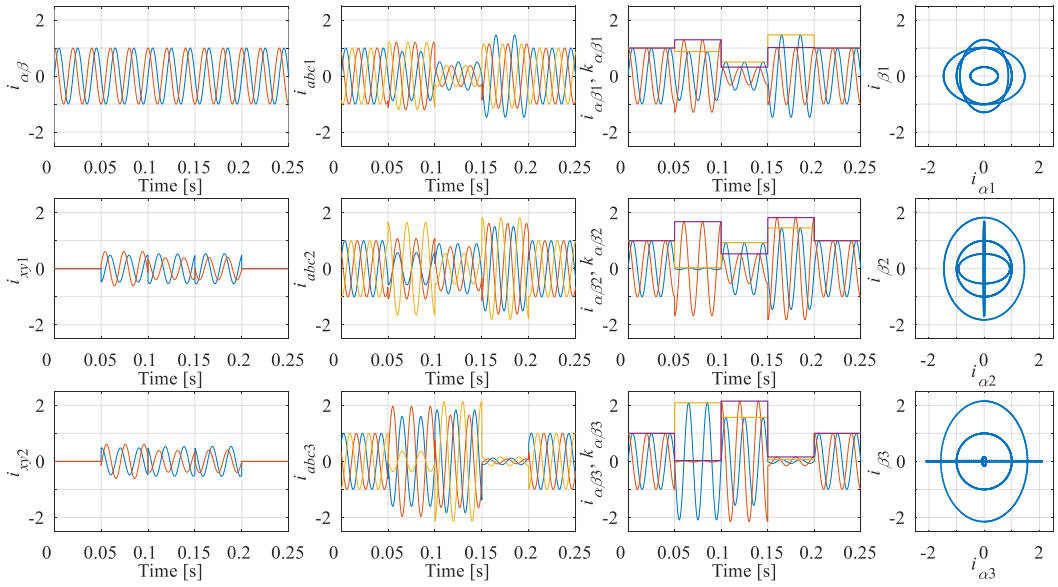

Figure 5.3 – Current sharing in stationary reference frame for a 9-phase machine.

red trace – i_y) with corresponding coefficients, and the fourth column shows polar plot of α-β currents of each winding set.

Simulation results for the 6-phase and 9-phase case are given in the Figs. 5.2 – 5.3. Corresponding simulation results for the 12-phase and 15-phase cases can be found in the Figs. 5.4 – 5.5. The number of rows in the Figs. 5.2 – 5.5 increases as the number of phases increases, due to the increase of the number of *x*-*y* planes and the number of 3-phase winding sets.

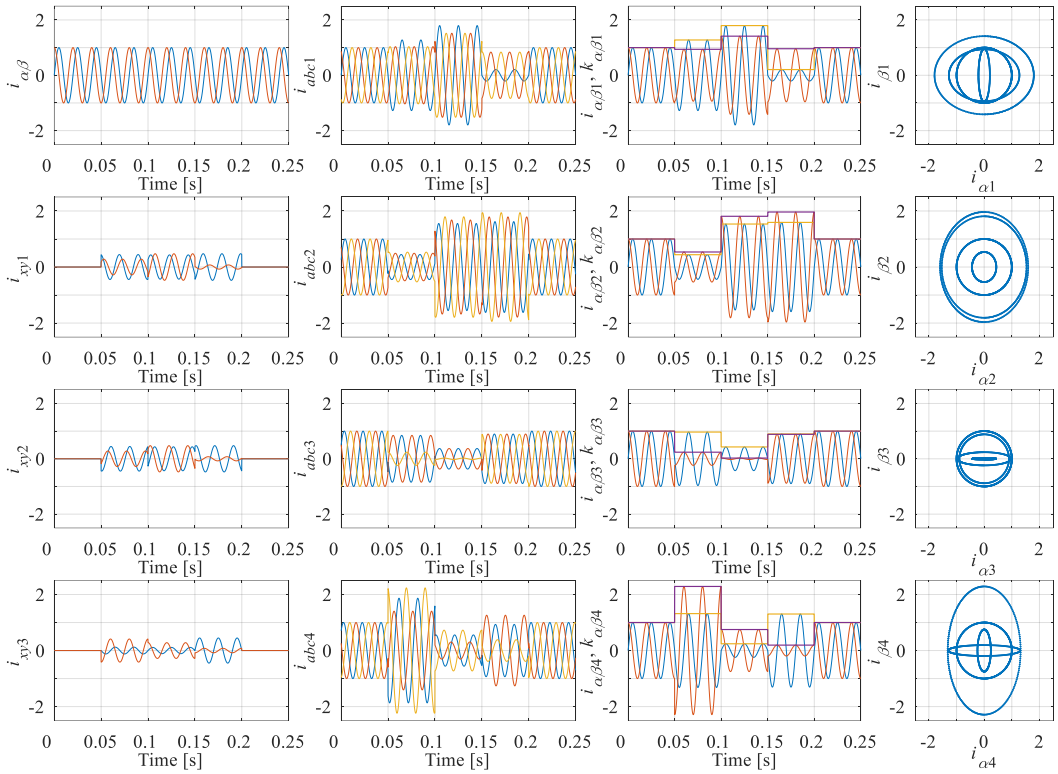

Figure 5.4 – Current sharing in stationary reference frame for a 12-phase machine.

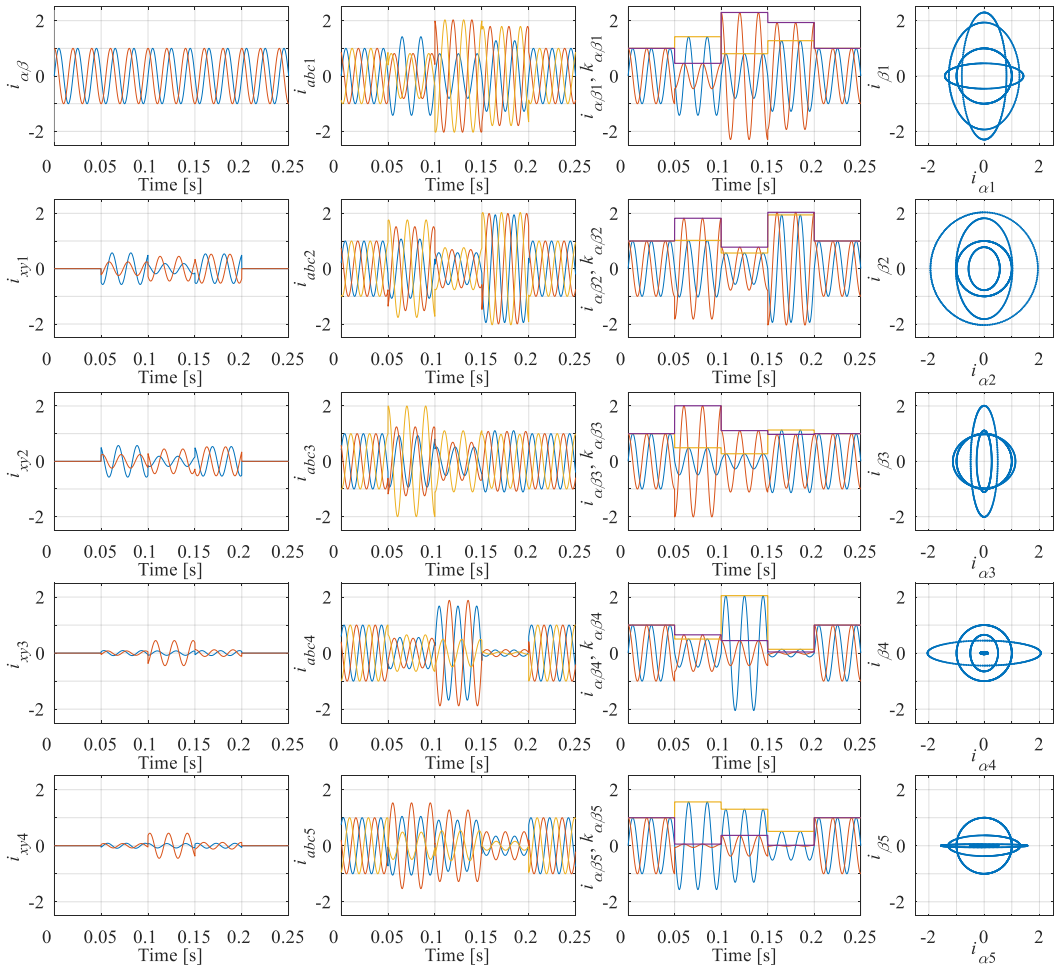

Figure 5.5 – Current sharing in stationary reference frame for a 15-phase machine.

Since the amplitude of the flux/torque producing $i_{\alpha\beta}$ current is equal to one and an amplitude invariant transformation is used, coefficient values should be equal to the corresponding current amplitude in each of the winding sets. The third column of the results verifies this behaviour. Total flux/torque producing $i_{\alpha\beta}$ current is unchanged, as seen in the first plot of each figure. The fourth column shows that due to random coefficients values, individual winding sets α-β current vectors move along an elliptical path instead of circular. As a result, phase currents within each winding set are unbalanced, as shown in the second column. This behaviour can be further extended to develop fault-tolerant operation, while keeping the total flux/torque producing current unchanged. However, this is out of scope of this chapter.

5.3 Current Sharing in the Rotational Reference Frame

Machine control is usually implemented in such a way that both flux and torque can be arbitrarily set. This often involves relating flux and torque to the *d-q* currents in a rotational reference frame, e.g. IRFOC. Therefore, it is beneficial to relate current sharing coefficients to the flux/torque producing currents i_d and i_q, so that currents in each winding set can be related to the actual flux and torque requirements of the machine.

The relationship between individual winding set currents and VSD currents in the stationary reference frame is given in (5.2). If the machine is operating under normal conditions, i.e. it is not faulted and there is no imbalance, it can be stated that VSD and winding set currents are governed with:

$$\begin{aligned}
&\underline{i}_{\alpha\beta} = I_{\alpha\beta} e^{j\varphi_i} \\
&\underline{i}_{\alpha\beta i} = I_{\alpha\beta i} e^{j\varphi_i}, \quad i = 1,2,3,...l \\
&\underline{i}_{\alpha\beta i} = I_{\alpha\beta i} e^{-j\varphi_i}, \quad i = 1,2,3,...l
\end{aligned} \tag{5.5}$$

Applying (5.5) to the (5.2) results in the following equations:

$$\begin{aligned}
&\underline{i}_{\alpha\beta} = \frac{1}{l}\sum_{i=1}^{l} I_{\alpha\beta i} e^{j\varphi_i} \\
&\underline{i}_{xyss} = \begin{Bmatrix} \frac{1}{l}\sum_{i=1}^{l} I_{\alpha\beta i} e^{-j\varphi_i} e^{j(ss+1)(i-1)\frac{\pi}{l}}, & ss = 1,3,5,... \\ \frac{1}{l}\sum_{i=1}^{l} I_{\alpha\beta i} e^{j\varphi_i} e^{jss(i-1)\frac{\pi}{l}}, & ss = 2,4,6,... \end{Bmatrix}
\end{aligned} \tag{5.6}$$

In order to get individual winding set flux/torque producing currents in the rotational reference frame, i.e. i_{dqi}, rotational transformation is applied to (5.6) as follows:

$$\begin{aligned}
&\underline{i}_{dq} = \underline{i}_{\alpha\beta} e^{-j\varphi} \\
&\underline{i}_{dqi} = \underline{i}_{\alpha\beta i} e^{-j\varphi_i}, \quad i = 1,2,3,...l \\
&\underline{i}_{dqi} = \underline{i}_{\alpha\beta i} e^{j\varphi_i}, \quad i = 1,2,3,...l
\end{aligned} \tag{5.7}$$

Angle φ is an arbitrary angle of rotation, usually governed by RFOC. The resulting equations are as follows:

$$\underline{i}_{dq} = \frac{1}{l}\sum_{i=1}^{l}\underline{i}_{dqi}$$
$$\underline{i}_{dqxyss} = \begin{cases} \frac{1}{l}\sum_{i=1}^{l}\underline{\bar{i}}_{dqi}\, e^{j(ss+1)(i-1)\frac{\pi}{l}}, & (\text{anti}-\text{sync. rot}) \quad ss = 1,3,5,... \\ \frac{1}{l}\sum_{i=1}^{l}\underline{i}_{dqi}\, e^{jss(i-1)\frac{\pi}{l}}, & (\text{sync. rot}) \quad ss = 2,4,6,... \end{cases} \tag{5.8}$$

It can be seen that odd-numbered *x-y* subspaces have anti-synchronous rotation and the even-numbered ones should be rotated at synchronous frequency, as per complex conjugate in expression for odd-ordered *x-y* subspaces in (5.2). In order to implement arbitrary current sharing of flux/torque producing currents, the current sharing coefficients are now defined as follows:

$$\begin{aligned} \underline{i}_{dqi} &= k_{di}i_d + jk_{qi}i_q, \quad i = 1,2,3,...,l \\ \underline{\bar{i}}_{dqi} &= k_{di}i_d - jk_{qi}i_q, \quad i = 1,2,3,...,l \end{aligned} \tag{5.9}$$

Consequently, the flux and torque contributions of each winding set are related to the total flux and torque of the machine by the introduced coefficients, i.e. $k_{di} = i_{di}/i_d$ and $k_{qi} = i_{qi}/i_q$. Finally, current sharing equations in rotational reference frame are as follows:

$$i_d + ji_q = \frac{1}{l}i_d\sum_{i=1}^{l}k_{di} + \frac{1}{l}ji_q\sum_{i=1}^{l}k_{qi} \quad \rightarrow \quad \sum_{i=1}^{l}k_{di} = l, \ \sum_{i=1}^{l}k_{qi} = l$$
$$\underline{i}^{*}_{dqxyss} = \begin{cases} \frac{1}{l}\sum_{i=1}^{l}\left(k_{di}i_d - jk_{qi}i_q\right)e^{j(ss+1)(i-1)\frac{\pi}{l}}, & (\text{anti}-\text{sync. rot}) \quad ss = 1,3,5,... \\ \frac{1}{l}\sum_{i=1}^{l}\left(k_{di}i_d + jk_{qi}i_q\right)e^{jss(i-1)\frac{\pi}{l}}, & (\text{sync. rot}) \quad ss = 2,4,6,... \end{cases} \tag{5.10}$$

The same applies to the current sharing in a rotational reference frame, as shown previously for the current sharing in the stationary reference frame. The first part of (5.10) sets the limitation of having the sum of all current sharing coefficients along the same axis (*d* or *q*) equal to the winding set number *l* ($\Sigma k_{di} = l$, $\Sigma k_{qi} = l$). When this limitation is met, the second part of (5.10) can be used to define *x-y* current references in synchronous/anti-synchronous reference frames. Imposed *x-y* currents will then set the contribution of each winding set to the total flux and torque producing *d-q* currents as per defined coefficients and current flux and torque requirements of the machine.

It should be noted that even though the *q*-axis current of each winding set can be arbitrarily set, in the case of an induction machine it does not imply that electrical power production in a given winding set is directly governed by the current sharing coefficient k_{qi}. On the contrary, it depends as well on the flux producing *d*-axis current of the given winding set as it will be shown further on in the chapter. This fact should be kept in mind when power sharing is developed.

The main difference between this current sharing implementation and the one in the stationary reference frame is that in this case currents within each winding set are balanced. Therefore, α-β current vector of each winding set travels along circular path, while in the previous case it makes an ellipse, as shown in the Fig. 5.3. This behaviour is due to the applied rotational transformation.

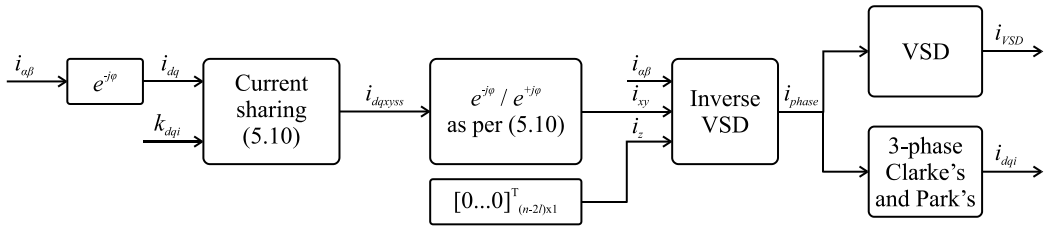

Figure 5.6 – Simulation block diagram of the current sharing in rotational reference frame.

Furthermore, *d-q* currents are usually readily available from the flux/torque control so that current sharing can be easily implemented by use of (5.10) and additional *l*-1 current controllers in *x-y* subspaces.

The developed theory is verified in a similar manner as in the previous section, by randomly varying the current sharing coefficients. Amplitudes of the flux and torque producing VSD current i_α and i_β are equal to one, while the frequency is 50 Hz, i.e. $\underline{i}_{\alpha\beta} = e^{j2\pi 50t}$. The current sharing coefficients have been randomly varied in three time intervals as follows:

- 0.00 s – 0.05 s – all coefficients are equal to one (balanced operation)
- 0.05 s – 0.10 s – coefficients take the 1st random value
- 0.10 s – 0.15 s – coefficients take the 2nd random value
- 0.15 s – 0.20 s – coefficients take the 3rd random value
- 0.20 s – 0.25 s – all coefficients are equal to one (balanced operation).

Since current sharing is implemented in rotational reference frame, φ is defined as $2\pi 50t - \pi/6$, where *t* represents time. Angle $\pi/6$ is taken as a random value so flux/torque producing currents i_d/i_q are both non-negative; hence current sharing can be properly demonstrated. Multiple 3-phase winding machines up to 15 phases (6, 9, 12, and 15) have been simulated and the results are provided. In the following simulation results, the first column shows VSD currents measured at the output, the second column shows phase currents in each winding sets, the third column shows *d-q* currents of each winding set with the corresponding current references ($i_{di}^* = k_{di}i_d$, $i_{qi}^* = k_{qi}i_q$), and the last row shows polar plot of *d-q* currents of each winding set.

It should be pointed out that the coefficients are limited to positive values; hence, polar plot shows only the first quadrant. However, there is no limitation to set them to negative value as well. For example, negative coefficient for i^{th} winding set torque producing current k_{qi}, depending on the operating point, may set corresponding winding set in different operating mode than the machine (motoring/generating). A block diagram of the simulated system is shown in the Fig. 5.6.

Figs. 5.7, 5.8, 5.9, and 5.10 show simulation results for 6-, 9-, 12-, and 15-phase machine. Total flux/torque producing currents i_d/i_q are shown in the first plot (yellow trace – i_d, purple trace – i_q) together with i_α/i_β currents (blue trace – i_α, red trace – i_β). Since current sharing coefficients now define values in rotational reference frame, phase currents within each winding set are now balanced (the second column). The third column shows that references for winding set *d-q* currents (dashed yellow

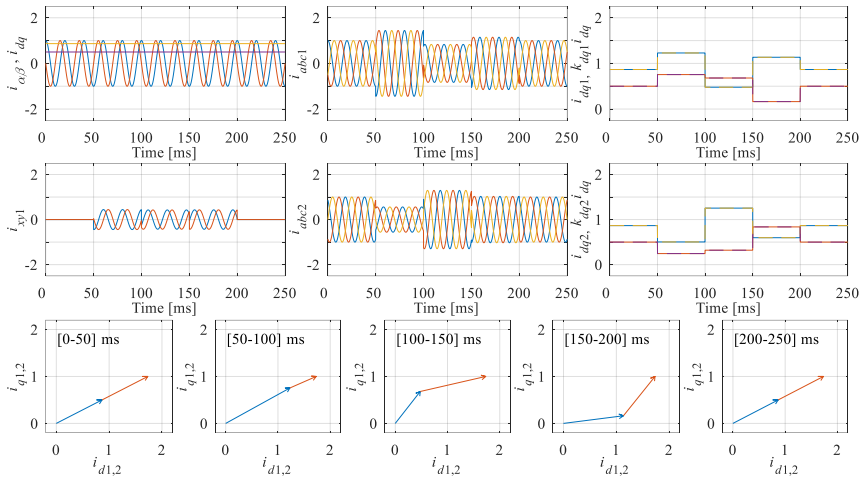

Figure 5.7 – Current sharing in rotational reference frame for a 6-phase machine.

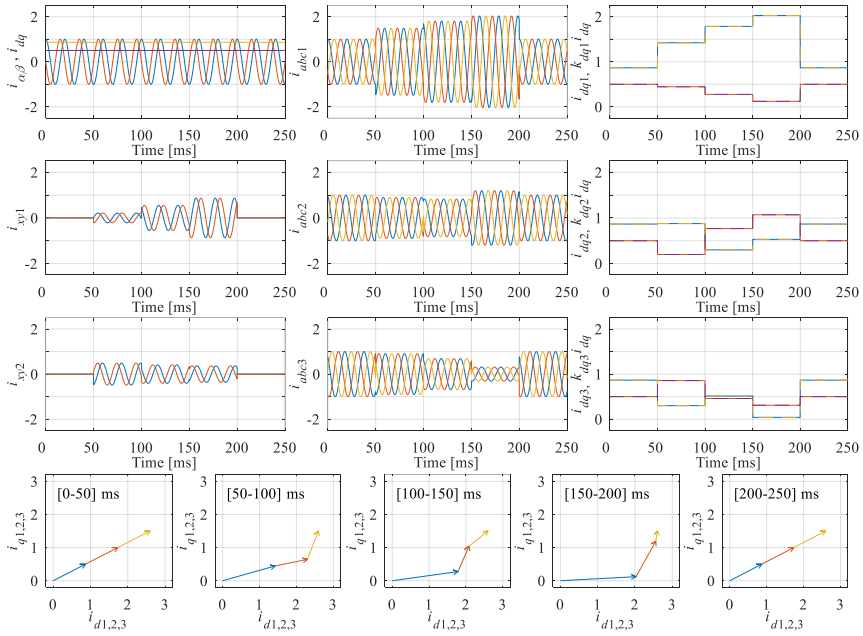

Figure 5.8 – Current sharing in rotational reference frame for a 9-phase machine.

trace – i_d, dashed purple trace – i_q) are overlapped with actual *d-q* currents (solid blue trace – i_d, solid red trace – i_y) of the winding sets confirming validity of the developed equations. Last row shows *d-q* current vector of each winding set for all 5 time intervals. It should be emphasised that total flux/torque current is not changed throughout the simulation, despite variation in flux/torque production in each winding set. This behaviour can be seen in the first plot of each figure and in the last row where all *d-q* vectors sum to the same point at all times.

Although the simulated machine configuration is asymmetrical with single neutral point, the results would be similar for any other configuration, with the difference being only the phase shift in phase currents. This conclusion follows from the fact that the developed current sharing is independent of the machine configuration when the VSD, developed in chapter 4, is used.

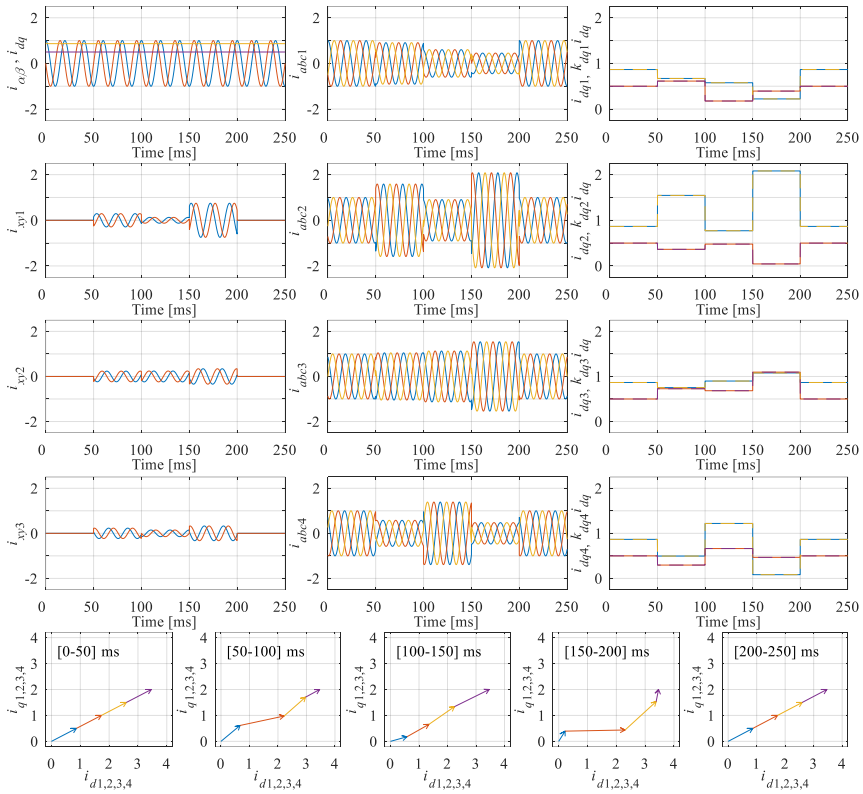

Figure 5.9 – Current sharing in rotational reference frame for a 12-phase machine.

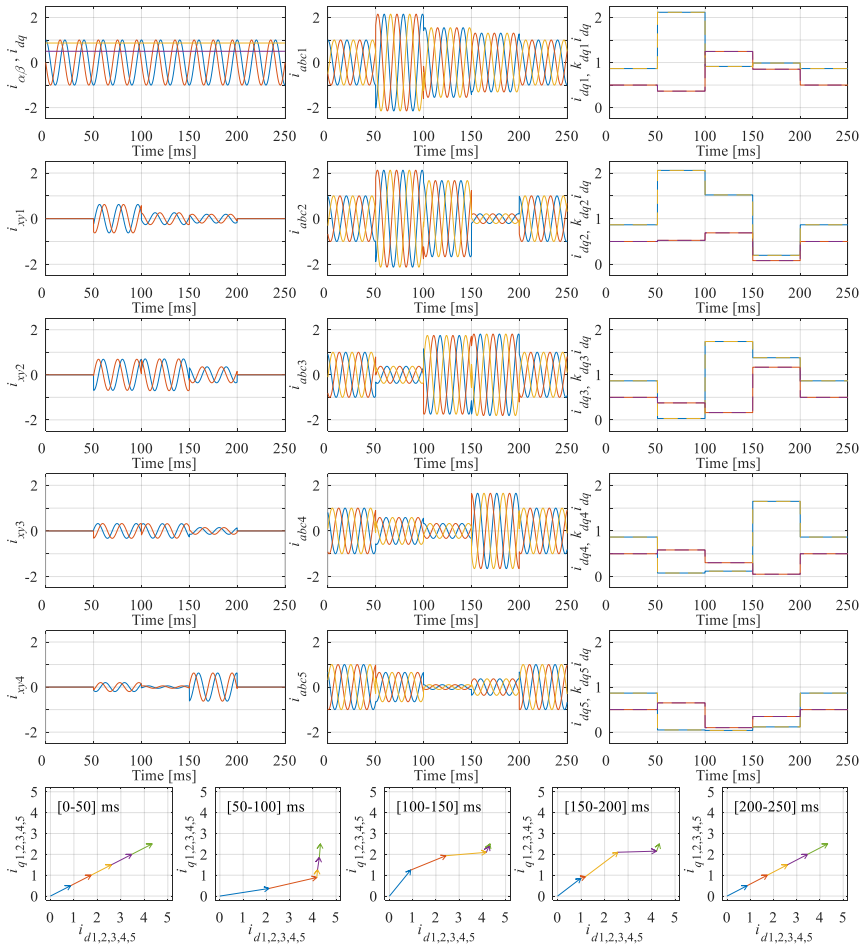

Figure 5.10 – Current sharing in rotational reference frame for a 15-phase machine.

5.4 Equalised *d-q* current sharing

Current sharing between winding sets has been developed in both stationary and rotational reference frames for general case in the previous two sections of this chapter. This section shows implementation of the current sharing on the example of 9-phase induction machine where *d-q* axes current sharing coefficients are equally varied. Both current sharing techniques can be used since the only difference between the two is the rotational transformation. However, *d-q* currents in a rotational reference frame are usually readily available in flux/torque control strategy; hence, current sharing in rotational reference frame described in (5.10) is used as the starting point.

In order to implement power sharing, it is required to arbitrarily set the torque production in each winding set; hence, this power sharing technique is sometimes referred to as torque sharing. With the IRFOC controlled induction machines, VSD *d-q* reference frame is aligned with the rotor field so that *d*-axis current controls flux and *q*-axis currents controls torque production. The same applies for the individual winding set *d-q* currents. Following the derivation for the MS modelling presented in section 4.3, the expression for torque production in each winding set is governed with:

$$T_{emi} = \frac{3}{2} P \frac{L_m}{L_r} \psi_{dr} i_{qi}, \quad i = 1,2,,...,l \tag{5.11}$$

The torque contribution of each winding set is governed by rotor flux and the given winding set current. Assuming constant rotor flux ($\psi_{dr} = L_m i_d$), torque sharing can be implemented by changing only the *q*-axis current of the winding set, while flux-producing *d*-axis current is kept constant.

However, in this section both *d*- and *q*-axis currents of each winding set are equally varied. Consequently, only current amplitudes in each winding set are changed, while current vector angle is kept the same. An example for the 9-phase machine is shown in the Fig. 5.11, where it can be seen that all winding set *d-q* current vectors sum up to three times the VSD *d-q* current vector. This is a consequence of the amplitude invariant transformations used. Fig. 5.11a shows the case where *d*-axis currents of all winding sets are kept constant, while *q*-axis currents are arbitrarily varied. On the other hand, Fig. 5.11b shows the case when both *d*- and *q*-axis currents are varied equally for the same value of *q*-axis currents as in the Fig. 5.11a. In both cases torque/power sharing between winding sets is identical since *q*-axis currents are equally changed. However, second scenario keeps the winding set current vectors aligned along the same axis.

When individual winding set *d-q* current vectors $\underline{i}_{dqi}$ (i = 1, 2, 3, …) are aligned with VSD *d-q* current vector $\underline{i}_{dq}$, current sharing coefficients k_{di}/k_{qi} (i = 1, 2, 3, …) from (5.10) are equal and become k_i. The current sharing coefficient k_i governs both *d*- and *q*-axis currents of the i^{th} winding set and at the same time, as per (5.11), governs the torque/power sharing between winding sets. Due to the amplitude invariant transformations used, k_i defines the ratio between the current amplitude in each winding set and the amplitude of VSD *d-q* currents. In other words, if any k_i is set to zero, given winding set currents

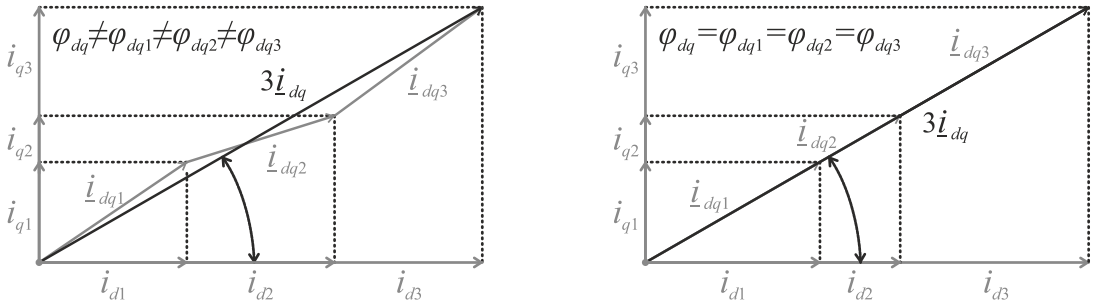

Figure 5.11 – Non-equalised (a) and equalised (b) power sharing between winding sets.

are brought to zero, i.e. basic fault tolerance by switching the complete winding set off is achieved. Current sharing equations (5.10) are now as follows:

$$\sum_{i=1}^{l} k_i = l, \quad k_i = k_{di} = k_{qi} = \frac{I_{dqi}}{I_{dq}} = \frac{T_{emi}}{T_{em}} = \frac{P_{emi}}{P_{em}}$$

$$\underline{i}^{*}_{dqxyss} = \begin{Bmatrix} \frac{1}{l}\sum_{i=1}^{l} k_i\, e^{j(ss+1)(i-1)\frac{\pi}{l}}\, \underline{i}_{dq}, & (\text{anti}-\text{sync. rot}) \quad ss = 1,3,5,... \\ \frac{1}{l}\sum_{i=1}^{l} k_i\, e^{jss(i-1)\frac{\pi}{l}}\, \underline{i}_{dq}, & (\text{sync. rot}) \quad ss = 2,4,6,... \end{Bmatrix} \tag{5.12}$$

Equations (5.12) provide *x*-*y* current references for torque/converted power sharing between winding sets of any multiple 3-phase winding machine. Since the starting point is the equations that are valid regardless of the machine configuration, i.e. symmetrical/asymmetrical with single or multiple neutral points, the same applies for (5.12) as well. Even though (5.12) is developed keeping the induction machine in mind, it is applicable to the synchronous machines with multiple 3-phase winding sets as well. Of course, depending on the machine type, *d*-axis current may be kept at zero, e.g. a synchronous machine with surface permanent magnets, so (5.11) directly governs active power of each winding set as well. The only constraint is that the machine windings are of a standard symmetrical or asymmetrical configuration and that the machine can be decoupled by use of VSD. Moreover, in the high power applications, the machine efficiency can be very high, i.e. 95 %, and the difference between converted power and electrical active power is very small. Hence, the designed power sharing technique may be considered as active power sharing between winding sets.

Unequal currents in individual winding sets lead to an unavoidable increase in the stator copper losses. An analytical expression can be found by analysing copper losses in each winding set. If I_{dqi} is the amplitude of *d*-*q* current vector in the i^{th} winding set and amplitude invariant transformation is used, the copper losses in said winding set are:

$$P_{\Omega si} = \frac{3}{2} R_s I_{dqi}^2 = \frac{3}{2} R_s k_i^2 I_{dq}^2, \quad I_{dqi} = k_i I_{dq}, \quad i = 1,2,3,...,l \tag{5.13}$$

The total stator copper losses are then expressed as the sum of copper losses in all winding sets as follows:

$$P_{\Omega s} = \sum_{i=1}^{l} P_{\Omega si} = \frac{3}{2} R_s I_{dq}^2 \sum_{i=1}^{l} k_i^2 \tag{5.14}$$

It is obvious that, when the machine is balanced, (5.14) provides the well-known expression for stator copper losses. On the other hand, (5.14) is at maximum when only one winding set is in operation ($k_i = l$, $k_{j\neq i} = 0$). In this case, the stator copper losses are l times larger than in the balanced operation.

When it comes to the limits of the torque sharing constants, the nominal phase currents of the machine should be taken into account. The upper limit is determined by total flux and torque requirements of the machine (i_d, i_q currents). Considering that currents in all winding sets should not exceed rated RMS value (I_n), the following expression must hold true:

$$\left|i_{dqi}\right| = k_i\sqrt{i_d^2 + i_q^2} \leq \sqrt{2}I_n \quad \rightarrow \quad k_i \leq \frac{\sqrt{2}I_n}{\sqrt{i_d^2 + i_q^2}}, \quad i = 1,2,3,...,l \tag{5.15}$$

If the torque-sharing coefficient is negative, power flow sign of the given winding set may be changed. However, sum of all k_i needs to be equal to l, as per (5.12), so other coefficients are going to increase to compensate for the lack of torque production. This behaviour is not an issue as long as all of the coefficients adhere to (5.15), so that phase currents are kept below or equal to nominal value.

In the case of a fault, expressions (5.14) – (5.15) impose derating factor of the machine. When a fault occurs in a multiple number of winding sets (j), their torque sharing coefficients should be set to zero imposing the zero phase currents. All other sets should equally distribute the torque production by setting torque sharing coefficients to $k_i = l/(l-j)$. When this condition is applied to (5.15), derating factor of the machine in terms of maximum flux/torque producing current amplitude is as follows:

$$I_{dq} = \left(1 - \frac{j}{l}\right)\sqrt{2}I_n \tag{5.16}$$

Derating of the machine (5.16) keeps the stator currents in the remaining winding sets at rated value; hence, the stator copper losses governed by (5.14) are at rated value as well. Any increase in the amplitude of the flux/torque producing I_{dq} current above (5.16) will increase the stator resistive losses above nominal and result in overheating of the machine in continuous operation.

The torque sharing technique has been confirmed using numerical simulations and experimentally using an asymmetrical 9-phase induction machine with three isolated neutral points. In order to implement proposed control, the machine model is decoupled by VSD transformation, detailed in section 4.4.2. The machine control structure is based on the standard indirect rotor flux oriented control (IRFOC). Current control in the first subspace is performed in the rotor flux oriented (d-q) reference frame using PI controllers with cross-coupling decoupling (PIccd). The machine is operated in the base speed region, so that the flux is kept at a constant value during the simulation/experimental runs. The torque is governed by the outer speed loop consisting of a standard PI regulator. More details regarding control loops are available in the third chapter of the thesis.

Since flux/torque control is implemented in the d-q reference frame, torque sharing control is also realised in the synchronous/anti-synchronous reference frames, as per (5.12). The inputs to the current sharing block are d-q current references (i_d^*, i_q^*), which are provided by the IRFOC block. It should be

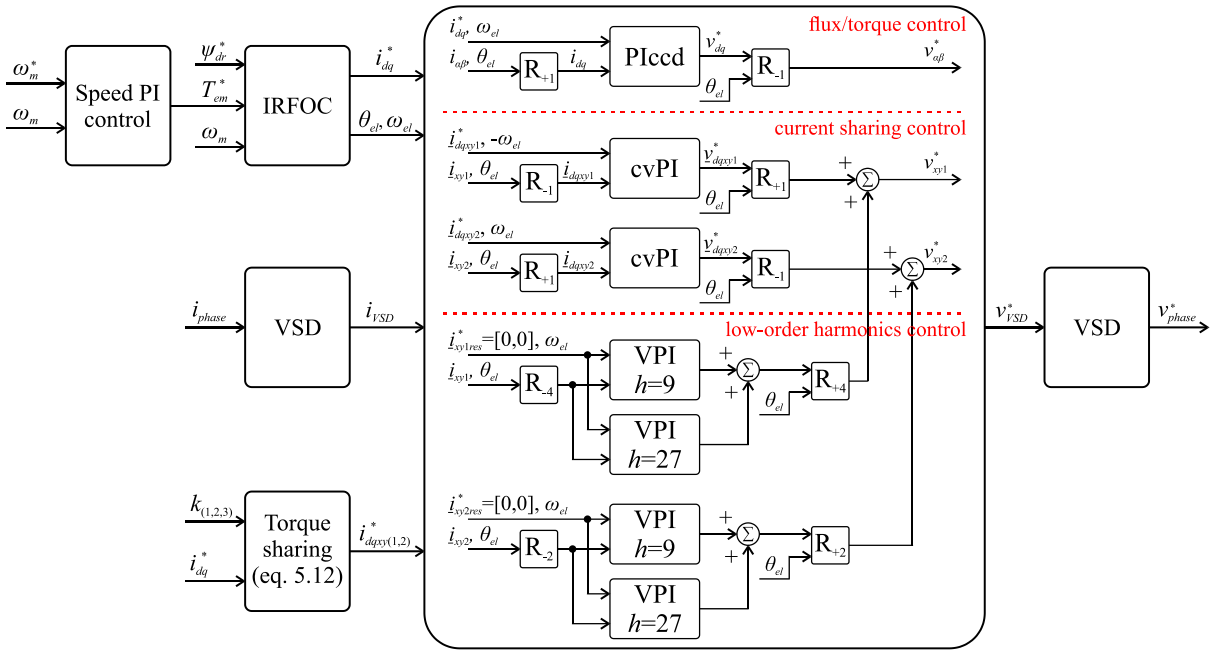

Figure 5.12 – Schematic of the control system with torque sharing capability for induction machines.

noted that the current limit (5.15) is not imposed. Consequently, the phase currents can rise above the rated values, allowing the torque sharing to be tested fully. Complex vector PI (cvPI) regulators are used for current control in the *x-y* subspaces.

The inverter supplying the machine is a two-level VSI with the dc-link voltage set to 600 V. Carrier based pulse width modulation is used for inverter control. In the case of the numerical simulation VSI switches are ideal. On the other hand, for the purpose of the experimental verification, the 9-phase supply is provided by two custom-made 8-phase inverters with dead time equal to 6 μs. This leads to output waveforms containing the 5th and 7th order current harmonics. In addition, -29th and -31st harmonics were found to be present due to the non-ideal machine construction. Hence, in addition to flux/torque and torque sharing control, low order harmonic elimination by use of resonant VPI current regulators in a rotating reference frame has been implemented as well. A detailed description of the low order harmonic elimination is provided in section 3.6, while more detailed description of the experimental setup is available in the Appendix B of the thesis. A schematic of the complete control system is shown in Fig. 5.12. It should be noted that the presented control system is valid for any multiple 3-phase machine configuration and not just the 9-phase case, with the only difference being the number of subspaces and *x-y* current controllers.

The control system shown in Fig. 5.12 can be significantly simplified when there is no need for low-order harmonics elimination, i.e. PIccd regulator is kept for flux/torque control and single cvPI regulators per each *x-y* plane for current sharing, so that there is a total of 2*l* equivalent of real current controllers. This is the same number of current controller as in the case of control in MS variables.

The torque sharing capabilities are firstly tested for steady state operation while the 9-phase machine is used as an induction generator. In the simulation, the load torque is set to be -7 Nm, while in the experiment the induction machine is coupled to a dc machine that works in constant torque mode

providing the torque of -7 Nm. The nine-phase machine keeps the speed at the set value of 1250 rpm. The current sharing coefficients are set according to the following sequence:

- 0.0 s – 0.2 s $k_1 = 1.0$, $k_2 = 1.0$, $k_3 = 1.0$;
- 0.2 s – 0.6 s $k_1 = 0.4$, $k_2 = 1.2$, $k_3 = 1.4$;
- 0.6 s – 1.0 s $k_1 = 0.7$, $k_2 = 1.8$, $k_3 = 0.5$;
- 1.0 s – 1.4 s $k_1 = 1.5$, $k_2 = 0.0$, $k_3 = 1.5$;
- 1.4 s – 1.8 s $k_1 = 0.0$, $k_2 = 3.0$, $k_3 = 0.0$;
- 1.8 s – 2.0 s $k_1 = 1.0$, $k_2 = 1.0$, $k_3 = 1.0$;

In the beginning and at the end of the simulation/experimental run (0.2 s intervals) the machine is balanced and the current sharing coefficients are equal to one. The first two unbalanced sequences (0.4 s intervals) demonstrate the ability to arbitrarily control the torque production, and consequently the phase current amplitudes, in each winding set. The subsequent coefficient variations consider a case when one or two winding sets are completely switched off (0.4 s intervals). As a result, the machine operates as a 6- or a 3-phase one, respectively. This demonstrates one of the solutions for fault-tolerant operation, by switching off an entire winding set.

Both simulation and experimental results are shown next to each other. Current/torque sharing coefficients, VSD currents, and *d-q* currents of individual winding sets are shown in Fig. 5.13. The currents in *x-y* subspaces (the third and fourth plot in Fig. 5.13) are governed by the current/torque sharing coefficients (the first plot in Fig. 5.13) and instantaneous flux/torque producing *d-q*/α-β currents (the second/fifth plot in Fig. 5.13). Consequently, current and torque sharing between winding sets is achieved according to the applied coefficients, as can be seen from the individual winding *d-q* current plots in Fig. 5.13 and phase currents shown in Fig. 5.14. Even more importantly, phase currents within one winding set are always kept balanced. Since the total flux and torque producing currents i_d/i_q are kept constant, the total power transmitted to the shaft is unchanged. On the other hand, torque production in each winding set is varied as per torque producing *q*-axis current of a given set, as per (5.11).

Phase currents in Fig. 5.14b are obtained using the inverter's internal LEM sensors. Since acquisition is happening just before the control loop is executed, in the beginning and in the middle of the switching period, the acquired data represents currents averaged over one switching period. Hence, current ripple cannot be captured. On the other hand, phase currents i_{a1}, i_{a2}, and i_{a3} are captured by the oscilloscope and they are shown in the Fig. 5.15 for the same operating sequence as in Fig. 5.14. Further details about the experimental setup are available in the Appendix B of the thesis.

The machine speed, measured torque and generated electrical powers (total and in individual winding sets) are shown in Fig. 5.16. It can be observed that the power sharing between winding sets corresponds to the coefficient values. A noticeable drop in the total extracted power is due to the increased stator winding losses, as per (5.14). The machine under test here is a low power one, with a relatively large stator resistance; hence the increase in copper losses and drop in extracted power, which

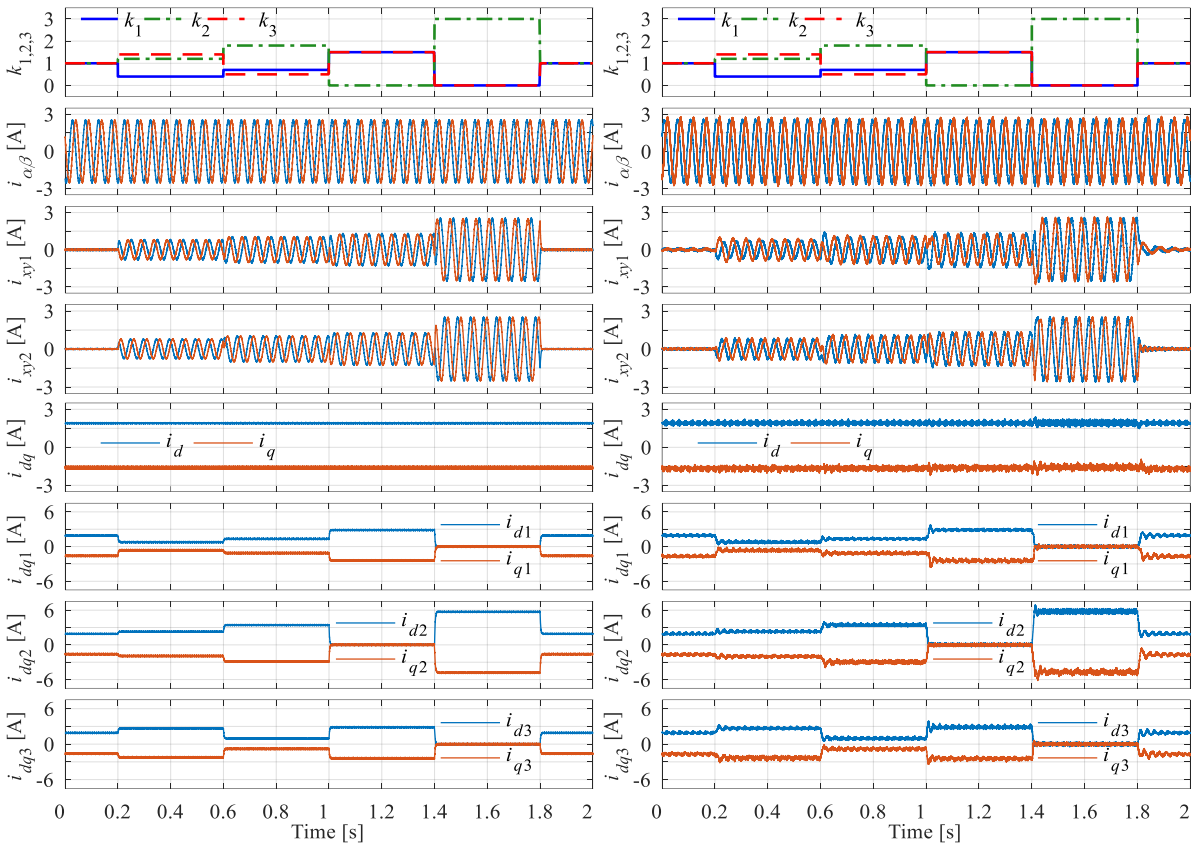

(a) Simulation (b) Experiment

Figure 5.13 – Current sharing coefficients, VSD currents and winding set *d-q* currents during steady-state operation.

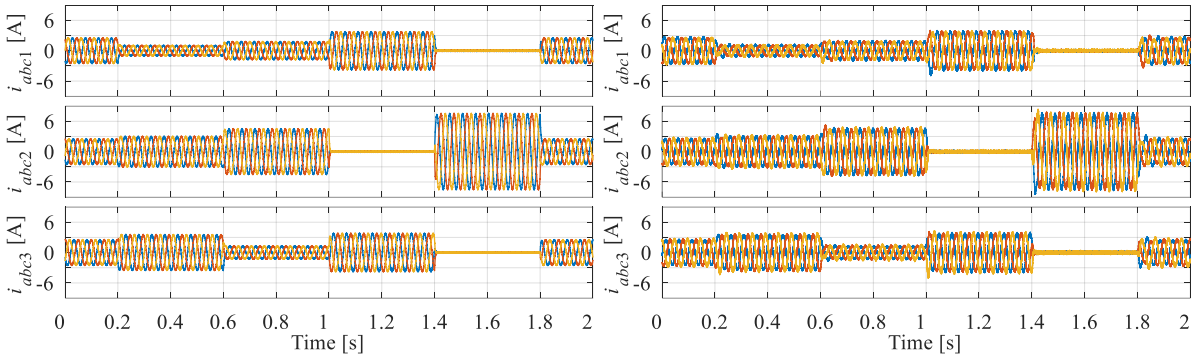

(a) Simulation (b) Experiment

Figure 5.14 – Phase currents during steady-state operation for the same conditions as in Fig. 5.13.

is especially severe when only one three-phase winding is operational, is expected. The last plot in Fig. 5.16 shows that there is no substantial increase in the phase voltages during the current/power sharing. Therefore, an increase in dc-link voltage would not be required during implementation of the proposed current/power sharing technique.

The previous simulation and experimental runs verify current sharing in steady state operation. Next, the same experiment is performed during a speed transient. The machine is accelerated from 1000 rpm to 1500 rpm within 2 seconds. The measured torque is now -6 Nm, with acceleration torque of 1 Nm (hence the prime mover torque stays at -7 Nm, as in the steady state test). The same set of results, as for

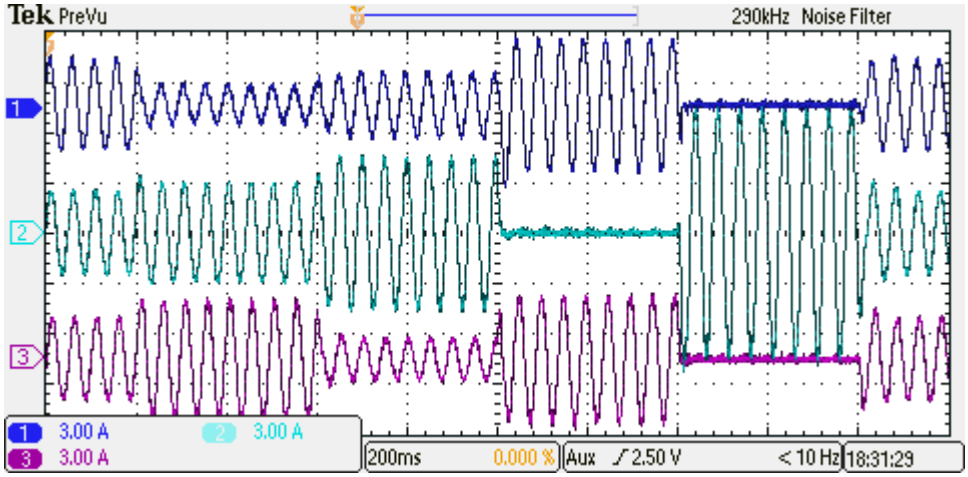

Figure 5.15 – Oscilloscope screenshot of the phase currents (i_{a1}, i_{a2}, i_{a3}) during steady-state operation.

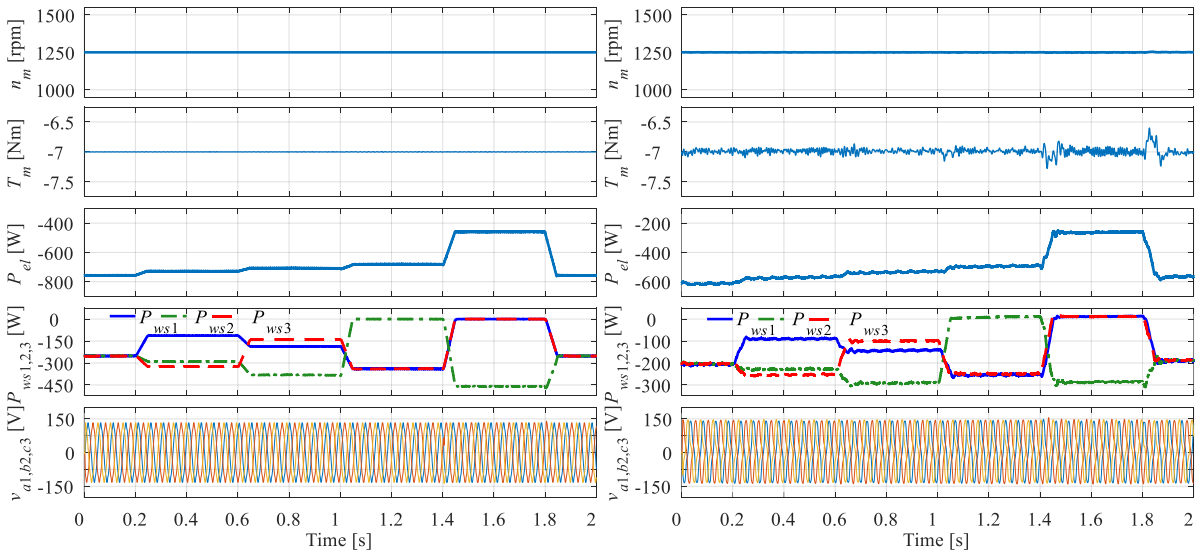

(a) Simulation (b) Experiment

Figure 5.16 – Machine speed, measured torque, electrical powers (total and winding sets) and phase voltages (v_{a1}, v_{b2}, v_{c3}) during steady state operation.

the steady state, are shown in Figs. 5.17 – 5.20. It can be seen that the developed current/torque sharing technique is also valid during the speed transient and the flux and torque producing d-q/α-β currents are not affected by applied current sharing between winding sets. Once again, phase currents i_{a1}, i_{a2}, and i_{a3}, shown in Fig. 5.19, are recorded by the oscilloscope. Since machine is now accelerating, while the torque is unchanged, extracted powers (Fig. 5.20) are changing during the experimental run. It should be noted that, in both experimental runs, a brief change in torque during the activation/deactivation of one or two winding sets is evident and it is the result of a sudden change in machine operation and the finite bandwidth of the current controllers.

A decrease in the extracted power during the current/power sharing, caused by an increase in the stator copper losses according to (5.14), is obvious in Figs. 5.16 and 5.20. Fig. 5.21 shows the stator winding losses obtained using the measured phase currents ($P_{\Omega m} = \Sigma R_s i_i^2$, i = 1, 2 … 9) and using (5.14) ($P_{\Omega s}$) for the constant speed operation for both simulation and experimental runs. A good

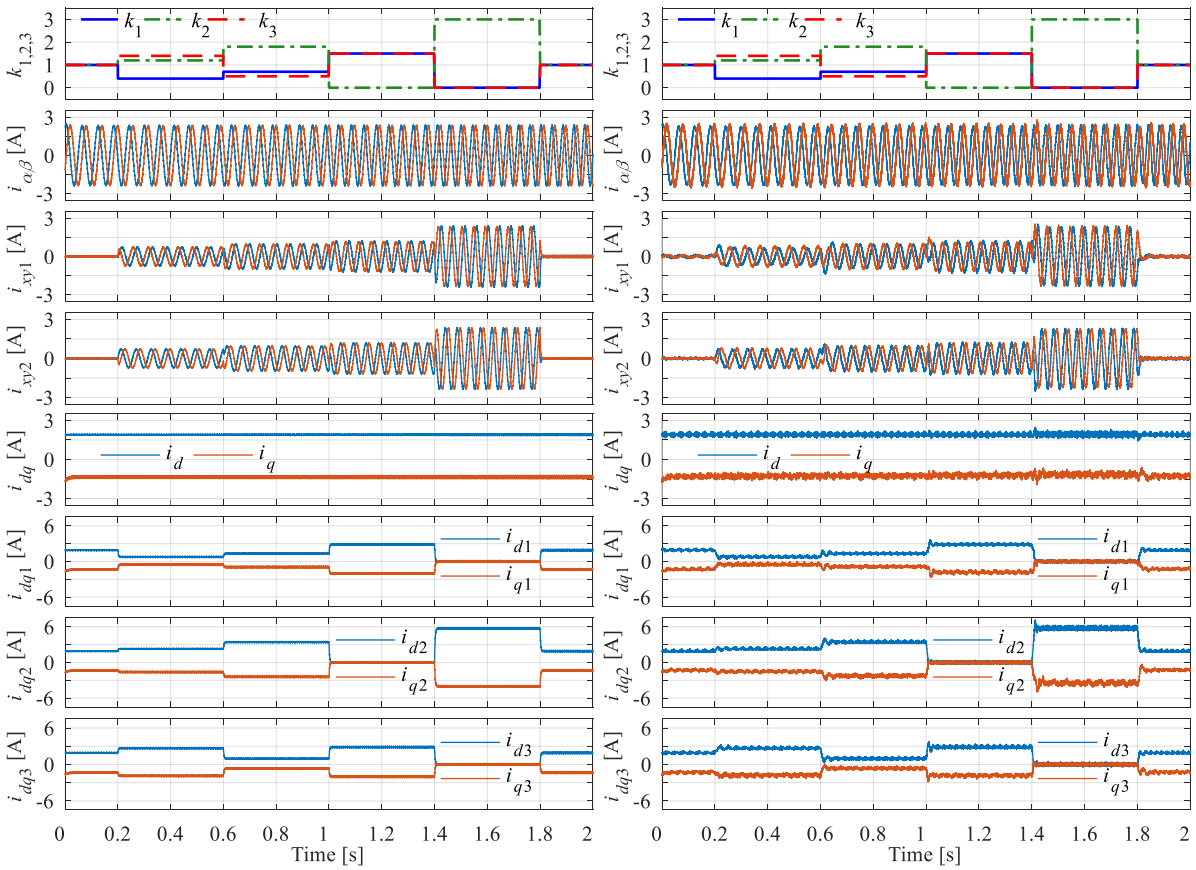

(a) Simulation (b) Experiment

Figure 5.17 – Current sharing coefficients, VSD currents and winding set *d*-*q* currents during speed transient.

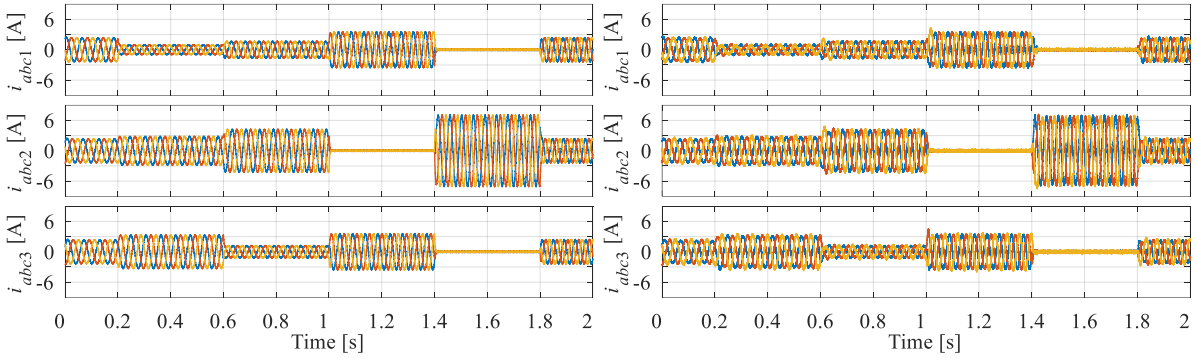

(a) Simulation (b) Experiment

Figure 5.18 – Phase currents during speed transient depicted in Fig. 5.17.

agreement between the two values is evident, thus confirming the validity of (5.14).

An increase in the torque ripple during the deactivation of one or two winding sets, which is evident in Figs. 5.20b, is expected and it is the result of machine working as a 6- or a 3-phase one. The stator winding of the machine is of a single layer type, so that only one third of the slots is used in the mode when a single three-phase winding is operational.

The conducted simulation and experimental results confirm the feasibility of the torque/current sharing technique in the case of the asymmetrical 9-phase machine. A comparison of the results shows that the differences are negligible, except in generated electrical powers (total and per winding). This is

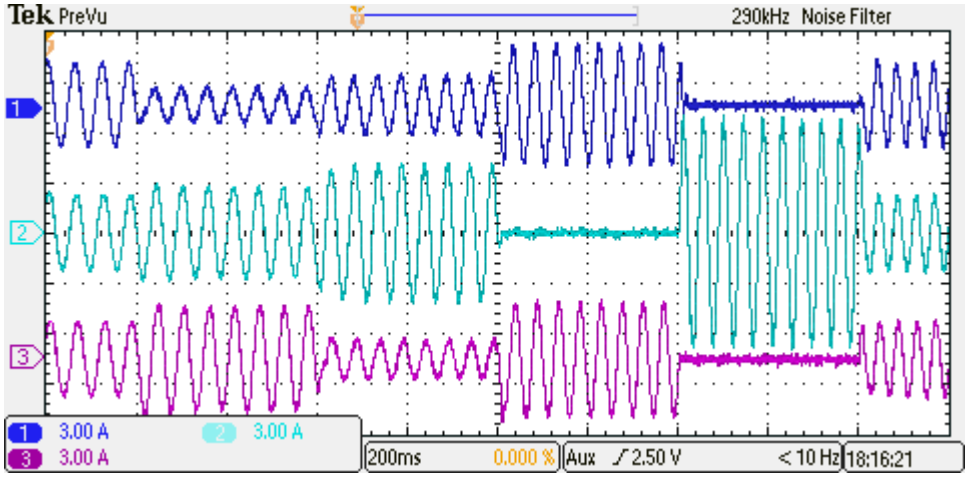

Figure 5.19 – Oscilloscope screenshot of the phase currents (i_{a1}, i_{a2}, i_{a3}) during speed transient.

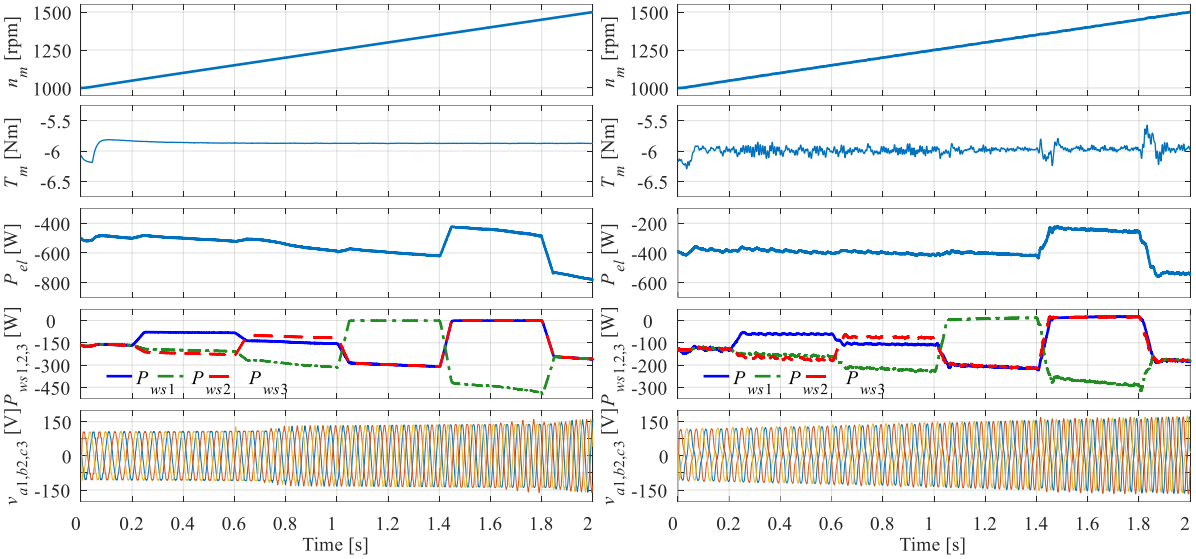

(a) Simulation (b) Experiment

Figure 5.20 – Machine speed, measured torque, electrical powers (total and winding sets) and phase voltages (v_{a1}, v_{b2}, v_{c3}) during speed transient.

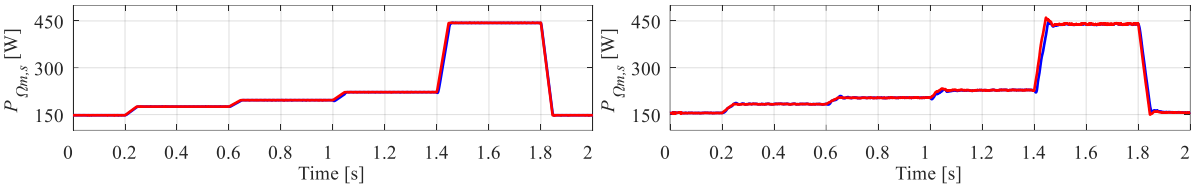

(a) Simulation (b) Experiment

Figure 5.21 – Stator winding losses $P_{\Omega m}$ (blue) and $P_{\Omega s}$ (red) during steady state operation.

to be expected – the experimental results include un-modelled effects (iron losses, mechanical losses due to friction and ventilation of two coupled machines and the torque-meter, saturation, stray no-load and stray load losses). However, except for the actual values, it is easy to see that the trends and the nature of the responses are the same.

5.5 Arbitrary *d-q* current sharing

Previous section has shown a simple implementation of torque/power sharing between winding sets of a 9-phase induction machine when both *d*- and *q*-axis currents of each winding set are changed equally according to current/power sharing coefficients. However, it may be of interests to vary winding set *d-q* currents arbitrarily, so that both active and reactive power of each winding set can be arbitrarily set. This section uses full form of equation (5.10) so that both *d*- and *q*-axis currents of each winding sets are governed by flux/torque producing VSD *d-q* current and two current sharing coefficients.

Although arbitrary current sharing of winding set *d-q* currents is already developed in section 5.3 for general case and transformation is tested for 6-, 9-, 12-, and 15-phase machines, it is intention of this section to implement actual control in the case of a 9-phase induction machine with 3 neutral points. The same simulation and experimental setup detailed in the section 5.4 is used here, so it will not be discussed any further. Moreover, control structure shown in the Fig. 5.12 is the same as well, with only difference being in the calculation of *x-y* current references. In the Fig. 5.12, *x-y* current references (bottom-left block) are calculated according the equation (5.12), whereas here they are calculated as per equation (5.10), so that there are six current sharing coefficients in total, instead of three. In this particular case of a 9-phase machine, actual *x-y* current references in appropriate rotational reference frame, as per (5.10), are as follows:

$$\begin{bmatrix} i_{dxy1}^{*} \\ i_{qxy1}^{*} \end{bmatrix} = \frac{1}{6}\begin{bmatrix} (2k_{d1} - k_{d2} - k_{d3}) & \sqrt{3}(k_{q2} - k_{q3}) \\ \sqrt{3}(k_{d2} - k_{d3}) & -(2k_{q1} - k_{q2} - k_{q3}) \end{bmatrix}\begin{bmatrix} i_{d}^{*} \\ i_{q}^{*} \end{bmatrix}$$
$$\begin{bmatrix} i_{dxy2}^{*} \\ i_{qxy2}^{*} \end{bmatrix} = \frac{1}{6}\begin{bmatrix} (2k_{d1} - k_{d2} - k_{d3}) & -\sqrt{3}(k_{q2} - k_{q3}) \\ \sqrt{3}(k_{d2} - k_{d3}) & (2k_{q1} - k_{q2} - k_{q3}) \end{bmatrix}\begin{bmatrix} i_{d}^{*} \\ i_{q}^{*} \end{bmatrix} \quad (5.17)$$

Two test scenarios have been considered in order to verify operation of the developed current sharing control. In the first test scenario, *d*-axis currents of all winding sets are kept equal ($k_{d1} = k_{d2} = k_{d3} = 1$) so that all winding sets equally contribute to the rotor flux production, while the torque producing *q*-axis currents of all winding sets are varied in the same manner as *d-q* currents in previous section by changing the corresponding coefficients in six time intervals as follows:

- 0.0 s – 0.1 s $k_{q1} = 1.0,$ $k_{q2} = 1.0,$ $k_{q3} = 1.0;$
- 0.1 s – 0.3 s $k_{q1} = 0.4,$ $k_{q2} = 1.2,$ $k_{q3} = 1.4;$
- 0.3 s – 0.5 s $k_{q1} = 0.7,$ $k_{q2} = 1.8,$ $k_{q3} = 0.5;$
- 0.5 s – 0.7 s $k_{q1} = 1.5,$ $k_{q2} = 0.0,$ $k_{q3} = 1.5;$
- 0.7 s – 0.9 s $k_{q1} = 0.0,$ $k_{q2} = 3.0,$ $k_{q3} = 0.0;$
- 0.9 s – 1.0 s $k_{q1} = 1.0,$ $k_{q2} = 1.0,$ $k_{q3} = 1.0;$

In the second test scenario both *d*-axis and *q*-axis currents of all winding sets are varied. Torque producing currents are varied in the same manner as in the first test, while the flux producing currents are varied in five time intervals as follows:

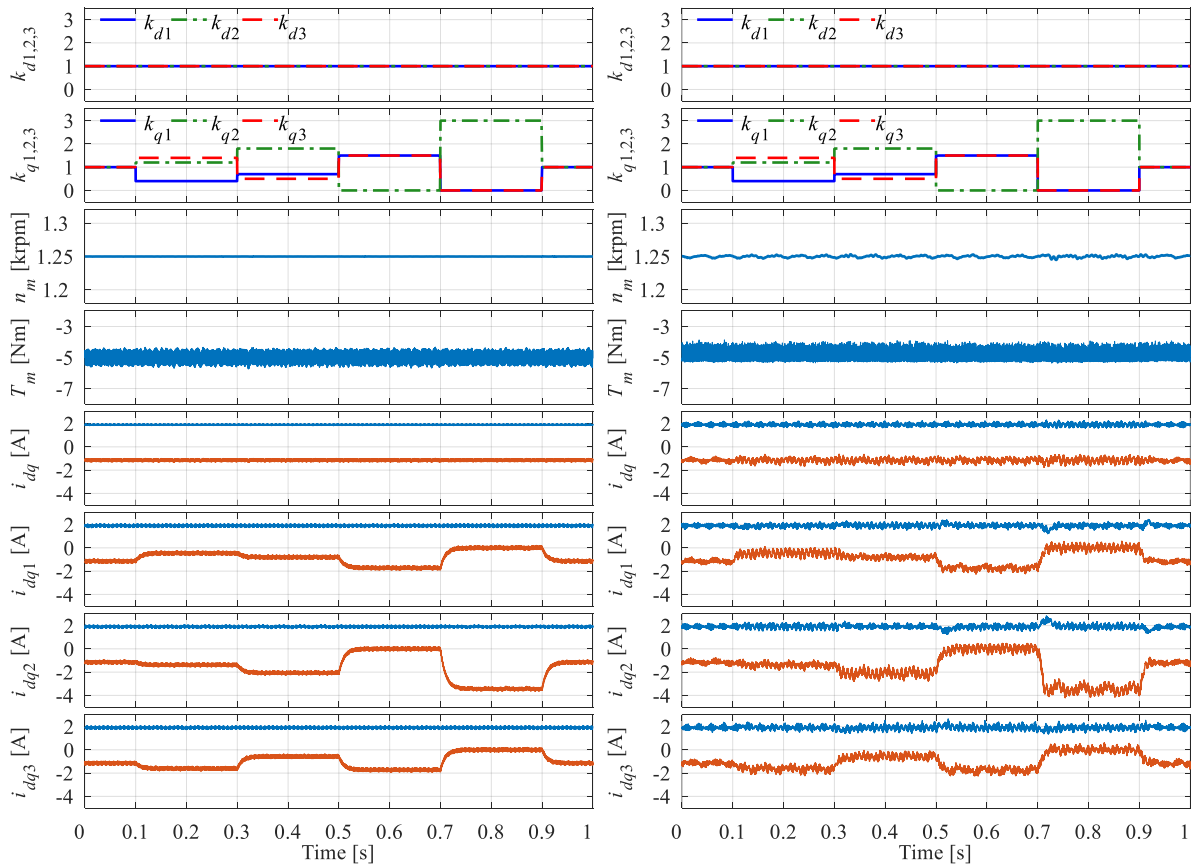

(a) Simulation (b) Experiment

Figure 5.22 – First test scenario: current sharing coefficients $k_{dq1,2,3}$, machine speed n_m, mechanical torque T_m, VSD and individual winding set currents i_{dq}, $i_{dq1,2,3}$ (blue trace *d*-axis currents and red trace *q*-axis currents).

- 0.0 s – 0.2 s $k_{d1} = 1.0$, $k_{d2} = 1.0$, $k_{d3} = 1.0$;
- 0.2 s – 0.4 s $k_{d1} = 1.5$, $k_{d2} = 0.0$, $k_{d3} = 1.5$;
- 0.4 s – 0.6 s $k_{d1} = 0.0$, $k_{d2} = 3.0$, $k_{d3} = 0.0$;
- 0.6 s – 0.8 s $k_{d1} = 1.3$, $k_{d2} = 0.5$, $k_{d3} = 1.2$;
- 0.8 s – 1.0 s $k_{d1} = 1.0$, $k_{d2} = 1.0$, $k_{d3} = 1.0$;

The first test scenario is obviously more realistic since all winding sets equally contribute to the rotor flux creation (reactive power), while torque producing *q*-axis currents govern active power of each winding set, enabling power sharing between winding sets. The second test scenario is aimed at demonstrating the ability to arbitrarily change both *d*- and *q*-axis currents of each winding set. In both test scenarios currents are changed to random values and to the extreme cases, where either *q*- or *d*-axis currents are zero in one or two winding sets. During both tests machine operates at constant speed of 1250 rpm and generating mode with load torque equal to -5 Nm. It should be noted that there are no limits imposed on the current controller, so that phase current can rise above nominal and current sharing can be tested to the full extent.

Simulation and experiment results for the first test scenario are shown in Figs. 5.22 – 5.24. Fig. 5.22 shows current sharing coefficients, machine speed and mechanical torque, VSD *d*-*q* currents, as well as

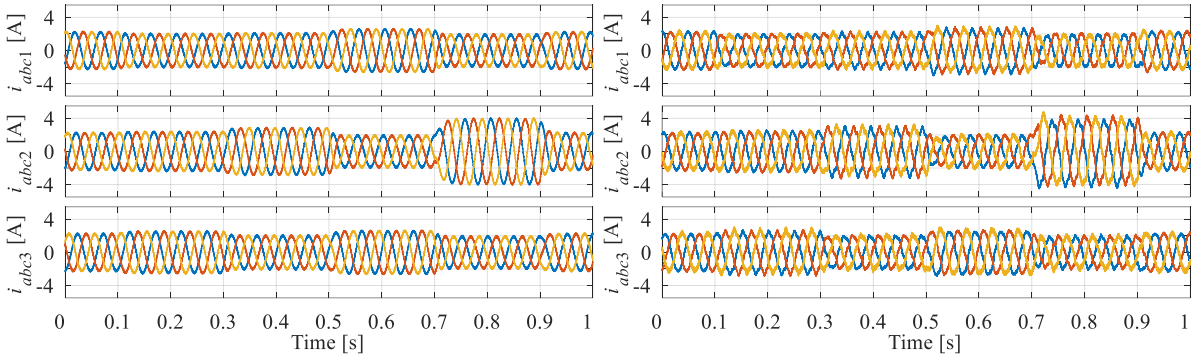

(a) Simulation (b) Experiment

Figure 5.23 – First test scenario: Phase currents for the same conditions as in Fig. 5.22.

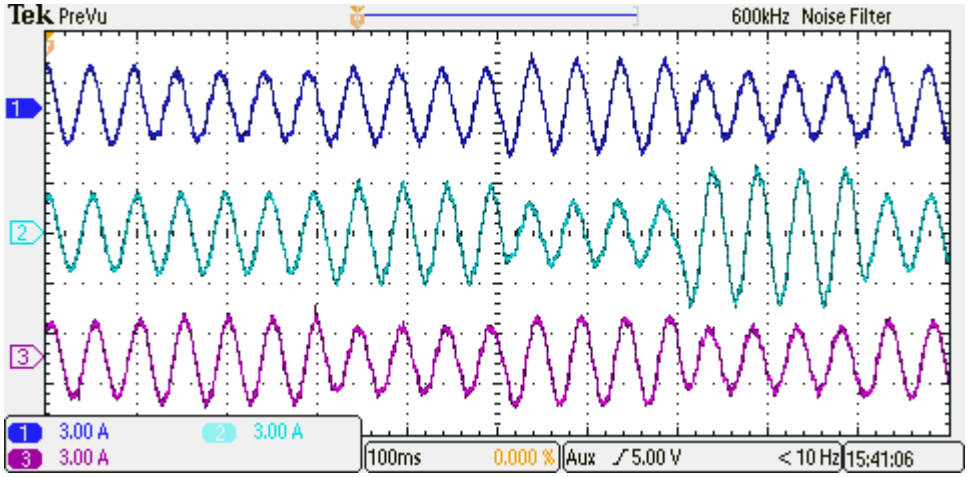

Figure 5.24 – First test scenario, experiment: Oscilloscope screenshot of the phase currents (i_{a1}, i_{a2}, i_{a3}).

d-q currents of each winding set. Since current sharing coefficients defining winding set *d*-axis currents are kept constant and equal to 1, there is no change in flux producing currents $i_{d1,2,3}$, i.e. flux contribution of all winding set is the same. On the other hand, winding sets *q*-axis currents are changed according to the imposed current sharing coefficients $k_{q1,2,3}$ and VSD *q*-axis current, as shown in bottom three plots of Fig. 5.22. Fifth plot of the same figure shows that despite change of individual winding set *d-q* currents, VSD *d-q* currents are unaffected and there is no change in the machine torque and speed. This behaviour is shown previously and is a consequence of changing only flux/torque non-producing *x-y* currents.

Phase currents obtained from the simulation and measured by dSPACE from the experiment are shown in the Fig. 5.23, as well as the oscilloscope screenshot of the phase currents in the 1st phase of each winding set (Fig. 5.24). When compared to the previous section, where both *d*- and *q*-axis winding set currents where changed equally, change in phase current amplitude in this case is less severe due to the equal contribution of all winding sets to flux producing *d*-axis current. Since current sharing is implemented in the rotational reference frame, phase currents within each winding set are balanced.

Second test scenario considers arbitrary change of both *d*- and *q*-axis currents in each winding set. Simulation and experiment results are available in the Figs. 5.25 – 5.27. Current sharing coefficients,

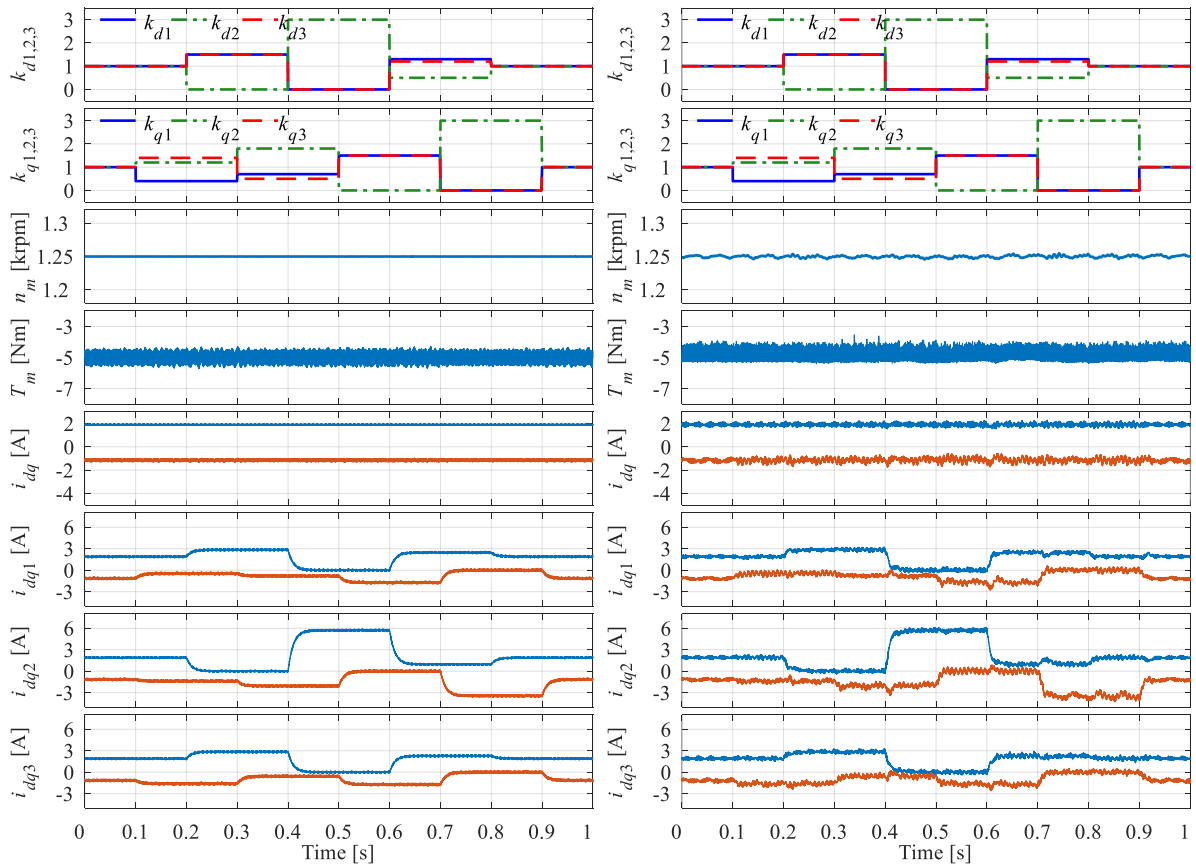

(a) Simulation (b) Experiment

Figure 5.25 – Second test scenario: current sharing coefficients $k_{dq1,2,3}$, machine speed n_m, mechanical torque T_m, VSD and individual winding set currents i_{dq}, $i_{dq1,2,3}$ (blue trace *d*-axis currents and red trace *q*-axis currents).

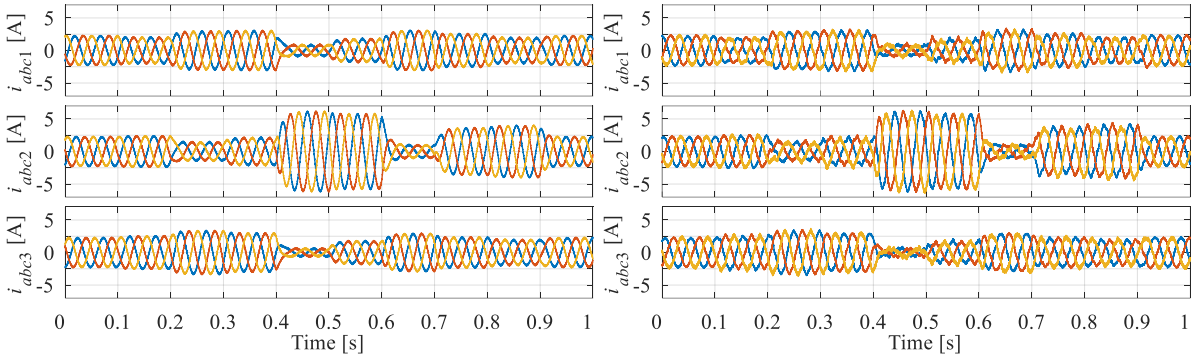

(a) Simulation (b) Experiment

Figure 5.26 – Second test scenario: Phase currents for the same conditions as in Fig. 5.25.

machine speed and torque, VSD *d-q* currents and individual winding set *d-q* currents are shown in the Fig. 5.25. It can be seen in both simulation and experimental results that individual winding set *d-q* currents are changed according to the current sharing coefficients and VSD *d-q* current, confirming the feasibility of the proposed solution. Once again, VSD flux/torque producing current i_{dq} is unchanged, so that machine flux and torque are not affected.

Phase currents for the second test scenario are shown in Fig. 5.26 for both simulation and experiment, while oscilloscope screenshot of the currents in first phase of each winding set can be seen

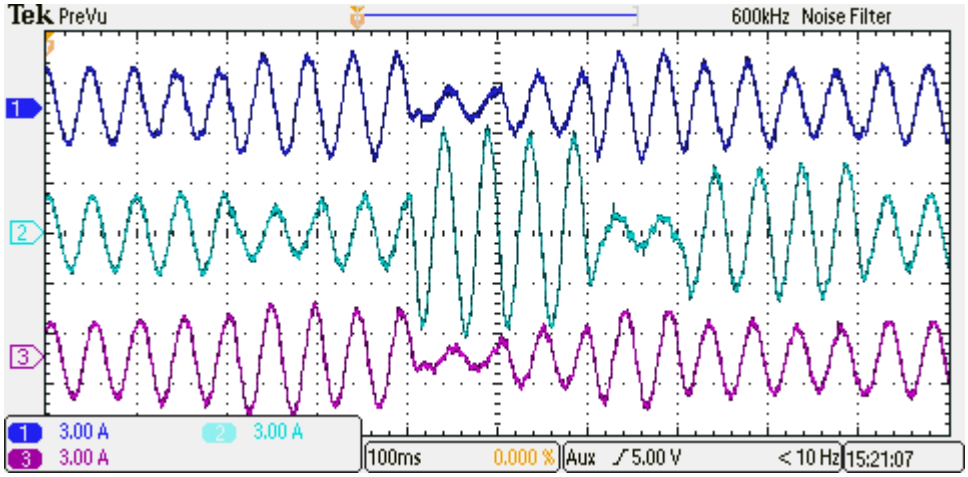

Figure 5.27 – Second test scenario, experiment: Oscilloscope screenshot of the phase currents (i_{a1}, i_{a2}, i_{a3}).

in Fig. 5.27. Amplitude of the phase currents is governed by the imposed winding set *d-q* currents and it can be seen that its value is greatly increased for certain combination of current sharing coefficients due to the absence of current limiting (in a real-world application care should be taken to ensure that phase current does not exceed maximum allowed value).

Both scenarios tested here are the extreme cases of step change of current sharing coefficients within very short time interval, which demonstrate high dynamic capability of the system. In normal operation rapid current change within 0.1/0.2 s interval would not be required. A good agreement between simulation and experiment results in evident in both test scenarios, confirming the proposed theory.

5.6 Summary

This chapter discuses different techniques for current and power sharing between winding sets of a multiple 3-phase winding machines. Theoretical considerations regarding the relationships between MS and VSD modelling approaches, presented in the chapter 4, are used here as a basis for development of current and power sharing.

Firstly, a current sharing technique between winding sets in the stationary reference frame is developed. It provides ability to vary α-β currents of each winding set while the VSD flux/torque producing α-β currents are unchanged, assuring that total flux and torque of the machine are undisturbed. Since current sharing is realised in stationary coordinates, α-β current vector travels along an elliptical path enabling creation of an imbalance between currents of the single winding set. This behaviour provides the means to implement fault-tolerant operation by producing such an imbalance that will impose zero current in an individual phase of a winding set. However, fault tolerance is beyond the scope of this chapter and is not considered any further.

Since flux and torque control is usually implemented in rotational coordinates, the current sharing between winding sets is realised in rotational coordinates as well. Consequently, the *d-q* current vector of each winding set takes a circular path and the phase currents in each winding set are balanced. Of course, the total flux and torque production of the machine is not affected. This current sharing

technique is later used to define torque/power sharing, allowing for torque production by each winding set to be arbitrarily varied while total torque is unchanged. In addition, two sets of simulations and experiments were realised. In the first test, both *d*- and *q*-axis current sharing coefficients were equally varied allowing for unchanged angle of each winding set *d*-*q* current vector. On the other hand, in the second test, *d*- and *q*-axis current sharing coefficients were independently changed allowing for arbitrary change of flux/and torque contribution of all winding sets.

All the developed current sharing techniques are valid for any multiphase machine with a standard winding configuration, i.e. asymmetrical/symmetrical with single/multiple neutral points. The theory is verified by numerical simulations in the case of the current sharing techniques for asymmetrical 6-, 9-, 12- and 15-phase configurations with a single neutral point, while current/power sharing is verified by both numerical simulations and experiments in the case of the asymmetrical 9-phase induction machine with three neutral points.

Chapter 6

DC-LINK VOLTAGE BALANCING OF THE CASCADED VOLTAGE SOURCE INVERTERS

6.1 Introduction

Previous two chapters of the thesis have showed three different multiphase machine modelling approaches and a technique for arbitrary current and power sharing between winding sets of a multiple 3-phase machines. Furthermore, topologies where developed current/power sharing can be utilised are presented as well. One of the possibilities, especially interesting for the off-shore WECS, is a topology where a multiple 3-phase winding machine with multiple isolated neutral points is supplied by 3-phase VSIs with cascaded dc links. This configuration produces a single high voltage dc link which is highly desirable feature in WECS where transmission lines are high-voltage dc or ac and a step-up converter and/or transformer is used.

Series connection of the dc links has recently been examined for multiphase machines. A 6-phase generator for WECS is considered in [Che et al (2012b), Che et al (2012c), Che et al (2014b)] where two winding sets are supplied by VSIs with series-connected dc links. It is shown that this configuration is capable of balancing dc-link voltages of the machine-side converters even in the case of imbalance in machine phases.

As far as machines with more than two 3-phase winding sets are concerned, a 12-phase permanent magnet machine has been considered in [Sulligoi et al (2011)], where uncontrolled bridge rectifiers were used with additional series connected dc-dc converters. Next, hybrid [Xiang-Jun et al (2012)] and modular configurations [Yuan et al (2012), Ng et al (2008)] have been proposed to increase the dc-link voltage by using series-connected converters. However, all these solutions require special converter or machine structure. In contrast to this, the solution developed here uses standard 3-phase inverters and is capable of balancing individual dc-link voltages.

The fact that the 9-phase machine's stator consists of three mutually isolated winding sets is utilised in this chapter to increase the dc-link supply voltage without increasing the rating of the switches or capacitors used in the individual 3-phase inverters. This is achieved by cascading the dc links of the 3-phase inverters that provide supply for each of the winding sets. It is shown that in order to balance

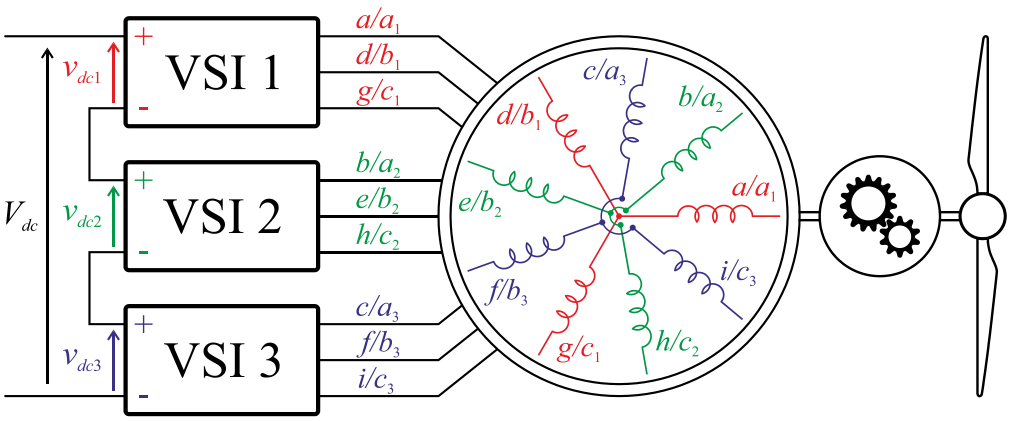

Figure 6.1 – Symmetrical 9-phase machine with cascaded VSIs.

voltages of individual dc links, it is necessary to use current sharing between winding sets of the machine. The work presented in this chapter has been published in [Zoric et al (2017a)].

Modelling and control of the system is based here on the VSD. This enables machine control with fully decoupled flux and torque producing and non-producing current components. Since VSIs are connected in series any imbalance in machine phases will have an impact on currents and powers of individual winding sets and consequently produce an imbalance in the dc-link voltages. In order to keep dc-link voltages at the set level, the system is analysed and a balancing controller is derived. It is shown that in order to balance dc-link voltages, control of power flow between winding sets is necessary. A current and power sharing algorithm based on the considerations of chapter 5 is utilised here. A complete controller structure capable of balancing individual dc-link voltages is devised. It is shown and verified by simulation and experimental results that the introduced system is viable in the presence of imbalance of a whole winding set or in an individual phase.

6.2 System Model of a Nine-Phase Machine with Cascaded dc Links

The considered machine is a symmetrical 9-phase induction machine with three isolated neutral points. Individual phase spatial position angles are therefore governed with:

$$[\theta_{9s}] = \left[0 \quad \frac{2\pi}{9} \quad \frac{4\pi}{9} \quad \frac{2\pi}{3} \quad \frac{8\pi}{9} \quad \frac{10\pi}{9} \quad \frac{4\pi}{3} \quad \frac{14\pi}{9} \quad \frac{16\pi}{9}\right] \tag{6.1}$$

Each 3-phase winding set is supplied by one 2-level 3-phase voltage source inverter (VSI), while the VSI's dc links are cascaded in order to produce higher dc-link voltage. A schematic of the system is shown in Fig. 6.1.

Voltages v_{dc1}, v_{dc2}, v_{dc3}, and V_{dc} represent local VSI dc-link voltages and the total dc-link voltage, respectively. It is obvious that, by cascading the inverter dc links, the total dc-link voltage is three times higher than the dc-link voltage of any individual 3-phase inverter. It follows that inverter switches and, more importantly, dc-link capacitors can have three times lower voltage rating when compared to the output dc-link voltage.

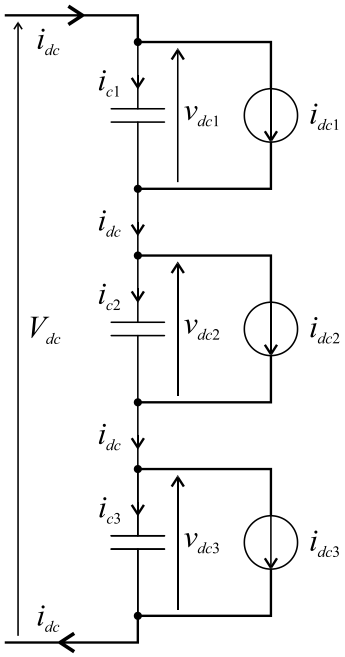

Figure 6.2 – Dc-link capacitors currents and voltages.

It is assumed that the system is connected to the high-voltage dc grid or a grid connected inverter. In both cases V_{dc} is kept constant by external means not shown here. On the other hand, dc-link voltages v_{dc1}, v_{dc2}, v_{dc3} are controlled by the local VSIs. The problem that arises here is that these voltages are dependent on power/current of the corresponding inverter and any imbalance in machine phases or inverter switches may produce imbalance in the dc-link voltages. Consequently, one of the local dc-link voltages may exceed switch or capacitor rating, while simultaneously leading to unequal power sharing between the windings. Hence, dc-link capacitor voltage balancing control needs to be devised.

In order to analyse the problem, a schematic representation of the cascaded inverters is given in Fig. 6.2. Capacitor currents are i_{c1}, i_{c2}, and i_{c3}, while VSI currents are denoted with i_{dc1}, i_{dc2}, and i_{dc3}. Current i_{dc} is the total dc-link current and it depends on the instantaneous machine's power. Capacitor currents are governed with:

$$i_{cj} = i_{dc} - i_{dcj}, \quad j = 1, 2, 3 \tag{6.2}$$

If C is the dc-link capacitance, dc-link voltages and their Laplace transforms are as follows:

$$\begin{aligned} v_{cj} &= \frac{1}{C}\int \left(i_{dc} - i_{dcj}\right) dt \\ v_{cj} &= \frac{1}{sC}\left(i_{dc} - i_{dcj}\right) \end{aligned} \tag{6.3}$$

In the shown system i_{dc} is not controllable; however, i_{dcj} (j = 1, 2, 3) can be individually regulated. Since dc-link voltage references are constants, feed-forward control can be easily employed. Considering this and the fact that the plant model is an integrator ($1/(sC)$), error-free control of v_{dcj} in steady state can be achieved by a simple PI regulator with a negative gain. In this configuration the voltage balancing regulator affects only Δi_{dcj}, as shown in Fig. 6.3.

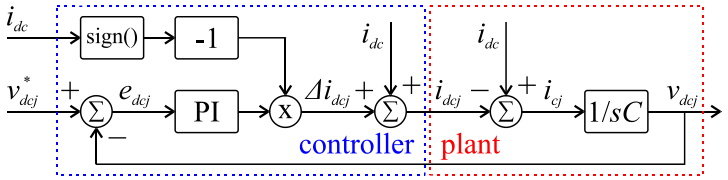

Figure 6.3 – Dc-link voltage balancing controller.

The presented analysis holds true if the machine is operating in motoring mode, as per current directions shown in Fig. 6.2. However, if the machine is in the generating mode, dc-link currents have opposite sign and consequently gain in the PI regulator needs to change sign to a positive value. A simple way of establishing whether the machine operates in motoring or generating mode is to find the sign of the dc-link current i_{dc}. Taking this into consideration yields the control scheme for one of the dc-link voltages shown in Fig. 6.3.

It should be noted that the goal is to balance the individual dc-link voltages. Since the total dc-link voltage is constant and equal to the sum of the individual dc-link voltages, the controller of Fig. 6.3 should be employed only for two dc-link currents. In order to implement dc-link voltage balancing control, current control should be developed first. Moreover, if one dc-link current is increased, another one should be decreased so that the produced power stays the same. Hence current/power sharing between the 3-phase winding sets should be implemented while keeping the machine operation (flux and torque) unaffected.

6.3 Machine Model and Current Sharing between Winding Sets

A machine with multiple winding sets, such as the machine considered here, is usually controlled either by applying (MS) or VSD transformations, as it is shown in the previous chapters. In this case (MS) modelling approach would be an obvious choice due to the possibility of individual control of each winding set and consequently each VSI dc-link current. On the other hand, VSD modelling approach provides decoupling of the machine into flux/torque producing α-β subspace and non-producing x-y subspaces. It therefore provides clearer and unique harmonic mapping and eases the current control design. Hence, machine is modelled using VSD, i.e. control can be implemented in decoupled VSD subspaces, but individual winding set flux/torque producing currents (α-β) are represented by multiple d-q (i.e., α-β) variables. By doing so, advantages of both modelling approaches are utilised.

Machine modelling and relationship between MS and VSD modelling approaches have been discussed in great detail in chapter 4, where induction machine equations in both MS and VSD variables can be found in (4.22) – (4.24) and (4.45), respectively, while the relationship between individual winding set variables (MS) and the VSD subspace variables is established in general case in (4.62) and (4.63). Furthermore, it is shown in chapter five that this relationship can be utilised for current and power sharing between winding sets, without disturbing total flux and torque production of the machine.

If equalised current sharing is used (here in stationary α-β reference frame), coefficients are k_1, k_2 and k_3. Machine currents in VSD subspaces in complex form are as follows:

$$\begin{aligned}
\underline{i}_{\alpha\beta} &= \frac{1}{3}\left(k_1 + k_2 + k_3\right) I_{\alpha\beta} e^{j\varphi_{\alpha\beta}} \\
\underline{i}_{xy1} &= \frac{1}{3}\left(k_1 + k_2 e^{j\frac{2\pi}{3}} + k_3 e^{-j\frac{2\pi}{3}}\right) I_{\alpha\beta} e^{-j\varphi_{\alpha\beta}} \\
\underline{i}_{xy2} &= \frac{1}{3}\left(k_1 + k_2 e^{j\frac{2\pi}{3}} + k_3 e^{-j\frac{2\pi}{3}}\right) I_{\alpha\beta} e^{j\varphi_{\alpha\beta}}
\end{aligned} \tag{6.4}$$

Since each winding set is supplied by a single 3-phase VSI, power sharing coefficients k_1, k_2, k_3 directly regulate power of each VSI and therefore the dc-link currents. The last two equations provide references for *x*-*y* currents based on the desired power sharing coefficients and flux/torque producing currents $i_{\alpha\beta}$. As current balancing is achieved by imposing currents in the *x*-*y* planes, the flux and torque of the machine are unaffected. When the last two equations of (6.4) are returned into scalar form, references for *x*-*y* currents are obtained as:

$$\begin{aligned}
\begin{bmatrix} i_{x1}^* \\ i_{y1}^* \end{bmatrix} &= \frac{1}{6}\begin{bmatrix} 2k_1 - k_2 - k_3 & \sqrt{3}\left(k_2 - k_3\right) \\ \sqrt{3}\left(k_2 - k_3\right) & -2k_1 + k_2 + k_3 \end{bmatrix}\begin{bmatrix} i_\alpha \\ i_\beta \end{bmatrix} \\
\begin{bmatrix} i_{x2}^* \\ i_{y2}^* \end{bmatrix} &= \frac{1}{6}\begin{bmatrix} 2k_1 - k_2 - k_3 & \sqrt{3}\left(-k_2 + k_3\right) \\ \sqrt{3}\left(k_2 - k_3\right) & 2k_1 - k_2 - k_3 \end{bmatrix}\begin{bmatrix} i_\alpha \\ i_\beta \end{bmatrix}
\end{aligned} \tag{6.5}$$

Equations (6.5) provide the means for successful implementation of the dc-link voltage balancing control.

6.4 Dc-Link Voltage Balancing Control Structure

Coefficients k_1, k_2 and k_3 define current amplitudes in each of the three winding sets and consequently the power flow. Hence, they can be used for dc-link voltage balancing. In balanced operation all *k* coefficients are equal to unity and the average values of currents i_{dc}, i_{dc1}, i_{dc2}, and i_{dc3} over one switching period are the same. On the other hand, when there is an imbalance in the dc-link voltages, the coefficients can be changed accordingly in order to return the system to balanced dc-link voltage operation. It follows that feed-forward control that sets all coefficients to unity can be used to improve the system response. In this case PI regulators only have to control difference in the current sharing coefficients Δk. Furthermore, sum of all coefficients needs to be always equal to three, so only two coefficients are controlled while the third one is calculated based on values of the first two. This is in accordance with the conclusion from the previous section with regard to the control of only two dc-link voltages. Complete dc-link voltage balancing controller structure including the flux/torque control and transformation matrices is shown in Fig. 6.4.

The dc-link voltage balancing control provides current sharing coefficients (k_1, k_2, k_3), which are then converted into *x*-*y* current references by current sharing equations (6.5). Since *x*-*y* subspace equations (4.45b) are equivalent to those of an *R*-*L* load, two complex vector PI regulators are used for

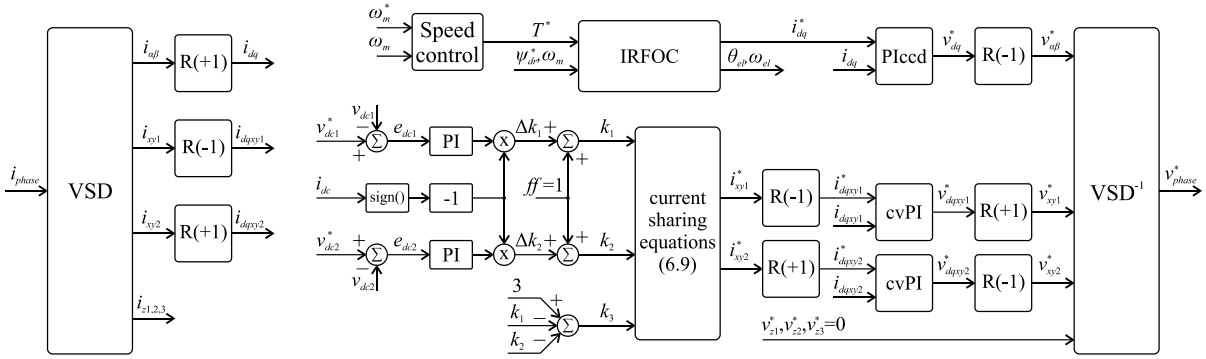

Figure 6.4 – Complete structure of dc-link voltage balancing controller.

x-y current control, as discussed in chapter 3. The regulator for the first *x-y* subspace is implemented in an anti-synchronous reference frame, while the regulator for the second subspace is implemented in the synchronous reference frame, as shown in Fig. 6.4 by R(-1) and R(+1) blocks, respectively. Required direction of rotation is governed by (6.4).

It should be noted that the dc-link voltage balancing technique is quite easily extendable to any multiple 3-phase winding machine with isolated neutral points. It is only required to apply current sharing technique presented in the chapter 5 for a given number of phases, while the analysis for the individual dc-link voltages is the same regardless of the number of winding sets. The number of PI controllers needed for balancing individual dc-link voltages is always going to be equal to *l*-1, where *l* is the number of winding sets.

Obviously, besides dc-link voltage balancing, flux and torque control must be implemented as well. Since the machine is modelled by VSD, decoupled flux and torque control can be implemented in the same way as for the 3-phase induction machine, i.e. by controlling currents in flux/torque producing α-β subspace. In this case, flux and torque are controlled by use of IRFOC, where actual implementation is detailed in chapter 3. The machine is tested further on with closed loop speed control and a PI controller is used for this purpose.

6.5 Simulation Results

The symmetrical 9-phase induction machine with single pole pair, three neutral points and cascaded 3-phase VSIs, as shown in Fig. 6.1, is tested using Matlab simulations. The machine parameters are given in Table 6.1. The VSIs are 2-level, with 600 V dc links. Cascaded connection creates an 1,800 V dc link. Switches are taken as ideal, so that the dead-time harmonics are not present. Carrier-based pulse width modulation (CBPWM) is used for VSI control with switching frequency equal to 5 kHz. Used machine model is in terms of phase variables, as explained in chapter 4, while control structure is shown in Fig. 6.4. All current controllers, IRFOC and CBPWM are implemented as discussed in chapter three.

Table 6.1 – Parameters of the symmetrical 9-phase Machine.

P_n	U_n	I_n	n_n	R_s	R_r	L_{ls}	L_{lr}	L_m
2.2 kW	230 V	1.5 A	2880 rpm	4.85 Ω	1.82 Ω	18 mH	8.6 mH	1383.6 mH

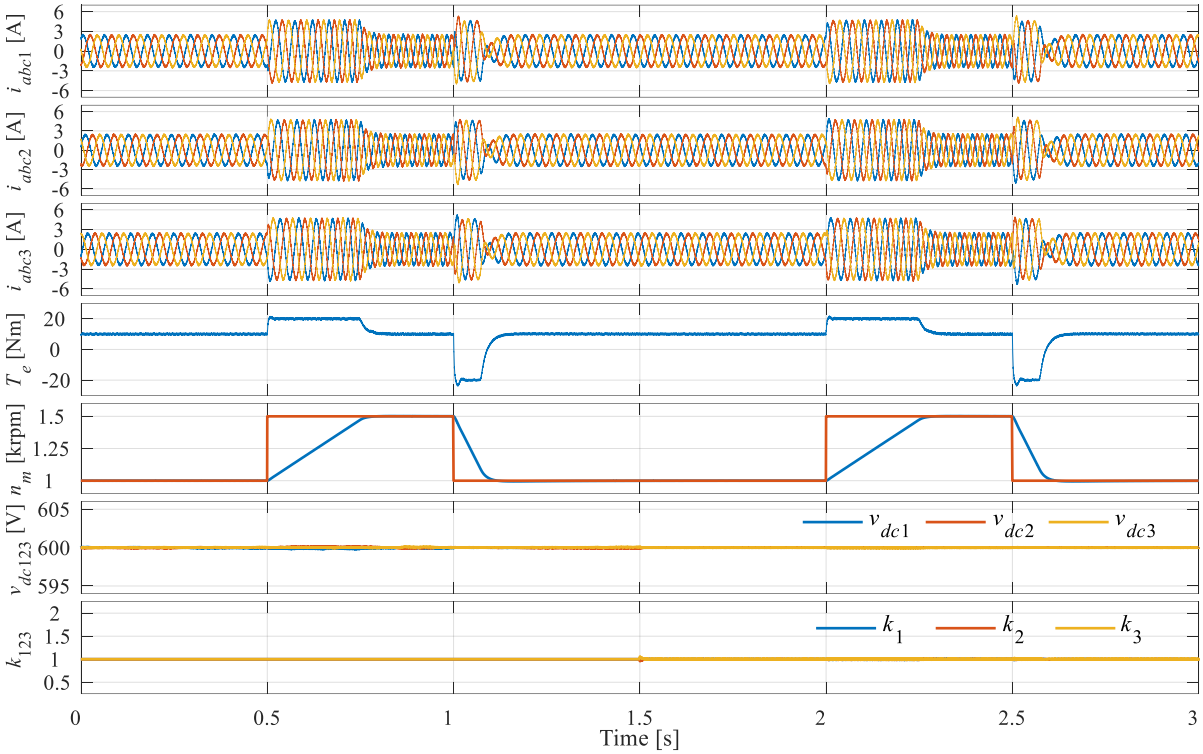

Figure 6.5 – Phase currents in the 3-phase windings, torque, speed, dc-link voltages and current sharing coefficients in the case of the balanced machine.

Simulation is performed at first with the balanced machine, Fig. 6.5. In the initial steady state, the load torque is 10 Nm and the machine runs at 1000 rpm. The speed reference is stepped to 1500 rpm and later returned back to 1000 rpm. The same sequence is repeated twice. During the first sequence v_{dc} control is switched off. It is then switched on before the second speed stepping to 1500 rpm, at 1.5 s. Since the machine is balanced, there are no fluctuations in the dc-link voltages throughout the entire simulation. Even though dc-link voltage balancing control is switched on in the second half of the simulation, it does not affect the machine operation. Phase currents are balanced and identical during both sequences, as shown in the first three plots. This test was carried out to verify that additional control structures, i.e. dc-link voltage balancing control and *x-y* current controllers, will not affect behaviour of the drive. It is easily seen that voltage balancing controller is inactive since there is no change in current sharing coefficients.

The previous simulations are done again. However, there is now imbalance in the phase windings. The second winding set has an additional resistance of 3 Ω in each phase. Results are shown in Fig. 6.6. It can be seen that without the dc-link voltage balancing control phase currents of the 2nd winding set (second plot in Fig. 6.6) have smaller amplitude when compared with the other two winding sets. Consequently, there is a substantial imbalance in dc-link voltages (the sixth plot in Fig. 6.6). On the other hand, when balancing control is turned on (at t = 1.5 s) imbalance in dc-link voltages is removed and $v_{dc(1,2,3)}$ are all kept at the set level even during transient. As shown in the last plot of Fig. 6.6, current

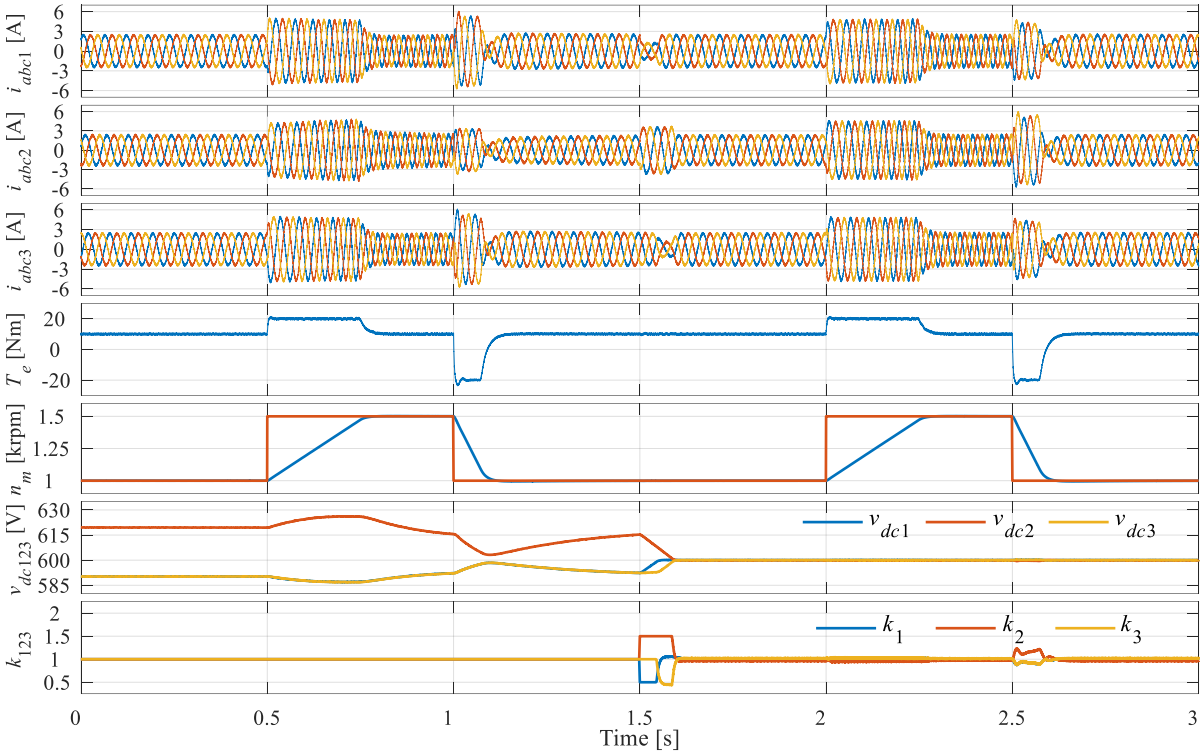

Figure 6.6 – Phase currents in the 3-phase windings, torque, speed, dc-link voltages and current sharing coefficients in the case of the imbalance in one of the winding sets.

sharing coefficients are varied to correct dc-link voltages. The first two coefficients are limited to the range [0.5 – 1.5], so that the third coefficient cannot be negative or rise above 2. Imposed limits ensure that all winding sets always work in the same regime (motoring or generating) and current amplitudes in the third winding set are kept at a reasonable value. It should be emphasised that in the last plot v_{dc1} and v_{dc3} are overlapped for the most of the simulation time due to the nature of the introduced imbalance.

Motoring operation was considered so far. To show that the control works just as well in generation, an additional test has been carried out. The speed reference is now kept constant while the mechanical torque is changed from +10 Nm to -10 Nm and back. Hence the machine works in both motoring and generating modes. Moreover, a different type of imbalance has been simulated. A resistance (5 Ω) is added in the first phase of the third winding set. Results are shown in Fig. 6.7. Once again, there is substantial imbalance in the dc-link voltages during the first sequence where voltage balancing controller is switched off. On the other hand, when balancing control is switched on (at t = 1.5 s), dc-link voltages are brought to 600 V and kept constant. Step change in load torque affects the machine speed, where change in speed is governed by speed controller time constant. However, even though both speed and torque are changed, dc-link voltages are still kept at the set level by dc-link voltage balancing control.

It should be noted that, when an imbalance exists only in one machine phase, torque ripple is increased. Since the developed current/power sharing control deals with the whole winding sets, this ripple cannot be mitigated with the proposed controller structure.

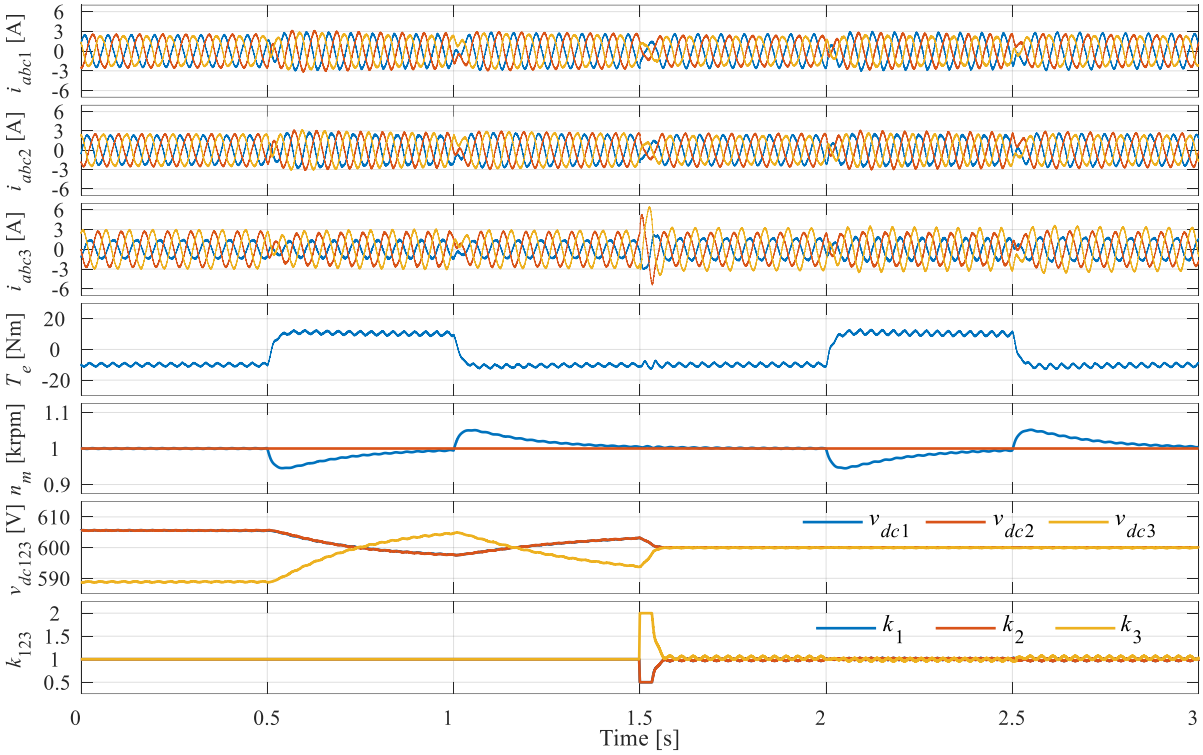

Figure 6.7 – Phase currents in the 3-phase windings, torque, speed, dc-link voltages and current sharing coefficients in the case of the imbalance in one of the machine phases.

This test completes verification by Matlab simulations of the proposed voltage balancing techniques. Both steady state and transient operation have been considered and it was found that control is valid in both cases. Next section deals with the experimental verification, where the same technique is applied to the asymmetrical 9-phase machine.

6.6 Experimental Verification

Developed dc-link voltage balancing control has been implemented and verified by simulation for a symmetrical 9-phase induction machine. However, topology shown in the Fig. 6.1 is identical regardless of the machine winding configuration, i.e. symmetrical or asymmetrical. Hence, the same voltage balancing controller can be used for an asymmetrical case as well. Moreover, it is shown in chapter five that, if appropriate VSD transformations are used, current sharing equations are identical for both symmetrical and asymmetrical cases. It follows that control shown in Fig. 6.4 is valid for both topologies with the only difference being the applied VSD transformation.

This section provides experimental verification of the developed dc-link voltage balancing technique. Namely, an asymmetrical 9-phase machine is supplied by three 3-phase VSIs with cascaded dc links in the same manner as shown for the symmetrical case in Fig. 6.1. Used inverters are two 2-level and one 3-level, where difference in used VSIs is dictated by the equipment availability in the laboratory. VSIs are supplied by single high voltage dc link created by Spitzenberger & Spies linear amplifier PAS2500, which is capable of sinking power by use of accompanying resistive load RL4000.

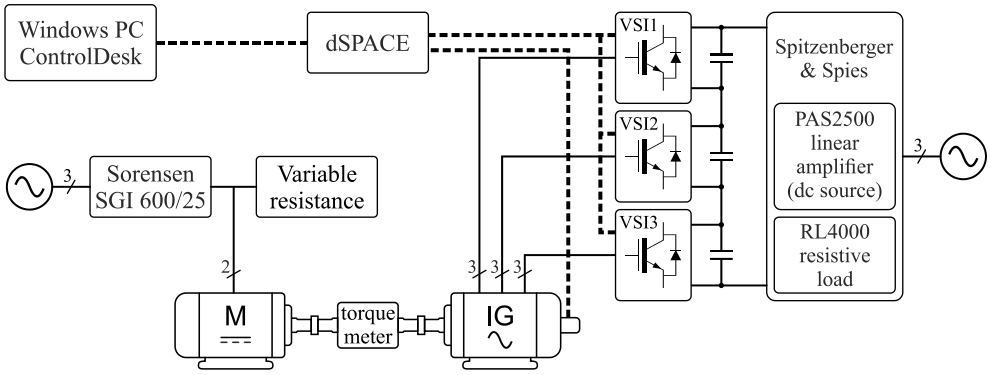

Figure 6.8 – Schematic of the experimental setup.

High voltage dc link is set to 600 V, while the individual dc-link voltages are 200 V. These reduced values are necessary due to the insulation requirements of the machine. Nevertheless, experimental results are still valid and the only constraint is in the maximum achievable machine speed, which is obviously reduced due to the limited input voltage.

Control and measurement are performed by a dSPACE rapid prototyping system, while additional measurements are available through Tektronix oscilloscopes and isolated current and high voltage differential voltage probes. Used machine has 2 poles and is rated at 230 V and 2.2 kW with the parameters given in the Table 6.2. Machine is mechanically coupled to the permanent magnet dc machine which can act as a load or a prime mover. This is achieved by connecting a resistor bank to the permanent magnet dc machine (i.e. it acts as a load), or constant current source, in which case it behaves as a constant torque source. Constant current is provided by a Sorensen SGI 600/25 dc source. Mechanical torque is measured by torque sensor and captured by one of the oscilloscope channels. Torque sensor provides positive signal when dc machine acts as a prime mover and induction machine operates as a generator. Schematic of the experimental setup is shown in Fig. 6.8, while a more detailed description is available in the Appendix B of the thesis.

Table 6.2 – Parameters of the asymmetrical 9-phase Machine.

P_n	U_n	I_n	n_n	R_s	R_r	L_{ls}	L_{lr}	L_m
2.2 kW	230 V	1.5 A	2880 rpm	5.3 Ω	2 Ω	24 mH	11 mH	520 mH

Similar test scenarios to the ones completed in the simulations are repeated here. The machine is firstly tested without any imbalance between the phases by changing the speed from 250 rpm to 550 rpm while driven by constant 3 Nm torque. Next, the same test is repeated with imbalance in the machine phases, i.e. the second winding set has additional 5.4 Ω resistance in all phases. The final test is performed with the machine running at the constant speed of 500 rpm, while the load torque is changed from positive to negative to observe both motoring and generating modes of operation. In this last test, additional 5.4 Ω are added to the first phase of the third winding set. All tests are repeated with and without dc-link voltage balancing control.

Results for the balanced machine operation are shown in the Fig. 6.9. Dc-link voltage balancing

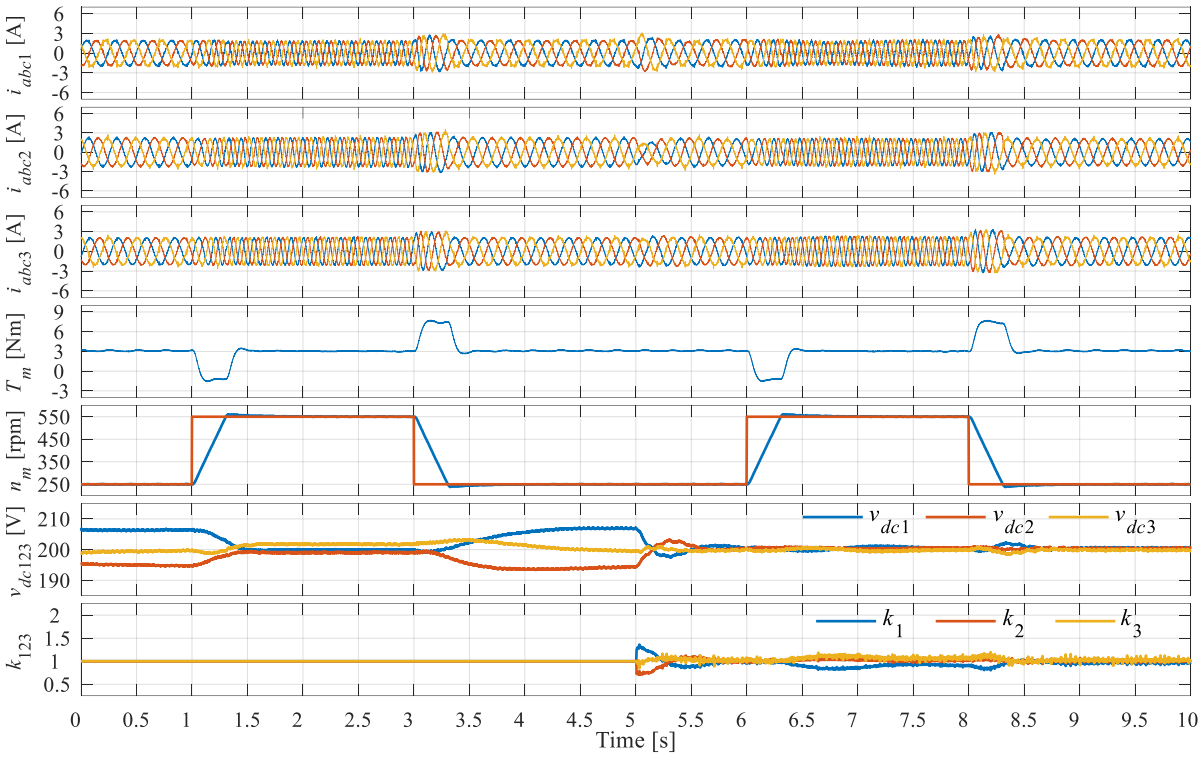

Figure 6.9 – Phase currents in the 3-phase windings, torque, speed, dc-link voltages and current sharing coefficients in the case of the balanced machine.

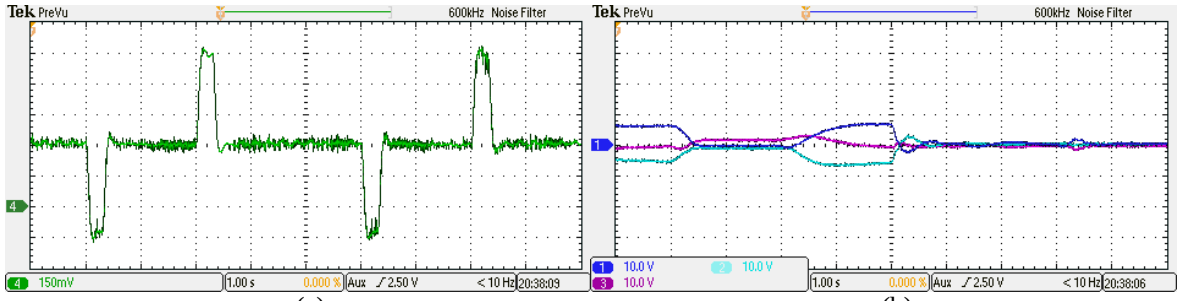

(a) (b)

Figure 6.10 – Oscilloscope screenshots of the machine mechanical torque (a) and dc-link voltages (b) in the case of the balanced machine.

controller is switched off during the first 5 seconds of the experiment. It can be easily seen that there is an imbalance in dc-link voltages even though there is no additional imbalance in any winding set. This behaviour can be attributed to the difference in used VSIs and imbalance in the machine parameters. Nevertheless, after the dc-link voltage balancing controller is switched on at $t = 5$ s, dc-link voltages are brought to 200 V and kept at the set value with very little oscillations during the speed transient. Oscilloscope screenshots of the machine torque and dc-link voltages are available in the Fig. 6.10. Torque sensor gain is 0.1 V/Nm, while offset for dc-link voltages is set to 200 V.

In the second test additional 5.4 Ω are added to each phase of the second winding set, while the same speed profile has been imposed and machine is driven at constant 3 Nm torque. Phase currents, mechanical torque, speed, dc-link voltages and current sharing coefficients are shown in the Fig. 6.11.

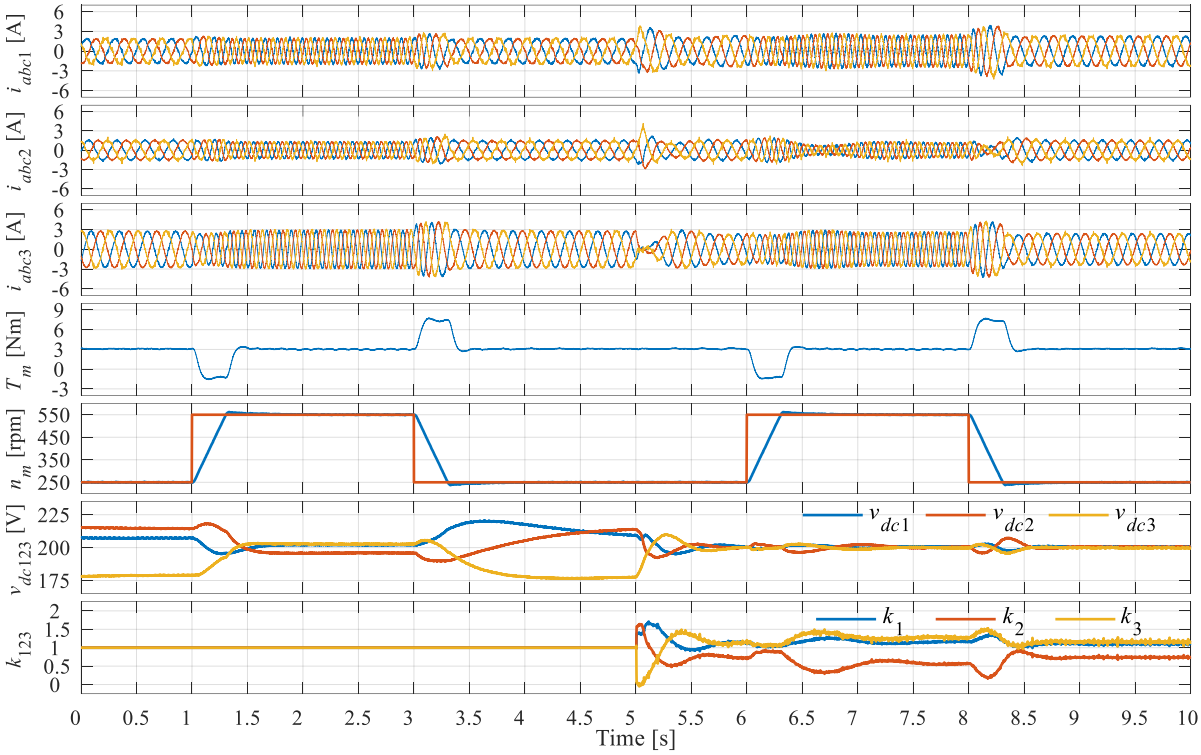

Figure 6.11 – Phase currents in the 3-phase windings, torque, speed, dc-link voltages and current sharing coefficients in the case of the imbalance in one of the winding sets.

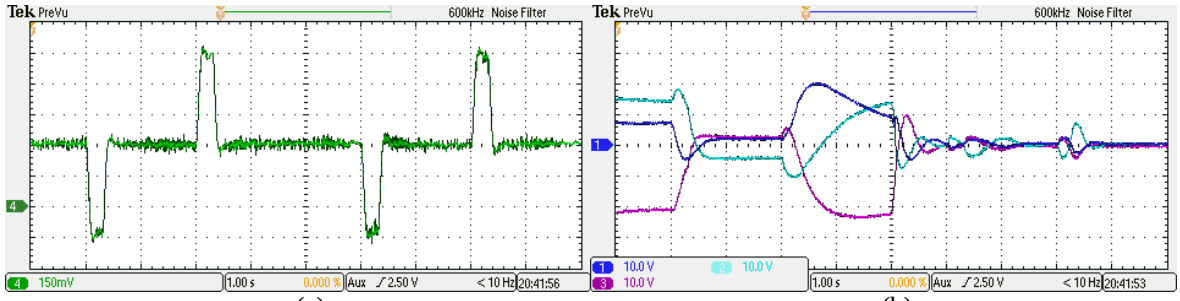

(a) (b)

Figure 6.12 – Oscilloscope screenshots of the machine mechanical torque (a) and dc-link voltages (b) during the imbalance in one of the winding sets.

It can be seen that the difference in dc-link voltages is now more severe during the first 5 seconds of the experiments due to the added imbalance in phase resistances. On the other hand, when dc-link voltage balancing control is switched on (t = 5 s) dc-links are stabilised at 200 V. Small oscillations during transient are due to controllers' finite response. A noticeable change in the current sharing coefficients can now be seen in the last plot of the Fig. 6.11 which is present due to the increased imbalance. Once again, oscilloscope screenshots of the torque and dc-link voltages are available in the Fig. 6.12. (a) and (b), respectively.

The final test is performed at a constant speed of 500 rpm with the torque changed from positive to negative. The experimental results are available in the Fig. 6.13. In this case imbalance is present only in a single phase of the machine, hence the actual difference in dc-link voltages is very small (i.e. bellow 5 V) even when the dc-link voltage balancing control is switched off. Still, this voltage difference is

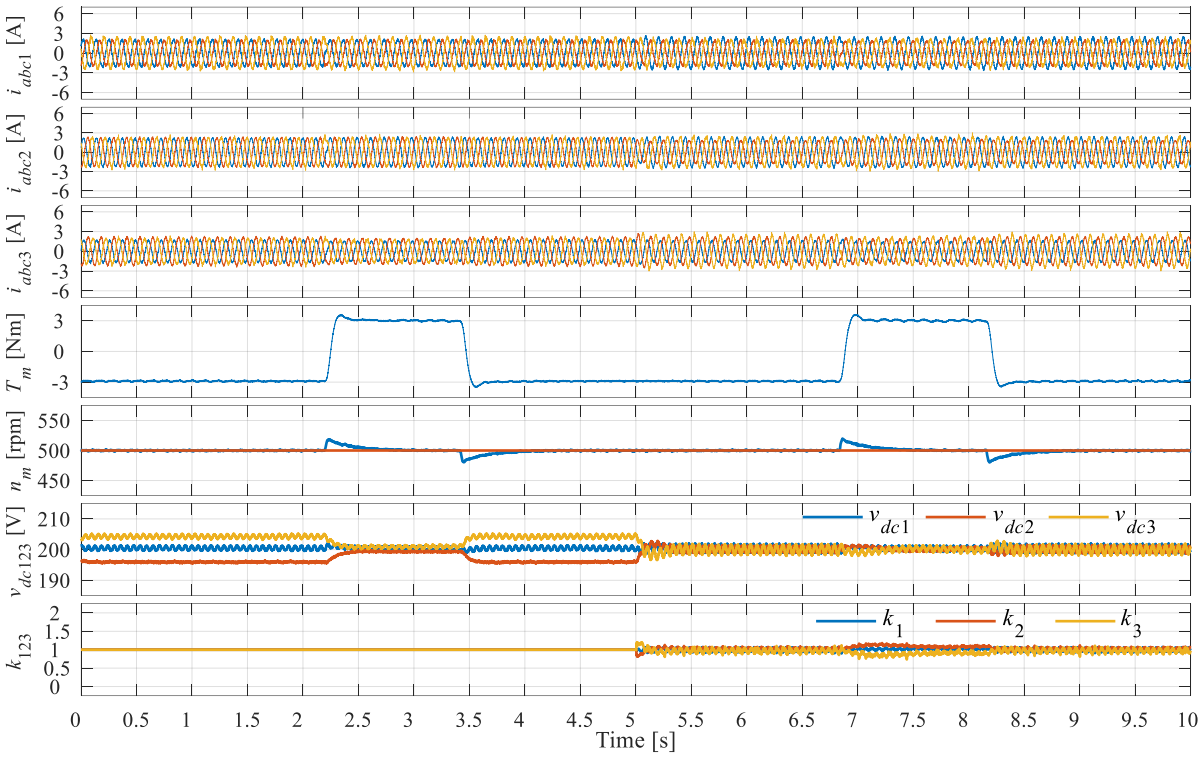

Figure 6.13 – Phase currents in the 3-phase windings, torque, speed, dc-link voltages and current sharing coefficients in the case of the imbalance in one of the machine phases.

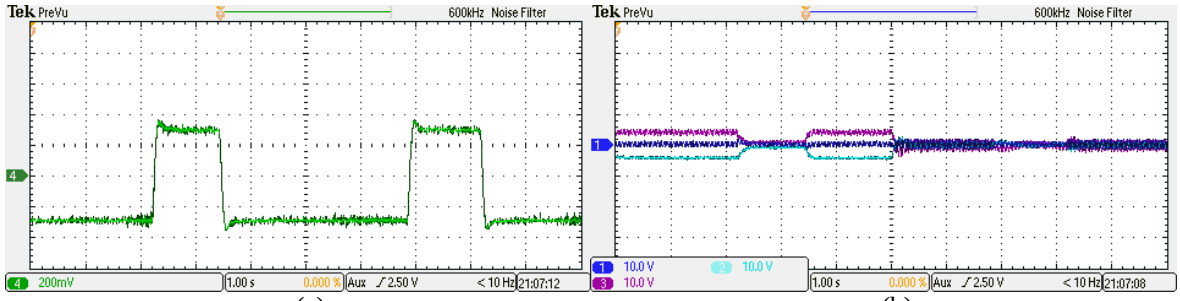

(a) (b)

Figure 6.14 – Oscilloscope screenshots of the machine mechanical torque (a) and dc-link voltages (b) in the case of the imbalance in one of the machine phases.

removed when dc-link voltage balancing controller is switched on at t = 5 s. It should be noted that in this particular sort of imbalance, there is a noticeable voltage ripple in dc-link voltages. This behaviour is a consequence of imbalance within the winding set and for its removal additional control in x-y planes is needed as indicated in [Che et al (2014c)]. Furthermore, imbalance within the winding set causes a torque ripple as well, as shown in the simulation results in the Fig. 6.7. However, in the experimental results, this ripple is not seen since it is supressed by the internal torque sensors low pass filter.

6.7 Summary

The additional degrees of freedom provided by the multiphase machine are used to produce a high-voltage dc link with cascaded inverters of a lower voltage rating. A 9-phase induction machine with isolated neutral points is supplied by three 3-phase inverters with cascaded dc links, therefore forming one high-voltage dc link with three times higher voltage than that of the individual VSI dc links. The

topology enables use of switches, and more importantly capacitors, with three times lower voltage rating in a system where high dc-link voltage is mandatory or highly desirable, such as a wind turbine with high-voltage dc or ac transmission lines. It should be noted that, although dc-link voltage is elevated, so is the insulation requirement on the 3-phase windings. This can be mitigated to a certain extent by proper selection of voltage vectors [Che (2013)]. However, this is outside the scope of the thesis and is not discussed any further.

The developed solution is based on the presented analysis of the inverters with series connected dc links and arbitrary current/power sharing between winding sets. The performance of the topology is verified using multiple simulation and experimental scenarios including both steady state and transient operation. Moreover, different types of imbalance in machine phases have been considered in both motoring and generating modes. A machine with symmetrical winding configuration has been used in simulation, while experiments have been run on an asymmetrical 9-phase machine.

It should be emphasised that implemented topology with cascaded dc links has one major drawback when fault tolerance is concerned. Namely, if a fault occurs in any 3-phase VSI, that particular inverter needs to be switched off, resulting in shutting down the whole system due to the series connection of inverter dc links. In other words, fault tolerance of a multiphase machine is traded for the single high voltage dc link. In safety critical application, where high reliability is required, this behaviour is not acceptable, so more favourable topology would be the parallel connection of the inverters discussed in the chapter five of the thesis.

Chapter 7

CONCLUSION

7.1 Summary and Conclusions

The thesis explored use of multiple 3-phase winding induction machines as a generator in wind energy conversion systems. This specific type of the multiphase machines is selected since it is the most frequently used multiphase machine type in both industry and academia. Benefits of having multiple 3-phase winding sets have been utilised to accommodate specific supply needs that might arise when a wind turbine is connected to the standard 3-phase grid, ac or dc micro-grids, or isolated loads, e.g. different power requirements of each winding set or complete shutdown of a winding set due to the fault. In order to achieve the best possible control of multiple 3-phase winding machines, both MS and VSD modelling have been explored and relationship between machine variables in the two modelling approaches has been found for the general case. This has enabled to implement the control by use of decoupled machine model, i.e. multiple orthogonal two-dimensional subspaces of VSD modelling, while information on individual winding sets is preserved, a feature of MS modelling. Since the relationship has been found by only comparing VSD and MS transformation, it is applicable to any multiple 3-phase winding machine type regardless of machine construction, i.e. synchronous or induction. In order to generalise the said relationship, a unified way of creating the VSD matrix for both symmetrical and asymmetrical configurations has been developed. Ultimately, derived correlation has been employed to implement current and power sharing between winding sets while keeping the control in decoupled VSD subspaces. Theoretical development has been verified by simulation and by experimental investigation using as an example an asymmetrical 9-phase induction machine with three isolated neutral points. It has been shown that power can be arbitrarily shared between winding sets without disturbing total flux and torque production of the machine. Furthermore, the same machine has been used to increase dc-link voltage by cascading three VSIs supplying each winding set. By doing so, total dc-link voltage can be tripled when compared to rated dc-link voltage of the individual VSIs. The same power sharing technique has been used to balance dc-link voltages in the case of the imbalance in machine phases.

After a brief introduction into the multiphase machines and WECS areas, the thesis starts with literature survey of published work relevant for this particular field of study. Firstly, literature covering

multiphase machines in general and WECS is covered. Next, a survey of modelling techniques for multiphase induction machine is completed, where modelling in phase, MS, and VSD variables is considered. In order to complete the literature survey related to machine-side control structures, work on PWM modulation techniques and current control of multiphase machines is presented next. Since one of the main contributions of this thesis is current and power sharing between winding sets, the available literature on the subject is subsequently covered. Examples of power sharing by use of both VSD and MS modelling approaches can be found. Because current sharing can be used to switch off complete winding set, work dealing with operation under fault has been reviewed as well. Finally, literature survey is completed with literature covering converter topologies and control system needed for WECS operation.

The next chapter provides more details on the operation of WECS in general. Modelled wind turbine is of horizontal type with gearbox and pitch control mechanism, where used model is as simple as possible since thesis deals with the electrical subsystem only. The goal of this chapter is to provide detailed considerations for various WECS subsystems and to show implementation of common control techniques related to WECS so that they can be simply referred to later in the thesis, with the emphasis in subsequent chapters being placed on the novelty. Furthermore, possible topologies where advantages of multiple 3-phase winding machines are utilised are shown as well. Back-to-back configuration, where 9-phase two-level VSI supplies 9-phase induction generator and three-level NPC VSI connects system to the grid, is taken as an example to demonstrate operation of all major control systems needed for WECS operation. On the machine side, implemented controls are MPPT, IRFOC, decoupled current control of 9-phase induction generator by means of VSD and multiple current controller structure (PIccd for flux/torque control, cvPI for *x-y* current control, resonant VPI for low order harmonics elimination), and 9-phase two-level CBPWM as a modulation strategy. In order to connect WECS to the grid, VOC control is used for the active and reactive power control, and consequently for dc-link voltage control, while PLL is implemented for grid voltage synchronisation. Grid-side NPC inverter gating signals are provided by three-level CBPWM.

Machine modelling has been dealt with in the fourth chapter of the thesis. All three modelling approaches are considered, i.e. modelling using phase, MS and VSD variables. Phase variables where used to implement machine model for the general case so that it is easily implemented in Simulink environment. On the other hand, modelling in MS and VSD variables has been considered for the purpose of implementing flux and torque control, low order harmonic elimination and current and power sharing between winding sets. Benefits of both modelling approaches have been utilised resulting in relationship between VSD and MS variables applicable to the general case. Consequently, all control loops can be implemented in the multidimensional space defined with the VSD transformation of the machine, while it is still possible to access variables of individual winding sets, a feature of MS modelling approach. This was made possible by developing an algorithm for creation of the VSD transformation matrix, such that it is applicable to the general case as well. In the same chapter,

discussion on resulting odd order harmonic mapping for the most commonly used multiphase machines is offered. By providing the correlation between MS and VSD variables, this section has set basis for current and power sharing between winding sets, discussed in the following chapter. The last section of this chapter contains discussion on imbalance in zero-sequence harmonics of phase voltages in the case of an asymmetrical multiphase machines with single neutral point. It has been analytically proven that imbalance exists even in the case when all the leg voltage harmonics are balanced.

Relationship between MS and VSD variables, derived in chapter 4, is used in chapter 5 to develop current and power sharing between winding sets while the actual current control is implemented on the basis of the decoupled VSD model of the machine. Firstly, current sharing between winding sets in the stationary reference frame is developed, using α-β current components of the winding sets. Next, current sharing using *d-q* currents of each winding set is developed as well. Both techniques are applicable in the general case and are valid for any multiple 3-phase winding machine, regardless of the machine configuration, i.e. asymmetrical or symmetrical, and with single or multiple neutral points. Current sharing in *d-q* coordinates is further utilised to develop power sharing between winding sets, again applicable in the general case as well. Theoretical findings were confirmed by simulation and experimentation using as an example the asymmetrical 9-phase induction machine with three neutral points. Since all developed current and power sharing techniques are implemented by imposing *x-y* currents of fundamental frequency, total flux and torque of the machine are unaffected.

Chapter 6 shows that benefit of having multiple isolated points can be utilised to produce single high voltage dc link without increasing VSI voltage ratings, an important factor in the design of WECS where step-up conversion is usually mandatory. This is achieved by connecting each winding set of a 9-phase machine to a single 3-phase VSI, and then connecting these dc links in series so that a single high voltage dc link is obtained. It is shown that any imbalance between winding sets will result in different individual dc-link voltages, a problem which can be solved by varying the power produced by each winding set. Therefore, dc-link voltage balancing controller has been devised, where power sharing is done according to the principles exposed in the chapter 5 of the thesis. Although developed dc-ink voltage balancing has been applied for a 9-phase case only, it can be easily extended to any multiple 3-phase winding machine. Simulation and experimental runs confirm the appropriateness of this control strategy.

This chapter completes the main body of the thesis. Subsequent material in the thesis includes the list of references and Appendices, which provide more details on hardware and software used and the list of publication resulting from the thesis.

7.2 Future Work

The work presented in this thesis has contributed to control of multiple 3-phase winding machines by relating two transformations (MS and VSD), almost exclusively used to decouple the machine model and enable implementation of independent flux/torque control. Developed theoretical concepts have been used to develop means for current and power sharing between individual winding sets, with subsequent simulation and experimental verification on the example of asymmetrical 9-phase machine with three neutral points. A further development has been directed at specific WECS structure which can increase dc-link voltage by cascading dc links of mutually isolated VSIs. Power sharing has been used in this structure to balance individual VSI dc-link voltages. Even though presented theory and current/power sharing techniques are applicable to any multiple 3-phase winding machine, work conducted here can be further continued as follows:

- Relationship between MS and VSD approaches may be developed for the machines with a number of phases in the winding set different from three, e.g. 15-phase winding consisting of three 5-phase winding sets. This would enable realisation of current and power sharing in these machines in the same manner.
- Current sharing in the stationary α-β coordinates enables imposing an arbitrary imbalance within each winding set without disturbing the total flux production. This can be utilised to impose such an imbalance so that the current in one or more phases is zero, which can be used for fault tolerant operation. Of course, both single and multiple neutral point configurations should be considered.
- Developed power sharing is based on varying the converted power of each winding set while the total power of the machine is unchanged. However, expressions for electrical power of each winding set should be derived, and power sharing considering these expressions should be developed as well, taking into account both active and reactive powers.
- Since WECS topologies were considered in the thesis, all the sub-windings of the machine were operated in generating mode or, in the extreme, with zero power. However, if one considers use of a multiphase machine in electrical vehicles with multiple electric energy sources or as an interconnecting generator between two (or more) microgrids, there may be a need to change the power flow direction in some winding sets, i.e. to operate one (or more) winding set(s) in motoring, while other one (or more) operates in generating. This behaviour is not considered in the thesis, so it should be explored further.
- Different direction of power flow in the winding sets may be used to increase both stator and rotor currents to nominal values without necessarily producing any resultant torque and with no load connected to the machine shaft. This would enable testing of the machine using so-called synthetic loading principles, since the machine could be operated with different apparent loadings (i.e. currents) without actually loading the machine mechanically. In this scenario one would get an equivalent of the back-to-back testing scheme that requires two identical machines, while

using a single machine. In essence, taking a six-phase machine as an example, one winding can operate in motoring while the other winding generates. The net power taken from the grid would equal only the losses in the machine, while the testing can take place with any current up to the rated in the winding.

Chapter 8

REFERENCES

Abbas, M. A., Christen R., Jahns T. M., (1984), Six-phase voltage source inverter driven induction motor, *IEEE Trans. on Industry Applications*, vol. IA-20, no. 5, pp. 1251-1259.

Alberti, L., Bianchi, N., (2012), Experimental tests of dual three-phase induction motor under faulty operating condition, *IEEE Trans. on Industrial Electronics*, vol. 59, no. 5, pp. 2041-2048.

Anaya-Lara, O., Jenkins, N., Ekanayake, J., Cartwright, P., Hughes, M., (2009), *Wind Energy Generation: Modelling and Control*, West Sussex, UK, John Wiley and Sons.

Andresen, B., Birk, J., (2007), A high power density converter system for the Gamesa G10x 4.5 MW wind turbine, *Proc. EPE European Conf. on Power Electronics and Applications*, Aalborg, Denmark, pp. 1-8.

Apsley, J., Williamson, S., (2006), Analysis of multiphase induction machines with winding faults, *IEEE Trans. on Industry Applications*, vol. 42, no. 2, pp. 465-472.

Apsley, J., (2010), Open-circuit fault mitigation for multiphase induction motors with a unified control structure, *Proc. IET Int. Conf. on Power Electronics, Machines and Drives PEMD*, Brighton, UK, pp. 1-6.

Arruda, L. N., Silva, S. M., Filho, B. J. C., (2001), PLL structures for utility connected systems, *Proc. IEEE IAS Annual Meeting*, Pittsburgh, PA, USA, pp. 2655-2660.

Barrero, F., Duran M. J., (2016), Recent advances in the design, modelling, and control of multiphase machines - part I, *IEEE Trans. on Industrial Electronics*, vol. 63, no. 1, pp. 449-458.

Benatmane, M., McCoy, T., (1998), Development of a 19 MW PWM converter for U.S. navy surface ships, *Proc. Int. Conf. on Electronic Ship*, Istanbul, Turkey, pp. 109-103.

Blaabjerg, F., Chen, Z., (2006), *Power Electronics for Modern Wind Turbines*, USA, Synthesis Lectures on Power Electronics, Morgan & Claypool Publishers.

Blaabjerg, F., Teodorescu, R., Liserre, M., Timbus, A. V., (2006), Overview of control and grid synchronization for distributed power generation systems, *IEEE Trans. on Industrial Electronics*, vol. 53, no. 5, pp. 1398-1409.

Bojoi, R., Tenconi, A., Profumo, F., Griva, G., Martinello, D., (2002), Complete analysis and comparative study of digital modulation techniques for dual three-phase AC motor drives, *Proc. IEEE Power Electronics Specialists Conf. PESC*, Cairns, Australia, pp. 851-857.

Bojoi, R., Lazzari, M., Profumo, F., Tenconi, A., (2003a), Digital field-oriented control for dual three-phase induction motor drives, *IEEE Trans. on Industry Applications*, vol. 39, no. 3, pp. 752-760.

Bojoi, R., Profumo, F., Tenconi, A., (2003b), Digital synchronous frame current regulation for dual three-phase induction motor drives, *Proc. IEEE Power Electronics Specialists Conf. PESC*, Acapulco, Mexico, pp. 1475-1480 vol.3.

Bojoi, R., Levi, E., Farina, F., Tenconi, A., Profumo, F., (2006a), Dual three-phase induction motor drive with digital current control in the stationary reference frame, *IEE Proceedings - Electric Power Applications*, vol. 153, no. 1, pp. 129-139.

Bojoi, R., Tenconi, A., Griva, G., Profumo, F., (2006b), Vector control of dual-three-phase induction-motor drives using two current sensors, *IEEE Trans. on Industry Applications*, vol. 42, no. 5, pp. 1284-1292.

Bojoi, R., Cavagnino, A., Tenconi, A., Vaschetto, S., (2016), Control of shaft-line-embedded multiphase starter/generator for aero-engine, *IEEE Trans. on Industrial Electronics*, vol. 63, no. 1, pp. 641-652.

Brisset, S., Vizireanu, D., Brochet, P., (2008), Design and optimization of a nine-phase axial-flux PM synchronous generator with concentrated winding for direct-drive wind turbine, *IEEE Trans. on Industry Applications*, vol. 44, no. 3, pp. 707-715.

Briz, F., Degner, M. W., Lorenz, R. D., (2000), Analysis and design of current regulators using complex vectors, *IEEE Trans. on Industry Applications*, vol. 36, no. 3, pp. 817-825.

Che, H. S., Hew, W. P., Rahim, N. A., Levi, E., Jones, M., Duran, M. J., (2012a), Current control of a six-phase induction generator for wind energy plants, *Proc. EPE Int. Power Electronics and Motion Control Conf. PEMC*, Novi Sad, Serbia, pp. LS5b.2-1-LS5b.2-7.

Che, H. S., Hew, W. P., Rahim, N. A., Levi, E., Jones, M., Duran, M. J., (2012b), A six-phase wind energy induction generator system with series-connected DC-links, *Proc. IEEE Int. Symposium on Power Electronics for Distributed Generation Systems PEDG*, Aalborg, Denmark, pp. 26-33.

Che, H. S., Duran, M. J., Hew, W. P., Rahim, N. A., Levi, E., Jones, M., (2012c), Dc-link voltage balancing of six-phase wind energy systems with series-connected machine-side converters and NPC grid-side converter, *Proc. IEEE Annual Conf. of the Industrial Electronics Society IECON*, Montreal, Canada, pp. 3541-3546.

Che, H. S., (2013), Contributions to control of an asymmetrical six-phase induction machine, Liverpool John Moores University, *PhD Thesis*, Liverpool, UK.

Che, H. S., Duran, M. J., Levi, E., Jones, M., Hew, W. P., Rahim, N. A., (2014a), Postfault operation of an asymmetrical six-phase induction machine with single and two isolated neutral points, *IEEE Trans. on Power Electronics*, vol. 29, no. 10, pp. 5406-5416.

Che, H. S., Levi, E., Jones, M., Duran, M. J., Hew, W. P., Rahim, N. A., (2014b), Operation of a six-phase induction machine using series-connected machine-side converters, *IEEE Trans. on Industrial Electronics*, vol. 61, no. 1, pp. 164-176.

Che, H. S., Levi, E., Jones, M., Hew, W. P., Rahim, N. A., (2014c), Current control methods for an asymmetrical six-phase induction motor drive, *IEEE Trans. on Power Electronics*, vol. 29, no. 1, pp. 407-417.

Chung, S. K., (2000a), A phase tracking system for three phase utility interface inverters, *IEEE Trans. on Power Electronics*, vol. 15, no. 3, pp. 431-438.

Chung, S. K., (2000b), Phase-locked loop for grid-connected three-phase power conversion systems, *IEE Proceedings - Electric Power Applications*, vol. 147, no. 3, pp. 213-219.

Correa, M. B. R., Jacobina, C. B., da Silva, C. R., Lima, A. M. N., da Silva, E. R. C., (2003), Six-phase AC drive system with reduced common-mode voltage, *Proc. IEEE Int. Electric Machines & Drives Conf. IEMDC*, Madison, WI, USA, pp. 1852-1858.

De Camillis, L., Matuonto, M., Monti, A., Vignati, A., (2001), Optimizing current control performance in double winding asynchronous motors in large power inverter drives, *IEEE Trans. on Power Electronics*, vol. 16, no. 5, pp. 676-685.

Deilamani, M., Kianinezhad, R., Seifossadat, S. G. H., Keramatzade, M., (2011), A new insight into six phase induction machine modelling under open phase fault condition, *Proc. IEEE Int. Aegean Conf. on Electrical Machines and Power Electronics ACEMP & Electromotion Joint Conf.*, Istanbul, Turkey, pp. 201-204.

Di Gerlando, A., Foglia, G., Iacchetti, M. F., Perini, R., (2012), Analysis and test of diode rectifier solutions in grid-connected wind energy conversion systems employing modular permanent-magnet synchronous generators, *IEEE Trans. on Industrial Electronics*, vol. 59, no. 5, pp. 2135-2146.

Dong, L., Jia, Q. Y., Jin, H., Hai-bo, J., Min, K., (2008), Realization of a SPWM inverter for multi-phase induction motor drives, *Proc. Int. Conf. on Electrical Machines and Systems ICEMS*, Wuhan, China, pp. 1287-1290.

Dordevic, O., Bodo, N., Jones, M., (2010), Model of an induction machine with an arbitrary phase number in Matlab/Simulink for educational use, *Proc. Int. Universities Power Engineering Conf. UPEC*, Cardiff, UK, pp. 1-6.

Dordevic, O., (2013a), PWM strategies for multilevel multiphase AC drives, Liverpool John Moores Univeristy, *PhD Thesis*, Liverpool, UK.

Dordevic, O., Levi, E., Jones, M., (2013b), A vector space decomposition based space vector PWM algorithm for a three-level seven-phase voltage source inverter, *IEEE Trans. on Power Electronics*, vol. 28, no. 2, pp. 637-649.

Dujic, D., Iqbal, A., Levi, E., (2007a), A space vector PWM technique for symmetrical six-phase voltage source inverters, *EPE Journal*, vol. 17, no. 1, pp. 24-32.

Dujic, D., Jones, M., Levi, E., (2007b), Space vector PWM for nine-phase VSI with sinusoidal output voltage generation: analysis and implementation, *Proc. IEEE Annual Conf. of the Industrial Electronics Society IECON*, Taipei, Taiwan, pp. 1524-1529.

Dujic, D., Levi, E., Jones, M., (2010), Dc bus utilisation in multiphase VSI supplied drives with a composite stator phase number, *Proc. IEEE Int. Conf. on Industrial Technology ICIT*, Vina del Mar, Chile, pp. 1495-1500.

Duran, M. J., Levi, E., Jones, M., (2005), Independent vector control of asymmetrical nine-phase machines by means of series connection, *Proc. IEEE International Electric Machines & Drives Conf. IEMDC*, San Antonio, TX, USA, pp. 167-173.

Duran, M. J., Kouro, S., Bin, W., Levi, E., Barrero, F., Alepuz, S., (2011), Six-phase PMSG wind energy conversion system based on medium-voltage multilevel converter, *Proc. EPE European Conf. on Power Electronics and Applications*, Birmingham, UK, pp. 1-10.

Duran M. J., Barrero, F., (2016a), Recent advances in the design, modelling, and control of multiphase machines - part II, *IEEE Trans. on Industrial Electronics*, vol. 63, no. 1, pp. 459-468.

Duran, M. J., Gonzalez Prieto, I., Bermudez, M., Barrero, F., Guzman, H., Arahal, M. R., (2016b), Optimal fault-tolerant control of six-phase induction motor drives with parallel converters, *IEEE Trans. on Industrial Electronics*, vol. 63, no. 1, pp. 629-640.

Duran, M. J., Gonzalez Prieto, I., Gonzalez Prieto, A., Barrero, F., (2017), Multiphase energy conversion systems connected to microgrids with unequal power-sharing capability, *IEEE Trans. on Energy Conversion*, vol. 32, no. 4, pp. 1386-1395.

Fortescue, C. L., (1918), Method of symmetrical co-ordinates applied to the solution of polyphase networks, *Trans. of the American Institute of Electrical Engineers*, vol. 37, no. 2, pp. 1027-1140.

Feifei, B., Wenxin, H., Yuwen, H., Kai, S., (2012), An integrated AC and DC hybrid generation system using dual-stator-winding induction generator with static excitation controller, *IEEE Trans. on Energy Conversion*, vol. 27, no. 3, pp. 810-812.

Fu, J.R., Lipo, T. A., (1994), Disturbance-free operation of a multiphase current-regulated motor drive with an opened phase, *IEEE Trans. on Industry Applications*, vol. 30, no. 5, pp. 1267-1274.

Gonzalez, I., Duran, M. J., Che, H. S., Levi, E., Aguado, J., (2014), Fault-tolerant efficient control of six-phase induction generators in wind energy conversion systems with series-parallel machine-side converters, *Proc. IET Int. Conf. on Power Electronics, Machines and Drives PEMD*, Manchester, UK, pp. 1-6.

Gonzalez Prieto, I., Duran, M. J., Che, H. S., Levi, E., Bermudez, M., Barrero, F., (2016), Fault-tolerant operation of six-phase energy conversion systems with parallel machine-side converters, *IEEE Trans. on Power Electronics*, vol. 31, no. 4, pp. 3068-3079.

Grandi, G., Serra, G., Tani, A., (2007a), Space vector modulation of a mine-phase voltage source inverter, *Proc. IEEE Int. Symposium on Industrial Electronics ISIE*, Vigo, Spain, pp. 431-436.

Grandi, G., Serra, G., Tani, A., (2007b), Space vector modulation of nine-phase voltage source inverters based on three-phase decomposition, *Proc. EPE European Conf. on Power Electronics and Applications*, Aalborg, Denmark, pp. 1-12.

Guillaud, X., Degobert, P., Teodorescu, R., (2007), Use of resonant controller for grid-connected converters in case of large frequency fluctuations, *Proc. EPE European Conf. on Power Electronics and Applications*, Aalborg, Denmark, pp. 1-8.

Guzman, H., Duran, M. J., Barrero, F., (2012), A comprehensive fault analysis of a five-phase induction motor drive with an open phase, *Proc. EPE Int. Power Electronics and Motion Control Conf. PEMC*, Novi Sad, Serbia, pp. LS5b.3-1-LS5b.3-6.

Guzman, H., Duran, M. J., Barrero, F., Bogado, B., Toral, S., (2014), Speed control of five-phase induction motors with integrated open-phase fault operation using model-based predictive current control techniques, *IEEE Trans. on Industrial Electronics*, vol. 61, no. 9, pp. 4474-4484.

Hadiouche, D., Baghli, L., Rezzoug, A., (2006), Space-vector PWM techniques for dual three-phase AC machine: analysis, performance evaluation, and DSP implementation, *IEEE Trans. on Industry Applications*, vol. 42, no. 4, pp. 1112-1122.

Holmes, D. G., Lipo, T. A., (2003), *Pulse Width Modulation for Power Converters: Principles and Practice*, New Jersey, USA, IEEE Press Series on Power Engineering, John Wiley and Sons.

Holmes, D. G., McGrath, B. P., Parker, S. G., (2012), Current regulation strategies for vector-controlled induction motor drives, *IEEE Trans. on Industrial Electronics*, vol. 59, no. 10, pp. 3680-3689.

Hu, H., Yang, J., (2011), Rotor field oriented control strategy of multiphase induction motor, *Proc. IEEE Conf. on Robotics, Automation and Mechatronics ICMA*, Beijing, China, pp. 108-112.

Hu, Y., Zhu, Z., Liu, K., (2014), Current control for dual three-phase permanent magnet synchronous motors accounting for current unbalance and harmonics, *IEEE Journal of Emerging and Selected Topics in Power Electronics*, vol. 2, no. 2, pp. 272-284.

Hua, L., Yunping, Z., Bi, H., (2006), The vector control strategies for multiphase synchronous motor drive systems, *Proc. IEEE Int. Symposium on Industrial Electronics ISIE*, Montreal, Canada, pp. 2205-2210.

Jones, M., Vukosavic, S. N., Dujic, D., Levi, E., (2009a), A synchronous current control scheme for multiphase induction motor drives, *IEEE Trans. on Energy Conversion*, vol. 24, no. 4, pp. 860-868.

Jones, M., Vukosavic, S. N., Levi, E., (2009b), Parallel-connected multiphase multidrive systems with single inverter supply, *IEEE Trans. on Industrial electronics*, vol. 56, no. 6, pp. 2047-2057.

Jones, M., Dujic, D., Levi, E., Prieto, J., Barrero, F., (2011), Switching ripple characteristics of space vector PWM schemes for five-phase two-level voltage source inverters - part 2: current ripple, *IEEE Trans. on Industrial electronics*, vol. 58, no. 7, pp. 2799-2808.

Jordan, S., Apsley, J., (2011), Diode rectification of multiphase synchronous generators for aircraft applications, *Proc. IEEE Energy Conversion Congress and Exposition ECCE*, Phoenix, AZ, USA, pp. 3208-3215.

Jung, E., Yoo, H., Seung-Ki, S., Hong-Soon, C., Yun-Young, C., (2009), Nine-phase permanent magnet motor drive system for ultra high-speed elevator, *Proc. IEEE Energy Conversion Congress and Exposition ECCE*, San Jose, CA, USA, pp. 1841-1846.

Kallio, S., Andriollo, M., Tortella, A., Karttunen, J., (2013), Decoupled d-q model of double-star interior-permanent-magnet synchronous machines, *IEEE Trans. on Industrial Electronics*, vol. 60, no. 6, pp. 2486-2494.

Kato, S., Hoshi, N., Oguchi, K., (2001), A low-cost system of variable-speed cascaded induction generators for small-scale hydroelectricity, *Proc. IEEE IAS Annual Meeting*, Pittsburg, PA, USA, pp. 1419-1424 vol.2.

Kats, Y., (1997), Adjustable-speed drives with multiphase motors, *Proc. IEEE Int. Electric Machines & Drives Conf. IEMDC*, Milwaukee, WI, USA, pp. TC2/4.1-TC2/4.3.

Kelly, J. W., Strangas, E. G., Miller, J. M., (2003), Multiphase space vector pulse width modulation, *IEEE Trans. on Energy Conversion*, vol. 18, no. 2, pp. 259-264.

Kianinezhad, R., Nahid, B., Betin, F., Capolino, G. A., (2005), Multi-vector SVM: a new approach to space vector modulation control for six-phase induction machines, *Proc. IEEE Annual Conf. of the Industrial Electronics Society IECON*, Raleigh, NC, USA, pp. 1359-1394.

Kianinezhad, R., Nahid-Mobarakeh, B., Baghli, L., Betin, F., Capolino, G. A., (2008), Modelling and control of six-phase symmetrical induction machine under fault condition due to open phases, *IEEE Trans. on Industrial Electronics*, vol. 55, no. 5, pp. 1966-1977.

Klingshirn, E. A., (1983a), High phase order induction motors - part I - description and theoretical considerations, *IEEE Trans. on Power Apparatus and Systems*, vol. PAS-102, no. 1, pp. 47-53.

Klingshirn, E. A., (1983b), High phase order induction motors - part II - experimental results, *IEEE Trans. on Power Apparatus and Systems*, vol. PAS-102, no. 1, pp. 54-59.

Krishnan, R., (2001), *Electric Motor Drives Modelling, Analysis, and Control*, New Jersey, USA, Prentice Hall.

Lascu, C., Asiminoaei, L., Boldea, I., Blaabjerg, F., (2007), High performance current controller for selective harmonic compensation in active power filters, *IEEE Trans. on Power Electronics*, vol. 22, no. 5, pp. 1826-1835.

Lascu, C., Asiminoaei, L., Boldea, I., Blaabjerg, F., (2009), Frequency response analysis of current controllers for selective harmonic compensation in active power filters, *IEEE Trans. on Industrial Electronics*, vol. 56, no. 2, pp. 337-347.

Levi, E., Bojoi, R., Profumo, F., Toliyat, H. A., Williamson, S., (2007), Multiphase induction motor drives - a technology status review, *IET Electric Power Applications*, vol. 1, no. 4, pp. 489-516.

Levi, E., (2008), Multiphase electric machines for variable-speed applications, *IEEE Trans. on Industrial Electronics*, vol. 55, no. 5, pp. 1893-1909.

Levi, E., Dujic, D., Jones, M., Grandi, G., (2008), Analytical determination of DC-bus utilization limits in multiphase VSI supplied AC drives, *IEEE Trans. on Energy Conversion*, vol. 23, no. 2, pp. 433-443.

Levi, E., (2016), Advances in converter control and innovative exploitation of additional degrees of freedom for multiphase machines, *IEEE Trans. on Industrial Electronics*, vol. 63, no. 1, pp. 433-448.

Liccardo, F., Marino, P., Raimondo, G., (2011), Robust and fast three-phase PLL tracking system, *IEEE Trans. on Industrial Electronics*, vol. 58, no. 1, pp. 221-231.

Lipo, T. A., (1980), A d-q model for induction machines, *Proc. Int. Conf. on Electrical Machines*, Athens, Greece, pp. 860-867.

Liserre, M., Cardenas, R., Molinas, M., Rodriguez, J., (2011), Overview of multi-MW wind turbines and wind parks, *IEEE Trans. on Industrial Electronics*, vol. 58, no. 4, pp. 1081-1095.

Liu, Z., Zheng, Z., Xu, L., Wang, K., Li, Y., (2016), Current balance control for symmetrical multiphase inverters, *IEEE Trans. on Power Electronics*, vol. 31, no. 6, pp. 4005-4012.

Liu, Z., Peng, L., Li, Y., Zheng, Z., (2013), Vector control of fixed joint double fifteen-phase induction motors system with propeller load, *Proc. European Conf. on Power Electronics and Applications EPE*, Lille, France, pp. 1-9.

Ma, K., Tutelea, L., Boldea, I., Ionel, D. M., Blaabjerg, F., (2015), Power electronic drives, controls, and electric generators for large wind turbines - an overview, *Electric Power Components and Systems*, vol. 43, no. 12, pp. 1406-1421.

Malinowski, M., (2001), Sensorless control strategies for three-phase PWM rectifiers, Warsaw University of Technology, *PhD Thesis*, Warsaw, Poland.

Marouani, K., Baghli, L., Hadiouche, D., Kheloui, A., Rezzoug, A., (2008), A new PWM strategy based on a 24-sector vector space decomposition for a six-phase VSI-fed dual stator induction motor, *IEEE Trans. on Industrial Electronics*, vol. 55, no. 5, pp. 1910-1920.

Martinez-G., D., Aguilar-M., O., Tapia-O., R., Garcia-B., A., (2013), Comparison of different PLL strategies for applications in a wind generation system, *Proc. Iberoamerican Conf. on Electronics Engineering and Computer Science*, San Luis Potosi, Mexico, pp. 150-157.

Mengoni, M., Sala, G., Zarri, L., Tani, A., Serra, G., Gritli, Y., Duran, M. J., (2016), Control of a fault-tolerant quadruple three-phase induction machine for more electric aircrafts, *Proc. IEEE Annual Conf. of the Industrial Electronics Society IECON*, Florence, Italy, pp. 5747-5753.

MHI Vestas (2016), The V164-8.0 MW turbine, *available at http://www.mhivestasoffshore.com/innovations*, date accessed: [10/03/2016].

Miranda, R. S., (2013), Current control of six phase induction motor under open phase fault condition, *Proc. IEEE Int. Electric Machines & Drives Conf. IEMDC*, Chicago, IL, USA, pp. 1391-1396.

Moinoddin, S., Abu-Rub, H., Iqbal, A., Alammari, R., (2015), Modelling and implementation of SVPWM technique for a fifteen-phase voltage source inverter for sinusoidal output waveform, *Proc. IEEE Int. Conf. on Industrial Technology ICIT*, Seville, Spain, pp. 1075-1080.

Munoz, A. R., Lipo, T. A., (2000), Dual stator winding induction machine drive, *IEEE Trans. on Industry Applications*, vol. 36, no. 5, pp. 1369-1379.

Nabae, A., Takahashi, I., Akagi, H., (1981), A new neutral-point-clamped PWM inverter, *IEEE Trans. on Industry Applications*, vol. IA-17, no. 5, pp. 518-523.

Nelson, R. H., Krause, P. C., (1974), Induction machine analysis for arbitrary displacement between multiple winding sets, *IEEE Trans. on Power Apparatus and Systems*, vol. PAS-93, no. 3, pp. 841-848.

Ng, C. H., Parker, M. A., Ran, L., Tavner, P. J., Bumby, J. R., Spooner, E., (2008), A multilevel modular converter for a large, light weight wind turbine generator, *IEEE Trans. on Power Electronics*, vol. 23, no. 3, pp. 1062-1074.

Nounou, K., Marouani, K., Benbouzid, M., Tabbache, B., (2014), Six-phase induction machine operating as a standalone self-excited induction generator, *Proc. IEEE Int. Conf. on Green Energy ICGE*, Sfax, Tunisia, pp. 158-163.

Park, R. H., (1929), Two-reaction theory of synchronous machines generalized method of analysis - Part I, *Trans. of the American Institute of Electrical Engineers*, vol. 48, no. 3, pp. 716-727.

Parsa, L., (2005), On advantages of multi-phase machines, *Proc. IEEE Annual Conf. of the Industrial Electronics Society IECON*, Raleigh, NC, USA, pp. 6.

Pereira, I., Martins, A., (2009), Neutral-point voltage balancing in three-phase NPC converters using multicarrier PWM control, *Proc IEEE Int. Conf. on Power Engineering, Energy and Electrical Drives POWERENG*, Lisbon, Portugal, pp. 570-574.

Prieto, J., Barrero, F., Jones, M., Levi, E., (2010), A modified continuous PWM technique for asymmetrical six-phase induction machines, *Proc. IEEE Int. Conf. on Industrial Technology ICIT*, Vina del Mar, Chile, pp. 1489-1494.

REN21 (2016), Renewables 2016: Global status report, *available at www.ren21.net*, date accessed: [10/03/2016].

Rockhill, A., Lipo, T. A., (2009), A simplified model of a nine phase synchronous machine using vector space decomposition, *Proc. IEEE Power Electronics and Machines in Wind Applications PEMWA*, Lincoln, NE, USA, pp. 1-5.

Rockhill, A., Lipo, T. A., (2015), A generalised transformation methodology for polyphase electric machines and networks, *Proc. IEEE International Electric Machines & Drives Conf. IEMDC*, Coeur d'Alene, ID, USA, pp. 27-34.

Rodriguez, J., Bernet, S., Bin, W., Pontt, J. O., Kouro, S., (2007), Multilevel voltage-source-converter topologies for industrial medium-voltage drives, *IEEE Trans. on Industrial Electronics*, vol. 54, no. 6, pp. 2930-2945.

Rodriguez, A., Moranchel, M., Bueno, E. J., Rodriguez, F. J., (2012), Tuning of resonant controllers applied to the current control of voltage-source converters, *Proc. IEEE Annual Conf. of the Industrial Electronics Society IECON*, Montreal, Canada, pp. 4463-4468.

Ruba, M., Fodorean, D., (2012), Analysis of fault-tolerant multiphase power converter for a nine-phase permanent magnet synchronous machine, *IEEE Trans. on Industry Applications*, vol. 48, no. 6, pp. 2092-2101.

Rubino, S., Bojoi, R., Cavagnino, A., Vaschetto, S., (2016), Asymmetrical twelve-phase induction starter/generator for more electric engine in aircraft, *Proc. IEEE Energy Conversion Congress and Exposition ECCE*, Milwaukee, WI, USA, pp. 471-478.

Scarcella, G., Scelba, G., Cacciato, M., Spampinato, A., Harbaugh, M. M., (2016), Vector control strategy for multidirectional power flow in integrated multidrives starter-alternator applications, *IEEE Trans. on Industry Applications*, vol. 52, no. 6, pp. 4816-4826.

Siemens AG (2016), Siemens expands portfolio with 8 MW offshore wind turbine, *available at https://www.siemens.com/press/PR2016070338WPEN*, date accessed: [10/03/2016].

Singh, G. K., Nam, K., Lim, S. K., (2005a), A simple indirect field-oriented control scheme for multiphase induction machine, *IEEE Trans. on Industrial Electronics*, vol. 52, no. 4, pp. 1177-1184.

Singh, G. K., Yadav, K. B., Saini, R. P., (2005b), Modelling and analysis of multi-phase (six-phase) self-excited induction generator, *Proc. Int. Conf. on Electrical Machines and Systems ICEMS*, Nanjing, China, pp. 1922-1927.

Singh, G. K., Yadav, K. B., Saini, R. P., (2006), Capacitive self-excitation in a six-phase induction generator for small hydro power - an experimental investigation, *Proc. IEEE Int. Conf. on Power Electronics, Drives and Energy Systems PEDES*, New Delhi, India, pp. 1-6.

Singh, G. K., Kumar, A. S., Saini, R. P., (2009), Selection of capacitor for the self-excited six-phase induction generator, *Proc. Int. Conf. on Power Systems ICPS*, Kharagpur, India, pp. 1-6.

Subotic, I., Bodo, N., Levi, E., Jones, M., Levi, V., (2016), Isolated chargers for EVs incorporating six-phase machines, *IEEE Trans. on Industrial Electronics*, vol. 63, no. 1, pp. 653-664.

Sulligoi, G., Tessarolo, A., Benucci, V., Baret, M., Rebora, A., Taffone, A., (2010), Modelling, simulation, and experimental validation of a generation system for medium-voltage DC integrated power systems, *IEEE Trans. on Industry Applications*, vol. 46, no. 4, pp. 1304-1310.

Sulligoi, G., Tessarolo, A., Benucci, V., Trapani, A. M., Baret, M., Luise, F., (2011), Design, implementation and testing of a shipboard medium-voltage DC generation system based on a ultra-high speed 12-phase alternator, *Proc. IEEE Electric Ship Technologies Symposium ESTS*, Alexandria, VA, USA, pp. 388-395.

Sun, C., Ai, S., Hu, L., Chen, Y., (2015), The development of a 20MW PWM driver for advanced fifteen-phase propulsion induction motors, *KIPE Journal of Power Electronics*, vol. 15, no. 1, pp. 146 - 159.

Tani, A., Mengoni, M., Zarri, L., Serra, G., Casadei, D., (2012), Control of multiphase induction motors with an odd number of phases under open-circuit phase faults, *IEEE Trans. on Power Electronics*, vol. 27, no. 2, pp. 565-577.

Tani, A., Serra, G., Mengoni, M., Zarri, L., Rini, G., Casadei, D., (2013), Dynamic stator current sharing in quadruple three-phase induction motor drives, *Proc. IEEE Annual Conf. of the Industrial Electronics Society IECON*, Vienna, Austria, pp. 5173-5178.

Tessarolo, A., (2009a), On the modelling of poly-phase electric machines through vector-space decomposition: theoretical considerations, *Proc IEEE Int. Conf. on Power Engineering, Energy and Electrical Drives POWERENG*, Lisbon, Portugal, pp. 519-523.

Tessarolo, A., (2009b), On the modelling of poly-phase electric machines through vector-space decomposition: numeric application cases, *Proc IEEE Int. Conf. on Power Engineering, Energy and Electrical Drives POWERENG*, Lisbon, Portugal, pp. 524-528.

Tessarolo, A., (2010a), Experimental performance assessment of multiphase alternators supplying multiple AC/DC power converters, *Proc. IET Int. Conf. on Power Electronics, Machines and Drives PEMD*, Brighton, UK, pp. 1-6.

Tessarolo, A., (2010b), Benefits of increasing the number of stator phases in terms of winding construction technology in high-power electric machines, *Proc. IET Int. Conf. on Power Electronics, Machines and Drives PEMD*, Brighton, UK, pp. 1-6.

Tessarolo, A., Bortolozzi, M., Contin, A., (2013a), Modelling of split-phase machines in Park's coordinates. Part I: Theoretical foundations, *Proc. IEEE Int. Conf. on Computer as a Tool EUROCON*, Zagreb, Croatia, pp. 1308-1313.

Tessarolo, A., Bortolozzi, M., Contin, A., (2013b), Modelling of split-phase machines in Park's coordinates. Part II: Equivalent circuit representation, *Proc. IEEE Int. Conf. on Computer as a Tool EUROCON*, Zagreb, Croatia, pp. 1314-1319.

Vizireanu, D., Brisset S., Kestelyn X., Brochet P., Milet Y., Laloy D., (2007), Investigation on multi-star structures for large power direct-drive wind generator, *Electric Power Components and Systems*, vol. 35, no. 2, pp. 135-152.

Vukosavic, S. N., Jones, M., Levi, E., Varga, J., (2005), Rotor flux oriented control of a symmetrical six-phase induction machine, *Electric Power Systems Research*, vol. 75, no. 2-3, pp. 142-152.

Wang, J., Qu, R., Liu, Y., (2013), Comparison study of superconducting generators with multiphase armature windings for large-scale direct-drive wind turbines, *IEEE Trans. on Applied Superconductivity*, vol. 23, no. 3, pp. 1-6.

Wang, J., Qu, R., Liu, Y., Li, J., (2014), Study of multiphase superconducting wind generators with fractional-slot concentrated windings, *IEEE Trans. on Applied Superconductivity*, vol. 24, no. 3, pp. 1-6.

Wei, K., Wang, D., Zheng, X., Cheng, S., (2014), Research on relationship between harmonic currents and resultant harmonic magnetomotive forces in multiphase machines, *Proc. IEEE Transportation Electrification Conf. and Expo ITEC*, Beijing, China, pp. 1-4.

White, C. W., Woodson, H. H., (1959), *Electromechanical Energy Conversion*, New York, USA, John Wiley & Sons.

Wu, B., Lang, Y., Zargari, N., Kuoro, S., (2011), *Power Conversion and Control of Wind Energy Systems*, New Jersey, USA, IEEE Press Series on Power Engineering, John Wiley and Sons.

Xiang-Jun, Z., Yongbing, Y., Hongtao, Z., Ying, L., Luguang, F., Xu, Y., (2012), Modelling and control of a multi-phase permanent magnet synchronous generator and efficient hybrid 3L-converters for large direct-drive wind turbines, *IET Electric Power Applications*, vol. 6, no. 6, pp. 322-331.

Yepes, A. G., (2011), Digital resonant current controllers for voltage source converters, University of Vigo, *PhD Thesis*, Vigo, Spain.

Yepes, A. G., Vidal, A., Freijedo, F. D., Malvar, J., Lopez, O., Doval-Gandoy, J., (2012), Transient response evaluation of resonant controllers for AC drives, *Proc. IEEE Energy Conversion Congress and Exposition ECCE*, Raleigh, NC, USA, pp. 471-478.

Yepes, A. G., Malvar, J., Vidal, A., Lopez, O., Doval-Gandoy, J., (2013), Current harmonic compensation in symmetrical multiphase machines by resonant controllers in synchronous reference frames - Part 1: Extension to any phase number, *Proc. IEEE Annual Conf. of the Industrial Electronics Society IECON*, Vienna, Austria, pp. 5155-5160.

Yepes, A. G., Doval-Gandoy, J., Baneira, F., Perez-Estevez, D., Lopez, O., (2016), Current harmonic compensation for n-phase machines with asymmetrical winding arrangement, *Proc. IEEE Energy Conversion Congress and Exposition ECCE*, Milwaukee, WI, USA, pp. 1-8.

Yuan, X., Chai, J., Li, Y., (2012), A transformer-less high-power converter for large permanent magnet wind generator systems, *IEEE Trans. on Sustainable Energy*, vol. 3, no. 3, pp. 318-329.

Zabaleta, M., Levi, E., Jones, M., (2016), Modelling approaches for an asymmetrical six-phase machine, *Proc. IEEE International Symposium on Industrial Electronics ISIE*, Santa Clara, CA, USA, pp. 173-178.

Zabaleta, M., Levi, E., Jones, M., (2016), Modelling approaches for triple three-phase permanent magnet machines, *Proc. International Conf. on Electrical Machines ICEM*, Lausanne, Switzerland, pp. 466-472.

Zarri, L., Mengoni, M., Gritli, Y., Tani, A., Filippetti, F., Serra, G., Casadei, D., (2011), Behaviour of multiphase induction machines with unbalanced stator windings, *Proc. IEEE Int. Symposium on Diagnostics for Electric Machines, Power Electronics and Drives SDEMPED*, Bologna, Italy, pp. 84-91.

Zhao, Y., Lipo, T. A., (1995), Space vector PWM control of dual three-phase induction machine using vector space decomposition, *IEEE Trans. on Industry Applications*, vol. 31, no. 5, pp. 1100-1109.

Zhuoran, Z., Jianbin, H., Yangguang, Y., (2010), Fault-tolerant characteristic analysis of a new 12-phase PM brushless DC generator, *Proc. Int. Conf. on Electrical Machines ICEM*, Rome, Italy, pp. 1-5.

Zmood, D. N., Holmes, D. G., Bode, G. H., (2001), Frequency-domain analysis of three-phase linear current regulators, *IEEE Trans. on Industry Applications*, vol. 37, no. 2, pp. 601-610.

Zoric, I., Jones, M, Levi, E., (2016), Phase voltage harmonic imbalance in asymmetrical multiphase machines with single neutral point, *Proc. IEEE Annual Conf. of the Industrial Electronics Society IECON*, Florence, Italy, pp. 4343-4348.

Zoric, I., Zabaleta, M., Jones, M, Levi, E., (2017), Techniques for power sharing between winding sets of multiple three-phase machines, *Proc. Workshop on Electrical Machines Design, Control and Diagnosis WEMDCD*, Nottingham, UK, pp. 208-215.

Zoric, I., Jones, M, Levi, E., (2017a), Voltage balancing control of a symmetrical nine-phase machine with series-connected DC links, *Proc. IEEE Int. Symposium on Industrial Electronics ISIE*, Edinburgh, UK, pp. 1052-1057.

Zoric, I., Jones, M, Levi, E., (2017b), Vector space decomposition algorithm for asymmetrical multiphase machines, *Proc. IEEE Int. Symposium on Power Electronics*, Novi Sad, Serbia, pp. 1-6.

Zoric, I., Jones, M, Levi, E., (2018a), Arbitrary power sharing among three-phase winding sets of multiphase machines, *IEEE Trans. on Industrial Electronics*, vol. 65, no. 2, pp. 1128-1139.

Zoric, I., Jones, M, Levi, E., (2018b), Arbitrary d-q current sharing in three-phase winding sets of multiphase machines, *Proc. IET Int. Conf. on Power Electronics, Machines and Drives PEMD*, Liverpool, UK, pp. 1-6.

Appendix A

DERIVATION AND IMPLEMENTATION CODES

A.1 Machine Model Implemented in Phase Variables (Simulink)

All simulations in the thesis use a model of an induction machine implemented in phase variables. The advantage of this modelling approach over modelling in terms of MS or VSD variables is that there is no need to use direct/inverse Clarke's and/or rotational transformation. Instead, the machine is modelled in its natural *n*-dimensional space; hence, it is quite simple to understand and implement the model. Equations governing the machine model in terms of phase variables are detailed in the section 4.2 and they are valid for any *n*-phase squirrel cage induction machine with distributed windings. Standard assumptions in machine modelling are taken into account, i.e. linear magnetic core without flux saturation or magnetic losses, balanced machine with uniform air gap, constant resistances, etc. Furthermore, in order to decrease simulation execution time, machine rotor is modelled as a 2-phase one. Hence, instead of having 2*n* differential equations to model the electromagnetic part of the machine, only *n*+2 are needed.

Developed Simulink block is shown in the Fig. A.1a, while the parameter user interface of the model can be seen shown in Fig. A.1b and A.1c. Here, an example of an asymmetrical 9-phase machine is shown. Simulink block has a mask built in such a way that it provides information on the machine parameters and depicts chosen machine configuration. Inputs to the model are phase voltages and load torque, whereas outputs are stator phase currents, machine's torque and machine's rotational speed in rad/s.

Machine parameters can be changed by parameter tab shown in Fig. A.1b, which is set in mask editor Parameters & Dialog tab. Moreover, one of the additional features required for the thesis (chapter 6) is to model the imbalance between the phases. This has been implemented by adding a new tab where additional resistances to each phase can be modified, as shown in Fig. A.1c.

Block diagram is set by Icon & Ports tab in the machine mask editor, where the used code is as follows:

```
% get block size
pos = get_param(gcbh,'Position');
block_size = [pos(3)-pos(1), pos(4)-pos(2)];

% display parameters
machine_type = [num2str(phase_num), '-phase'];
if length(factor(phase_num)) > 1
```

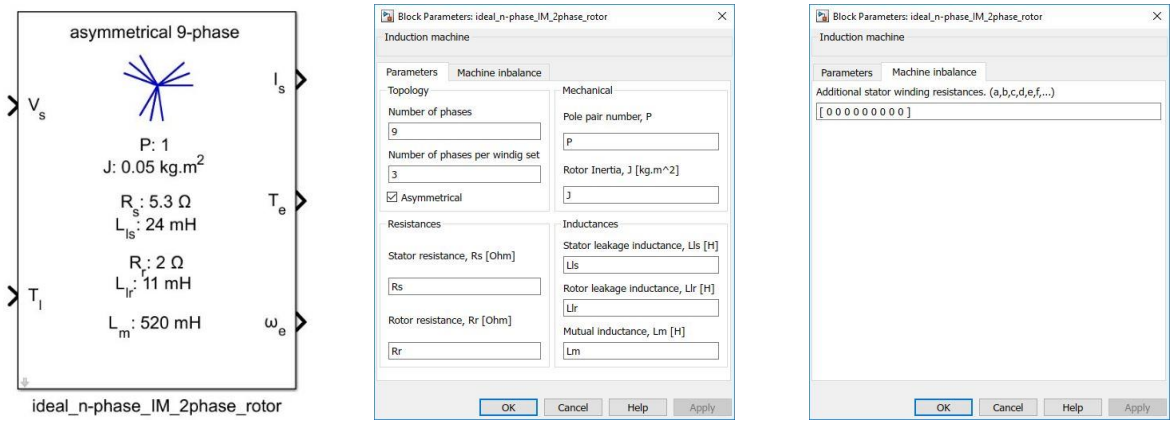

(a) (b) (c)

Figure A.1 – Simulink block of the induction machine model (a), properties (b) and machine imbalance (c) tabs.

```
    if (asymmetrical)
        machine_type = ['asymmetrical ', machine_type];
    else
        machine_type = ['symmetrical ', machine_type];
    end
end

text(block_size(1)/2, block_size(2)-10, machine_type, 'hor','center', 'texmode','on');
text(block_size(1)/2, block_size(2)-75, ['P: ', num2str(P)], 'hor','center', 'texmode','on');
text(block_size(1)/2, block_size(2)-87, ['J: ', num2str(J), ' kg.m^2'], 'hor','center',
'texmode','on');
text(block_size(1)/2, block_size(2)-110, ['R_s: ', num2str(Rs), ' \Omega'], 'hor','center',
'texmode','on');
text(block_size(1)/2, block_size(2)-123, ['L_{ls}: ', num2str(Lls*10^3), ' mH'],
'hor','center', 'texmode','on');
text(block_size(1)/2, block_size(2)-145, ['R_r: ', num2str(Rr), ' \Omega'], 'hor','center',
'texmode','on');
text(block_size(1)/2, block_size(2)-157, ['L_{lr}: ', num2str(Llr*10^3), ' mH'],
'hor','center', 'texmode','on');
text(block_size(1)/2, block_size(2)-180, ['L_m: ', num2str(Lm*10^3), ' mH'], 'hor','center',
'texmode','on');

% display port label
color('black');
port_label('input',  1, ' V_s', 'texmode','on');
port_label('input',  2, ' T_l', 'texmode','on');
port_label('output', 1, 'I_s ', 'texmode','on');
port_label('output', 2, 'T_e ', 'texmode','on');
port_label('output', 3, '\omega_e ', 'texmode','on');
% plot machine diagram
color('blue');
ends = 20 .* exp(1i.*ps);
x=[]; y=[];
x0 = block_size(1)/2;
y0 = block_size(2)-42.5;
for ii = 1:1:phase_num
    x = [x, x0+[0, real(ends(ii))] ];
    y = [y, y0+[0, imag(ends(ii))] ];
end
plot(x,y);
```

All parameters are available either directly from the parameters tab or from the initialisation of the block, which is as follows:

```
% check number of phases
if ( phase_num < 3 )
   error('Phase number must be larger than 3 !!!');
end
% check number of phases per winding set
valid_num = factor(phase_num);
valid_num(valid_num<3) = [];
if ( ~any(phases_per_set == valid_num) )
    error('Wrong number of phases per set!!!');
end
```

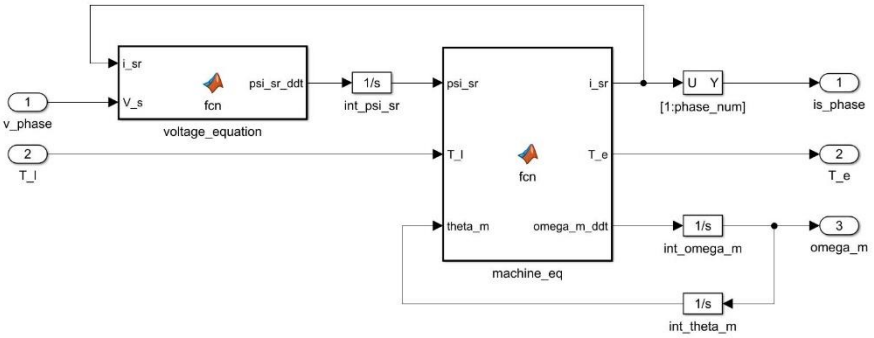

Figure A.2 – Internal structure of the developed induction machine model.

```
% phase shift calculation
ws_num = phase_num/phases_per_set;
ps = zeros(1, phase_num);
for jj = 1:1:ws_num
    for ii = 1:phases_per_set
        if asymmetrical
            ps(ws_num*(ii-1)+jj) = (pi/phase_num)*(2*ws_num*(ii-1)+jj-1);
        else
            ps(ws_num*(ii-1)+jj) = (2*pi/phase_num)*(ws_num*(ii-1)+jj-1);
        end
    end
end

% clear variables
clearvars valid_num w_sets_num index ii jj
```

Machine model has been split into voltage and current/torque equations for easier implementation, as shown in the Fig. A.2. Integration is done outside main equations so that generic integrators can be used. Consequently, model operation is affected by chosen solver. Code in the `voltage_equation` block is as follows:

```
function psi_sr_ddt   = fcn( i_sr, V_s, Rs, Rr, phase_num, Rs_inb )

%%% constant variables
persistent Rsr;
if isempty(Rsr)
    Rsr = diag( [Rs*ones(1,phase_num), (2/phase_num)*[Rr Rr] ]);
    % add inbalance in phase resistances
    if any(Rs_inb)
        Rsr = Rsr + diag( [Rs_inb, 0, 0] );
    end
end;

%%% d(flux)/dt calculation (voltage equation)
psi_sr_ddt = [ V_s; 0; 0; ] - Rsr * i_sr;
```

Block `machine_eq` contains the following code:

```
function [ i_sr, T_e, omega_m_ddt ] = fcn( psi_sr, T_l, theta_m, P, Lls, Llr, Lm, phase_num,
ps, J)

%%% constant variables
persistent M;
persistent Ls;
persistent Lr;

if isempty(M)
    M = (2./phase_num).*Lm;
end;

if isempty(Ls)
    Ls = M.* cos( repmat(ps, phase_num, 1) - repmat(ps', 1, phase_num) ) + Lls.*diag(ones(1,
phase_num));
end;

if isempty(Lr)
```

```
    Lr = (M+(2/phase_num)*Llr) * diag( [1, 1] );
end;

%%% theta-dependent variables
theta_e = P.*theta_m;
Lsr = M.* cos( repmat([0, pi/2]+theta_e, phase_num, 1) - repmat(ps', 1, 2) );
Lrs = Lsr.';
Lsr_ddtheta = -M.* sin( repmat([0, pi/2]+theta_e, phase_num, 1) - repmat(ps', 1, 2) );

%%% creating inductance matrix
Leq = [ Ls,  Lsr; ...
        Lrs, Lr   ...
        ];

%%% current calculation
i_sr = Leq \ psi_sr;
T_e = P.*(i_sr(1:phase_num,:).')*Lsr_ddtheta*i_sr(phase_num+1:phase_num+2,:);
%%% rotational mass equilibrium
omega_m_ddt = (T_e - T_l)/J;
```

Actual code which models the machine is very short, i.e. it is contained in two Matlab function blocks and is valid for any phase number. Nevertheless, additional coding was found to be necessary so that use of the model is more straightforward and input parameter error-checking is properly implemented.

It should be noted that care has been taken so that all variables which are constant are not recalculated at each simulation step. Instead, they are attributed as persistent so that simulation speed is increased. For example, stator and rotor self-inductance matrices $[L_s]$ and $[L_r]$ are constant throughout the simulation and they are persistent variables. On the other hand, mutual inductance matrices $[L_{sr}]$ and $[L_{rs}]$ are θ dependant, so they are recalculated at every simulation step. All used parameters and variables are local to the block only and do not interfere with the simulation global parameters.

A.2 Derivation of Machine Model in MS Variables (Mathematica)

Machine model in MS variables, detailed in the section 4.3 of the thesis, is obtained when 3-phase Clarke's transformation is applied to each winding set of the multiple 3-phase induction machine. In order to verify the equations, a computer algebra system Wolfram Mathematica is used.

Starting point is the machine model in phase variables, where both stator and rotor of an *n*-phase machine are modelled by *n* differential equations. Although presented code uses 9-phase induction machine as an example, it is valid for any multiple 3-phase machine, i.e. parameter *l*, defining the number of winding sets, needs to be changed, as well as parameter *asymm* which defines whether the machine is asymmetrical or symmetrical. The Mathematica code is as follows:

Multi-stator derivation

Equations in phase variables, rotor represented as a single winding set

$$[v_j] = [R_s] \times [i_j] + \frac{d}{dt}[\psi_j],\ j = 1, 2, \ldots l$$

$$[0] = \frac{1}{l}[R_r] \times [i_r] + \frac{d}{dt}[\psi_r]$$

$$[\psi_j] = L_{ls} \times i_j + \sum \left([L_{jk}].[i_k] \right) + [L_{jr}].[i_r],\ j = 1, 2, \ldots l;\ k = 1, 2, \ldots l$$

$$[\psi_r] = \frac{1}{l} L_{lr} \times i_r + \sum ([L_{rk}].[i_k]) + [L_{rr}].[i_r],\ k = 1, 2, \ldots l$$

$$[v_x] = \begin{bmatrix} v_{ax} \\ v_{bx} \\ v_{cx} \end{bmatrix},\ [i_x] = \begin{bmatrix} i_{ax} \\ i_{bx} \\ i_{cx} \end{bmatrix},\ [\psi_x] = \begin{bmatrix} \psi_{ax} \\ \psi_{bx} \\ \psi_{cx} \end{bmatrix},\ x = [j, k, r]$$

Machine type:

```
l = 3;(* number of 3-phase winding sets *)
asymm = 1;(* 1 → asymmetrical configuration, else → symmetrical *)
(* phase propagation angles are splitted into 3 parts:
   phases a, phases b, and phases c *)
θa = (asymm × π / (3 × l)) × Range[0, l - 1];
θb = θa + (2 π / 3) × Table[1, l];
θc = θa + (4 π / 3) × Table[1, l];
Print["θa = ", θa * 180 / π];
Print["θb = ", θb * 180 / π];
Print["θc = ", θc * 180 / π];
θa = {0, 20, 40}
θb = {120, 140, 160}
θc = {240, 260, 280}
```

Inductances in phase variables (as per initial equations):

```
Ljk[j_, k_] := M × {{Cos[θa[[k]] - θa[[j]]], Cos[θb[[k]] - θa[[j]]], Cos[θc[[k]] - θa[[j]]},
                    {Cos[θa[[k]] - θb[[j]]], Cos[θb[[k]] - θb[[j]]], Cos[θc[[k]] - θb[[j]]],
                    {Cos[θa[[k]] - θc[[j]]], Cos[θb[[k]] - θc[[j]]], Cos[θc[[k]] - θc[[j]]]};
Lje[j_] := M × {{Cos[θa[[j]] - θe[t]], Cos[θa[[j]] - θe[t] - 2 π / 3], Cos[θa[[j]] - θe[t] - 4 π / 3]},
                {Cos[θb[[j]] - θe[t]], Cos[θb[[j]] - θe[t] - 2 π / 3], Cos[θb[[j]] - θe[t] - 4 π / 3]},
                {Cos[θc[[j]] - θe[t]], Cos[θc[[j]] - θe[t] - 2 π / 3], Cos[θc[[j]] - θe[t] - 4 π / 3]}};
Lek[k_] := M × {{Cos[θa[[k]] - θe[t]], Cos[θb[[k]] - θe[t]], Cos[θc[[k]] - θe[t]]},
                {Cos[θa[[k]] - (θe[t] + 2 π / 3)], Cos[θb[[k]] - (θe[t] + 2 π / 3)], Cos[θc[[k]] - (θe[t] + 2 π / 3)]},
                {Cos[θa[[k]] - (θe[t] + 4 π / 3)], Cos[θb[[k]] - (θe[t] + 4 π / 3)], Cos[θc[[k]] - (θe[t] + 4 π / 3)]}};
Lee = M × {{Cos[0], Cos[2 π / 3], Cos[4 π / 3]},
           {Cos[2 π / 3], Cos[0], Cos[2 π / 3]},
           {Cos[4 π / 3], Cos[2 π / 3], Cos[0]}};
C3[alpha_] := 2 / 3 × {{Cos[alpha], Cos[alpha + 2 π / 3], Cos[alpha + 4 π / 3]},
                       {Sin[alpha], Sin[alpha + 2 π / 3], Sin[alpha + 4 π / 3]},
                       {1 / 2, 1 / 2, 1 / 2}};
M = 2 / 3 Lmms;
(* Lmms mutual inductance in multi-stator domain *)
```

Currents (relation between phase and multi-stator):

```
For[j = 1, j ≤ l, j++, i[j] = Inverse[C3[θa[[j]]]].{{iα[j][t]}, {iβ[j][t]}, {iz[j][t]}}];
i[r] = Inverse[C3[θe[t]]].{{iα[r][t]}, {iβ[r][t]}, {iz[r][t]}};
```

Flux linkage equations (currents in multi-stator domain):

```
For[j = 1, j ≤ l, j++,
  ψ[j] = L1s × i[j] + Sum[Ljk[j, k].i[k], {k, 1, l}] + Lje[j].i[r];
 ];
ψ[r] = 1 / l L1r × i[r] + Sum[Lrk[k].i[k], {k, 1, l}] + Lrr.i[r];
```

Machine equations:
- this should be modified to optimise symbolic calculation and to enable smooth calculation for any machine type !!!

```
θe'[t] = ωe[t];(* speed is derivative of position *)
For[j = 1, j ≤ l, j++,
  v[j] = FullSimplify[TrigReduce[Rs × C3[θa[[j]]].i[j]]] +
         FullSimplify[TrigReduce[C3[θa[[j]]].D[ψ[j], t]]];
 ];
v[r] = FullSimplify[TrigReduce[1 / l Rr × C3[θe[t]].i[r]]] +
       FullSimplify[TrigReduce[C3[θe[t]].D[ψ[r], t]]];
For[j = 1, j ≤ l, j++,
  Print["vαβz[", j, "] = ", v[j] // MatrixForm];
 ];
Print["vαβz[r] = ", v[r] // MatrixForm];
(*Print[ψ[r]//MatrixForm];*)
```

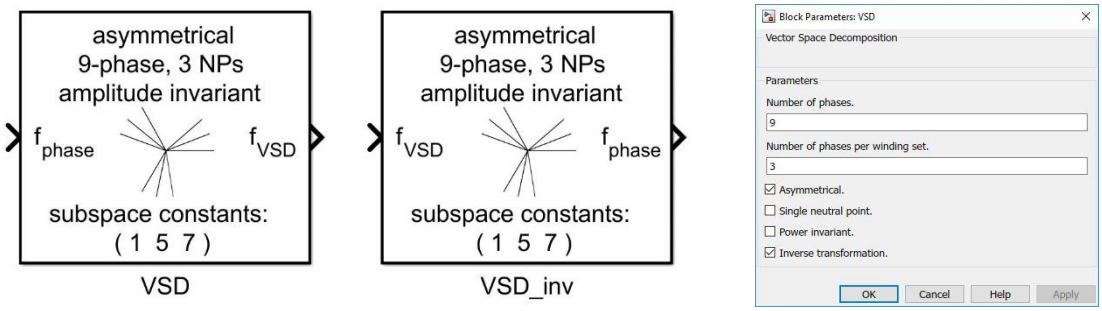

(a) (b) (c)

Figure A.3 – Simulink block for VSD transformation in direct (a) and inverse (b) form, and the properties tab (c).

$$v_{\alpha\beta z}[1] = \begin{pmatrix} L_{ls}\, i_\alpha[1]'[t] + L_{mms}\,(i_\alpha[1]'[t] + i_\alpha[2]'[t] + i_\alpha[3]'[t] + i_\alpha[r]'[t]) + R_s\, i_\alpha[1][t] \\ L_{ls}\, i_\beta[1]'[t] + L_{mms}\,(i_\beta[1]'[t] + i_\beta[2]'[t] + i_\beta[3]'[t] + i_\beta[r]'[t]) + R_s\, i_\beta[1][t] \\ L_{ls}\, i_z[1]'[t] + R_s\, i_z[1][t] \end{pmatrix}$$

$$v_{\alpha\beta z}[2] = \begin{pmatrix} L_{ls}\, i_\alpha[2]'[t] + L_{mms}\,(i_\alpha[1]'[t] + i_\alpha[2]'[t] + i_\alpha[3]'[t] + i_\alpha[r]'[t]) + R_s\, i_\alpha[2][t] \\ L_{ls}\, i_\beta[2]'[t] + L_{mms}\,(i_\beta[1]'[t] + i_\beta[2]'[t] + i_\beta[3]'[t] + i_\beta[r]'[t]) + R_s\, i_\beta[2][t] \\ L_{ls}\, i_z[2]'[t] + R_s\, i_z[2][t] \end{pmatrix}$$

$$v_{\alpha\beta z}[3] = \begin{pmatrix} L_{ls}\, i_\alpha[3]'[t] + L_{mms}\,(i_\alpha[1]'[t] + i_\alpha[2]'[t] + i_\alpha[3]'[t] + i_\alpha[r]'[t]) + R_s\, i_\alpha[3][t] \\ L_{ls}\, i_\beta[3]'[t] + L_{mms}\,(i_\beta[1]'[t] + i_\beta[2]'[t] + i_\beta[3]'[t] + i_\beta[r]'[t]) + R_s\, i_\beta[3][t] \\ L_{ls}\, i_z[3]'[t] + R_s\, i_z[3][t] \end{pmatrix}$$

$$v_{\alpha\beta z}[r] = \begin{pmatrix} \frac{1}{3} R_r\, i_\alpha[r][t] + \frac{1}{3} L_{lr}\,(i_\alpha[r]'[t] + \omega_e[t]\, i_\beta[r][t]) + L_{mms}\,(i_\alpha[1]'[t] + i_\alpha[2]'[t] + i_\alpha[3]'[t] + i_\alpha[r]'[t] + \omega_e[t]\,(i_\beta[1][t] + i_\beta[2][t] + i_\beta[3][t] + i_\beta[r][t])) \\ \frac{1}{3} L_{lr}\,(i_\beta[r]'[t] - \omega_e[t]\, i_\alpha[r][t]) + L_{mms}\,(i_\beta[1]'[t] + i_\beta[2]'[t] + i_\beta[3]'[t] + i_\beta[r]'[t] - \omega_e[t]\,(i_\alpha[1][t] + i_\alpha[2][t] + i_\alpha[3][t] + i_\alpha[r][t])) + \frac{1}{3} R_r\, i_\beta[r][t] \\ \frac{1}{3} L_{lr}\, i_z[r]'[t] + \frac{1}{3} R_r\, i_z[r][t] \end{pmatrix}$$

A.3 Creation of VSD Matrix (Matlab and Mathematica)

Section 4.4 of the thesis deals with the machine model in terms of VSD variables. In particular, subsection 4.4.1 proposes unified algorithm for the creation of the VSD matrix in a general case, i.e. valid for any standard asymmetrical or symmetrical configuration with single or multiple neutral points. Furthermore, VSD matrices created by the proposed algorithm are used throughout the thesis whenever there was a need for direct or inverse VSD matrix, in both simulations and experiments.

Matlab implementation of the proposed algorithm is in a form of Simulink block which acts as the direct/inverse VSD transformation for a symmetrical/asymmetrical *n*-phase polyphase system where *n* is a phase number larger or equal to three. Both power and amplitude invariant transformation are considered. Developed Simulink block is shown in the Fig. A.3a and A.3b in the direct and inverse VSD configuration, respectively. In this example, selected VSD transformations are intended for the asymmetrical 9-phase machine with three neutral points; hence, in the properties tab, shown in the Fig. A.3c, the number of phases is 9, number of phases per winding set is 3 and asymmetrical ‘tick box’ is checked. Similarly as in the case of the induction machine Simulink block, information on the selected configuration are shown here in the block icon as well, i.e. text at the top and schematic of selected machine configuration. In addition, subspace constants, as per subsection 4.4.2, are written at the bottom of the block icon. Code in Icon & Ports of the VSD Simulink block mask is as follows:

```
% display text
text(block_size(1)/2, block_size(2)-8, symmetry, 'hor', 'center', 'texmode','on');
text(block_size(1)/2, block_size(2)-20, machine_type, 'hor', 'center', 'texmode','on');
text(block_size(1)/2, block_size(2)-32, pow_inv, 'hor', 'center', 'texmode','on');
text(block_size(1)/2, 22, 'subspace constants:', 'hor', 'center', 'texmode','on');
text(block_size(1)/2, 10, ['( ', num2str(coeff_list), ' )'], 'hor', 'center', 'texmode','on');

% display port label
```

```
if inverse
    port_label('input',  1, ' f_{VSD}', 'texmode','on');
    port_label('output', 1, 'f_{phase} ', 'texmode','on');
else
    port_label('input',  1, ' f_{phase}', 'texmode','on');
    port_label('output', 1, 'f_{VSD} ', 'texmode','on');
end

% plot machine diagram
ends = 20 .* exp(1i.*phase_shift);
x=[]; y=[];
x0 = block_size(1)/2;
y0 = block_size(2)/2-5;
for ii = 1:1:phase_num
    x = [x, x0+[0, real(ends(ii))] ];
    y = [y, y0+[0, imag(ends(ii))] ];
end
plot(x,y);
```

All parameters and variables used are either defined in the block properties or in the block initialisation as follows:

```
% parameter checking
np_num = phase_num / phases_per_set;
if ( phase_num < 3 | phase_num ~= floor(phase_num) | ...
     phases_per_set < 3 | ~isprime(phases_per_set) | ...
     np_num ~= floor(np_num) | ...
     (phase_num == phases_per_set) & (asymmetrical == 1) | ...
     (phase_num == phases_per_set) & (single_NP == 0) ...
     ) ...
    error('Wrong input parameters!!!');
end

% parameters for symbol drawing
pos = get_param(gcbh,'Position');
block_size = [pos(3)-pos(1), pos(4)-pos(2)];
if ( asymmetrical & np_num~=1 ), symmetry = ['asymmetrical'];
else symmetry = ['symmetrical']; end
if ( single_NP | np_num==1 ), np = ['1 NP'];
else np = [num2str(np_num), ' NPs']; end
machine_type = [num2str(phase_num), '-phase, ', np];
if ( power_invariant ), pow_inv = ['power invariant'];
else pow_inv = ['amplitude invariant']; end

%%% phase propagation angles (for symbol drawing only)
phase_shift = zeros(phase_num);
for jj = 1:1:np_num
    for ii = 1:1:phases_per_set
        if asymmetrical % asymmetrical case
            phase_shift((ii-1)*np_num+jj) = (pi/phase_num)*((ii-1)*2*np_num+jj-1);
        else % symmetrical case
            phase_shift((ii-1)*np_num+jj) = (2*pi/phase_num)*((ii-1)*np_num+jj-1);
        end
    end
end

%%% subspace coefficients (for display only)
if asymmetrical % asymmetrical
    coeff_list = 1:2:phase_num;
    coeff_list = coeff_list( coeff_list < phase_num );
else % symmetrical
    coeff_list = 1:1:(phase_num/2);
    coeff_list = coeff_list( coeff_list < phase_num/2 );
end
if single_NP
    coeff_list = [ coeff_list( mod(coeff_list, phases_per_set) ~= 0 ), ...
                   coeff_list( mod(coeff_list, phases_per_set) == 0 ) ];
else
    coeff_list = coeff_list( mod(coeff_list, phases_per_set) ~= 0 );
end
```

VSD transformation block is created as Matlab function where icon is modified to depict selected machine configuration, as previously described. Therefore, actual VSD creation algorithm, detailed in the subsection 4.4.1 of the thesis, is contained inside Matlab function and is as follows:

```
function out = vsd( in, phase_num, phases_per_set, asymmetrical, single_NP, power_invariant,
inverse)

persistent trans;
if isempty(trans)
    trans = zeros(phase_num, phase_num);
    ws_num = phase_num/phases_per_set;

    % VSD and zero-sequence coefficients
    if power_invariant
        vsd_coeff = sqrt(2/phase_num);
        zs_coeff = sqrt(1/2);
    else
        vsd_coeff = 2/phase_num;
        zs_coeff = 1/2;
    end

    % defining phase propagation angles
    ps = zeros(1,phase_num);
    for jj = 1:1:ws_num
        for ii = 1:1:phases_per_set
            if asymmetrical % asymmetrical case
                ps((ii-1)*ws_num+jj) = (pi/phase_num)*((ii-1)*2*ws_num+jj-1);
            else % symmetrical case
                ps((ii-1)*ws_num+jj) = (2*pi/phase_num)*((ii-1)*ws_num+jj-1);
            end
        end
    end

    % defining subspace coefficients
    if asymmetrical % asymmetrical
        all_coeffs = 1:2:phase_num;
        all_coeffs = all_coeffs( all_coeffs < phase_num );
    else % symmetrical
        all_coeffs = 1:1:(phase_num/2);
        all_coeffs = all_coeffs( all_coeffs < phase_num/2 );
    end

    % non-neutral point sub-spaces
    index = 1;
    for jj = all_coeffs
        if mod(jj, phases_per_set) ~= 0
            trans(index, :)   = cos(jj*ps);
            trans(index+1, :) = sin(jj*ps);
            index = index + 2;
        end
    end

    % neutral point sub-spaces
    for jj = all_coeffs
        if (mod(jj, phases_per_set) == 0)
            trans(index, :)   = cos(jj*ps);
            trans(index+1, :) = sin(jj*ps);
            index = index + 2;
        end
    end

    % zero sequence/s for single neutral point
    if mod(phase_num,2) % odd number of phases
        trans(index,:) = zs_coeff.*cos(phase_num*ps);
    else % even number of phases
        if ~asymmetrical
            trans(index, :)   = zs_coeff.*cos(phase_num*ps);
            trans(index+1, :) = zs_coeff.*cos((phase_num/2)*ps);
        end
    end

    % amplitude or power invariant transformation
    trans = vsd_coeff.*trans;
```

```
    % account for additional zero-sequences in the case of the multiple NPs
    if ~single_NP
        if power_invariant
            one_zero_seq = repmat([1/sqrt(phases_per_set), zeros(1, ws_num-1)], 1,
phases_per_set);
        else
            one_zero_seq = repmat([1/phases_per_set, zeros(1, ws_num-1)], 1, phases_per_set);
        end
        for jj = phase_num-(ws_num-1):1:phase_num
            trans(jj, :) = one_zero_seq;
            one_zero_seq = circshift(one_zero_seq, [0,1]);
        end
    end

    % direct or inverse VSD
    if (inverse)
        trans = inv(trans);
    end
end

% calculation
out = trans * in;
```

Creation of actual transformation matrix is constrained to the initialisation of persistent variable *trans*, hence it is executed only once, while only matrix multiplication takes place at each simulation step, as can be seen in the last line of the shown code.

VSD creation algorithm is implemented in the Wolfram Mathematica as well so that it can be used to find relationship between MS and VSD variables in the following section. This is done by creating a Mathematica function and exporting it to the Mathematica package. Inputs to the function are number of phases per winding set, number of winding sets, whether the machine is asymmetrical or symmetrical with single or multiple neutral points, and should the transformation be power or amplitude invariant. Mathematica function that returns VSD matrix as a result is as follows:

```
(* VSD matrix *)
Vsd[k_, l_, asymmetrical_, singleNP_, powerInv_] := Module[
  {n, ps, coeffs, tVsd, sigma, sigmaZS, jj, zs},
  n = k × l;
  (* define phase propagation angles and subspace coefficients *)
  If[asymmetrical == 1, (* asymmetrical case *)
   ps = ArrayFlatten[Table[π/n × (2 × l × (ii - 1) + jj - 1), {ii, 1, k}, {jj, 1, l}], 1];
   coeffs = Join[Cases[Range[1, n, 2], x_ /; Mod[x, k] ≠ 0 && x < n], Cases[Range[1, n, 2], x_ /; Mod[x, k] == 0 && x < n]];
   , (* symmetrical case *)
   ps = ArrayFlatten[Table[2 × π/n × (l × (ii - 1) + jj - 1), {ii, 1, k}, {jj, 1, l}], 1];
   coeffs = Join[Cases[Range[1, n/2, 1], x_ /; Mod[x, k] ≠ 0 && x < n/2], Cases[Range[1, n/2, 1], x_ /; Mod[x, k] == 0 && x < n/2]];
  ];
  (* define subspaces *)
  tVsd = Table[0, 2 × Length[coeffs], n];
  For[jj = 1, jj ≤ Length[coeffs], ++jj,
   tVsd[[2 × jj - 1]] = Cos[coeffs[[jj]] × ps];
   tVsd[[2 × jj]] = Sin[coeffs[[jj]] × ps];
  ];
  (* deffine power invariance coefficient *)
  If[powerInv == 1, (* power invariant *)
   sigma = √(2/n); sigmaZS = 1/√2;
   , (* amplitude invariant *)
   sigma = 2/n; sigmaZS = 1/2;
  ];
```

```
(* define zero sequence/s if any exist *)
 If[OddQ[n], (* odd number of phases → single zero-sequence *)
   AppendTo[tVsd, sigmaZS × Cos[n × ps]];
   , (* symmetrical with even number of phases → two zero-sequences *)
   If[asymmetrical == 0,
     AppendTo[tVsd, sigmaZS × Cos[n × ps]];
     AppendTo[tVsd, sigmaZS × Cos[n/2 × ps]];
    ];
  ];
 (* amplitude/phase invariance *)
 tVsd = sigma × tVsd;
 (* single or multiple neutral points *)
 If[singleNP ≠ 1,
   coeffs = 1/√k /. _ /; powerInv ≠ 1 → 1/k;
   zs = Flatten[Table[{coeffs, Table[0, l - 1]}, k], 2];
   For[jj = n - l + 1, jj ≤ n, ++jj,
    tVsd[[jj]] = zs;
    zs = RotateRight[zs, 1];
   ];
  ];
 Return[tVsd];
 ];
(* export to Mathematica package *)
Save[NotebookDirectory[] <> "VSD_matrix.m", {Vsd}];
```

A.4 Correlation Between VSD and MS Variables (Mathematica)

Relationship between VSD and MS variables has been developed in the section 4.5 of the thesis, while the results are verified here by Wolfram Mathematica. Firstly, relationship equations (4.62) and (4.63) are implemented in a form of Mathematica function as follows:

```
(* relation between multi-stator and Vector Space Decomposition *)
VSDtoMS[l_, asymmetrical_] := Module[
 {ss, ii, ssNum, out},
 out = Table[{0}, l];
 (* αβ subspace *)
 out[[1]] = 1/l × Sum[fαβ[ii], {ii, 1, l}];
 (* non zero-sequence xy subspaces *)
 For[ss = 1, ss < l, ++ss,
  If[OddQ[ss],
   out[[ss + 1]] = 1/l × Sum[fαβ[ii]* × e^(i×(ss+1)×(ii-1)×π/l), {ii, 1, l}];
   ,
   out[[ss + 1]] = 1/l × Sum[fαβ[ii] × e^(i×ss×(ii-1)×π/l), {ii, 1, l}];
   ];
 ];
 (* zero-sequence xy subspaces *)
 If[OddQ[l],
  ssNum = (3 × l - 1)/2;
  ,
  If[asymmetrical == 1, ssNum = 3 × l/2;, ssNum = (3 × l - 2)/2;];
 ];
 For[ss = l, ss < ssNum, ++ss,
  If[asymmetrical == 1,
   AppendTo[out, 2/l × Sum[fz[ii] × e^(i×(2×(ss-l)+1)×(ii-1)×π/l), {ii, 1, l}]];
   ,
   AppendTo[out, 2/l × Sum[fz[ii] × e^(i×2×(ss-l+1)×(ii-1)×π/l), {ii, 1, l}]];
   ];
```

```
];
  (* zero-sequence homopolar components *)
  If[OddQ[l],
    If[asymmetrical == 1,
      AppendTo[out, 1/l * Sum[fz[ii] * Cos[(ii - 1) * π], {ii, 1, l}]];
      ,
      AppendTo[out, 1/l * Sum[fz[ii] * Cos[(ii - 1) * 2 * π], {ii, 1, l}]];
     ];
    ,
    If[asymmetrical ≠ 1,
      AppendTo[out, 1/l * Sum[fz[ii] * Cos[(ii - 1) * 2 * π], {ii, 1, l}]];
      AppendTo[out, 1/l * Sum[fz[ii] * Cos[(ii - 1) * π], {ii, 1, l}]];
     ];
   ];
  Return[out];
  ];
(* export to Mathematica package *)
Save[NotebookDirectory[] <> "VSD_MS_relation.m", {VSDtoMS}];
```

Then, a procedure to obtain relationship between VSD and MS described in the section 4.5 is implemented in Mathematica. Finally, results are compared for both symmetrical and asymmetrical case with a single neutral point. Input to the system is the number of 3-phase winding sets and information whether the calculation is going to be executed symbolically or numerically. Numerical calculation is necessary when there is no reasonably simple expression for sin/cos of the phase propagation angle, e.g. 15-phase case. Mathematica code that executes aforementioned, with the example of a 9-phase case, is as follows:

```
(* define number of winding sets *)
l = 3;
(* set numerical to 1 if cannot compute symbolically, e.g. l=5 *)
numerical = 0;
(* some initialisation code *)
Get[NotebookDirectory[] <> "VSD_matrix.m"];
Get[NotebookDirectory[] <> "VSD_MS_relation.m"];
n = 3 * l;
$Assumptions = {Table[{f[ii], fα[ii], fβ[ii], fz[ii]}, {ii, 1, l}] ∈ Reals};
(* phase propagations angles *)
psS = ArrayFlatten[Table[2 * π/n * (l * (ii - 1) + jj - 1), {ii, 1, 3}, {jj, 1, l}], 1];
psA = ArrayFlatten[Table[π/n * (2 * l * (ii - 1) + jj - 1), {ii, 1, 3}, {jj, 1, l}], 1];
(* create VSD matrices *)
(* Vsd[k,l,asymmetrical,single_neutral_point,powerInvariant] *)
TvsdS = Vsd[3, l, 0, 1, 0];
TvsdA = Vsd[3, l, 1, 1, 0];
If[numerical == 1, TvsdS = TvsdS // N; TvsdA // N;];
(* 3-phase Clarke's transformation *)
C3[alpha_] := 2/3 * {{Cos[alpha], Cos[alpha + 2π/3], Cos[alpha + 4π/3]},
                    {Sin[alpha], Sin[alpha + 2π/3], Sin[alpha + 4π/3]},
                    {1/2, 1/2, 1/2}}
(* Symmetrical case calculation *)
For[jj = 1, jj ≤ l, ++jj, (* apply inverse Clark's transformation *)
  {{f[jj]}, {f[jj + l]}, {f[jj + 2 * l]}} = Inverse[C3[psS[[jj]]]].{{fα[jj]}, {fβ[jj]}, {fz[jj]}};
 ];
fPhase = Table[{f[ii]}, {ii, 1, n}];
fVsd[1] = FullSimplify[Expand[TvsdS.fPhase]];(* apply VSD transformation *)
(* Asymmetrical case calculation *)
For[jj = 1, jj ≤ l, ++jj, (* apply inverse Clark's transformation *)
  {{f[jj]}, {f[jj + l]}, {f[jj + 2 * l]}} = Inverse[C3[psA[[jj]]]].{{fα[jj]}, {fβ[jj]}, {fz[jj]}};
 ];
```

```
fPhase = Table[{f[ii]}, {ii, 1, n}];
fVsd[2] = FullSimplify[Expand[TvsdA.fPhase]]; (* apply VSD transformation *)
(* transform to complex form and simplify coefficients *)
For[mm = 1, mm ≤ 2, ++mm,
 (* first l subspaces *)
 For[jj = 1, jj < n/2, ++jj,
  re = fVsd[mm][[2 × jj - 1, 1]];
  im = fVsd[mm][[2 × jj, 1]];
  coeff = 1/l /. _ /; jj > l → 2/l; (* jj>l ? 2/1 , 1/1 *)
  cpx = Solve[(* solve for temp *)
    Eliminate[(* eliminate fα, fβ and express by fαβ/fαβ* *)
     Flatten[{temp == re + I * im, Table[{fαβ[ii] == fα[ii] + i × fβ[ii], fαβ[ii]* == fα[ii] - i × fβ[ii]}, {ii, 1, l}]}],
     Flatten[Table[{fα[ii], fβ[ii]}, {ii, 1, l}]]
    ],
    temp];
  simpConstant[cc_] := Abs[cc] × e^(i × Mod[Arg[cc], 2π]); (* define function to simplify coefficients *)
  subspace = HoldForm[Evaluate[coeff]] × (* simpify coefficients to magxe^(i×arg) form *)
    Collect[cpx[[1, 1, 2]]/coeff, Flatten[Table[{fαβ[ii], fαβ[ii]*, fz[ii]}, {ii, 1, l}]], simpConstant];
  If[jj == 1, (* save variables *)
   fVsdCmp[mm] = {{"fαβ = ", subspace}};,
   AppendTo[fVsdCmp[mm], {"fxy" <> ToString[jj - 1] <> " = ", subspace}];];
 ];
 (* remaining subspace/zero-sequence/s *)
 If[OddQ[n], (* single zero-sequence homopolar component *)
  AppendTo[fVsdCmp[mm], {"fz+ = ", fVsd[mm][[n, 1]]}];
  ,
  If[mm == 2, (* single zero-sequence subspace (asymmetrical case) *)
    subspace = HoldForm[Evaluate[2/1]] ×
      Collect[1/2 × (fVsd[mm][[n - 1, 1]] + i × fVsd[mm][[n, 1]]), Table[fz[ii], {ii, 1, l}], simpConstant];
    AppendTo[fVsdCmp[mm], {"fxy" <> ToString[n/2] <> " = ", subspace}];
    , (* two zero-sequence homopolar components (symmetrical case) *)
    AppendTo[fVsdCmp[mm], {"fz+ = ", fVsd[mm][[n - 1, 1]]}];
    AppendTo[fVsdCmp[mm], {"fz- = ", fVsd[mm][[n, 1]]}];
   ];
 ];
];
(* print meaningful output *)
Print["Phase propagation angles:"];
Print["θ_symm = ", psS * 180 / π];
Print["θ_asymm = ", psA * 180 / π];
Print["Expression produced by the calculation: (real form)"];
Print["VSDs = ", MatrixForm[fVsd[1]], "     VSDa = ", MatrixForm[fVsd[2]]];
Print["Expression produced by the calculation: (complex form)"];
Print["VSDs = ", MatrixForm[fVsdCmp[1]] // TraditionalForm, "     VSDa = ", MatrixForm[fVsdCmp[2]] // TraditionalForm];
Print["Expression produced by the equation for general case: (complex form)"];
Print["VSDs = ", MatrixForm[VSDtoMS[1, 0]] // TraditionalForm, "     VSDa = ", MatrixForm[VSDtoMS[1, 1]] // TraditionalForm];
Print["VSDtoMS(calculated) - VSDtoMS(equations): (shoud be zero vector)"];
Print["VSDs = ", fVsdCmp[1][[ ;; , 2]] - VSDtoMS[1, 0] // ReleaseHold // FullSimplify // Chop // MatrixForm // TraditionalForm,
   "     VSDa = ", fVsdCmp[2][[ ;; , 2]] - VSDtoMS[1, 1] // ReleaseHold // FullSimplify // Chop // MatrixForm // TraditionalForm];
```

```
Phase propagation angles :
θ_symm = {0, 40, 80, 120, 160, 200, 240, 280, 320}
θ_asymm = {0, 20, 40, 120, 140, 160, 240, 260, 280}
Expression produced by the calculation : (real form)
```

$$\text{VSDs} = \begin{pmatrix} \frac{1}{3}(f\alpha[1]+f\alpha[2]+f\alpha[3]) \\ \frac{1}{3}(f\beta[1]+f\beta[2]+f\beta[3]) \\ \frac{1}{6}\left(2f\alpha[1]-f\alpha[2]-f\alpha[3]+\sqrt{3}\,(f\beta[2]-f\beta[3])\right) \\ \frac{1}{6}\left(\sqrt{3}\,f\alpha[2]-\sqrt{3}\,f\alpha[3]-2f\beta[1]+f\beta[2]+f\beta[3]\right) \\ \frac{1}{6}\left(2f\alpha[1]-f\alpha[2]-f\alpha[3]+\sqrt{3}\,(-f\beta[2]+f\beta[3])\right) \\ \frac{1}{6}\left(\sqrt{3}\,f\alpha[2]-\sqrt{3}\,f\alpha[3]+2f\beta[1]-f\beta[2]-f\beta[3]\right) \\ \frac{1}{3}(2fz[1]-fz[2]-fz[3]) \\ \frac{fz[2]-fz[3]}{\sqrt{3}} \\ \frac{1}{3}(fz[1]+fz[2]+fz[3]) \end{pmatrix} \quad \text{VSDa} = \begin{pmatrix} \frac{1}{3}(f\alpha[1]+f\alpha[2]+f\alpha[3]) \\ \frac{1}{3}(f\beta[1]+f\beta[2]+f\beta[3]) \\ \frac{1}{6}\left(2f\alpha[1]-f\alpha[2]-f\alpha[3]+\sqrt{3}\,(f\beta[2]-f\beta[3])\right) \\ \frac{1}{6}\left(\sqrt{3}\,f\alpha[2]-\sqrt{3}\,f\alpha[3]-2f\beta[1]+f\beta[2]+f\beta[3]\right) \\ \frac{1}{6}\left(2f\alpha[1]-f\alpha[2]-f\alpha[3]+\sqrt{3}\,(-f\beta[2]+f\beta[3])\right) \\ \frac{1}{6}\left(\sqrt{3}\,f\alpha[2]-\sqrt{3}\,f\alpha[3]+2f\beta[1]-f\beta[2]-f\beta[3]\right) \\ \frac{1}{3}(2fz[1]+fz[2]-fz[3]) \\ \frac{fz[2]+fz[3]}{\sqrt{3}} \\ \frac{1}{3}(fz[1]-fz[2]+fz[3]) \end{pmatrix}$$

Expression produced by the calculation : (complex form)

$$VSDs = \begin{pmatrix} f\alpha\beta = \frac{1}{3}\left(f\alpha\beta(1) + f\alpha\beta(2) + f\alpha\beta(3)\right) \\ fxy1 = \frac{1}{3}\left(f\alpha\beta(1)^{*} + e^{\frac{2i\pi}{3}}\, f\alpha\beta(2)^{*} + e^{-\frac{2i\pi}{3}}\, f\alpha\beta(3)^{*}\right) \\ fxy2 = \frac{1}{3}\left(f\alpha\beta(1) + e^{\frac{2i\pi}{3}}\, f\alpha\beta(2) + e^{-\frac{2i\pi}{3}}\, f\alpha\beta(3)\right) \\ fxy3 = \frac{2}{3}\left(fz(1) + e^{\frac{2i\pi}{3}}\, fz(2) + e^{-\frac{2i\pi}{3}}\, fz(3)\right) \\ fz+ = \frac{1}{3}\left(fz(1) + fz(2) + fz(3)\right) \end{pmatrix} \qquad VSDa = \begin{pmatrix} f\alpha\beta = \frac{1}{3}\left(f\alpha\beta(1) + f\alpha\beta(2) + f\alpha\beta(3)\right) \\ fxy1 = \frac{1}{3}\left(f\alpha\beta(1)^{*} + e^{\frac{2i\pi}{3}}\, f\alpha\beta(2)^{*} + e^{-\frac{2i\pi}{3}}\, f\alpha\beta(3)^{*}\right) \\ fxy2 = \frac{1}{3}\left(f\alpha\beta(1) + e^{\frac{2i\pi}{3}}\, f\alpha\beta(2) + e^{-\frac{2i\pi}{3}}\, f\alpha\beta(3)\right) \\ fxy3 = \frac{2}{3}\left(fz(1) + e^{\frac{i\pi}{3}}\, fz(2) + e^{\frac{2i\pi}{3}}\, fz(3)\right) \\ fz+ = \frac{1}{3}\left(fz(1) - fz(2) + fz(3)\right) \end{pmatrix}$$

Expression produced by the equation for general case : (complex form)

$$VSDs = \begin{pmatrix} \frac{1}{3}\left(f\alpha\beta(1) + f\alpha\beta(2) + f\alpha\beta(3)\right) \\ \frac{1}{3}\left(f\alpha\beta(1)^{*} + e^{\frac{2i\pi}{3}}\, f\alpha\beta(2)^{*} + e^{-\frac{2i\pi}{3}}\, f\alpha\beta(3)^{*}\right) \\ \frac{1}{3}\left(f\alpha\beta(1) + e^{\frac{2i\pi}{3}}\, f\alpha\beta(2) + e^{-\frac{2i\pi}{3}}\, f\alpha\beta(3)\right) \\ \frac{2}{3}\left(fz(1) + e^{\frac{2i\pi}{3}}\, fz(2) + e^{-\frac{2i\pi}{3}}\, fz(3)\right) \\ \frac{1}{3}\left(fz(1) + fz(2) + fz(3)\right) \end{pmatrix} \qquad VSDa = \begin{pmatrix} \frac{1}{3}\left(f\alpha\beta(1) + f\alpha\beta(2) + f\alpha\beta(3)\right) \\ \frac{1}{3}\left(f\alpha\beta(1)^{*} + e^{\frac{2i\pi}{3}}\, f\alpha\beta(2)^{*} + e^{-\frac{2i\pi}{3}}\, f\alpha\beta(3)^{*}\right) \\ \frac{1}{3}\left(f\alpha\beta(1) + e^{\frac{2i\pi}{3}}\, f\alpha\beta(2) + e^{-\frac{2i\pi}{3}}\, f\alpha\beta(3)\right) \\ \frac{2}{3}\left(fz(1) + e^{\frac{i\pi}{3}}\, fz(2) + e^{\frac{2i\pi}{3}}\, fz(3)\right) \\ \frac{1}{3}\left(fz(1) - fz(2) + fz(3)\right) \end{pmatrix}$$

VSDtoMS (calculated) - VSDtoMS (equations): (shoud be zero vector)

$$VSDs = \begin{pmatrix} 0 \\ 0 \\ 0 \\ 0 \\ 0 \end{pmatrix} \qquad VSDa = \begin{pmatrix} 0 \\ 0 \\ 0 \\ 0 \\ 0 \end{pmatrix}$$

Appendix B

DESCRIPTION OF THE EXPERIMENTAL SETUP

B.1 Hardware Description

Three different experimental setups have been used in the thesis: configuration with RL load in the section 4.6 to demonstrate imbalance in the phase voltages harmonics of an asymmetrical machine with single neutral point, configuration with two two-level VSIs with dc links connected in parallel in chapter 5 and topology with two two-level and single three-level VSI with dc links connected in series in chapter 6. Since schematics of the used experimental setup are available in the respective parts of the thesis, they are not repeated here. Instead, a more detailed description of the used components, which is not available elsewhere in the thesis, is provided. Nevertheless, for the sake of completeness, a picture of the most used experimental setup, the one used in chapter 5, is shown in the Fig. B.1. The following equipment can be seen:

- Asymmetrical 9-phase induction machine.
- Dc machine shaft-coupled to the 9-phase induction machine.
- Magtrol TM250 torque meter.
- Two custom made two-level 8-phase voltage source inverters.
- dSPACE rapid prototyping system and Windows PC used for control.
- Two Tektronix oscilloscopes with active high voltage differential and current probes.
- Spitzenberger & Spies PAS2500 linear power amplifier capable of 4 quadrant operation with accompanying resistive load RL4000.
- Sorensen SGI600/25 single quadrant dc-voltage source.

Besides shown, additional pieces of equipment used in the experiments in the chapter 6 are as follows:

- Single custom made three-level 6-phase NPC voltage source inverter.
- Current and voltage measurement sensors adapted to work with dSPACE.
- Resistor box used to load the dc machine.

The additional equipment used in experiments of the fourth chapter is a simple RL load, which has been already described; hence, it is not discussed here any further.

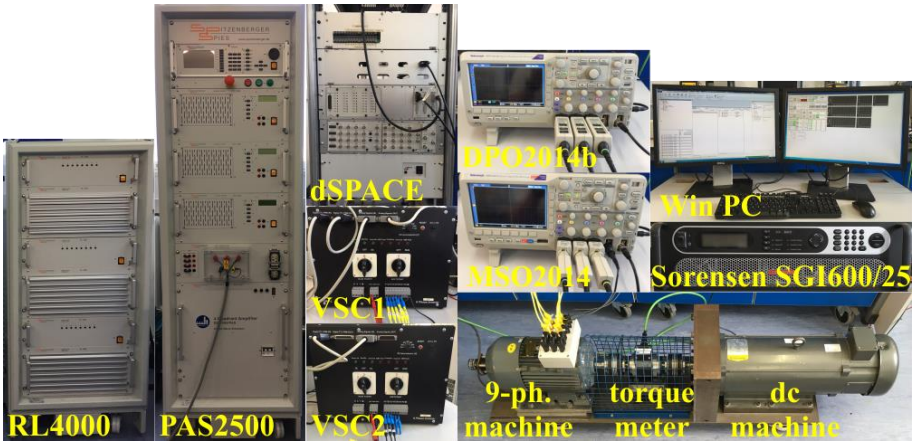

Figure B.1 – Experimental setup.

Experiments in chapters 5 and 6 use a custom made asymmetrical 9-phase induction machine. It is created by rewinding the stator winding of the standard 3-phase induction machine. Original machine is a 3-phase induction machine with squirrel cage rotor, made by FFD Austria, with model number 2SIE100L4A. It had two pole pairs, 36 stator slots and distributed windings, rated at 230 V phase-to-neutral, 2.2 kW, 4.5 A. After rewinding the stator in such a way that windings of each phase take 4 slots, resulting machine has nine phases with asymmetrical winding configuration; both ends of each phase are available so that machine can be supplied in single and double sided configurations. New 9-phase machine is with single pole pair, with the same voltage and power rated values, while rated phase current is 1.5 A. Parameters are given in the table B.1.

Table B.1 – Parameters of the Asymmetrical 9-phase induction machine.

R_s	R_r	L_{ls}	L_{lr}	L_m
5.3 Ω	2 Ω	24 mH	11 mH	520 mH

Machine has shaft-mounted Omron E6B2-CWZ1X rotary incremental encoder for position measurement. Encoder resolution is 1000 pulses per revolution and it is connected to dSPACE DS3002 encoder board.

Controlled 9-phase machine is shaft-coupled to the dc-machine which can produce positive or negative torque depending on the winding current. Used dc machine is Baldor VP3605D rated at 3.7 kW, 180 V, 24.5 A and 1750 rpm. Field is produced by permanent magnets; hence, there is no capability to operate above rated speed. Consequently, speed of both dc and induction machine is limited to 1750 rpm.

In order to produce both positive and negative torque and be able to make a step change in load torque (torque reversal), dc machine has been connected to the Sorensen SGI600/25 dc source and variable resistive load. Since used dc source is capable of operation in single quadrant, care should be taken when machine reverses, i.e. dc source cannot produce negative voltage nor sink current, so connecting cables need to be reversed. There are three possible scenarios of using this configuration:

- Dc machine operates in generating mode: stator current and torque are governed by machine speed and chosen resistive load.

- Dc machine operates in motoring mode: stator current and torque are set by dc source which operates in constant current mode (torque is unrelated to the rotational speed).
- Dc machine changes operation from generating to motoring mode in a step manner: stator current is initially set by resistor box (generation) and then dc source output is enabled (motoring) so that it sources current to both dc machine and resistor box.

In all three cases mechanical torque is measured by Magtrol TM-210 torque meter. It is supplied by accompanying signal amplifier Magtrol 6400. Information on mechanical torque, speed and power is available on amplifier display. Moreover, one of the single-ended basic oscilloscope voltage probes is connected to the torque meter output so that torque value is available on the oscilloscope as well. Torque meter voltage gain is 10 Nm/V. One of the features of the torque meter is a settable 2nd order Butterworth low-pass filter. In this case it set to 200 Hz.

Two level VSIs, used to supply the induction machine, are custom made. Output voltages are set by three Infineon FS50R12KE3 EUPEC IGBT 6-pack power modules. Eight legs are used as output, while the remaining one drives the braking resistor to protect dc-link capacitors in the case of the power reversal. Dc link can be supplied directly by dc-voltage source or by 3-phase grid. In the second scenario, grid voltage is rectified by three Semikron SKKD 46 rectifier modules. VSI is equipped with current measurement based on Honeywell CSNE151-100 current sensors. Each phase current is measured and made available to dSPACE DS2004 ADC board over DB50 connector. Gating signals to the VSI are provided by dSPACE DS5101 digital waveform output (DWO) board over DB37 connector.

In this particular case, when the 9-phase machine is supplied, two VSIs are needed. However, in order to control both VSIs with a single 16 channel DWO board, only seven channels are available per VSI while remaining two channels are used as enable signals, i.e. one for each VSI. Machine is connected in such a way that the first two winding sets are supplied by one VSI and the remaining winding set by the second inverter.

In the case when cascaded connection of VSI dc links is needed, two two-level VSIs and a single three-level VSI are used. Three-level VSI used here is set to provide two-level output. Each winding set is supplied by the individual inverter, as explained in the chapter 6. In this configuration, two dSPACE DWO boards are needed; the first one provides gating signals for two two-level VSIs, while the second one drives a single three-level VSI. Moreover, measurement is not done by the VSI internal current measurement sensors. Instead, phase currents and all three dc-link voltages are measured by separate measurement boxes. Current measurement box is created by using Honeywell CSNE151-100 current sensors, while LEM LV25-P voltage sensors are used to capture voltages in the voltage box. Both current and voltage box are connected to filter box which provides 1st order low-pass filtering and reroutes signals so that all can be captured by dSPACE ADC board over DB50 connector.

Used three-level VSI is of NPC type, created by use of Semikron SKM50GB12T4 IGBT modules and Semikron SKKD 46 rectifier modules. It can be supplied in the same manner as the two-level VSI, i.e. directly by dc-voltage source or by 3-phase grid. Even though external current measurement is used,

internal current measurement is possible in the same manner as in the two-level VSIs, by use of Honeywell CSNE151-100 current sensors.

In the experiments, dc-link voltage is provided by Spitzenberger & Spies linear power amplifier. It consists of three PAS2500 modules where each module is capable of four-quadrant operation up to 2.5 kW. Dc-link voltage of 600 V is created by setting the one module to +300 V, while the second one produces -300 V. To aid the operation in the 2^{nd} and 4^{th} quadrants, i.e. power sinking, resistive load RL4000 is connected to the main power amplifier.

Control and measurement in all experiments is achieved using dSPACE rapid prototyping system. It consists of main processor board DS1006 and multiple peripheral boards:

- DS5101, digital waveform output board, used for gating signal generation.
- DS2004, analogue to digital converter board, used for current/voltage measurements.
- DS3002, encoder board, used for capturing encoder pulses and finding position and speed.
- DS2101, digital to analogue converter board, used to provide synchronisation with oscilloscopes.

More details regarding the control system is available in the following section which describes software part of the experimental setup.

dSPACE system can only collect measurements at the control loop frequency. Therefore, two oscilloscopes are used for more precise measurements, i.e. Tektronix DPO2014b and MSO2014b. Both are 100 MHz, four channel, deep memory scopes with 1 GS/s sampling frequency and 1.25 million points memory depth, where the second one is a mixed signal oscilloscope as well. In this thesis, one scope is used to capture three voltages, while the other captures three currents and the torque. Voltage is measured using high voltage active differential probes Tektronix P5205A, while currents are measured by active current probes Tektronix TCP0030A. Torque is available from the torque sensor, as detailed before. Both scopes are synchronised to the same signal by an auxiliary channel.

B.2 Software Description

Although description of the control loops and implementation is described throughout the thesis where appropriate, it is felt that actual implementation in dSPACE rapid prototyping system should be provided as well. All experiments conducted in the thesis are initially tested by simulation in Simulink environment. Since dSPACE workflow is capable of using Simulink files by means of Simulink Coder, initial Simulink file is adapted by removing blocks that simulate hardware physically available in the laboratory and adding dSPACE specific blocks to create an interface to the dSPACE peripheral boards. This enables execution of the developed control on dSPACE processor board DS1006, while all user inputs are provided by graphic user interphase developed in Control Desk.

Firstly, machine model, VSI model, and PWM modulator are removed. Instead, dwell times are calculated and provided as variables to the DWO board (DS5101) by use of *DS5101DWO* block from the dSPACE specific Real-Time Interface (RTI) library. DS5101 board uses custom written code to

create gating signals based on calculated dwell time. Triangular carrier is assumed. Since DWO board uses high precision counter (250 ns ticks), it is used to generate an interrupt over PHS bus to the main processor board. DWO board interrupt is enabled and acknowledged by *System Start* and *System Outputs* blocks from the Simulink Coder library, respectively. Generated interrupt triggers the timer task and whole control code is executed. Furthermore, interrupt is synchronised with PWM signals so that control code is executed exactly at the beginning and in the middle of the switching period. By doing so, dSPACE sampling/execution frequency is double the switching frequency. Doubling of the control loop execution speed was found to be necessary in order to successfully eliminate 29^{th} and 31^{st} harmonics present in the machine phase current, as discussed in section 3.6 of the thesis. PWM switching frequency is set to 5 kHz, while control loop is executed at 10 kHz in all experiments.

Since DWO board has 16 channels, one board is enough for producing gating signals for both two-level inverters, e.g. experiments in the chapter 5. However, in the experiment conducted in the chapter 6, three VSI are needed, hence two DWO boards are used; board A creates gating signals for the two two-level inverters, while board B creates gating signals for the single three-level inverter.

Besides gating signal generation, phase current and rotor position values are required, so that IRFOC can be successfully implemented. Current measurements are provided by current sensors, while values are obtained by ADC board DS2004. Acquisition is started at each execution step by use of *DS2004ADC_BLx* block. Acquired current values are multiplied by predefined current sensor gains and offset is removed. Since acquisition is happening in the beginning and in the middle of the switching period, where current has an average value over switching period when triangular carrier is used, no additional filtering was needed.

In order to capture encoder pulses, encoder board DS3002 is used. Position measurement is realised by counting the number of encoder pulses between two sample intervals. This behaviour is embedded in the *DS3002POS_B1_C1* Simulink block which provides position and speed. Since this type of measurement is intended for high speed measurement and only few pulses were generated in one sampling interval when machine operates at 1000 rpm, error in measured position and speed could not be neglected. Therefore, position and speed measurement is started every 10 samples and additional filtering is implemented by use of the 2^{nd} order low-pass filter.

As mentioned earlier, all measurements are captured by dSPACE and oscilloscopes. However, these measurements need to be synchronised, so that both devices capture the same data. dSPACE and oscilloscopes are synchronised by use of DAC board DS2101, i.e. signal used to start the measurements over the dSPACE platform is used as a trigger signal for both oscilloscopes. For example, if a certain sequence needs to be recorded, starting of the sequence would be used to start both dSPACE and oscilloscope measurements. Control Desk Recorder is used to capture data by the dSPACE, while custom Matlab functions were created to access oscilloscopes and transfer captured data over VISA protocol. Communication between Matlab and oscilloscopes is made possible by use of Instrument Control Toolbox.

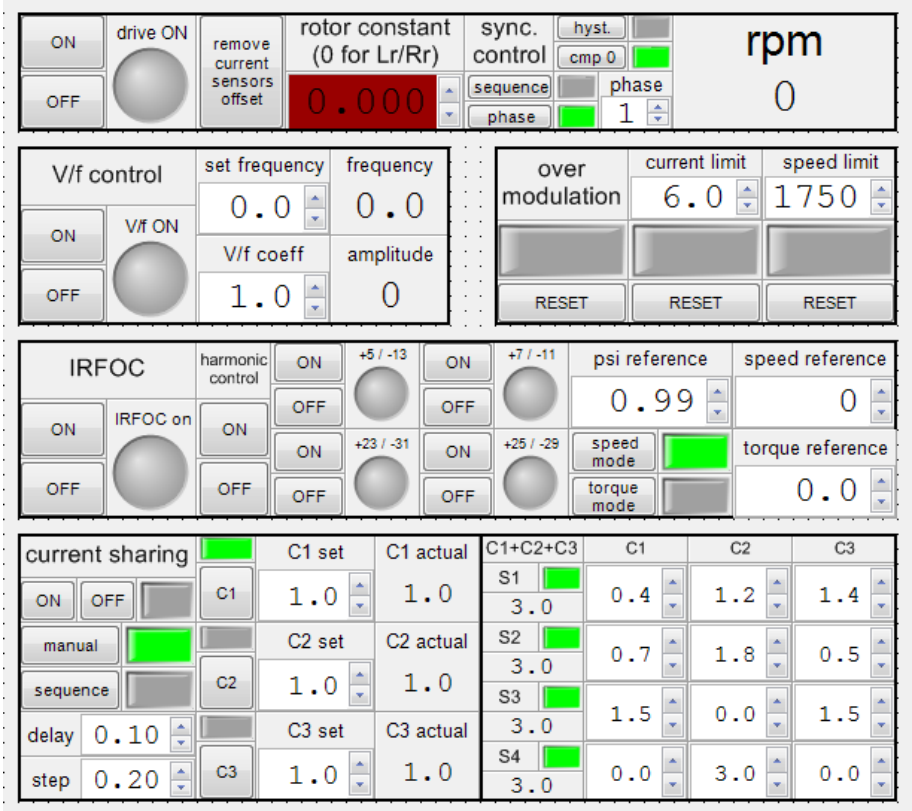

Figure B.2 – Example of the graphic user interface developed in Control Desk.

Last but not least, graphic user interface to the dSPACE platform is created by Control Desk. This software allows for real time access to the control variables. An example of the developed graphic user interface is shown in the Fig. B.2. All basic drive controls can be seen, such as: turn the drive on/off, set a speed reference, control the low order harmonics elimination or control the current sharing.

Appendix C

PUBLICATIONS RESULTING FROM THE THESIS

C.1 Journal Publications

Zoric, I., Jones, M, Levi, E., (2018), Arbitrary power sharing among three-phase winding sets of multiphase machines, *IEEE Transactions on Industrial Electronics*, vol. 65, no. 2, pp. 1128-1139.

C.2 Conference Publications

Zoric, I., Jones, M, Levi, E., (2016), Phase voltage harmonic imbalance in asymmetrical multiphase machines with single neutral point, *Proc. IEEE Annual Conference of the Industrial Electronics Society IECON*, Florence, Italy, pp. 4343-4348.

Zoric, I., Zabaleta, M., Jones, M, Levi, E., (2017), Techniques for power sharing between winding sets of multiple three-phase machines, *Proc. IEEE Workshop on Electrical Machines Design, Control and Diagnosis WEMDCD*, Nottingham, UK, pp. 208-215.

Zoric, I., Jones, M, Levi, E., (2017), Voltage balancing control of a symmetrical nine-phase machine with series-connected DC links, *Proc. IEEE International Symposium on Industrial Electronics ISIE*, Edinburgh, UK, pp. 1052-1057.

Zoric, I., Jones, M, Levi, E., (2017), Vector space decomposition algorithm for asymmetrical multiphase machines, *Proc. IEEE International Symposium on Power Electronics*, Novi Sad, Serbia, pp. 1-6.

Zoric, I., Jones, M, Levi, E., (2018), Arbitrary d-q current sharing in three-phase winding sets of multiphase machines, *Proc. IET International Conference on Power Electronics, Machines and Drives PEMD*, Liverpool, UK, pp. 1-6.